TECHNISCHE UNIVERSITÄT MÜNCHEN
LEHRSTUHL FÜR AERODYNAMIK UND STRÖMUNGSMECHANIK

Aeroacoustic Characteristics of a Shrouded Helicopter Tail Rotor

Jae Hun You

Vollständiger Abdruck der von der Fakultät für Maschinenwesen der Technischen Universität München zur Erlangung des akademischen Grades eines

Doktor-Ingenieurs

genehmigten Dissertation.

Vorsitzender:	Prof. Dr.-Ing. Steffen Marburg
Prüfer der Dissertation:	1. apl. Prof. Dr.-Ing. Christian Breitsamter
	2. apl. Prof. Dr.-Ing. habil. Stefan Becker

Die Dissertation wurde am 27.03.2017 bei der Technischen Universität München eingerichtet und durch die Fakultät für Maschinenwesen am 22.10.2017 angenommen.

Vorwort

Die vorliegende Arbeit entstand während meiner Tätigkeit als wissenschaftlicher Mitarbeiter am Lehrstuhl für Aerodynamik und Strömungsmechanik der Technischen Universität München.
Besonders möchte ich mich bei meinem Doktorvater Herrn apl. Prof. Dr.-Ing. Christian Breitsamter für die Möglichkeit zur Durchführung dieser Arbeit, deren ausgezeichnete Betreuung und die hervorragende Unterstützung bedanken. Ebenfalls möchte ich mich bei Herrn apl. Prof. Dr.-Ing. Stefan Becker für die Übernahme der Aufgabe des Zweitprüfers und Herrn Univ.-Prof. Dr.-Ing. Steffen Marburg für die Übernahme der Aufgabe des Vorsitzes der Prüfungskommission bedanken.
Mein besonderer Dank gilt Herrn M.Sc. Jithendra Tirakala für die wertvollen fachliche Diskussionen und Herrn Dr.-Ing. Christoph Scheit für die Bereitstellung des Akustik-Postprocessing-Tools SPySI. Weiterhin möchte ich meinen ehemaligen Kollegen am Lehrstuhl für das gute Arbeitsklima und die anregenden Diskussionen zu verschiedensten fachlichen Fragestellungen danken.
Mein größter herzlicher Dank für die umfangreiche Unterstützung zum Gelingen dieser Arbeit geht an meine Eltern in Südkorea, meine Mutter, meinen Vater und meine Schwiegermutter.
In besonderem Maße möchte ich mich bei meiner Frau Sun Ah Choi bedanken. Ohne ihre Unterstüzung wäre ich nicht an diesem Ziel angelangt.
Ich widme diese Arbeit meinen lieben Töchtern Hae Sun und Ji Sun. Papa liebt euch über alles.

Bonn, Mai 2018 Jae Hun You

Abstract

The shrouded tail rotor, a multibladed axial flow fan mounted in the helicopter vertical tail fin, is an advanced anti-torque device for the helicopter configuration equipped with a single main rotor. This type of tail rotor has been confirmed to be less noisy than a conventional open tail rotor due to its unique concept embedding the anti-torque rotor in the vertical tail fin and the multibladed rotor configuration. In certain tail rotor operating conditions, particularly under cross flow, the shrouded tail rotor is still a significant source of aerodynamic noise due to highly complex unsteady flow fields both inside and outside the shroud fairing and their interaction with rotating blades. The aim of this thesis is therefore to contribute to a better understanding of noise generation and propagation mechanisms of such complex flow fields by applying numerical approaches. Two helicopter operating conditions, namely the hovering and high-speed forward flight, are considered. The methodology used is a hybrid method of the computational aeroacoustics combining the unsteady Reynolds-averaged Navier-Stokes Equation (URANS) simulation with the Ffowcs Williams and Hawkings (FWH) acoustic analogy to predict sound pressure levels in the far field. For both flight conditions, the predictive capability of the hybrid method employed are assessed by comparison with data obtained by flight test campaigns.

The analysis of the hovering condition provides an in-depth understanding of the noise generation mechanism of the shrouded tail rotor without any cross-flow impacts. The rotor/stator interaction, particularly the potential field interaction between the rotor and stator row, is found as the most significant flow phenomenon that determines both the aerodynamic and acoustic characteristics of the shrouded tail rotor in the hovering flight. Accordingly, the drive shaft fairing is identified as the most significant noise source.

In the forward flight condition, the inflow of the anti-torque rotor is strongly disrupted by the fuselage wake, resulting from massive flow separation on the fuselage aft-body, and boundary layer separation on the inlet lip, leading to significant inlet flow distortion above the rotor plane. Detailed analysis of the noise generation by the interaction of the inlet flow distortion with the rotating blades is performed. For this purpose, a non-distorted case, achieved by active flow control using lip boundary layer suction, is introduced. In order to assess the effect of the turbulence model on the noise prediction, the shear-stress transport (SST) turbulence model is compared with the scale-adaptive simulation (SAS) method. Due to its capability to resolve turbulent flow scales, the SAS method provides enhanced noise levels in the relatively high frequency range compared to the SST turbulence model. In addition, the influence of the main rotor downwash on the acoustic characteristics of the shrouded tail rotor in the high-speed forward flight is examined by using the actuator disc approach. Furthermore, the effect of the horizontal stabilizer, installed upstream of the shrouded tail rotor, on the far-field sound pressure are also discussed.

Übersicht

Ein gekapselter Heckrotor ist eine fortgeschrittene Gegendrehmomentvorrichtung einer konventionellen Hubschrauberkonfiguration. Dieser Heckrotortyp besitzt bessere Charakteristiken bezüglich der Lärmemission im Vergleich zu konventionellen ungekapselten Heckrotoren. In bestimmten Betriebszuständen des Heckrotors, insbesondere unter Querströmungseinfluss, ist allerdings das vorherrschende Strömungsfeld innerhalb und außerhalb der Ummantelung sehr komplex. Dies kann bei Interaktion mit dem rotierenden Fan zu einer negativen Auswirkung auf die akustische Charakteristik des gekapselten Heckrotors führen. Ziel dieser Arbeit ist daher, einen Beitrag zum besseren Verständnis der Schallentstehungs- und Schallausbreitungsmechanismen derartiger komplexer Konfigurationen und zugehöriger Strömungsfelder mithilfe von numerischen Methoden zu leisten. In den hier durchgeführten Untersuchungen werden die akustischen Charakteristiken des gekapselten Heckrotors mittels eines hybriden Verfahrens für zwei hubschrauberrelevante Flugzustände, nämlich den Schwebe- und den Vorwärtsflug, bewertet. Die strömungsinduzierten Schallquellen werden dabei anhand numerischer Strömungssimulationen (URANS) erfasst, wobei die Schallausbreitung ins Fernfeld wird mittels eines FWH Integralverfahrens beschrieben wird. Die Aussagekraft des angewendeten hybriden Verfahrens wird anhand von Flugversuchsdaten für beide untersuchten Flugzustände bewertet.

Im Fall des Schwebefluges liefert die Analyse ein vertieftes Verständnis zur Schallentstehung des gekapselten Heckrotors ohne jegliche Querströmungseinflusse und Eintrittsstörungen. Dabei stellt die Rotor-Stator-Wechselwirkung, insbesondere die Rotor-Stator-Potentialfeld-Wechselwirkung, das bedeutendste Strömungsphänomen dar, das sowohl die aerodynamischen als auch die akustischen Eigenschaften des gekapselten Heckrotors im Schwebeflugzustand bestimmt. Dementsprechend wird die Verkleidung der Heckrotor-Antriebswelle als die signifikanteste Schallquelle in diesem Flugzustand identifiziert.

Im Vorwärtsflugzustand gestaltet sich das Strömungsfeld am Eintritt des gekapselten Heckrotors als sehr komplex aufgrund des Rumpf-Nachlaufes mit abgelöster und wirbeldominierter Strömung und der Eintrittsstörung, die aus der Grenzschichtablösung an der Eintrittslippe folgt. Detaillierte Analysen zum Schallentstehungsmechanismus bei der Interaktion zwischen der Eintrittsstörung und den rotierenden Fan-Blättern werden durch einen Vergleich mit dem störungsfreien Fall mittels Grenzschichtabsaugungen an der Eintrittslippe durchgeführt. Einflüsse des Turbulenzmodells auf die Vorhersagegenauigkeit des vom gekapselten Heckrotor abgestrahlten Lärms werden durch einen Vergleich des SST-Turbulenzmodells mit der skalenauflösenden SAS-Methode bewertet. Die Auswirkung des durch den Hauptrotor induzierten Abwindes auf die akustische Eigenschaft des Heckrotors wird unter der Verwendung eines Wirkscheibenansatzes, insbesondere für den schnellen Vorwärtsflugzustand, untersucht. Einflüsse des Höhenleitwerks auf die Schallentstehung des gekapselten Heckrotors werden in dieser Arbeit ebenfalls diskutiert.

Table of Contents

List of Figures

List of Tables

Nomenclature

Latin symbols	Unit	Description
A	m^2	area
A_0	Pa	amplitude of the fundamental sound pressure
C_n	-	normal force coefficient
C_p	-	pressure coefficient, $C_p = p_s - p_\infty / 0.5 \rho_\infty U_\infty^2$
$\overline{C}_p$	-	mean (time-averaged) pressure coefficient
C'_p	-	pressure coefficient fluctuation
C_T	-	thrust coefficient
$\overline{C}_T$	-	mean (time-averaged) thrust coefficient
C_x, C_y, C_z	-	streamwise, lateral, vertical force coefficient
C_μ	-	momentum coefficient
$CD_{k\omega}$	-	cross diffusion term of the SST turbulence model
c	m/s	speed of sound
c_r	m	wing root chord
D_f	m	fan diameter
D_{mic}	m	distance between the main rotor axis and the microphone
d	m	grid spacing
d_{op}	m	distance to the observer point
F_1	-	first blending function of the SST turbulence model
F_2	-	second blending function of the SST turbulence model
F_{BCD}	-	blending factor of the Bounded Central Differencing scheme
F_n	N	normal force on the actuator disc
F_x, F_y, F_z	N	streamwise, lateral, vertical force
f	Hz	frequency
f_{BPF}	Hz	blade passing frequency, $f_{\text{BPF}} = I_b f_R$
f_R	Hz	rotational frequency of the fan
H	m	flight altitude above the ground level
$H(f)$	-	Heaviside function of f
I_b	-	number of blade
k	m^2/s^2	turbulence kinetic energy
L	-	integral length scale of modeled turbulence
$L_{\nu K}$	-	von Kármán length scale
l_{ref}	m	reference length
Ma	-	Mach number
m_s	-	number of modulation cycle

$\dot{m}_f$	kg/s	mass flow rate through the fan mid-interface
$\dot{m}_s$	kg/s	mass flow rate through the collector lip suction slot
n_b	-	number of frequency bands
n_i	-	outward normal vector
P_b	deg	blade pitch angle
P_{ij}	Pa	compressible stress tensor
p'	Pa	sound pressure
p_s	Pa	static pressure
p'_s	Pa	static pressure fluctuation
p_t	Pa	total pressure
p_∞	Pa	reference static pressure
Q	$1/s^2$	second invariant of the velocity gradient tensor
Q_{SAS}	-	SAS source term
R	m	radius of the directivity sphere
Re	-	Reynolds number
r	m	fan radius
r_1	m	inner radius of the actuator disc
r_2	m	outer radius of the actuator disc
r_{lip}	m	collector lip radius
S	1/s	strain-rate magnitude
$S_{C'_p}$	1/Hz	power spectral density of C'_p
S_{ij}	1/s	strain-rate tensor
S_s	-	FWH control surface
S_v	N/m^3	volumetric source term of the actuator disc
ΔS	J/K	entropy rise
T_{ij}	Pa	Lighthill stress tensor
T_∞	K	ambient temperature
Tu	-	turbulence intensity
t	s	time
t_{adv}	s	advancing time
t_e	s	emission time
U, u	m/s	velocity
U_s	m/s	velocity at the collector lip suction slot
U_∞	m/s	freestream velocity, flight speed
U'	1/s	first velocity derivative
U''	$1/s^2$	second velocity derivative
u, v, w	m/s	velocity components
$\overline{u}, \overline{v}, \overline{w}$	m/s	mean (time-averaged) velocity components
u', v', w'	m/s	velocity fluctuation components
u_a, u_r, u_c	m/s	fan axial, radial, circumferential velocity
u_τ	m/s	friction velocity

V_s	-	volume enclosed by the control surface
v^s	m/s	velocity of the control surface
v_{exit}	m/s	fan exit velocity
$X'_{C'_p}(\omega)$	-	Fourier transform
x, y, z	m	Cartesian coordinates, helicopter-fixed coordinates
x_{L}	%	distance between the blade tip and the rotor shroud
x_c	m	stator vane chord length
x_r	m	blade chord length
y^+	-	dimensionless wall distance
y_1	m	distance between the nearest grid node and the solid surface
y_w	m	wall distance

Greek symbols	**Unit**	**Description**
α_{eff}	deg	effective blade incidence angle
α_∞	deg	angle of attack
β	deg	blade downwash angle
β_∞	deg	side-slip angle
β_B	-	specific blending factor of the High-Resolution scheme
Δ	-	difference, subtraction
δ	-	Dirac delta function
δ_{ij}	-	Kronecker delta
ϵ	m^2/s^3	turbulent dissipation rate
θ_i	deg	initial position of ith blade
θ'_i	deg	redistributed blade position of ith blade
$\Delta\theta$	deg	modulation amplitude
μ	kg/ms	dynamic viscosity
μ_f	-	non-dimensional mass flow rate
μ_t	kg/ms	eddy viscosity
ν	m^2/s	kinematic viscosity, $\nu = \frac{\mu}{\rho}$
ν_m	Hz	modulation frequency, $\nu_m = m_s f_R$
ν_s	deg	stator vane sweep angle
$\Delta\phi$	deg	phase modulation amplitude, $\Delta\phi = I_b \Delta\theta$
ψ	deg	azimuth
ψ_s	deg	stator vane lean angle
ρ	kg/m^3	density
ρ'	kg/m^3	acoustic density fluctuation
τ	s	retarded time
τ_w	Pa	wall shear stress
Ω	rad/s	rotational speed of fan
Ω_{ij}	1/s	vorticity tensor
ω	$1/s$	specific turbulence dissipation rate

$\omega_x, \omega_x, \omega_x$	1/s	axial, lateral, vertical vorticity
$\overline{\omega}_x, \overline{\omega}_y, \overline{\omega}_z$	1/s	mean (time-averaged) axial, lateral, vertical vorticity

Superscripts	**Description**
$^-$	mean (time-averaged) value
$'$	fluctuating value
*	conjugate

Subscripts	**Description**
0	ambient condition
1 : 1	full scale
1/3	1/3-octave band
1 : 7	model scale
70%	70% of the fan radius
adv	advancing time approach
BLS	boundary layer suction
BPF	blade passing frequency
CAA	acoustic computation
CFD	flow simulation
Flight	flight test
FWH	hybrid method
EXP	wind tunnel experiment
f	fan-fixed coordinate system
for	forward flight condition
h	helicopter-fixed coordinate system
hov	hovering condition
max	maximum
Ri	ith blade
ref	reference
ret	retarded time
SST	SST turbulence model
SAS	SAS turbulence model
tip	blade tip
∞	freestream

Abbreviations	**Description**
ACARE	Advisory Council for Aeronautical Research in Europe

AD	actuator disc
AHD	Airbus Helicopters Deutschland
BCD	Bounded Central Differencing
BEM	Blade Element Momentum
BLS	boundary layer suction
BPF	Blade Passing Frequency
BPP	blade passing period
BVI	Blade/Vortex Interaction
CAA	Computational Aeroacoustics
CD	Central Differencing
CFD	Computational Fluid Dynamics
CVP	counter rotating vortex pair
D_1	control surface 1 for the FWH computation
D_1	control surface 2 for the FWH computation
DBM	Discrete Blade Model
DES	Detached Eddy Simulation
DLR	Deutsches Zentrum für Luft- und Raumfahrt
DNS	Direct Numerical Simulation
EMS	Emergency Medical Services
EPNdB	Effective Perceived Noise Level in decibels
FAA	Federal Aviation Agency
FAU	Friedrich-Alexander University Erlangen-Nürnberg
FIW	fan-in-wing
FSH	Flying Helicopter Simulator
FWH	Ffowcs Williams and Hawkings
GenSim	Generic Simulation Tool
GGI	General Grid Interface
HFV	hub-fairing vortex
HS	horizontal stabilizer
HSV	horseshoe vortex of the shroud fairing
HSV-HS	horseshoe vortex of the horizontal stabilizer
HSW	corner separation and horizontal stabilizer wake
HSI	high-speed impulsive
IC	incoming side
ISB	inlet separation bubble
ICAO	International Civil Aviation Organization
iPAT	Institute of Process Machinery and Systems Engineering
KARI	Korea Aerospace Research Institute
LES	Large Eddy Simulation
LFV	lower fuselage vortex
LRZ	Leibniz-Rechenzentrum (Leibniz Supercomputing Centre)

LLFV	lower LFV
Mic	microphone
MPI	Message Passing Interface
MSM	Momentum Source Model
OG	outgoing side
OP	observer point
OSPL	Overall Sound Pressure Level
ONERA	Office national d'études et de recherches aérospatiales
PIV	Particle Image Velocimetry
PNLT	ton-corrected Perceived Noise Level
PS	pressure side
R	rotor (blade)
RANS	Reynolds-averaged Navier-Stokes
RSF	rotor/shaft-fairing
RSI	rotor/stator interaction
ROSI	Rotational Noise Source Identification
SA	Spalart-Allmaras
SAR	Search and Rescue
SAS	Scale-Adaptive Simulation
S	stator (vane)
SF	drive shaft fairing
SP	stagnation point
SPL	Sound Pressure Level
SPySI	Sound Prediction by Surface Integration
SS	suction side
SST	Shear-Stress Transport
STR	shrouded tail rotor
TRI	main-rotor-wake/tail-rotor interaction
UAV	Unmanned Aerial Vehicle
UFV	upper fuselage vortex
ULFV	upper LFV
URANS	Unsteady Reynolds-averaged Navier-Stokes
V/STOL	Vertical and Short Take-Off and Landing

Chapter 1

Introduction

1.1 Background and Motivation

Since the first flight of the practical rotary-wing aircraft in the late 1930s [56], helicopters had established a solid and important position in the field of both civil and military aviation. Nowadays, they are a substantial and irreplaceable means of transportation for Emergency Medical Services (EMS) and Search and Rescue (SAR) operations thanks to its unique hovering flight as well as vertical take-off and landing capability. However, with respect to aircraft noise issues, they often suffer from a negative image. Helicopter noise is often rated by the public as being more disturbing than fixed-wing aircraft because of its pulsating and impulsive noise characteristics resulting from the rotation of lifting surfaces (e.g. main and tail rotor). Moreover, complaints about helicopter noise have considerably increased over the past decades due to growing helicopter operations, particularly near and in densely populated areas, thus causing more frequent exposure to helicopter noise. Rising public awareness about helicopter noise pollution has resulted in civil aviation regulatory authorities making more stricter regulations for helicopter operations (see e.g. New York North Shore Helicopter Route Rule – Federal Aviation Agency (FAA) [31]) as well as noise certification rules (see e.g. International Civil Aviation Organization (ICAO) Annex 16 Chapter 8 and 11 [43] and Stage 3 Helicopter Noise Certification Standards by FAA [30]). As a consequence of these, helicopter manufactures and research institutes are required to develop new technologies that make the helicopter less noisy, as summarized in [44]. For instance, the Advisory Council for Aeronautical Research in Europe (ACARE) targets a reduction in perceived noise emission of both rotary- and fixed-wing aircraft in 2050 by 65% relative to that of aircraft in 2000, as suggested within the Europe's Vision for Aviation – Flightpath 2050 [1].

At a conventional single-rotor helicopter, there are various sources of aerodynamically induced noise, as indicated in Fig. 1.1. Among others, the main rotor and its interaction with unsteady turbulent flow (e.g. blade wake) are surely most significant noise sources, generating impulsive and to some extent disturbing noise (e.g. blade–vortex interaction (BVI) noise [115], high-speed impulsive (HSI) noise [87]). However, in certain helicopter operating conditions, the rather small tail rotor, necessary to counteract the torque from the main rotor, can become a predominant source of aerodynamic noise, and make a sub-

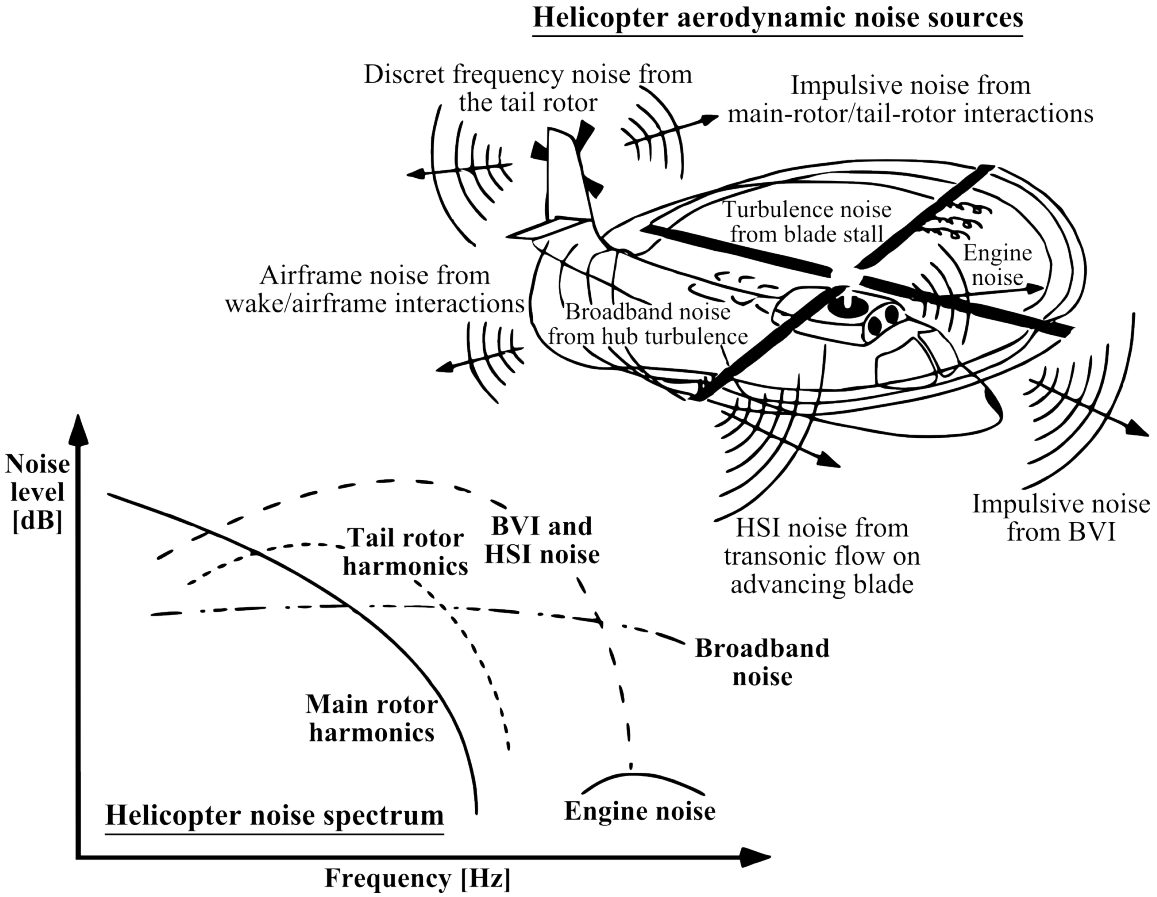

Figure 1.1: Diverse generation mechanisms and spectra of aerodynamically generated noise at a conventional helicopter configuration [56], figure originally from [26].

stantial contribution to increase the overall noise level of a single-rotor helicopter. This is due to the fact that the tail rotor operates in a strongly distorted flow environment resulting from tip vortices of the main rotor and other airframe (e.g. fuselage, tailboom) wakes, thus generating further interaction noise [39, 44]. Most considerable interaction noise occurs when the tail rotor blade hits the tip vortices of the main rotor, termed main-rotor-wake/tail-rotor interaction noise [58, 59].

Regarding the tail rotor noise, there are a large number of studies that suggest various noise reduction measures, such as modifying blade shape using swept and tapered tips [89, 90], reversing direction of the tail rotor rotation [58], reducing tip speed [45], increasing blade number [80], and modulating blade azimuth spacing [80]. In addition to these, a completely new design principle to the anti-torque system has been considered and developed: embedding the entire tail rotor construction in a large vertical tail fin. This type of the anti-torque system is called shrouded (ducted) or fan-in-fin type tail rotor. Airbus Helicopters – Fenestron (see Fig. 1.2) and FANTAIL of RAH-66 Comanche helicopter are the most well-known tail rotor configurations of this type.

In addition to the substantial improvement of operational safety, achieved by the duct construction that prevents any hazardous collisions of rotating blades with ground obstacles and personnel, the shrouded tail rotor design provides significant advantages in terms

of low noise emission compared to the conventional open tail rotor. The duct construction provides an acoustic shielding effect of the rotor noise, particularly in the plane of rotation. Furthermore, most shrouded tail rotor concepts are arranged with a large number of blades (10–13 blades for the Fenestron, eight blades for the FANTAIL) compared to an open tail rotor, which has typically two or four blades. The large number of rotor blades allows a shorter blade span and thus reducing the tip Mach number and consequently noise power. Especially in the case of the Fenestron, the blades are also unevenly spaced in the circumferential direction in order to break the acoustic repetition and thereby suppress noise annoyance at blade passing frequency (BPF), defined as multiple of the rotational frequency of the tail rotor, and at its high-order harmonics.

Figure 1.2: Airbus Helicopters H135 equipped with a Fenestron tail rotor [3].

Although the shrouded tail rotor has been confirmed as a successful solution to a quiet tail rotor design, further aeroacoustic studies are still to be done for a further improvement of its acoustic properties. The reason for this is that as a side effect of embedding the anti-torque rotor in the vertical fin, the shrouded tail rotor is often subject to undesired complex flow phenomena, which can have a negative impact on the acoustic properties of the shrouded tail rotor. For instance, under cross-flow conditions, such as in the high-speed forward flight, flow separation occurs at the curved inlet lip and consequently leads to a strongly distorted non-uniform inflow above the rotor plane. Studies from Krishnappa [53] and Stimpert [93] on fan-in-wing configurations, which bear a certain similarity to the shrouded tail rotor, point out that such inflow distortions can lead to significant fluctuations in blade loads and therefore be a considerable source of interaction noise.

To improve the acoustical design in terms of lower noise emission, it is essential to have an in-depth understanding of aerodynamic noise generation mechanisms of the shrouded tail rotor. For this, numerical methods, such as the hybrid method of the Computational Aeroacoustics (CAA) combining the Computational Fluid Dynamic (CFD) with the acoustic analogy, has a great advantage compared to experimental approaches. The hybrid method can provide a more detailed insight into the flow field in acoustic source regions as well as into the noise radiation mechanisms for such a complex rotating machinery, which may be comparably less expense than experiments. Hence, the hybrid method

may be a beneficial tool, which can be applied to determine the aeroacoustically beneficial tail rotor design already in the development stage.

In this context, the present thesis addresses comprehensive aerodynamic and acoustic investigations giving a more detailed insight into noise generation mechanisms of the Fenestron shrouded tail rotor. The methodology employed is the hybrid method that combines the unsteady Reynolds-averaged Navier-Stokes (URANS) simulations for capturing aerodynamic noise sources with the Ffowcs Williams and Hawkings (FWH) acoustic analogy for the prediction of noise radiation into the far field.

1.2 Shrouded Tail Rotor – Fenestron

The Fenestron shrouded tail rotor was developed in the late 1960s by the French company Aérospatiale and applied for the helicopter SA. 341 Gazelle for the first time [69]. Nowadays, the application of the Fenestron has been widely extended by Airbus Helicopters, successor of Aérospatiale, from light to medium-weight helicopter class, such as H120, H130, H135, H145, and currently H160. Since its invention, the Fenestron has been further developed and improved in terms of performance and acoustics characteristics. Therefore, the latest version of Fenestron considerably differs from its predecessor, as illustrated in Fig. 1.3. For instance, the latest version of Fenestron is equipped with ten unevenly distributed rotor blades and ten stator vanes with a drive shaft fairing, whereas an earlier version has 13 equally spaced rotor blades and three support struts including the drive shaft fairing. For many decades, it has been confirmed that the Fenestron has distinct advantages concerning operational safety, performance, and noise emission over the conventional open tail rotor. In the following, these advantages, pointed out in previous studies [38, 54, 65, 69, 70, 73, 74, 100, 102], are summarized and explained in more detail.

1.2.1 Safety Perspective

The Fenestron has been originally developed and introduced for the purpose of enhancing operational safety [102]. In low altitude flight operations, such as hovering, landing, and take-off maneuvers, the safety enhancement is achieved by the duct construction preventing any hazardous collisions of the blade with ground obstacles and/or personnel [54]. In forward flight conditions, the vertical fin installed on the upper part of the shroud fairing (see Fig. 1.3) provides further operational safety. This is because most of the anti-torque thrust required in the forward flight conditions is supplied by the large vertical fin, designed with cambered cross sections. Therefore, in case of total failure of the anti-torque rotor, Fenestron-equipped helicopters are still controllable and can be landed without using the relatively risky autorotation maneuver [69]. According to the accident statistics, the rate of reported accidents involving the Fenestron is 0.8×10^{-6} per flight hour, while the rate of accidents due to the conventional open tail rotor is 7.4×10^{-6} per flight hour [100].

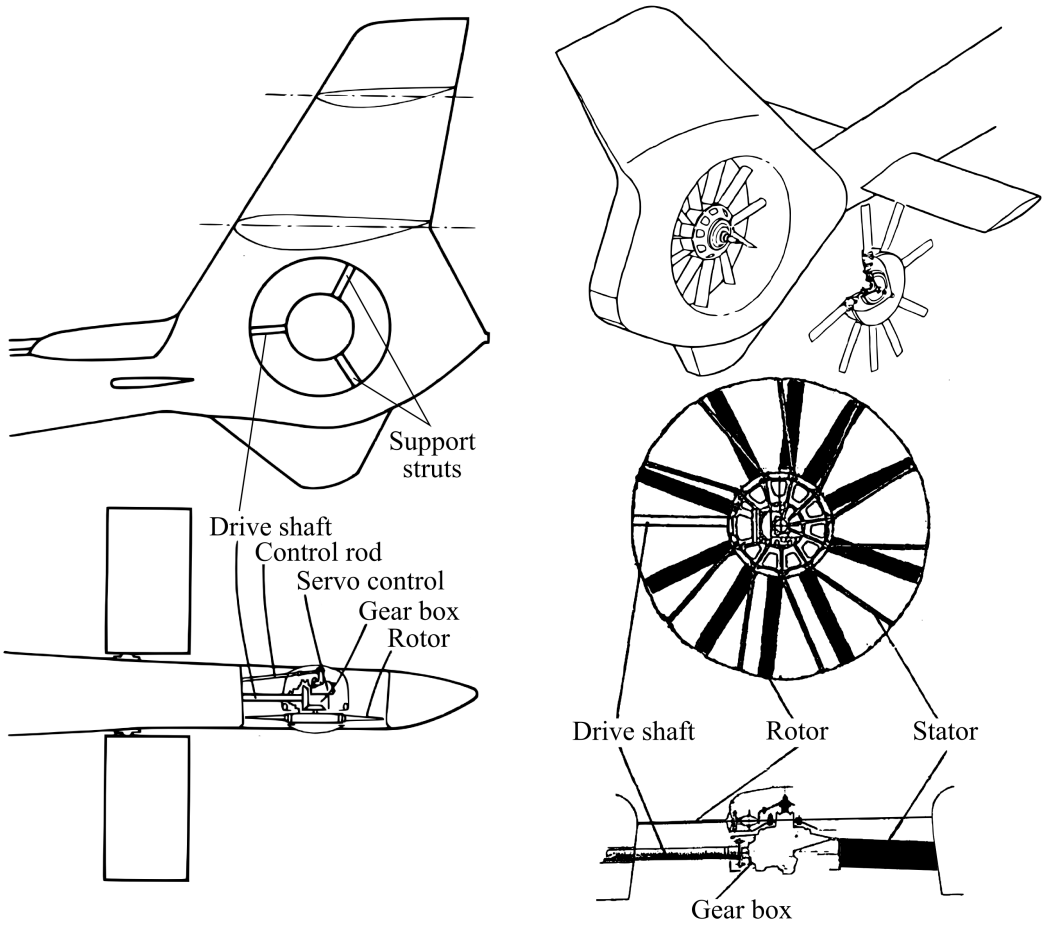

Figure 1.3: Fenestron arrangement for (a) SA. 341 (figure adopted from [69]) and (b) EC135 (figure adopted from [73]).

1.2.2 Aerodynamic Characteristics

Besides the safety improvement, the Fenestron provides further advantages in terms of overall helicopter and tail rotor performance with respect to the open tail rotor configuration. These advantages mainly result from unique aerodynamic characteristics of the Fenestron as pointed out in the following.

Shroud fairing and vertical fin. In the hovering flight, the shroud fairing improves both the helicopter overall and the tail rotor efficiency since approximately 50% of the anti-torque thrust required is provided by the suction effect occurring on the duct intake, featuring a curved collector lip (see Fig. 1.4). In the forward flight, the anti-torque rotor can be even completely unloaded because most of the necessary anti-torque thrust in this flight condition is provided by the vertical fin [54]. Consequently, the Fenestron requires only 30% of the power that is absorbed by the conventional open tail rotor to generate the same amount of anti-torque thrust [69] (see Fig. 1.5).

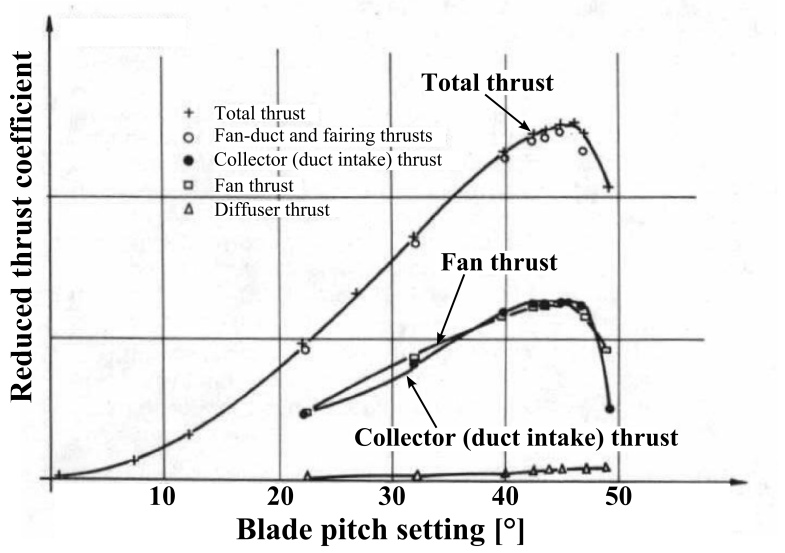

(a)

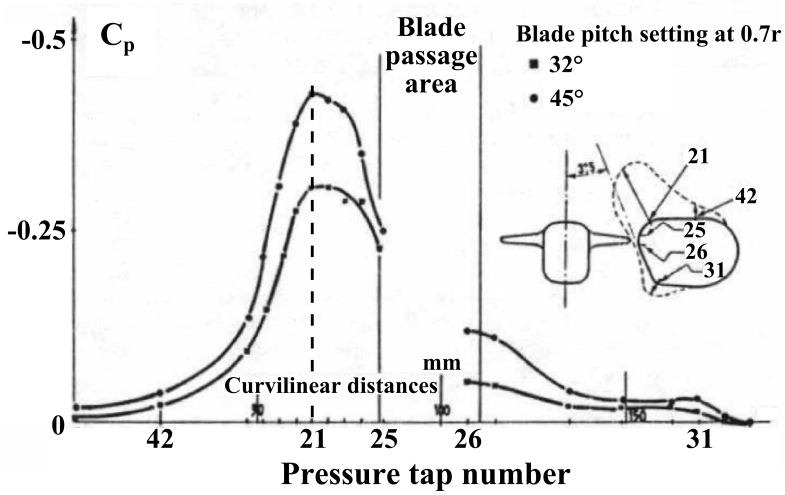

(b)

Figure 1.4: Aerodynamic characteristics of the Fenestron in hovering conditions, adopted from [70]: (a) thrust sharing and (b) surface pressure distribution along the shroud and duct fairing.

Multibladed anti-torque rotor. The Fenestron is equipped with a large number of blades. The multibladed configuration is highly advantageous with respect to reducing the blade-tip Mach number since the diameter of the Fenestron anti-torque rotor can be designed smaller than a conventional tail rotor equipped with two of four blades, to provide the same amount of anti-torque thrust. Furthermore, the total thrust generated by the anti-torque rotor is distributed over more blades, which leads to a decrease in individual blade load as well as less sensibility to a possible blade damage.

Stator vanes. The latest version of Fenestron is equipped with a single stator row featuring profiled thin vanes instead of the supporting struts with a relatively thick cross-

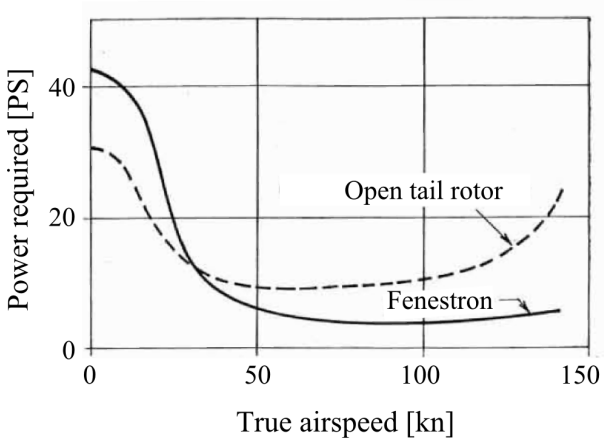

Figure 1.5: Tail rotor power requirement as a function of flight speed for a conventional open tail rotor and the Fenestron, adopted from [69].

sectional area. The stator vanes have not only the role of supporting the rotor hub and the gear box, but also of generating an additional anti-torque thrust through the conversion of the rotational energy of the rotor downwash to pressure energy. Moreover, the outlet side of the stator part is extended with a diverging duct of the frusto-conical diffuser (diffusion ratio close to one) for an additional gain of pressure energy [65].

1.2.3 Acoustic Characteristics

The Fenestron has been proven to be less noisy than the conventional open tail rotor, as demonstrated by microphone measurements of two helicopters equipped with a two-bladed conventional open tail rotor (EC145) and the latest version of Fenestron (EC145T2, now renamed as H145), respectively [38]. The measurement indicates that the Fenestron pro-

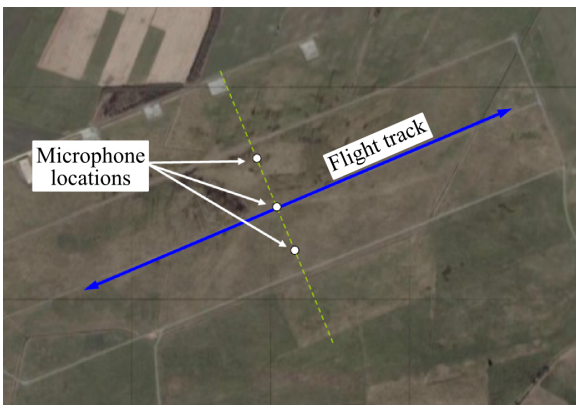

(a)

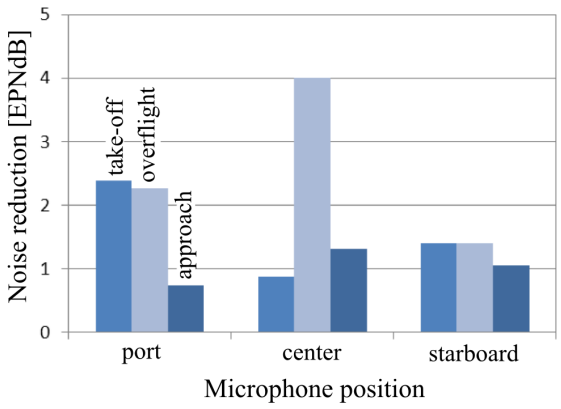

(b)

Figure 1.6: Noise reduction characteristics: (a) ground microphone positions and (b) comparison of noise reduction between helicopters equipped with the Fenestron (EC145T2) and an open tail rotor (EC145), adopted from [38].

vides a significant reduction in Effective Perceived Noise Level (EPNdB). The reduction in EPNdB is found in all certification flight conditions (take-off, overflight, and approach) as well as regarding all microphone positions, as indicated in Fig. 1.6. The most significant reduction (4 EPNdB relative to the open tail rotor) is observed at the center microphone in the overflight condition. The reason lies in the fact that the anti-torque thrust in the level flight is mostly generated by the vertical fin, therefore, the rotor system is comparably unloaded, which in turn results in a low acoustic emission. Furthermore, the sound propagation to the ground, particularly in the plane of the rotor, is effectively shielded by the shroud fairing.

Aerodynamic noise sources. Regarding the generation mechanism of flow-induced noise, the Fenestron tail rotor has certain similarities to an axial flow fan, such as a ducted fan propulsion for unmanned aerial vehicle (UAV) and jet engine. For an overview of noise sources and noise generation mechanisms in axial flow fans, the reader may refer to [64, 72]. Apart from broadband noise, the Fenestron emits characteristic tonal noise at the blade passing frequency (BPF) and its harmonics. Niesl et al. [74] summarized three typical noise generation mechanisms associated with the Fenestron, described as following (see also Fig. 1.7):

- Ingestion of atmospheric turbulence: interaction of the ingested turbulence with the rotating blade leads to blade load fluctuations. The resulting interaction noise can exhibit tonal noise characteristics if the ingested turbulence is large enough so that it is interrupted by all blades, otherwise the interaction generates broadband noise.
- Potential noise: the pressure field of the upstream rotor blade interacts with the downstream obstacle (e.g. stator vanes, supporting struts, drive shaft fairing) and vice versa, leading to periodic blade and stator vane load fluctuations. As a result, narrow peaks are produced at the BPF of the Fenestron and at its lower harmonics.
- Blade-wake/stator interaction: the stator vane also experiences load fluctuations due to the periodic impinging of the turbulent blade wake. Hence, the stator vane emits tonal noise at the BPF and its harmonics.

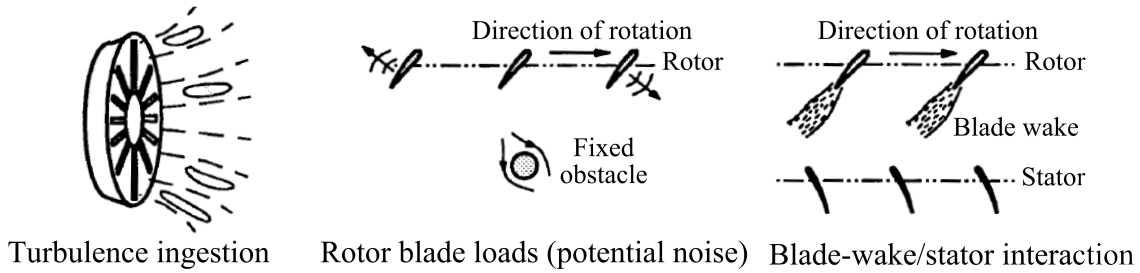

Figure 1.7: Schematic description of generation mechanisms of Fenestron noise, adopted from [74].

Shroud fairing and vertical fin. The advantages of shrouding of rotating blades by a duct construction in terms of low noise emission are manifold. The main advantage is that the shroud fairing provides a significant acoustic shield effect as it prevents any direct propagation of rotor noise to the ground. Thus, as mentioned above, the Fenestron indicates a low noise radiation, particularly in the plane of rotation (forward and backward of the helicopter flight direction as well as underneath the flight path) compared to the open tail rotor, by which the rotor noise can propagate unhinderedly in all directions. The shroud fairing also offers a better acoustic behavior with respect to the main-rotor-wake/tail-rotor interaction (TRI) noise. The experimental study on the influence of the shroud fairing on the TRI noise using a removable shroud fairing [103] indicates that the TRI leads to a significant generation of narrow peaks between existing rotational noise components, as shown in Fig. 1.8. The additional peaks are observed in either case (without and with shroud fairing), but the noise level is more significant in the one

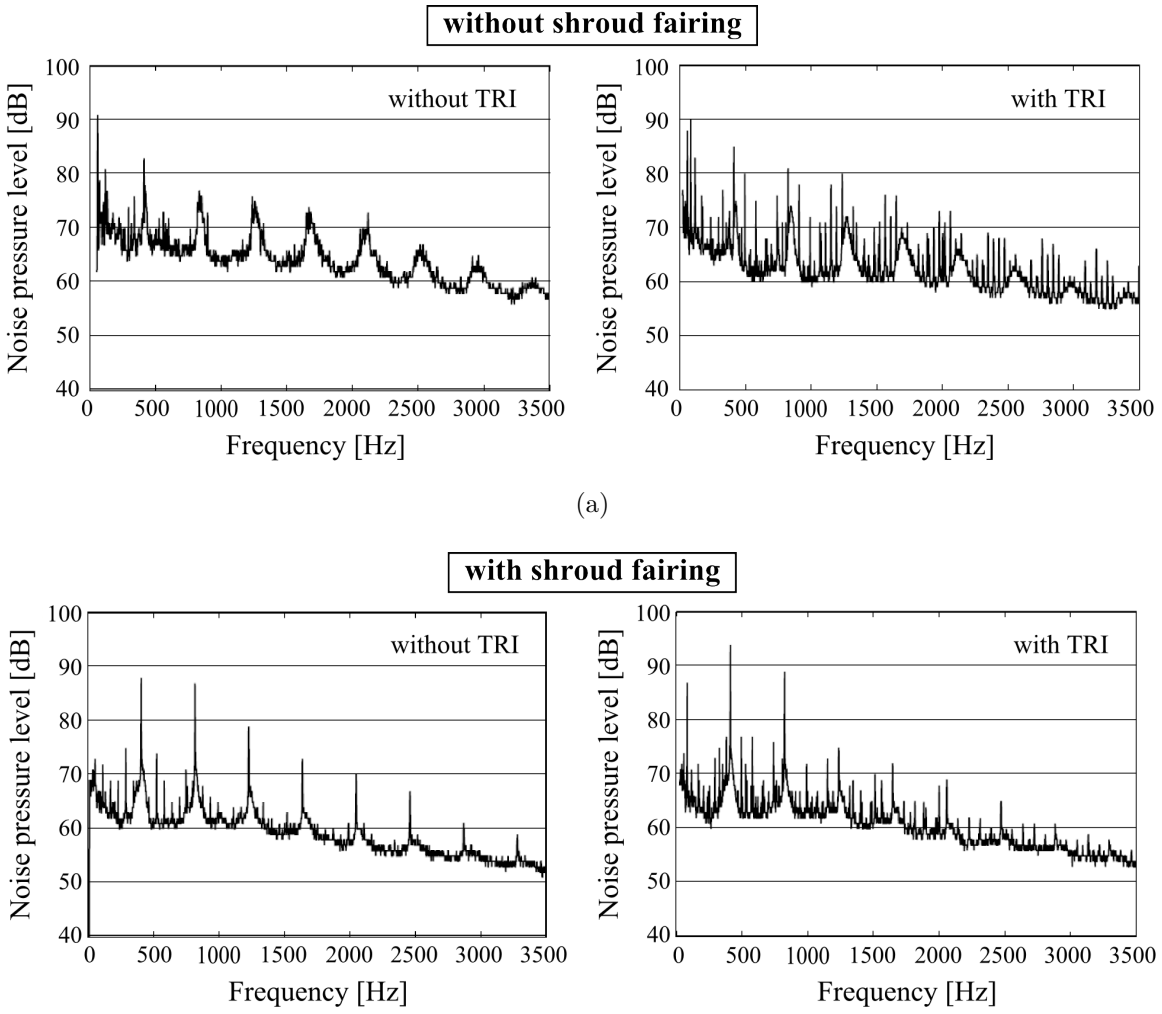

Figure 1.8: Influence of main-rotor-wake/tail-rotor interaction (TRI) on noise spectra for a (a) open and (b) shrouded tail rotor, adopted from [103].

without. Increase in measured noise level due to the TRI is 5.2 dB in the case of open rotor, while an increase by 3.7 dB is measured for the case of the shrouded rotor. Fenestron noise emission can be further reduced by installing passive sound absorption devices, such as Helmholtz Resonators, inside the duct fairing [13, 78]. Current studies also indicate that introducing an active tail fin rudder can achieve further noise reduction, particularly for approach conditions [13].

Multibladed anti-torque rotor. As mentioned above, multibladed configuration allows to design a smaller fan diameter than the conventional tail rotor to generate the same amount of the anti-torque thrust. As a result, the blade-tip Mach number, that is the most important parameter concerning acoustic power emitted from a rotor, can be considerably reduced. Furthermore, the rotational noise emitted at the BPF and its harmonics lies in a higher range, compared to the two- or four-bladed open tail rotor. Due to its high frequency characteristics, the Fenestron noise exhibits a more stronger atmospheric attenuation with increasing distance than the noise emitted by the open tail rotor [54, 102].

Uneven blade spacing. For the old version of Fenestron, equipped with evenly spaced blades, significant shrill tone emission was detected at the BPF and its harmonics in the frequency range between 700 to 1000 Hz. The shrill noise emission in this frequency range is on the one hand very disadvantageous concerning a noise certification penalty, and on the other hand, arising further noise pollution issue as the human ear has a high sensitivity in the 1000 Hz range [74]. To suppress the shrill noise emission, the latest version of Fenestron is equipped with unevenly spaced blades. The idea behind this concept is to break the symmetry of the rotating system, thus to suppress the acoustic repetition and superposition at the BPF and its high-order harmonics. The uneven blade spacing is based on the sinusoidal modulation law suggested by Ewald et al [29] and described as follows: first, a generic ten-bladed ($I_b = 10$), evenly spaced rotor is considered (see Fig. 1.9(a), rotor blades are demonstrated by solid lines). The even blade spacing of the rotor can be rearranged by using the sinusoidal modulation defined as:

$$\theta_i' = \theta_i + \Delta\theta \sin(m_s \theta_i) \tag{1.1}$$

with the initial position of ith blade θ_i, the redistributed blade position of ith blade θ_i', the modulation amplitude (maximum blade angle change) $\Delta\theta$, and the number of modulation cycle repeated within one fan revolution m_s. The redistributed blade position with $m_s = 2$ is now given in Fig. 1.9(a), denoted by dotted lines. Then, the pressure disturbance resulting from the rotating blades with uneven spacing can be determined by applying the classical sinusoidal phase modulation law defined as:

$$p'(t) = A_0 \sin(2\pi t f_{\mathrm{BPF}} + \Delta\phi \sin 2\pi \nu_m t), \tag{1.2}$$

where A_0 is the fundamental tone amplitude relating to the blade passing frequency ($f_{\mathrm{BPF}} = I_b f_R$), ν_m is the modulation frequency, defined as $m_s f_R$, and $\Delta\phi = I_b \Delta\theta$ is the

phase-modulation amplitude. Ewald et al. [29] rearranged this formulation by introducing a Fourier analysis and sinusoidal approximation of the pressure waveform for a more realistic prediction of the pressure amplitude for a rotor system with small number of blades ($I_b < 20$):

$$p'(t) = \hat{p}(t) + \sum_{n=1}^{\infty} B_n \sin(n\omega_m t) + \sum_{n=1}^{\infty} C_n \cos(n\omega_m t), \tag{1.3}$$

where $\omega_m = 2\pi f_R$,

$$B_n = \frac{1}{2\pi} \sum_{i=1}^{I_b} \left\{ \frac{\sin[(D_i - n)\theta - D_i\theta_i]}{D_i - n} - \frac{\sin[(D_i + n)\theta - D_i\theta_i]}{D_i + n} \right\}_{\theta_i}^{\theta_{i+1}},$$

and

$$C_n = -\frac{1}{2\pi} \sum_{i=1}^{I_b} \left\{ \frac{\cos[(D_i + n)\theta - D_i\theta_i]}{D_i + n} - \frac{\cos[(D_i - n)\theta - D_i\theta_i]}{D_i - n} \right\}_{\theta_i}^{\theta_{i+1}}$$

with

$$D_i = \frac{2\pi}{(\theta_{i+1} - \theta_i)}$$

Normalized sound pressure in time domain obtained with Eq. 1.3 at a random position on the rotor disc are presented in Figs. 1.9(b) and 1.9(c) for the even and uneven blade spacing, respectively, for one fan revolution. Corresponding spectra are then given in Figs. 1.9(d) and 1.9(e), respectively. Comparing the pressure spectra, it can be clearly found that the sinusoidal modulation reduces the amplitude at the BPF ($f/f_{\mathrm{BPF}} = 1$) considerably, but generates additional peaks over several frequencies in the lower ($f/f_{\mathrm{BPF}} = 1 - 0.2m$; $m = 1, 2$) and upper sideband ($f/f_{\mathrm{BPF}} = 1 + 0.2m$; $m = 1, 2$) of the BPF. Consequently, the spectrum of uneven spacing exhibits more broadband-like characteristics compared to that of the even blade spacing. The additional peaks are equidistantly distributed with a frequency offset corresponding to the modulation frequency $\nu_m/f_{\mathrm{BPF}} = m_s/I_b = 0.2$. In addition, the amplitude distribution in the lower and upper sideband is asymmetric with reference to the BPF. Now, the maximum pressure level appears not at $f/f_{\mathrm{BPF}} = 1$, but at the frequency $f/f_{\mathrm{BPF}} = 0.8$ in the lower sideband.

In Figs. 1.10(a) and 1.10(b), experimentally obtained Fenestron noise spectra in a hover condition [73] are presented for the Fenestron with evenly and unequally spaced blades, respectively. Similar to the analytically obtained spectrum in Fig. 1.9(e), the noise spectrum in the case of uneven blade spacing reveals a reduced noise level at the BPF as well as at its high-order harmonics and additional peaks in-between. The Fenestron equipped with unevenly spaced blades shows rather broadband-like noise characteristics. Further studies on the modulated blade spacing can be found in [7] for another type of shrouded tail rotor and in [94] for application to main rotor.

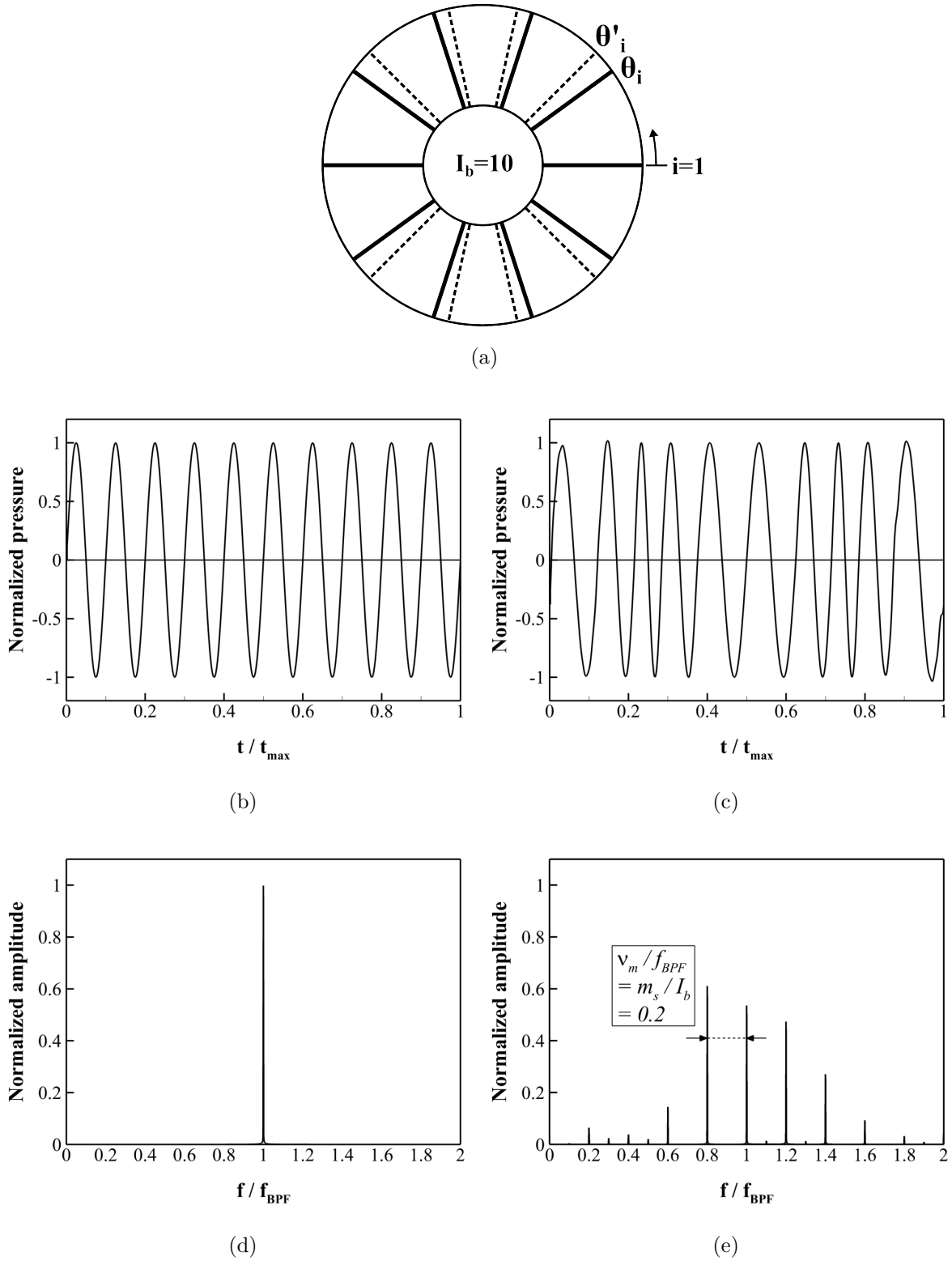

Figure 1.9: Sinusoidal phase modulation for a generic ten-bladed rotor, based on [29]: (a) schematic description of evenly (solid lines) and unevenly spaced blade position (dotted lines), (b) pressure signal in time domain for even blade spacing, (c) for uneven blade spacing, (d) pressure spectrum for even blade spacing, and (e) for uneven blade spacing.

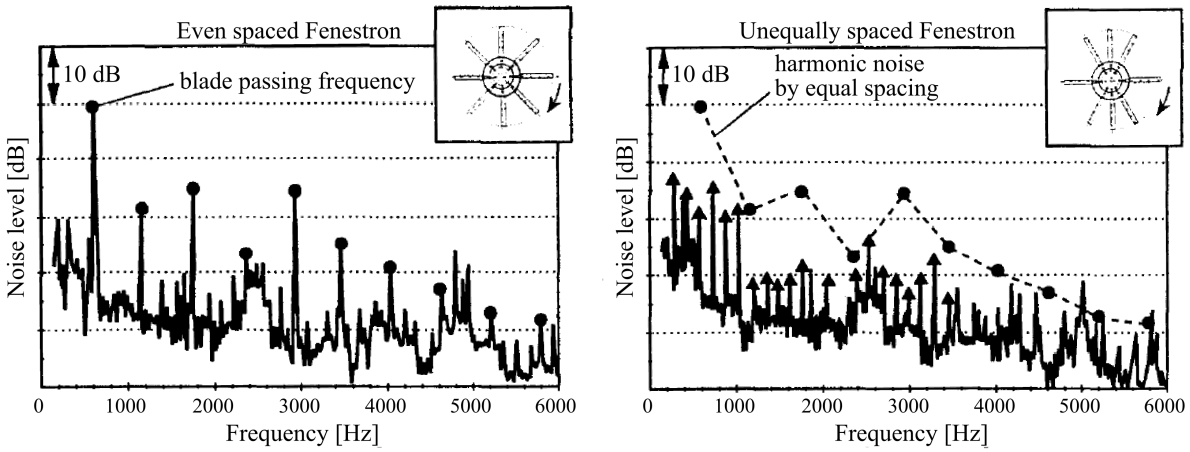

Figure 1.10: Comparison of experimentally obtained Fenestron noise spectra in a hovering flight: (a) Fenestron with evenly spaced blades and (b) unequally spaced blades, adopted from [73].

1.3 Literature Overview

Since its first flight in the late 60s, the shrouded tail rotor has been the subject of a number of experiments and numerical studies. In the following, numerical studies focusing on the aerodynamic and acoustic characteristics of the Fenestron as well as other fan-in-fin type tail rotors are outlined.

1.3.1 CFD and CAA Studies on Fenestron in Hovering Flight

Regarding CFD studies, comprehensive computations of the EC135 Fenestron were performed by Mouterde et al. [71] and D'Alascio et al. [21], giving detailed information about performance and aerodynamic characteristics of the latest version of Fenestron (ten blades with unequal spacing) in diverse hovering conditions. Both studies were undertaken based on the Chimera interpolation technique on overlapping meshes between the blade region and the background, and performed with different flow solvers (FLOWer, elsA). Furthermore, the CFD results were validated with data of the whirl tower tests. Both studies clearly show that a significant amount (more than 40%) of the anti-torque thrust required in the hovering conditions is provided by the duct fairing including the collector lip.

Based on a similar geometry, a further CFD study (Chimera method, FLOWer, and Wilcox k-ω turbulence model) was conducted by Kainz et al. [47] in order to assess the influence of the side wind on the Fenestron aerodynamics. This study indicates that the side wind leads to periodically fluctuating inflow distortions above the rotor plane as well as a lower thrust level compared to the ideal hovering condition without any side wind impacts. The study also shows that the rotor blade bears a significant peak loading when the rotor interacts with the drive shaft fairing being installed downstream. The amplitude

of the peak loading is stronger than that by the rotor-blade/stator-vane interaction and significantly varies depending on the angular distance between neighboring blades.

Regarding CAA studies, Roger et al. [82] studied the rotor/shaft-fairing potential interaction noise by means of the reversed Sears' Problem of calculating unsteady blade lift. They succeeded in reproducing a similar increasing trend of the interaction noise of measurements as a function of the blade pitch angle (an increase in noise level by 0.4 dB per degree).

Kainz et al. demonstrated that in their recent works, based on the single passage rotor-stator configuration with phase-lagged periodic boundary condition and conducted by using TRACE of DLR solving Favre-averaged Navier-Stokes equations, the optimization of the stator configuration plays an important roll in improving the near-field acoustic characteristic of the shrouded tail rotor. The studies show that the fan acoustic characteristics can be enhanced by modifying the stator vane geometry [49], such as chord length, vane sweep and lean angle, as well as by the choice of appropriate number of stator vanes [48], without any detrimental effects on the fan performance.

1.3.2 CFD and CAA Studies on Fenestron in Forward Flight

Because of its position relative to the fuselage and the main rotor, the Fenestron operates under highly disturbed flow condition in the forward flight. Roger and Fournier [81] numerically studied the influence of the anisotropy of inflow turbulence on the Fenestron acoustic property in a forward flight condition. The study based on the unsteady aerodynamic theory of isolated thin airfoils shows that the tone at the BPF becomes stronger and narrower, as the rate of anisotropy of inflow increases.

A comprehensive study of the aerodynamic and acoustic behavior of the Dauphin 6075 Fenestron, featuring 13 evenly spaced rotor blades and three hub support struts instead of stator vanes, was provided by Gardarein et al [36]. They studied the aeroacoustic behavior of the Fenestron by coupling of unsteady Navier-Stokes computations (elsA, Wilcox k-ω model with the Zheng limiter and correction of Kok) with the Ffowcs Williams and Hawkings (FWH) analogy (PARIS of ONERA) for both the level and high rate climb flight condition. The CFD study involves the entire airframe including the fuselage and the main rotor, modeled by a lifting surface of time-averaged disc load (actuator disc model). The study demonstrates that in forward flight condition, the operating environment of the Fenestron is very complex due to the fuselage wake and flow separation occurring on the inlet lip. As a result of the interaction between the rotor and the shaft fairing, the loading noise is identified as dominant compared to the thickness noise. Furthermore, the acoustic study shows that in the forward flight condition of reduced Fenestron thrust, the noise level is even increased, although the individual blade load is decreased compared to the case of high fan thrust. This is due to an acoustic blade-to-blade interference. Based on the identical Fenestron configuration, Falissard et al. [32] and Gardarein et al. [37] conducted validation of the hybrid method (elsA for CFD and KIM solver for FWH) by comparing it with both in-flight and ground measurements.

To date, there are no numerical studies available which deal with the aeroacoustic behavior of the latest version of Fenestron in the high-speed forward flight condition.

1.3.3 CFD and CAA Studies on Other Shrouded Tail Rotor Configurations

Regarding the RAH-66 FANTAIL, Rajagopalan and Keys [77] provided a detailed aerodynamic analysis based on steady-state CFD study using an incompressible, laminar Navier-Stokes equation solver for the hover and side flight condition. The study modeled the fan rotation by applying the time-averaged momentum source terms in the momentum equation (momentum source model, MSM) to take the advantage of its low computational costs. Validation of MSM for the specific application of the ducted fan simulation was provided by Nygaard and Dimanlig [75] by comparing the MSM to the discrete blade model (DBM) and wind tunnel as well as whirl tower experiments.

A further steady-state CFD study for the hovering FANTAIL was provided by Ruzicka and Strawn [84] by applying a discrete blade, modeled by overset grid method. They demonstrated the influence of the tip-leakage vortex on the generation of the reverse flow along the duct wall downstream of the rotor plane by comparing a finite blade-to-shroud-gap simulation with the sealed blade-to-shroud-gap computation. The study points out that handling the blade tip leakage has a strong influence on tip-leakage vortex and thus affecting the flow attachment in the duct divergence significantly.

Both steady-state and unsteady CFD simulations of the FANTAIL for the hovering, forward and sideward flight were provided by Alpman et al. in [5] and [6], respectively, for a better understanding of the directional control sensitivity of the ducted tail rotor system. The investigations based on the inviscid Euler equations involve a simplified Comanche fuselage with the FANTAIL including the upper vertical fin. The anti-torque rotor is modeled by a uniform actuator disc and blade element method, while the main rotor is excluded. The investigations show a complex flow field inside the duct, particularly in the forward flight condition. They found that the internal flow field in this low fan thrust condition is characterized by diverse recirculating flow regions due to the flow separation from sharp edges, even though the studies were performed based on the inviscid assumption.

A numerical study on the aerodynamic characteristics of the Russian Ka-60 shrouded tail rotor was conducted by Lee and Kwon [55] using an inviscid flow solver and based on unstructured meshes.

Chung et al. [19] developed within a research project of Korea Aerospace Research Institute (KARI) a low noise ducted tail rotor with uneven blade spacing. The influence of the unequal blade spacing on noise levels were investigated by coupling of the velocity potential equation for incompressible, inviscid and irrotational flow with the FWH analogy (generalized Farassat formulation 1A). They reported that the uneven blade spacing can achieve a reduction in the tone corrected perceived noise level (PNLT) of 5 dB.

1.3.4 CFD and CAA Studies on Ducted Fan Configurations

A CFD study and its validation with wind tunnel experiments were performed by Akturk and Camci [4] for a eight-bladed ducted fan designed for a vertical and short take-off and landing (V/STOL) unmanned aerial vehicle (UAV) application. The steady-state Reynolds-averaged Navier-Stokes (RANS) simulation provides a detailed insight into the tip-leakage flow in the hovering flight and reports that the tip clearance has a significant impact on the fan efficiency (increasing tip clearance decreases the fan efficiency and vice versa).

An extensive numerical study on a generic fan-in-wing (FIW) configuration was performed by Thouault et al. [96] based on unsteady RANS (URANS) simulation using the shear-stress transport (SST) turbulence model and the sliding mesh technique for a transition flight situation without ground effect. The CFD results provided a comprehensive description and explanation of the external and internal flow field characteristics (e.g. inflow distortion resulted from the inlet lip flow separation and its interaction with the blade, jet-in-cross-flow phenomenon on the fan outlet side). Thouault et al. [97] also conducted a more detailed investigation of the inlet distortion based on the URANS simulations. Regarding flow control measures against the lip boundary layer separation, they tested various lip radius-to-diameter ratio and active lip flow control via jet injection.

Corresponding aeroacoustic investigations have been performed by Tirakala et al. [98] based on the acoustic hybrid method combining the URANS simulation with the FWH porous surface integration method extended by Farassat. The far-field sound characteristics of the FIW configuration were compared with the microphone measurement in an acoustic wind tunnel. The predicted sound spectra show a good agreement with the measured one, particularly with respect to the discrete noise component at the blade passing frequency and its high-order harmonics.

1.4 Objectives and Outline of Present Work

The main objective of the present work is to provide a detailed insight into the flow physics linked to noise generation by the shrouded tail rotor in two representative helicopter operating conditions, namely the hovering and high-speed forward flight. In order to meet this objective, an acoustic hybrid is employed. Firstly, high-fidelity unsteady RANS simulations are performed based on the full-scale shrouded tail rotor model with minimum geometric simplifications and by use of the commercial flow solver ANSYS CFX for an accurate prediction of aerodynamic sound sources. Based on the source information obtained from the comprehensive flow analysis, the far-field acoustic pressure is computed by using acoustic post-processing tool SPySi. The tool is based on the FWH method of the permeable integration surface and provided by the Institute of Process Machinery and Systems Engineering (iPAT), Friedrich-Alexander University Erlangen-Nürnberg (FAU). Details about numerical methods and simulation setup for both the flow simulation and the acoustic computation as well as their predictive capabilities evaluated by wind tunnel

experiments are presented in chapters 2 and 3, respectively. The main emphasis of the present work lies on the following topics:

1. **Comprehensive flow field analysis for the shrouded tail rotor under superimposed cross flow.**
   The main focus of the present work is on the establishment of a comprehensive database of aeroacoustic characteristics of the shrouded tail rotor in the high-speed forward flight. This includes, among others, the assessment of noise emission of the shrouded tail rotor under superimposed cross-flow condition and the evaluation of the effect of installing such complex rotating machinery in highly turbulent fuselage wake region. For this purpose, the present study will start with an analysis of the hovering flight to give a detailed insight on the flow physics inside the shrouded tail rotor without any predominant inflow distortions and airframe wake ingestion (chapter 4). Subsequently, a comprehensive analysis is performed and presented in chapter 5 for the forward flight condition, in which both the external and internal flow field of the shrouded tail rotor are characterized by significant flow separation and complex wake flow. Further emphasis in this flight condition lies on the analysis of the inflow distortion provoked by collector lip boundary layer separation and resulting interaction noise. For this, a non-distorted case, achieved by introduction of active flow control via boundary layer suction is compared with the reference simulation case. The influence of the horizontal stabilizer on the inflow condition and consequently on the acoustic characteristics of the shrouded tail rotor is also investigated.

2. **Evaluation of the predictive capability of the hybrid CFD-CAA.**
   The predictive capability of the hybrid method is demonstrated by comparing the calculated acoustic signal with measured data obtained by flight measurements of Airbus Helicopters Deutschland (AHD) for the hovering condition and German Aerospace Center (Deutsches Zentrum für Luft-und Raumfahrt: DLR) for the forward flight case. The comparison is presented in chapters 4 and 5 for the hovering and forward flight, respectively.

3. **Assessment of the influence of the main rotor downwash on the shrouded tail rotor acoustic characteristics in forward flight.**
   If the blade wake of the main rotor and its interaction with other helicopter components are not of interest, the main rotor is often neglected in the CFD simulation due to its expensive modeling effort. Furthermore, the influence of the main rotor and its induced downwash velocity on the aeroacoustic characteristics of the shrouded tail rotor, in particular in the high-speed forward flight is assumed to be negligible. In order to conform this assumption, both aerodynamic and acoustic results of reference simulation case using the isolated fuselage with the shrouded tail rotor is compared with the case where the main rotor influence is modeled by using an actuator disc (AD) approach. The numerical technique used for the AD approach

and the comparison between the cases without and with main rotor influence are presented in chapter 5.

4. **Evaluation of the effect of the turbulence modeling on the accuracy of predicted noise.**
   The noise prediction capability of the hybrid method with respect to the approximation order of turbulent flow modeling in the acoustic source region is evaluated by comparing two different turbulence models, namely the shear-stress transport (SST) model and a scale resolving approach such as the scale-adaptive simulation (SAS) method. This topic is discussed only for the forward flight condition (chapter 5) since in this flight condition, the shrouded tail rotor operates under the highly turbulent fuselage wake region.

Chapter 2

Numerical Flow Simulation

This chapter deals with both the explanation of the employed numerical methods and the validation of the numerical flow simulation based on the unsteady Reynolds-averaged Navier-Stokes (URANS) equations. Firstly, details of helicopter configuration including a fan-in-fin type shrouded tail rotor (STR) are described. Subsequently, numerical approaches and computational setups of the flow simulation will be explained for both the hovering and high-speed forward flight condition. Finally, prediction capabilities of the numerical methods will be evaluated in particular for the fast forward flight case by comparison of the predicted flow quantities with the data obtained from wind tunnel experiments including surface pressure and aerodynamic force measurements.

2.1 Setup of Flow Simulations

2.1.1 Geometry Definition

In this thesis, a full-scale (1:1) lightweight, twin-engine utility helicopter equipped with the shrouded tail rotor as an anti-torque device is considered. The geometry studied in this work involves detailed helicopter components consisting of the fuselage, the tail boom, the horizontal stabilizer (HS) with end plates and the STR assembly, as given in Fig. 2.1(a). A minimum of geometrical simplifications are adopted in order to reduce the complexity with respect to the generation of numerical grids. Thus, the skid landing-gear is neglected, and both the engine intake and the engine exhaust are completely sealed. Furthermore, the main rotor as well as its rotor head are not modeled in the numerical simulation. This decision is based on the following assumptions: (1) main rotor influence (e.g. blade tip vortices, induced rotor downwash) on the STR flow field characteristics in the forward flight condition regarded here are not significant as pointed out in [36], (2) this kind of flight condition is mainly significant with respect to the STR noise emission. Consequently, neglecting main rotor geometry decreases modeling complexity significantly, which in turn allows to reduce computational costs considerably. A possible influence of the main rotor downwash on both the STR aerodynamic and aeroacoustic characteristics in the high-speed forward flight condition will be assessed in Sec. 5.2 by usage of the actuator disc approach. Since in hovering flight the flow field characteristics of the STR are not

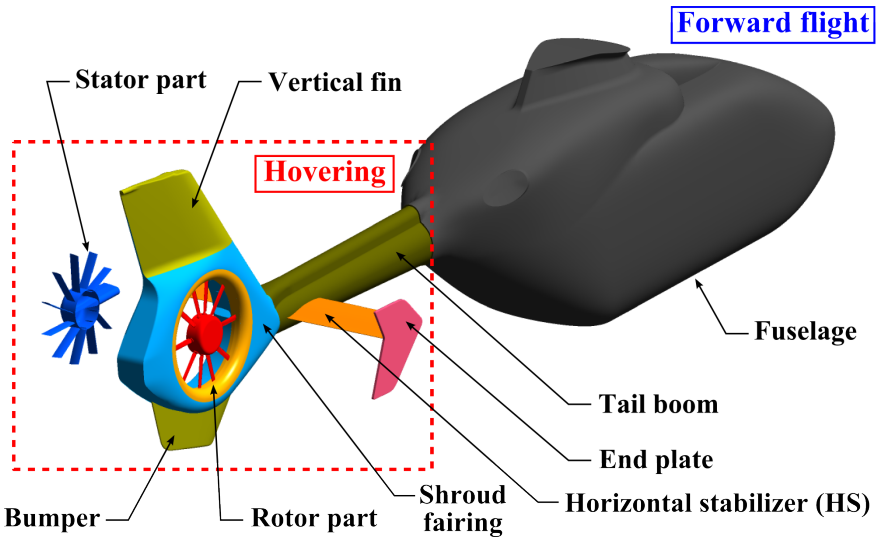

(a)

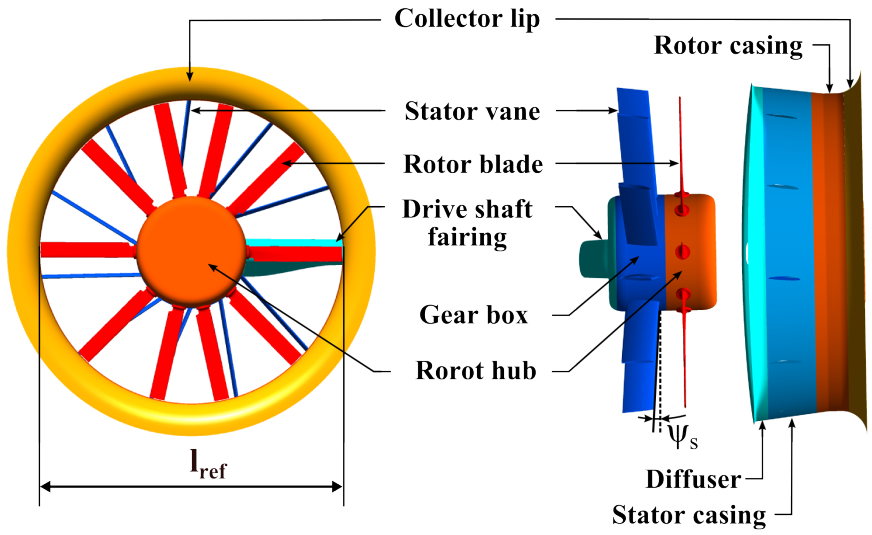

(b)

Figure 2.1: Description of the helicopter configuration: (a) overall configuration and (b) details of the rotor and stator part.

directly affected by the fuselage components, the entire fuselage geometry is removed in all simulation cases of the hovering flight and only the tail boom, the HS and the STR parts are considered with purpose of reducing computational costs. Similar approaches can be found e.g. in Refs. [21, 71].

The STR assembly consists of the rotor row, the stator row, the shroud fairing, the vertical fin, and the bumper, which is attached to the lower side of the shroud fairing. The vertical fin installed on the upper part of the shroud fairing features airfoil-like, cambered cross sections and a positive angle of incidence with respect to the helicopter center line to take over the function of torque balancing in the forward flight condition. The rotor and stator row are enclosed by a duct casing that can be divided into the collector part (collector lip and rotor casing) and the diffuser part (stator casing and diffuser), as

indicated in Fig. 2.1(b).

The rotor part involves ten twisted high-aspect-ratio blades anchored to the rotor hub. It features all geometrical details such as the cylindrical blade root, the rounded blade tip for adaptation of the casing contour, and the blade-tip leakage. The blades are unevenly distributed in the direction of rotation with three different angular spacings ($\theta_1 > \theta_2 > \theta_3$, see Fig. 2.2(a)) by using the sinusoidal modulation technique (see Eq. 1.1). This feature aims at suppressing tonal noise associated with the blade passing frequency (BPF) as well as with its high-order harmonics. The overall distribution is, however, mirror symmetry in the rotor plane (xz-plane) as the modulation cycle is repeated twice within one fan revolution ($m_s = 2$, see Eq. 1.1). In this thesis, two different blade pitch angles ($P_{b,\mathrm{hov}} > P_{b,\mathrm{for}}$) are used to model different flight conditions. The pitch angles are set at 70% of the fan radius, as indicated in Fig. 2.3.

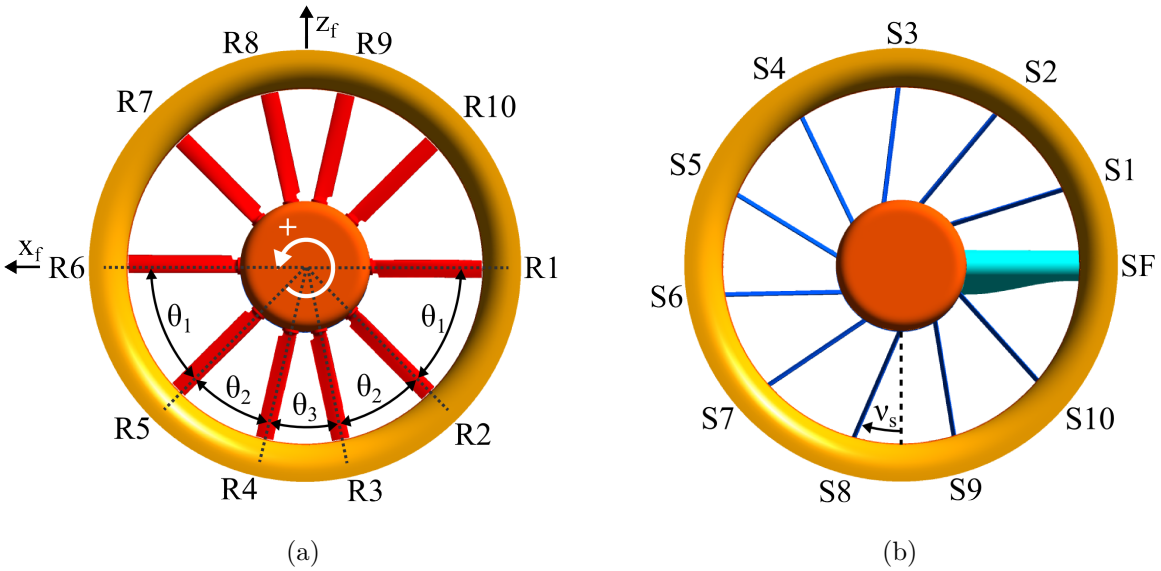

Figure 2.2: Details of (a) rotor blade and (b) stator vane distribution.

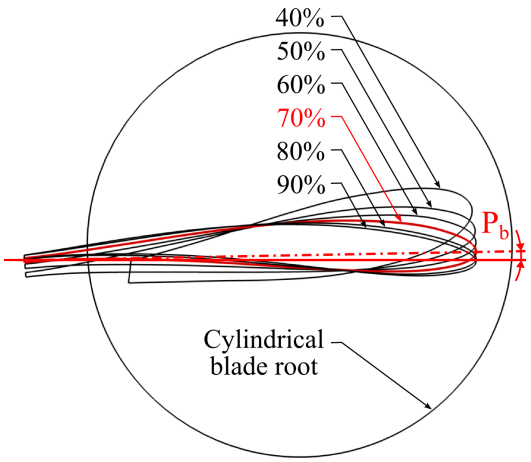

Figure 2.3: Cross sections of the rotor blade and the blade pitch angle P_b.

The stator part is composed of the gear box, ten rectangular vanes having thin airfoil, and the drive shaft fairing, which has a larger cross-sectional area and closer distance to the blade upper side than the stator vane. Unlike the blade spacing, the stator vanes could be considered as evenly distributed if the shaft fairing is counted as the 11th vane. In this way, the aimed mismatch between number of blades and stator vanes is achieved for a lower rotor–stator interaction (RSI) noise emission [14]. For the same purpose of reducing the RSI noise, the stator vanes are swept by an angle ψ_s towards downstream (see Fig. 2.1(b)) as well as leaned by an angle ν_s in the opposite direction of rotation (see Fig. 2.2(b)) at the stator casing. More detailed information about design aspects of the shrouded tail rotor studied in this thesis can be found in Refs. [65, 74].

2.1.2 Numerical Grids

Because of the geometric complexity and the modeling of fan rotation, the overall computation domain is divided into three sub-domains as depicted in Fig. 2.4. The subdivided domains represent the rotating region (labelled **ROTOR**), the stator domain (**STATOR**) and the fuselage geometry including other remaining helicopter parts (**DOMAIN**), respectively. In each sub-domains, numerical grids are generated separately. The computational domains for the forward flight case are discretized by a multi-block structured mesh approach, while a hybrid unstructured mesh is used for the flow simulation of the hovering flight. This decision was made in order to evaluate the predictive capability of the hybrid CFD-CAA approach with different meshing strategies. For both meshing methods, a commercial grid generator ANSYS ICEM CFD [10] is used.

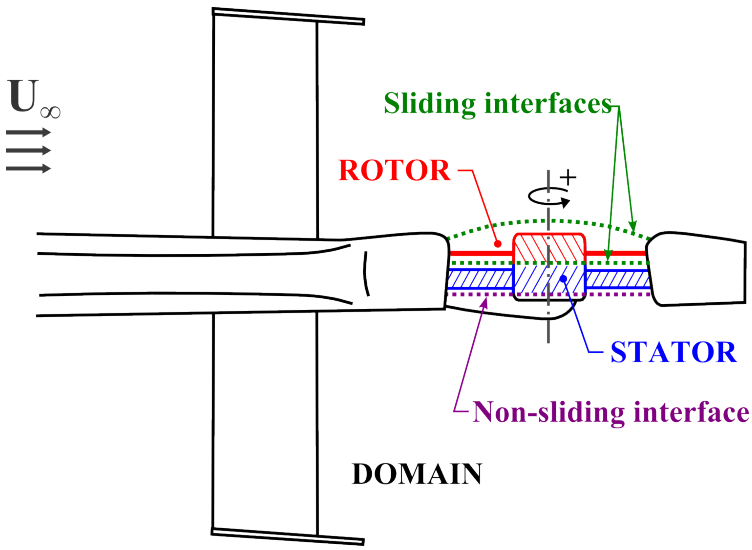

Figure 2.4: Schematic view of the subdivision of computational domains.

2.1.2.1 Numerical grid for the hovering case

For all computations with respect to the hovering flight, the hybrid-unstructured mesh method is applied (see Fig. 2.5). This method employs prism elements in the near-wall flow region and tetrahedral elements for the flow field far from solid surfaces. As the first step, a triangular mesh is generated on solid surfaces by means of the Octree method [10, 105]. Based on the surface mesh generated, the computational domain is then filled with the tetrahedral elements by using the Delaunay triangulation method [10] that ensures a more smoother expansion ratio of grid spacing between elements of different sizes. To prevent possible numerical reflections (mostly pressure reflection), the grid size is gradually increased from the near-wall region towards the outer domain boundaries (see Fig. 2.5). Finally, prism layers are extruded between the solid surfaces and the volume mesh to resolve the wall-bounded flow region precisely (see Fig. 2.6). Distance between the nearest grid node and the solid surface y_1 is properly chosen for all geometry components to take the advantage of the low-Reynolds approach in the viscous sub-layer. As a result, the dimensionless wall distance y^+ (see Eq. 2.1) is smaller than one in the most regions of the rotor blade as well as the stator vane. In total, 18 layers of the prism elements are generated perpendicular to the solid surfaces. In the region of the blade tip leakage, where the flow field is subject to strong pressure gradients and resulting tip-leakage vortex, special care is taken regarding the generation of the grid. Thus, the blade tip clearance is discretized with more than 40 nodes. With respect to acoustic propagation, the region between the upper side of the blade and the upper interface of the **ROTOR** is resolved by using around 15 grid points per wave length to capture up to the fourth harmonic of the fundamental frequency of the STR ($f/f_{\mathrm{BPF}} = 1$) appropriately. A further local mesh refinement is also performed in the vicinity of fan inlet and outlet, where FWH porous integration surfaces will be inserted in the subsequent acoustic calculation (see Fig. 2.5 and Sec. 3.2.1). The mesh of a medium grid density has a total of 103.8×10^6 elements and 33.5×10^6 nodes. Details of the number of elements and node points for the medium grid density are presented in Table 2.1.

$$y^+ = \frac{u_\tau \, y_1 \, \rho}{\mu}; \qquad u_\tau = \sqrt{\frac{\tau_w}{\rho}} \tag{2.1}$$

Parameter	ROTOR	STATOR	DOMAIN
Number of tetrahedrons ($\times 10^6$)	20.9	23.3	13.5
Number of prisms for 18 layers ($\times 10^6$)	30.9	11.9	3.3
Total number of elements ($\times 10^6$)	51.8	35.2	16.8
Total number of node points ($\times 10^6$)	19.5	10	4

Table 2.1: Grid details for simulations of the hovering flight (medium grid density).

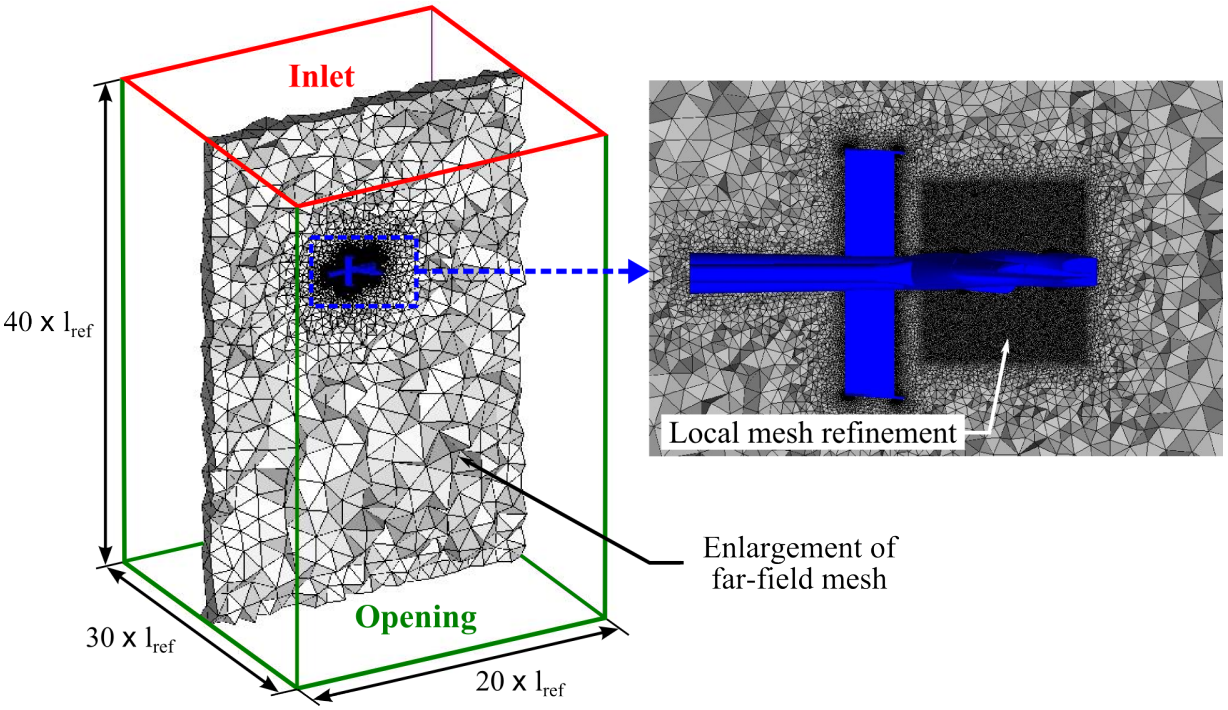

Figure 2.5: Computational domain and unstructured grid topology for simulations of the hovering flight.

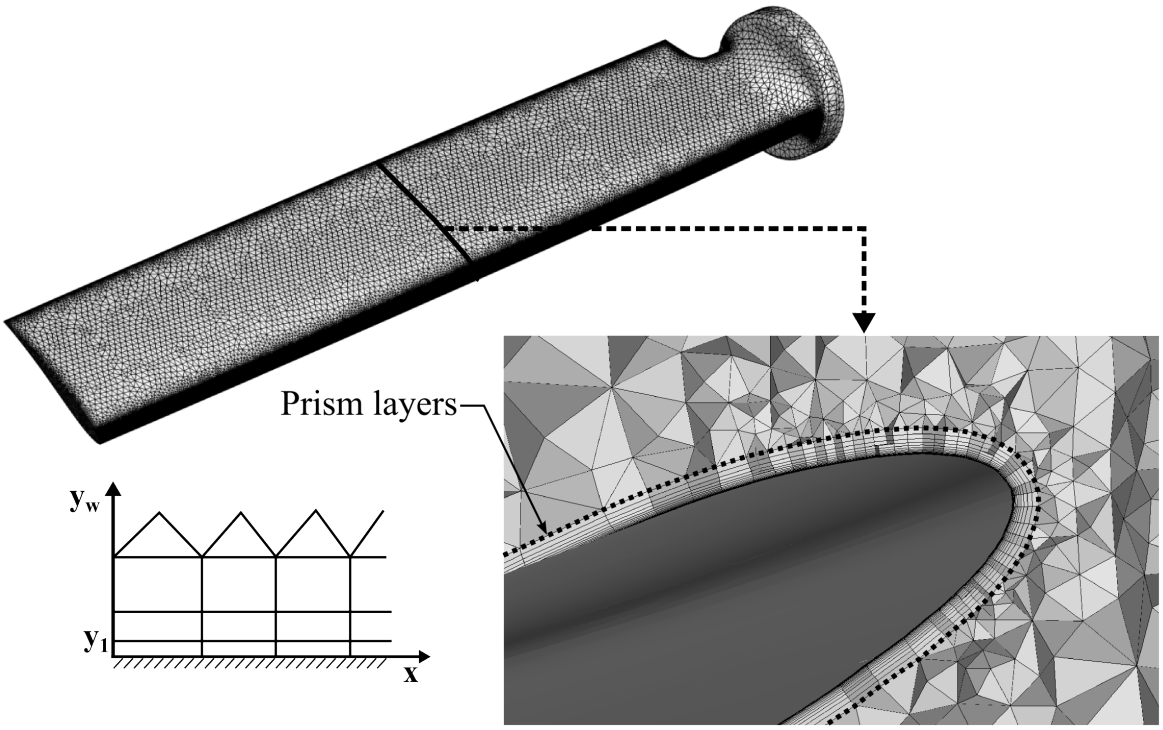

Figure 2.6: Surface mesh and prism layer extrusion around a rotor blade.

2.1.2.2 Numerical grid for the forward flight case

The multi-block structured mesh is used for all computations related to the forward flight condition (see Fig. 2.7(a)). The rotor blade is discretized by a C-type grid topology in the spanwise direction covering the region between the rotor hub and the rotor casing, while an O-grid topology is applied in the chrodwise direction (see 2.7(b)). In total, 21 node points are distributed between the blade tip face and the rotor casing to resolve the critical tip-leakage flow appropriately. The cylindrical blade root connecting the blade to the rotor hub is also modeled precisely. Similar to the simulation of the hovering flight, approximately 20 node points per wave length are distributed in the **ROTOR**–domain. For the stator part, a H-O type topology is applied, as indicated in Fig. 2.7(a). Detailed information about the node distribution on the rotor blade and the stator vane are presented in Table 2.2 for a medium grid density. Around the fuselage in the **DOMAIN**, a C-H type topology is applied. Special attention is given to the region between the fuselage aft-body and the STR to consider interactions occurring between the highly-turbulent fuselage wake and the STR. For the simulation using the scale-adaptive simulation (SAS) method (URANS-SAS), further mesh refinements are conducted in this region for a fine resolution of the fuselage wake (see Fig. 2.7(c)). Similar to the hovering case, the grid size is gradually increased towards the outer domain boundaries to prevent possible numerical reflections on the boundary surfaces as well as to reduce total number of elements. The value of y^+ is smaller than one in the most of regions on the rotor blade and the stator vane as well as on the fuselage surfaces to resolve the wall-bounded flows, and thus predicting flow separation precisely. The mesh of a medium grid density contains 3400 blocks and approximately 26.3×10^6 elements (10.6×10^6 in the **ROTOR**, 3.9×10^6 in the **STATOR**, and 11.8×10^6 in the **DOMAIN** for the simulation using the SST turbulence model (URANS-SST) and 13.5×10^6 in the **DOMAIN** for the URANS-SAS.

Parameter	Rotor blade	Stator vane
Normal layers	31	21
Spanwise node points	80	60
Circumferential node points	158	156
Total number of elements ($\times 10^6$)	10.6 in **ROTOR**	3.9 in **STATOR**

Table 2.2: Details of node distributions on the rotor blade and the stator vane for simulations of the forward flight case (medium grid density).

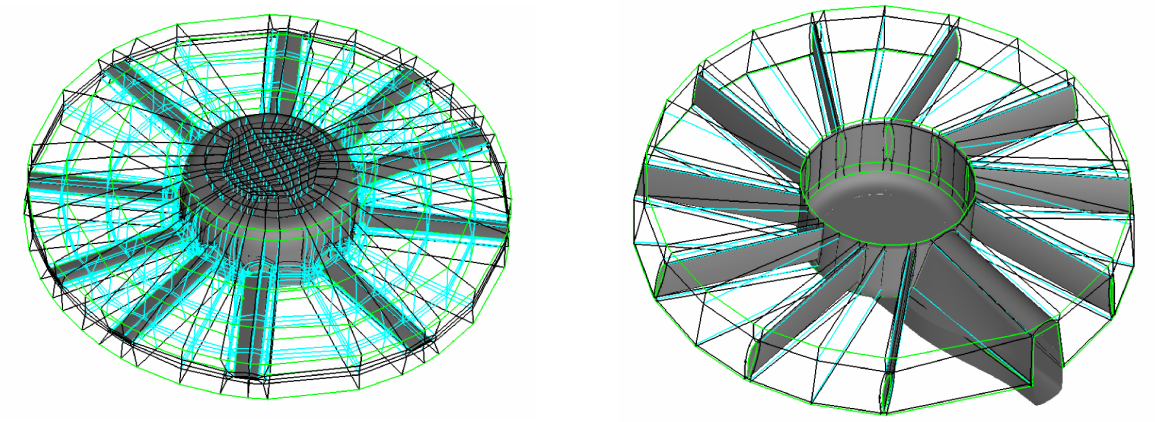

(a)

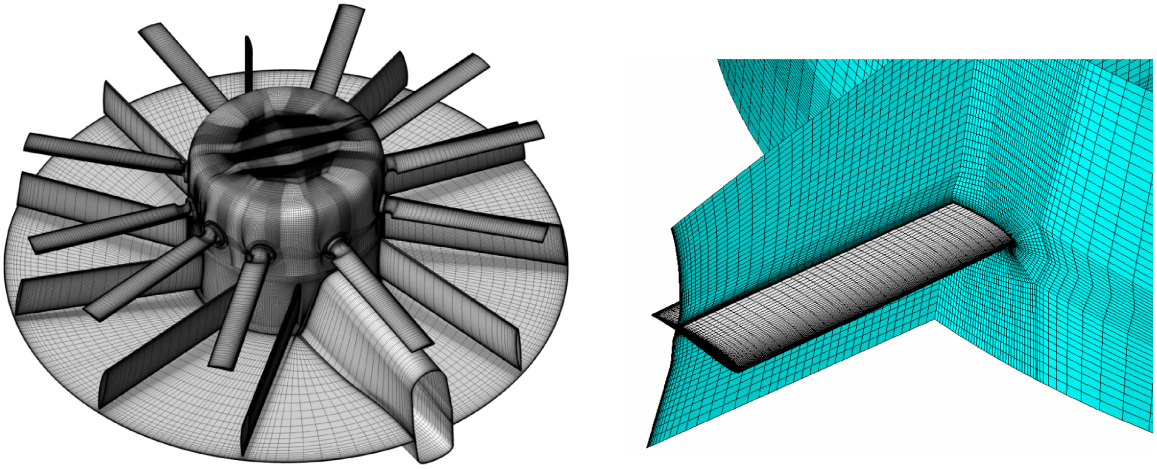

(b)

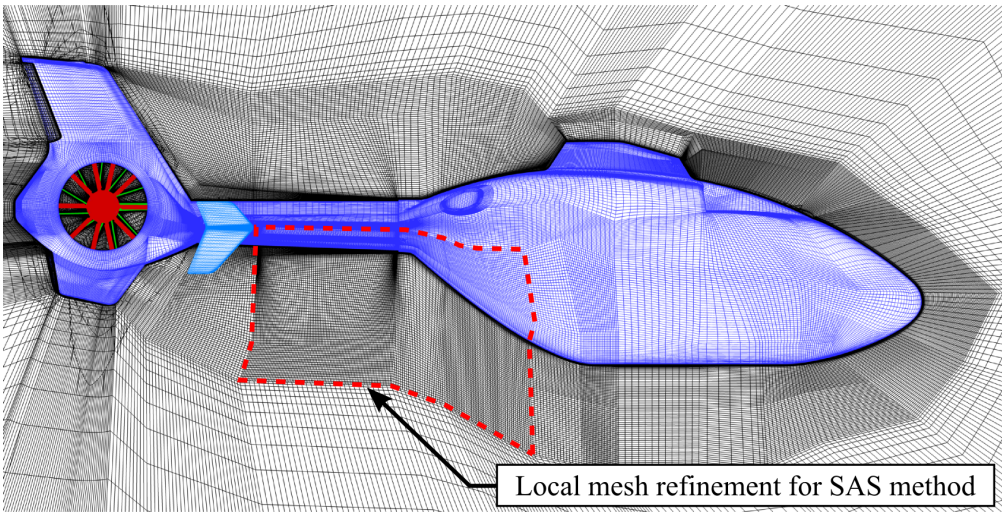

(c)

Figure 2.7: Multi-block structured mesh topology of the forward flight case: (a) edge distributions along blocks, (b) details of grid distributions in the **ROTOR** and **STATOR**, and (c) grid distribution around the helicopter configuration.

2.1.3 Boundary Conditions

Different boundary conditions are introduced depending on the flight conditions. The flight parameters as well as flow conditions employed for this thesis are listed in Table 2.3. Note that the rotational speed of the anti-torque rotor is identical for all flight conditions ($\Omega_{\text{hov}} = \Omega_{\text{for}}$).

Parameter	Forward flight	Hovering flight
Air temperature T_∞	288.15 K	
Reference pressure p_∞	101325 Pa	
Flight speed U_∞	62.5 m/s	0 m/s
Angle of attack α_∞	$-2\,^\circ$	$0\,^\circ$
Side-slip angle β_∞	$0\,^\circ$	
Blade pitch angle P_b	$2\,^\circ$	$26\,^\circ$
Rotational speed of anti-torque rotor Ω	$\Omega_{\text{hov}} = \Omega_{\text{for}} = 375.3$ rad/s	

Table 2.3: Flight parameters and air conditions.

2.1.3.1 Boundary conditions for the hovering case

The outer computation domain of the hovering case is a cuboid with $20\,l_{\text{ref}} \times 40\,l_{\text{ref}} \times 30\,l_{\text{ref}}$, length × height × width, respectively, as indicated in Fig. 2.5. The chosen reference length is identical to the fan diameter ($l_{\text{ref}} = 1$ m). Because of convergence and stability issues, the upper boundary located on the fan inlet side with a distance of about $15\,l_{\text{ref}}$ is defined with an Inlet boundary condition. Since the Inlet boundary condition requires specific information about the fluid flow entering into the computational domain, a normal speed of 0.01 m/s is specified on the upper boundary surface. Both the side and bottom boundary are defined with an Opening boundary condition because the direction of fluid flows can not be specified here. Contrary to a classical Outlet boundary condition, the Opening boundary condition allows bidirectional fluid flow across the boundary surface (out of domain as well as in opposite direction) [8]. All solid surfaces are defined with the no-slip boundary condition to fulfill the zero velocity condition of viscous flow on the solid surface. Interfaces are used for connecting the separately generated meshes of the sub-domains. Sliding interfaces are employed between the **DOMAIN** and the **ROTOR** as well as between the **ROTOR** and the **STATOR**, while a non-sliding interface is used to connect the **STATOR** with the **DOMAIN** (see Fig. 2.4). Possible non-matching and overlapping elements in the vicinity of the interface as well as fully conservative flux transfer across the interface are treated by the General Grid Interface (GGI) algorithm [9].

2.1.3.2 Boundary conditions for the forward flight case

The **DOMAIN** of the forward flight case has the form of a cuboid with $100\,l_{\text{ref}} \times 100\,l_{\text{ref}} \times 80\,l_{\text{ref}}$, length × height × width, respectively, as given in Fig. 2.8. The angle of attack $\alpha_\infty = -2°$ and the side-slip angle $\beta_\infty = 0°$ of the given flight condition (free stream velocity $U_\infty = 62.5$ m/s, $Re_{1:1}/l_{\text{ref}} = 4.18 \times 10^6$ 1/m) are taken into account at the domain inlet by introduction of a uniform velocity profile defined by three explicit velocity components u_∞, v_∞ and w_∞. Turbulence intensity at the domain inlet is assumed as low ($Tu = 1\%$, $\mu_t/\mu = 1$). Similar to the hovering case, the Opening boundary condition is imposed on the top and bottom side as well as on the sidewall of the **DOMAIN**. Primarily, the domain outlet was defined with a classical Outlet boundary condition. However, a problem arose due to the interaction between the Outlet boundary and the fuselage wake, which is characterized by strong vorticity and thus provoking a recirculating flow problem on the boundary surface. Since the classical Outlet boundary condition allows only the fluid flow passing though the boundary surface out of domain, the flow solver places artificial walls where local inflow is detected. The problem is eliminated by using the Opening boundary condition. Zero relative pressure across the boundary surface of the domain outlet is set ($\Delta p_s = p_s - p_\infty = 0$ Pa) to avoid an artificial pressure gradient downstream. The boundary conditions of all solid parts and interfaces between the sub-domains are set identical to the hovering case.

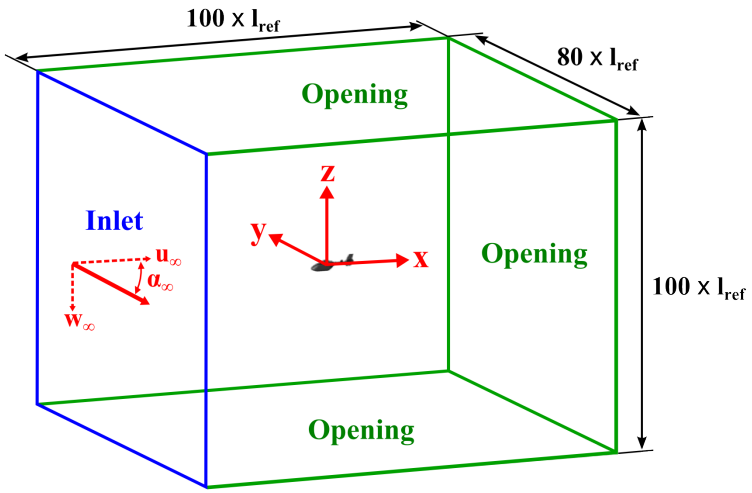

Figure 2.8: Sketch of the outer computational domain for the forward flight case.

2.1.4 Numerical Details

Unsteady RANS simulations were performed to predict the unsteady viscous flow field around the helicopter fuselage as well as inside the duct fairing of the STR. All computations were conducted by using a cell-vertex finite volume scheme based commercial flow solver ANSYS CFX (release 13/14/15) [8]. All simulations in this thesis were accom-

plished by parallel computing using the MPI algorithm on the high performance computers (HLRB II / SuperMuc) of the Leibniz Supercomputing Centre (LRZ) [63].

2.1.4.1 Turbulence models

Two different turbulence models are used for the simulation related to the forward flight condition: shear-stress transport (SST) model [9, 66] and scale-adaptive simulation (SAS) method [9, 27, 68]. This aims at the assessment of the noise prediction capabilities of the hybrid approach in terms of modeling order of turbulent flow. All simulations related to the hovering flight are performed with the SST model only.

The SST turbulence model developed by Menter is a two-equation eddy viscosity model combining the k–ω and k–ϵ model to take advantages of each formulations in the certain flow regime, such as the k–ω model for near-wall flow region and the k–ϵ model for far-field flow. A special blending function F_1 (defined in Eq. 2.4) based on the wall distance y_w allows a dynamic switching between each formulation: F_1 is equal to one in the near-wall flow region, while outside the boundary layer it is zero. The SST model is an established turbulence model for the prediction of complex flow fields involving massive flow separation, and used not only for industrial purposes but also for academic research due to its numerical robustness and acceptably low computational costs [11]. However, as like many other turbulence models of the classical URANS application, such as the k–ω, k–ϵ and Spalart-Allmaras (SA) model, the SST model is generally incapable to provide small scale eddies due to its averaging procedure, and thus furnishes only limited spectral information on the unsteady flow.

The SAS method is a second generation of the two-equation eddy viscosity model and primarily formulated through revision of the k–kL model suggested by Rotta [83]. Unlike the SST model, the SAS method can resolve turbulent fluctuations up to almost grid limitation of given grid size, thus being able to provide an Large Eddy Simulation (LES)-like resolution of eddies in the unstable flow regime. This scale resolving approach is based on the idea introducing an additional source term Q_{SAS} (defined in Eq. 2.6) into the transport equation of the turbulent eddy frequency ω, as formulated in the following set of equations [9]:

$$\frac{\partial(\rho k)}{\partial t}+\frac{\partial(\rho U_j k)}{\partial x_j}=\frac{\partial}{\partial x_j}\left[\left(\mu+\frac{\mu_t}{\sigma_k}\right)\frac{\partial k}{\partial x_j}\right]+P_k-\beta'\rho k\omega \tag{2.2}$$

$$\begin{aligned}\frac{\partial(\rho\omega)}{\partial t}+\frac{\partial(\rho U_j\omega)}{\partial x_j}&=\frac{\partial}{\partial x_j}\left[\left(\mu+\frac{\mu_t}{\sigma_\omega}\right)\frac{\partial\omega}{\partial x_j}\right]\\ &+\underbrace{(1-F_1)}_{\text{SST blending term}}\frac{2\rho}{\sigma_{\omega 2}\omega}\frac{\partial k}{\partial x_j}\frac{\partial\omega}{\partial x_j}+\alpha\frac{\omega}{k}P_k-\beta\rho\omega^2+\underbrace{Q_{\mathrm{SAS}}}_{\text{SAS source term}},\end{aligned} \tag{2.3}$$

where the SST blending function F_1 is formulated as:

$$F_1=\tanh\left\{\left\{\min\left[\max\left(\frac{\sqrt{k}}{\beta'\omega y},\frac{500\nu}{y^2\omega}\right),\frac{4\rho\sigma_{\omega 2}k}{CD_{k\omega}y^2}\right]\right\}^4\right\} \tag{2.4}$$

with the cross diffusion term $CD_{k\omega}$:

$$CD_{k\omega} = \max\left(\frac{2\rho\sigma_{\omega 2}}{\omega}\frac{\partial k}{\partial x_i}\frac{\partial \omega}{\partial x_i}, 10^{-10}\right) \tag{2.5}$$

and the SAS source term Q_{SAS}:

$$Q_{\mathrm{SAS}} = \max\left[\rho\zeta_2\kappa S^2\left(\frac{L}{L_{\nu K}}\right)^2 - C\frac{2\rho k}{\sigma_\Phi}\max\left(\frac{1}{\omega^2}\frac{\partial\omega}{\partial x_j}\frac{\partial\omega}{\partial x_j}, \frac{1}{k^2}\frac{\partial k}{\partial x_j}\frac{\partial k}{\partial x_j}\right), 0\right], \tag{2.6}$$

where L is the integral length scale of modeled turbulence:

$$L = \frac{\sqrt{k}}{\omega}, \tag{2.7}$$

and $L_{\nu K}$ is the von Kármán length scale:

$$L_{\nu K} = \kappa\frac{U'}{U''} \tag{2.8}$$

with the first U' and second velocity gradient U'':

$$U' = \sqrt{\frac{\partial U_i}{\partial x_k}\frac{\partial U_i}{\partial x_j}}, \quad U'' = \sqrt{\frac{\partial^2 U_i}{\partial x_k^2}\frac{\partial^2 U_i}{\partial x_j^2}} \tag{2.9}$$

A switch from the SST mode to the SAS mode, and vice versa, is achieved by the ratio of the integral length scale of modeled turbulence L (defined in Eq. 2.7) to the newly introduced von Kármán length scale $L_{\nu K}$ (defined in Eq. 2.8). The von Kármán length scale is defined as the ratio of the first U' to second derivative U'' of predicted velocity (see Eq. 2.9), and in general smaller in the unsteady flow than in the steady case [23]. Therefore, $L/L_{\nu K}$ and Q_{SAS} increase, where the flow field reveals sufficient occurrence of flow unsteadiness. Consequently, ω is increased, which in turn decreases the eddy viscosity μ_t, defined as follows [66]:

$$\mu_t = \nu_t\rho = \rho\frac{a_1 k}{\max\left(a_1\omega, SF_2\right)} \tag{2.10}$$

with the strain-rate magnitude S:

$$S = U' = \sqrt{2S_{ij}S_{ij}}, \quad S_{ij} = \frac{1}{2}\left(\frac{\partial U_i}{\partial x_j} + \frac{\partial U_j}{\partial x_i}\right) \tag{2.11}$$

and the second blending function F_2:

$$F_2 = \tanh\left\{\left[\max\left(\frac{2\sqrt{k}}{\beta'\omega y}, \frac{500\nu}{y^2\omega}\right)\right]^2\right\} \tag{2.12}$$

As the result of diminished dissipation effects of the eddy viscosity on turbulent structures, LES-like fine resolution of turbulent fluctuations is provided in the region of unsteady flow. Since the SAS approach used in the thesis is converted into the k–ω SST formulation (see Eq. 2.3), the flow solver turns back to the RANS mode of the SST turbulence model if the source term is eliminated ($Q_{\mathrm{SAS}} = 0$), such as in boundary layer flows. The SAS approach exhibits less grid dependence compared to the Detached Eddy Simulation (DES) as the SAS source term does not contain any parameters with respect to the grid spacing. However, a certain degree of fine grid spacing is still preferred to exclude numerical dissipation associated with coarse grid densities.

2.1.4.2 Numerical methods

Depending on the turbulence model, two different spatial discretization schemes are applied. The High-Resolution scheme [9, 12] employed for the simulation using the SST model (URANS-SST) allows a dynamical adjustment between robustness (first order Upwind scheme) and accuracy (second order Upwind scheme) of computation results, controlled by a specific blending factor β_B. In the case of the URANS-SAS, it is beneficial to employ a less dissipative discretization scheme to support the scale resolving capability of the SAS formulation. However, the SAS method in combination with the less dissipative scheme such as Central Differencing (CD) can lead to an undesirable numerical

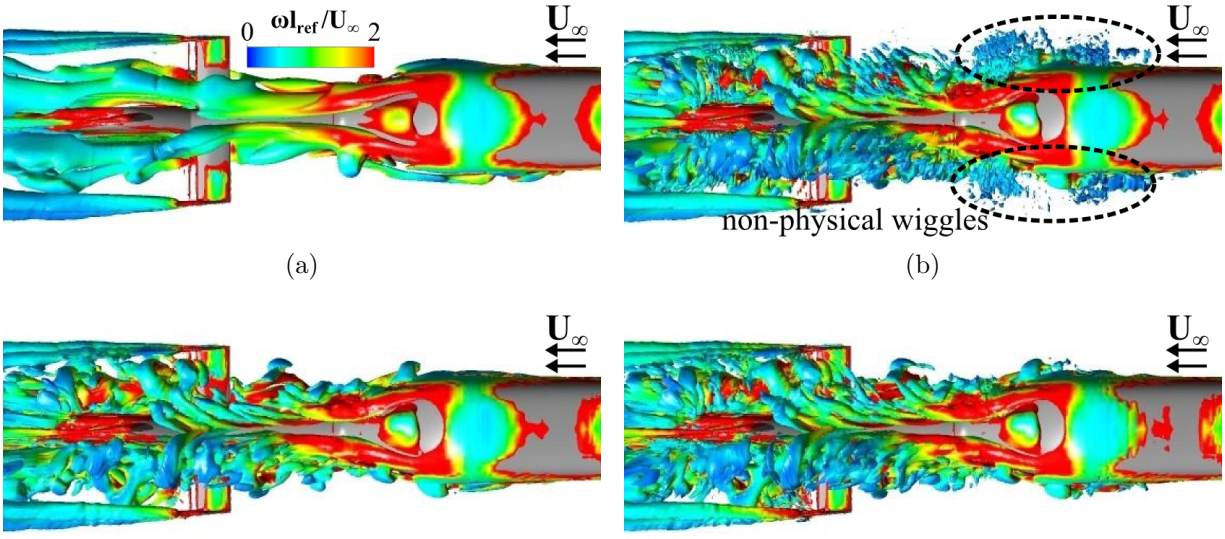

Figure 2.9: Influence of spatial discretization schemes : (a) URANS-SST with High-Resolution scheme, (b) URANS-SAS with CD scheme, (c) URANS-SAS with BCD scheme ($F_{\mathrm{BCD}} = 1$), and (d) URANS-SAS with BCD scheme ($F_{\mathrm{BCD}} = 0.25$), vortical structures are visualized by isosurface of Q-criterion (bottom view).

oscillations that appear under the form of non-physical wiggles in the resulting flow field (see Fig. 2.9(b)). Therefore, the Bounded Central Differencing (BCD) scheme [9, 46, 57] is employed for the URANS-SAS. It allows a dynamical blending between a variation of the second order CD scheme ($F_{\mathrm{BCD}} = 0$) and the first order Upwind scheme ($F_{\mathrm{BCD}} = 1$). Generally, the BCD scheme is more dissipative than the classical unbounded CD scheme, but less dissipative than the second order Upwind scheme, therefore still suitable for the scale resolving simulation approaches [67].

For both flight conditions, steady-state flow simulations are performed beforehand by using the Frozen-Rotor method [8] to obtain initial values of subsequent unsteady computations. The Frozen-Rotor method models the fan rotation by changing the frame of reference, but the rotor blades are kept fixed during the computations. Thus, this model is not able to predict unsteady phenomena, such as the rotor–stator interaction. However, it can provide a steady-state solution at acceptable computational costs. Based on the converged solution of the steady-state simulation, unsteady, time-accurate RANS simulations are performed with the sliding mesh technique (Transient-Rotor-Stator [8, 9]). Unlike the Frozen-Rotor method, the sliding mesh technique models the fan rotation by rotating the entire **ROTOR**–domain containing the blade mesh. The position of blades are updated at every time step. Therefore, the sliding interface is required between the **DOMAIN** and the **ROTOR** as well as between the **ROTOR** and the **STATOR** (see Fig. 2.4), to treat possible non-matching and overlapping grid elements, and to ensure the fully conservative flux transfer through these interfaces. Moreover, a counter rotating wall velocity with the no-slip boundary condition is applied on the solid surface of the rotor casing to model the non-rotating rotor casing. Note that the fan rotates counterclockwise when viewed from the fan inlet side (see Fig. 2.10).

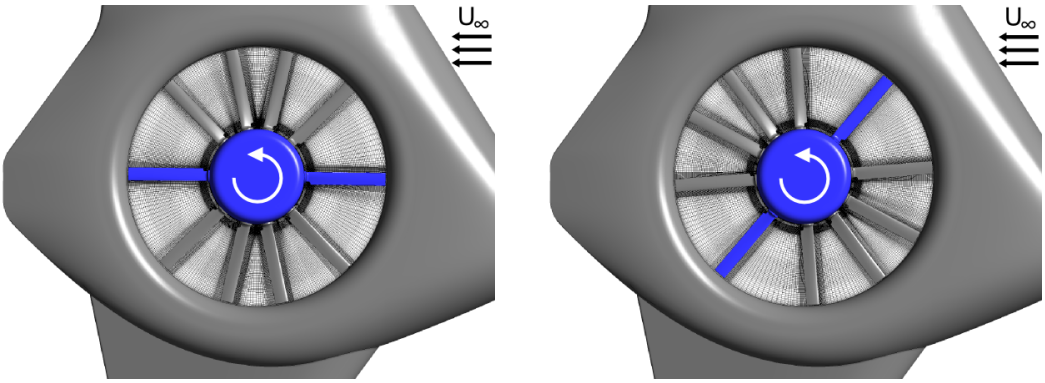

(a) (b)

Figure 2.10: Direction of rotation of the anti-torque rotor: (a) $\psi_f = 0°$ and (b) $\psi_f = 45°$.

All simulations are carried out under assumption of ideal gas conditions at 288.15 K and a fully turbulent boundary layer. The compressibility effect occurring in the vicinity of the blade tip at the given rotational speed of the anti-torque rotor ($Ma_{\mathrm{tip}} > 0.5$) is taken into account by using the total enthalpy form of the energy equation [8, 9]. In addition, double precision is set to all variations of the flow simulation as the CFD results serve as the input

data of subsequent acoustic computations. A second order accurate implicit time-stepping (second order Backward Euler) scheme [9] is used for the temporal discretization.

2.1.4.3 Simulation parameters for the hovering case

In the case of the hovering flight, a constant simulation time step of $\Delta t_{\mathrm{CFD}} = 4.7 \times 10^{-5}$ s is defined throughout all unsteady computations. It corresponds to a blade rotation of $\Delta\psi_f = 1.0106°$ per time step. Hence, at least 357 time steps are necessary to complete the computation of one fan revolution. The time step size can be further increased (e.g. $\Delta t_{\mathrm{CFD}} = 14.1 \times 10^{-5}$ s corresponding to $\Delta\psi_f = 3.0318°$) in order to reduce computational costs in the hovering flight condition since the flow field of the STR bears more homogeneous and periodic properties compared to that in the forward flight condition [110, 113].

Considering both the thrust coefficient C_T (defined in Eq. 2.13) and the non-dimensional fan exit velocity $v_{\mathrm{exit}}/U_{70\%}$, the convergence of the solution is achieved approximately after five fan revolutions, as shown in Fig.2.11. Note that $v_{\mathrm{exit}}/U_{70\%}$ is averaged over the fan outlet interface and made dimensionless by the tangential velocity $U_{70\%}$ measured at 70% of the fan radius.

$$C_T = \frac{F_y}{\rho_\infty (\Omega/60)^2 (D_f)^4} \tag{2.13}$$

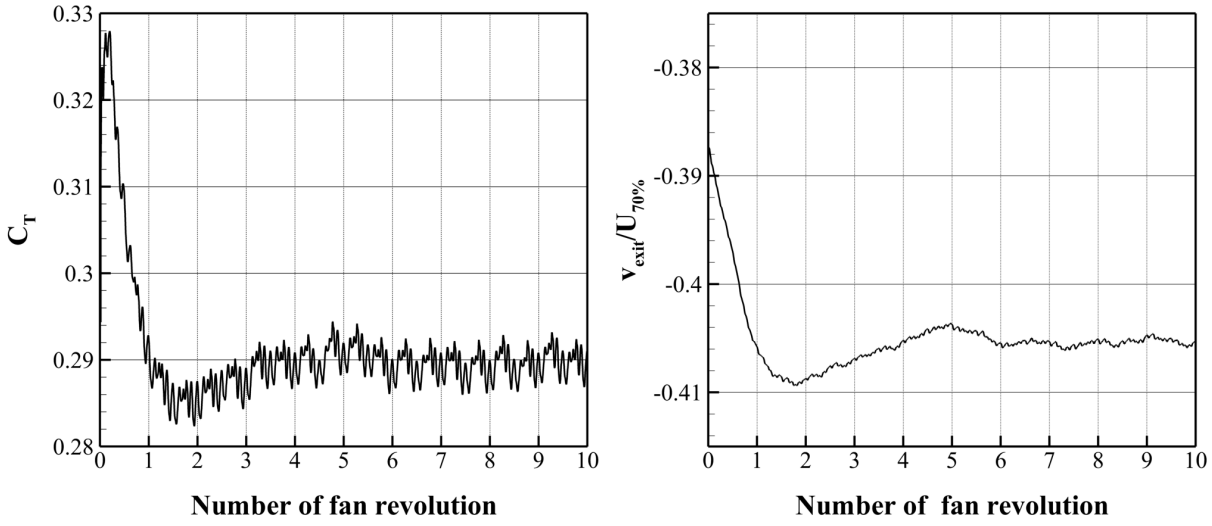

(a) (b)

Figure 2.11: Convergence history of the unsteady simulation of the hovering flight: (a) thrust coefficient C_T and (b) mean fan exit velocity ratio $v_{\mathrm{exit}}/U_{70\%}$.

Around 20240 CPU hours are necessary for computing one fan revolution by using a number of up to 220 processors on the thin node island of the LRZ SuperMuc (Phase 1, Intel Xeon E5-2680 8C processors with 2 GByte memory per core [63]). In total, ten fan revolutions are computed, whereby the acquisition of transient data sets for the acoustic computation is performed only during the last five fan revolutions.

2.1.4.4 Simulation parameters for the forward flight case

For the first four fan revolutions, the URANS-SST of the forward flight condition is performed with coarse time steps ($\Delta t_{\mathrm{CFD}} = 47 \times 10^{-5}$ s corresponding to $\Delta\psi_f = 10.106°$ and $\Delta t_{\mathrm{CFD}} = 23.5 \times 10^{-5}$ s corresponding to $\Delta\psi_f = 5.0532°$) to accelerate the convergence of the fan parameters (see Figs. 2.12(a) and 2.12(b)). After this phase, the reference time step of $\Delta t_{\mathrm{CFD}} = 4.7 \times 10^{-5}$ s is set throughout the whole analysis.

Quasi-stable state with respect to the fan parameters is achieved after the fifth fan revolution. However, noticeable variations around the mean value are still observed within 13 fan revolutions computed. They are related to unsteady flow phenomena induced by the cross flow, and will be explained in Chap. 5 in more detail. In contrast to the fan parameters, the aerodynamic force coefficients of the fuselage, C_x (Eq. 2.14) and C_z, (Eq. 2.16) indicate no distinct convergence behavior within 13 fan revolutions computed (see Figs. 2.12(c) and 2.12(d)). This is because the process of the vortex formation at the fuselage aft-body is much slower than the rotational speed of the anti-torque rotor. For the acoustic analysis, five fan revolutions are considered in order to account for the influence of the fuselage wake on the STR noise generation. This number of fan revolutions corresponds to the time that a fluid particle needs to travel from the fuselage aft-body to the STR at the given flight speed of $U_\infty = 62.5\, m/s$. Up to 160 processors are used, and about 7140 CPU hours are consumed for computing a single fan revolution by the reference time step size.

The URANS-SAS is performed based on the converged solution of the URANS-SST. Before the acquisition of transient data sets begins, further five fan revolutions were computed as the decomposition of the large scale turbulent structures of the previous URANS-SST into small eddies as well as their convection through the computation domain (at least one order of the helicopter model length) requires some developing time [67]. Due to the increased number of mesh nodes (14% with respect to the URANS-SST mesh) as well as the specific numerical schemes employed (e.g. turbulence model, BCD scheme), the URANS-SAS requires higher computational costs. For computing one fan revolution, the SAS simulation consumes approx. 13% more computational time than the SST simulation.

For all simulation cases, the acquisition of transient data involving density ρ, static pressure p_s and flow velocity components u, v, and w is performed at every time step during the last five fan revolutions (1781 samples) corresponding to a computed physical time range of $t_{\mathrm{CFD}} = 0.0084$ s.

$$C_x = \frac{F_x}{\frac{1}{2}\rho_\infty U_\infty^2 A_{\mathrm{ref}}} \tag{2.14}$$

$$C_y = \frac{F_y}{\frac{1}{2}\rho_\infty U_\infty^2 A_{\mathrm{ref}}} \tag{2.15}$$

$$C_z = \frac{F_z}{\frac{1}{2}\rho_\infty U_\infty^2 A_{\mathrm{ref}}} \tag{2.16}$$

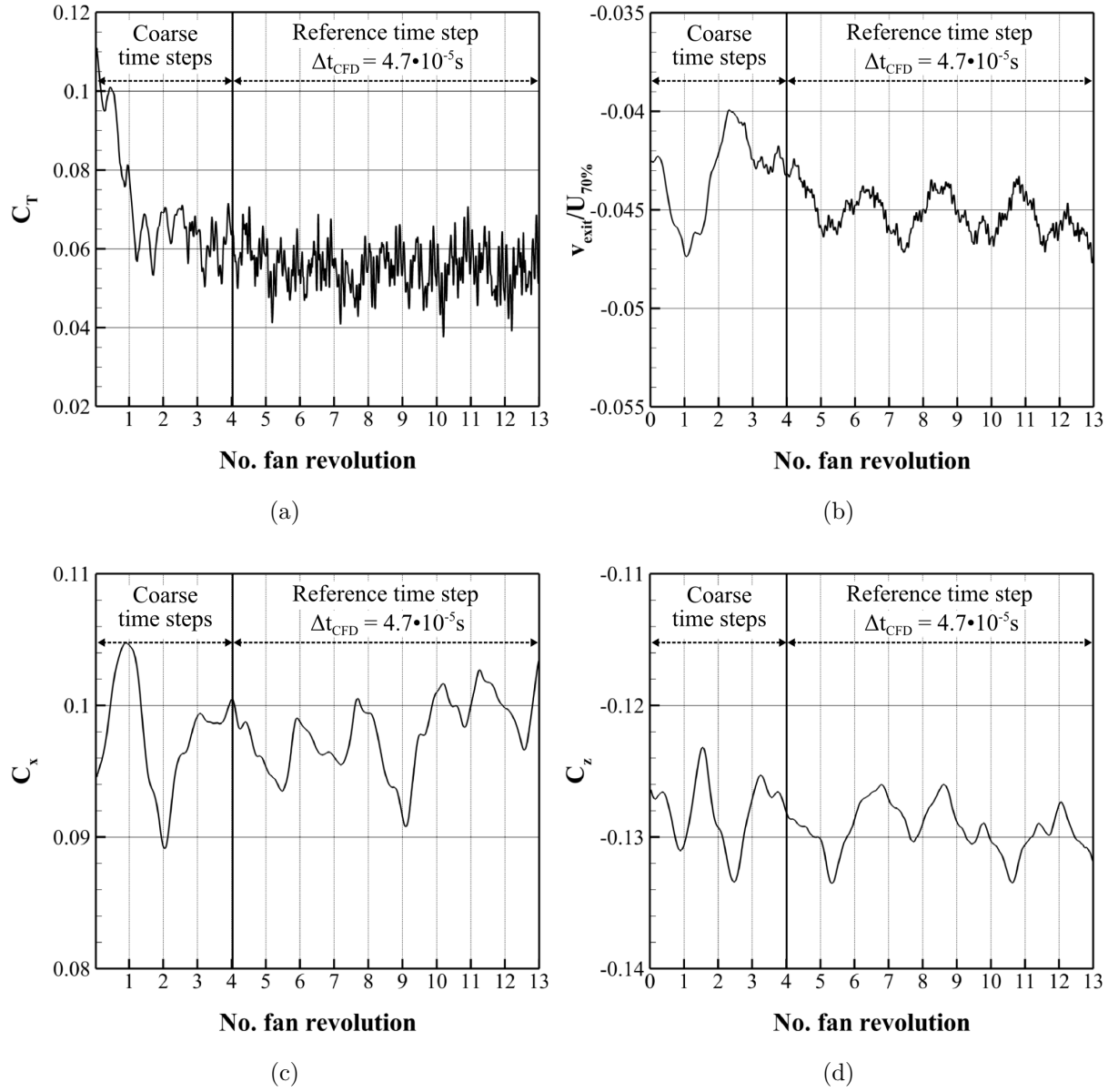

Figure 2.12: Convergence history of the forward flight case: (a) thrust coefficient C_T, (b) fan exit velocity ratio $v_{\text{exit}}/U_{70\%}$, (c) streamwise C_x, and (d) vertical force coefficient C_z of the helicopter fuselage as a function of the number of fan revolutions.

2.1.5 Grid Resolution Study

2.1.5.1 Grid sensitivity study for the hovering case

Grid sensitivity of the hovering case is assessed by comparison of three different blade grid densities (coarse, medium, and fine). The distance y_1 of the first grid node from the blade surface is fixed during the mesh refinement to retain the target value of $y^+ < 1$. Furthermore, the identical stator grid density is used throughout all grid sensitivity studies. Details of the grid densities investigated and the resulting mean thrust coefficient $\overline{C}_T$ are

presented in Table 2.4.

Comparing the time-averaged fan thrust coefficient $\overline{C}_T$ at different grid densities, it tends to decrease with decreasing grid spacing: the coarse grid density yields the highest value ($\overline{C}_T = 0.285$) and the fine grid density results in the lowest value ($\overline{C}_T = 0.279$). The relative deviation with respect to the medium grid density is $+0.7\,\%$ for the coarse grid and $-1.6\,\%$ for the fine grid. In Fig. 2.13, the surface pressure coefficient C_p distribution of different grid densities is compared on the upper surface of the rotor blade as well as on the rotor casing. All grid densities predict a significant magnitude of negative C_p on the rotor casing and on the blade suction side along the upper edge of the blade tip face. The former is due to the strong jet-like flow in the tip-leakage, induced by the strong pressure difference between the blade lower (pressure side) and upper side (suction side), and the latter is related to the reattachment of the resulting tip-leakage vortex. In the case of the coarse grid density, these flow regions of strong pressure gradients are underestimated. Since there are no significant differences between the medium and fine grid densities, the medium grid density is used for all productive simulations of the hovering flight.

Parameter	Coarse	Medium	Fine
Total number of nodes ($\times 10^6$)	6.9	19.4	22.3
Total number of elements ($\times 10^6$)	20.6	51.8	60.4
Mean thrust coefficient $\overline{C}_T$	0.285	0.283	0.279

Table 2.4: Grid sensitivity study for the hovering case.

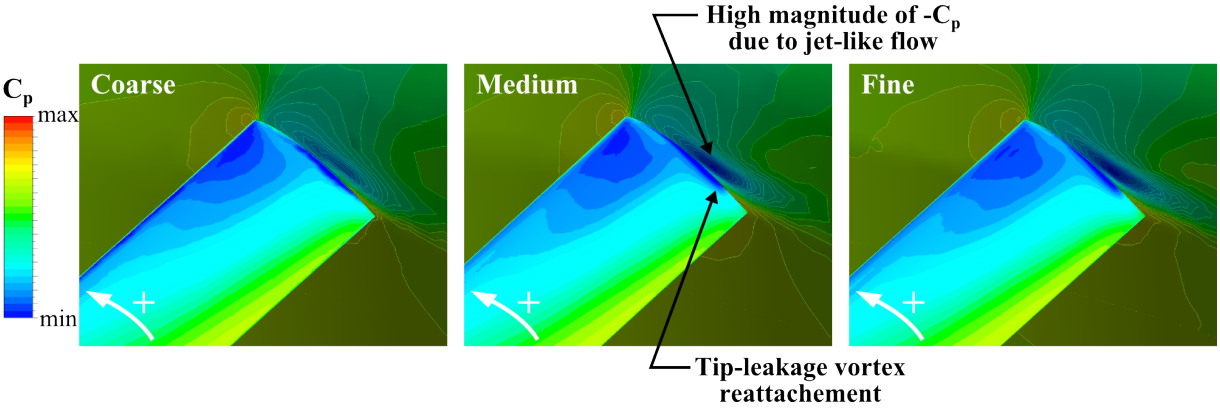

Figure 2.13: Surface pressure coefficient C_p on the rotor blade and the rotor casing.

2.1.5.2 Grid sensitivity study for the forward flight case

Three different fuselage grid densities are investigated based on the configuration with sealed STR inlet and outlet opening (see Fig. 2.14) to assess the sensitivity of flow phenomena, associated with the fuselage wake, to the grid spacing. Details about the fuselage

grids investigated are given in Table 2.5. Similar to the hovering case, the nearest wall distance y_1 is not changed during the mesh refinement to fix the value of $y^+ < 1$. Considering the time-averaged streamwise force coefficient $\overline{C}_x$, it is observed that the mesh refinement leads to a decrease in $\overline{C}_x$. The relative deviation with respect to the medium grid density is $-5.27\,\%$ for the coarse and $+3.35\,\%$ for the fine grid density.

In Fig. 2.14, the sectional distribution of the surface pressure coefficient C_p predicted on the fuselage aft-body ($z/l_{\text{ref}} = 2$) is given for the coarse, medium and fine grid densities. The medium and fine grid density reveal a quite similar pressure distribution. Both grid densities predict considerable change of C_p at $y/l_{\text{ref}} = -0.4$ and $y/l_{\text{ref}} = 0.4$, corresponding to the separation onset in the rear fuselage upsweep and the lateral tapering region. With the coarse grid, this region is considerably underestimated, which explains the reason of the relatively high level of $\overline{C}_x$.

Parameter	Coarse	Medium	Fine
Normal layers	27	33	38
Circumferential node points	188	222	267
Total number of elements ($\times 10^6$)	4.92	8.38	14.23
Mean streamwise force coefficient $\overline{C}_x$	0.517	0.491	0.475

Table 2.5: Grid sensitivity study of the helicopter fuselage for the forward flight case.

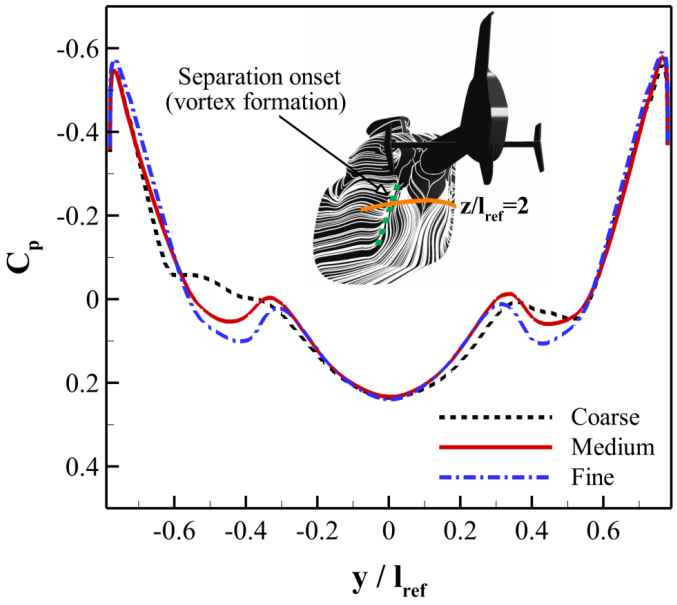

Figure 2.14: Sectional distributions of surface pressure coefficient C_p on the fuselage aft-body at $z/l_{\text{ref}} = 2$.

Based on the medium fuselage grid density, a further grid sensitivity study is performed

for the **ROTOR**–domain. Details on the grid information for the rotor blade are given in Table 2.6. Contrary to the fuselage, there is no noticeable grid dependency regarding the mean fan thrust coefficient $\overline{C}_T$. The relative deviation of $\overline{C}_T$ is 4 % between the coarse and medium grid and 2 % between the medium and fine grid density.

Fig. 2.15 depicts chordwise distributions of the blade C_p at 99 % of the fan radius. In general, all grid densities investigated provide a similar trend of C_p in chordwise direction on both the lower and upper surface. According to the C_p distribution, the effect of the grid resolution is limited to the flow region where a strong velocity gradient is expected: (1) suction peak on the lower blade surface close to the leading edge and (2) tip-leakage vortex reattachment on the upper blade surface near the trailing edge. Differences in C_p in these regions are, however, not significant ($\Delta C_{p,\max} = 0.007$). From 30 % ($x/x_r = 0.3$) to 80 % chord ($x/x_r = 0.8$), the influence of the grid refinement is even negligible small. Finally, the medium grid size is chosen for all computations of the forward flight condition.

Parameter	Coarse	Medium	Fine
Normal layers	25	31	38
Spanwise nodes	66	80	99
Circumferential nodes	126	158	194
Total number of elements ($\times 10^6$)	5.13	10.26	19.86
Mean thrust coefficient $\overline{C}_T$	0.052	0.050	0.051

Table 2.6: Grid sensitivity study of the rotor blade for the forward flight case.

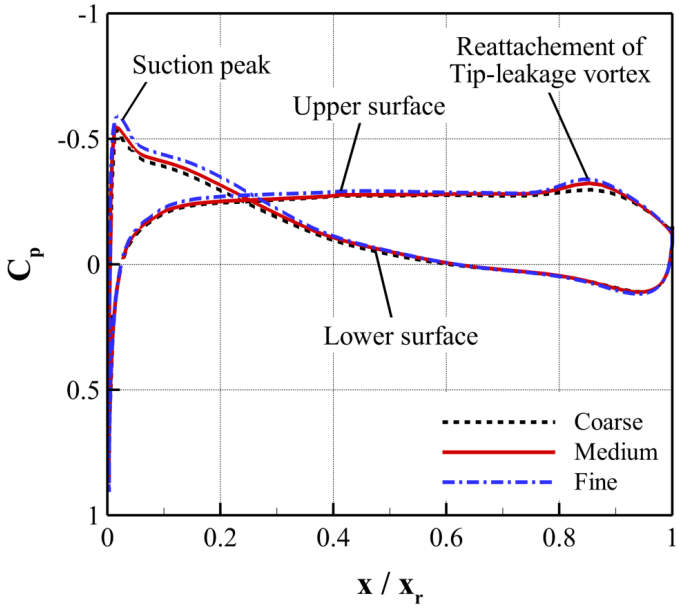

Figure 2.15: Chordwise distributions of C_p at 99 % of the fan radius.

2.2 Validation of Flow Simulation

The predictive capability of the flow simulation is evaluated in particular for the simulation case of the forward flight condition by comparison of numerically predicted flow quantities with the data obtained from the wind tunnel measurements. For this purpose, further numerical simulations are conducted based on the wind tunnel model size (1:7.333) [114]. To adapt to the wind tunnel model configuration (see Fig. 2.16(a)), the full-scale numerical model is scaled down to the model size, and both the STR inlet and outlet opening are sealed (see Fig. 2.16(b)). There are, however, still differences between the wind tunnel model and the helicopter configuration computed. For instance, the aerodynamic fairing attached to the front engine cowling and the curved surfaces representing the side windows of the wind tunnel model, as seen in Fig. 2.17, are not modeled in the numerical simulation. The block topology as well as the node distributions of the scaled grid are identical to those of the full-scale grid (see Sec. 2.1.2.2). Furthermore, the same computational parameters and numerical methods (e.g. SST turbulence model, High-Resolution scheme) as the full-scale simulation are used (see Sec. 2.1.3.2 and Sec. 2.1.4.4).

The experimental work [101] was conducted in the Goettingen-type wind tunnel facility A at the Chair of Aerodynamics and Fluid mechanics of Technical University of Munich. This low speed wind tunnel has an open test section with dimensions of $1.8\,\mathrm{m} \times 2.4\,\mathrm{m} \times 4.8\,\mathrm{m}$ (height $\times$ width $\times$ length). The free stream at the wind tunnel nozzle exit exhibits a homogeneous turbulence intensity of less than 0.4% [2]. Both the numerical simulations and the wind tunnel experiments were conducted for the free stream velocity of $U_\infty = 40\,\mathrm{m/s}$ ($Re_{1:7}/l_{\mathrm{ref}} = 3.6 \times 10^5\ 1/\mathrm{m}$) with an angle of attack of $\alpha_\infty = -2°$ and a side-slip angle of $\beta_\infty = 0°$. In the wind tunnel campaign, both force and surface pressure measurements (steady-state, unsteady) were conducted. Positions of the pressure taps used are presented in Fig. 2.17.

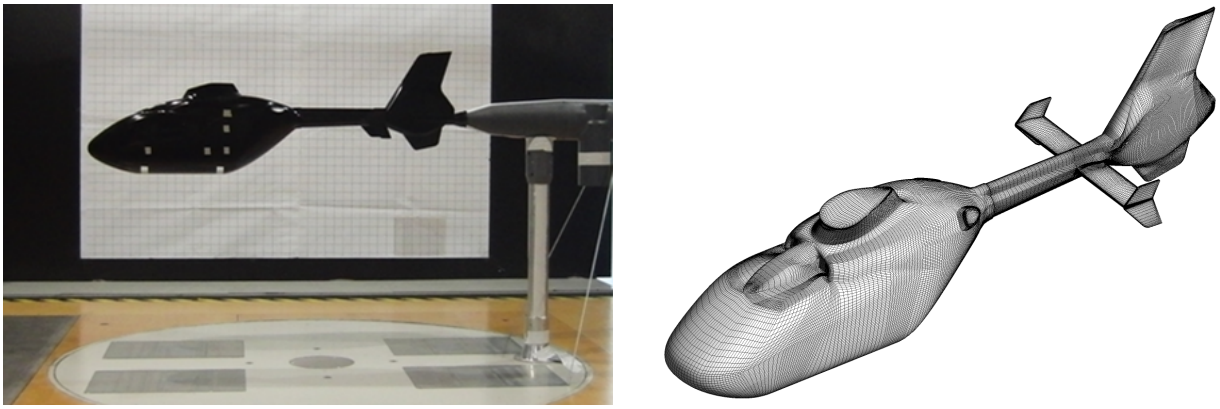

(a) (b)

Figure 2.16: Wind tunnel model (1:7.333) of the helicopter configuration with closed STR inlet and outlet opening: (a) wind tunnel model and (b) numerical model.

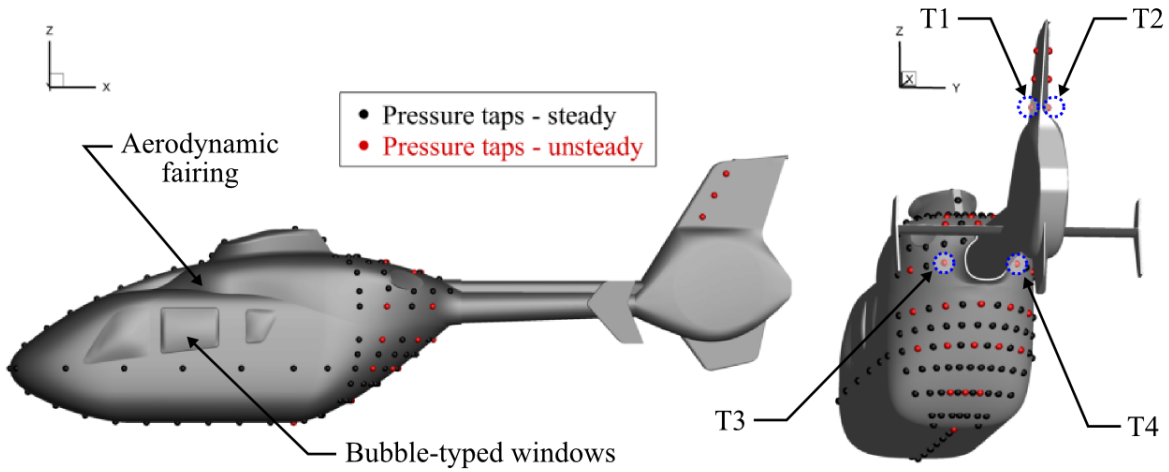

Figure 2.17: Position of pressure taps on the wind tunnel helicopter model.

2.2.1 Aerodynamic Forces

In Fig. 2.18, the time-averaged aerodynamic force coefficients $\overline{C}_x$ (streamwise), $\overline{C}_y$ (lateral), and $\overline{C}_z$ (vertical) are presented for the numerical simulations using the SST (CFD-SST) and the SAS turbulence model (CFD-SAS) as well as for the wind tunnel measurements. Considering $\overline{C}_x$ and $\overline{C}_z$, it is found that both turbulence models lead to an overprediction with respect to the experimental result, whereas $\overline{C}_y$ is somewhat underestimated ($-9\,\%$). The discrepancy mostly relates to the above-mentioned geometrical differences. For the numerical simulations, the engine inlet opening is closed with a surface, which is perpendicular to the direction of the incoming flow. Therefore, the numerical simulations predict significant levels of static surface pressure in this region (stagnation point). On the contrary, the wind tunnel model features the aerodynamic fairing, which prevents any

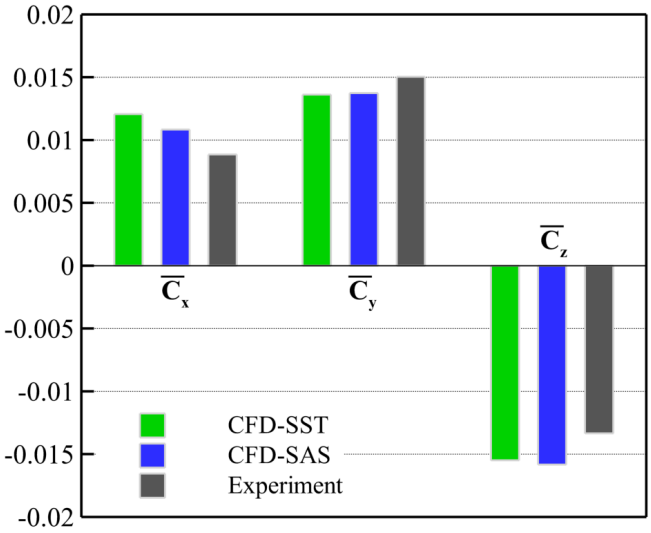

Figure 2.18: Comparison of time-averaged steamwise $\overline{C}_x$, lateral $\overline{C}_y$, and vertical $\overline{C}_z$ force coefficients between numerical simulations and wind tunnel measurements.

strong stagnation of fluid flow. Nevertheless, $\overline{C}_x$ and $\overline{C}_y$ of the SAS simulation case are in better agreement with those of the experiment than the SST simulation.

2.2.2 Steady-State Pressure Distributions

Fig. 2.19 depicts time-averaged distributions of the surface pressure coefficient $\overline{C}_p$ on the cross-sectional line located at $y/l_{\text{ref}} = 0$ (symmetry line). A fairly good agreement is found between the experimental and numerical result on both the lower (see Fig. 5.41(a)) and upper side of the fuselage (see Fig. 2.19(b)). On the lower side of the fuselage, both turbulence models indicate almost identical $\overline{C}_p$ distributions along the symmetry line and in good agreement with measurements, particularly in the front part of the fuselage, where the boundary layer remains attached. In this relatively stable flow regimes, the flow solver activates the SST formulation even for the SAS simulation. Contrary to this, slight discrepancies are found in the rear part of the fuselage where the boundary layer separates massively due to the aft-body contour. Similar conclusions are found on the upper part of the fuselage: a fairly good agreement in the region between the stagnation point ($\overline{C}_p = 1$) and $y/l_{\text{ref}} = 0.4$. Again, slight deviations between the numerical simulations and the experiment observed between $y/l_{\text{ref}} = 0.4$ and $y/l_{\text{ref}} = 0.5$ on the upper side of the fuselage are due to the influence of the aerodynamic fairing.

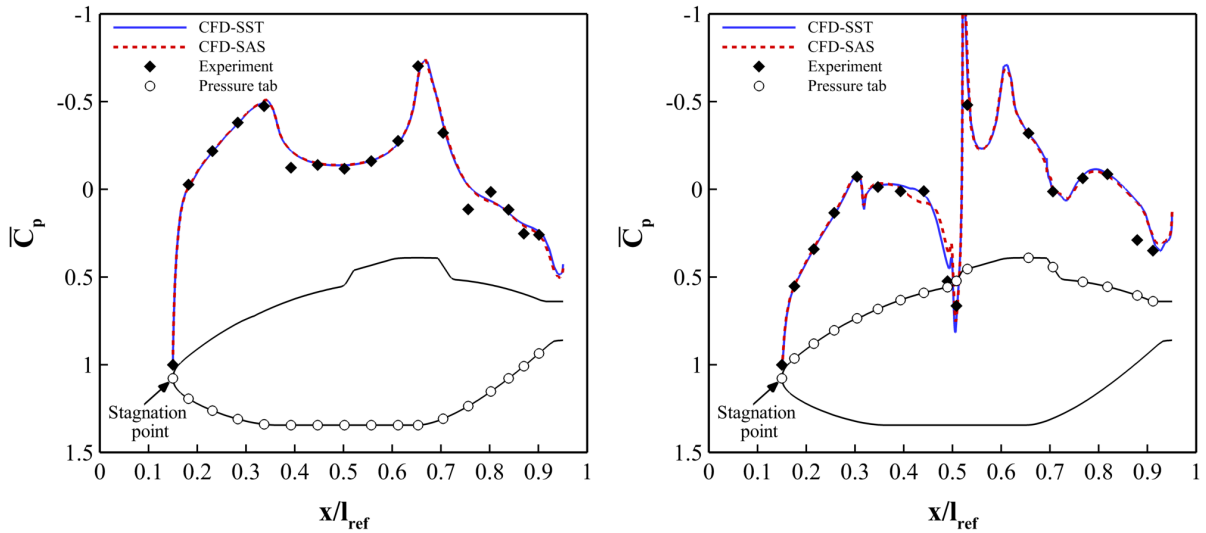

Figure 2.19: Time-averaged distributions of surface pressure coefficient $\overline{C}_p$ on the symmetry line ($y/l_{\text{ref}} = 0$): (a) lower side and (b) upper side of the fuselage.

In Figs. 2.20(a) and 2.20(b), flow patterns are visualized by time-averaged skin-friction lines, and $\overline{C}_p$ distributions are given for cross-sectional lines located on the fuselage aft-body. According to the skin-friction lines, both turbulence models predict quite similar flow fields with noticeable flow patterns, related to the massive boundary layer separation and the vortex formation at the aft body. Regarding the $\overline{C}_p$ distribution at $z/l_{\text{ref}} = 0.269$

and $z/l_{\text{ref}} = 0.295$, a fairly good agreement is found between the numerical simulations and measurements. Similar to the observation at $y/l_{\text{ref}} = 0$, the numerical results are in good agreement with the measured pressure levels on the fuselage side walls ($0.08 < |y/l_{\text{ref}}| < 0.1$) where the boundary layer is attached, and slight deviations are observed where the boundary layer separation occurs ($0.04 < |y/l_{\text{ref}}| < 0.06$). The SAS approach provides a slightly better result than the SST model in these unsteady flow regimes.

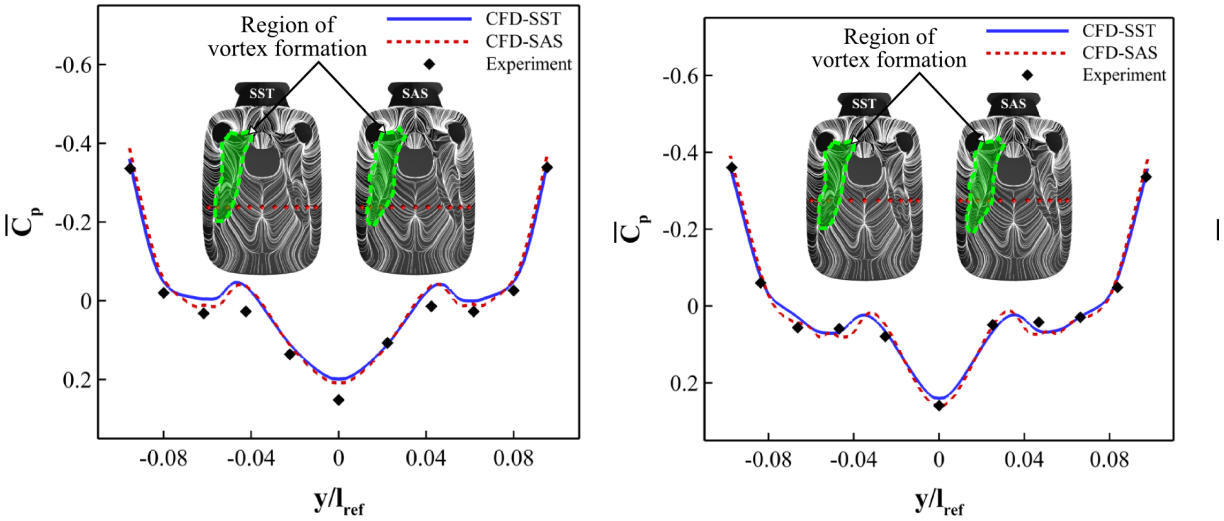

Figure 2.20: Time-averaged distributions of surface pressure coefficient $\overline{C}_p$ on cross-sectional lines on the fuselage aft-body: (a) $z/l_{\text{ref}} = 0.269$ and (b) $z/l_{\text{ref}} = 0.295$.

2.2.3 Spectral Analysis of Surface Pressure

The predictive capability of the turbulence model with respect to the spectral contents of the turbulent flow are assessed by means of the spectral analysis of the unsteady surface pressures. The analysis is based on the power spectral density of the surface pressure coefficient fluctuation $S_{C'_p}$. The position of unsteady pressure taps used are given in Fig 2.17. The pressure fluctuation obtained at a pressure-tap position x and at time t is defined as:

$$C'_p(x,t) = C_p(x,t) - \overline{C}_p(x) = C_p(x,t) - \int_0^T C_p(x,t)\,dt \tag{2.17}$$

The Fast Fourier Transformation $X_{C'_p}(x,w)$ of the discrete time signal $C'_p(x,t)$ can be formulated as:

$$X_{C'_p}(x,w) = \lim_{T\to\infty} \int_0^T C'_p(x,t)\, e^{-i\omega t}\,dt \tag{2.18}$$

Then, the power spectral density $S_{C_p'}$ can be obtained by multiplying the Fourier transform $X_{C_p'}(x,w)$ with its complex conjugate term $X^*_{C_p'}(x,w)$:

$$S_{C_p'}(x,w) = \lim_{T\to\infty} \frac{2}{T} X^*_{C_p'}(x,w)\, X_{C_p'}(x,w) \tag{2.19}$$

The power spectral density is then linearly averaged over frequency bands of $n_b = 2048$. Hence, the resulting frequency resolution Δf is the following:

$$\Delta f_{\mathrm{EXP}} = \frac{f_{\mathrm{EXP}}}{2n_b} = 0.49\,\mathrm{Hz} \tag{2.20}$$

$$\Delta f_{\mathrm{CFD}} = \frac{f_{\mathrm{CFD}}}{2n_b} = 5.19\,\mathrm{Hz} \tag{2.21}$$

with a sampling rate of $f_{\mathrm{EXP}} = 2000$ Hz and $f_{\mathrm{CFD}} = 21276.59$ Hz (based on $\Delta t_{\mathrm{CFD}} = 4.7 \times 10^{-5}\,s$) for the experiment and the numerical simulation cases, respectively. In this analysis, all spectra are plotted only for a limited frequency range up to 1000 Hz as an analog low-pass filter (1000 Hz) was applied during the wind tunnel measurements.

Regarding pressure taps T1 (see Fig. 2.21(a)) and T2 (see Fig. 2.21(b)) located both on the STR upper fin, the SAS approach exhibits a good agreement with the experiment, particularly in the low frequency range (up to 100 Hz), whereas the SST model reveals a significant disparity from the experiment. Here, the flow field is influenced mainly by the counter-rotating vortex pair formed at the upper rotor mast fairing and convected downstream by the mean flow (see Chap. 5). In the relatively high frequency range (beyond 100 Hz), the SAS approach also yields an underestimation at the pressure tap T1, located on the fan outlet side, but still provide a better result than the SST model. Contrary to the fin region, a very good agreement is found at the pressure taps T3 (see Fig. 2.21(c)) and T4 (see Fig. 2.21(d)) located on the fuselage aft-body where the spectral characteristics are determined by the aft-body boundary layer separation and the following vortex formation. Here, both simulation methods match quite well the experiment in terms of the spectral characteristics of pressure fluctuations as well as the amplitudes. As expected, the SAS method provides a better agreement with experiments than the SST model, particularly in the relatively high frequency range, which results from the scale resolving capability of the SAS approach. At all these pressure-tap locations, no tonal-noise-like spectral components are observed.

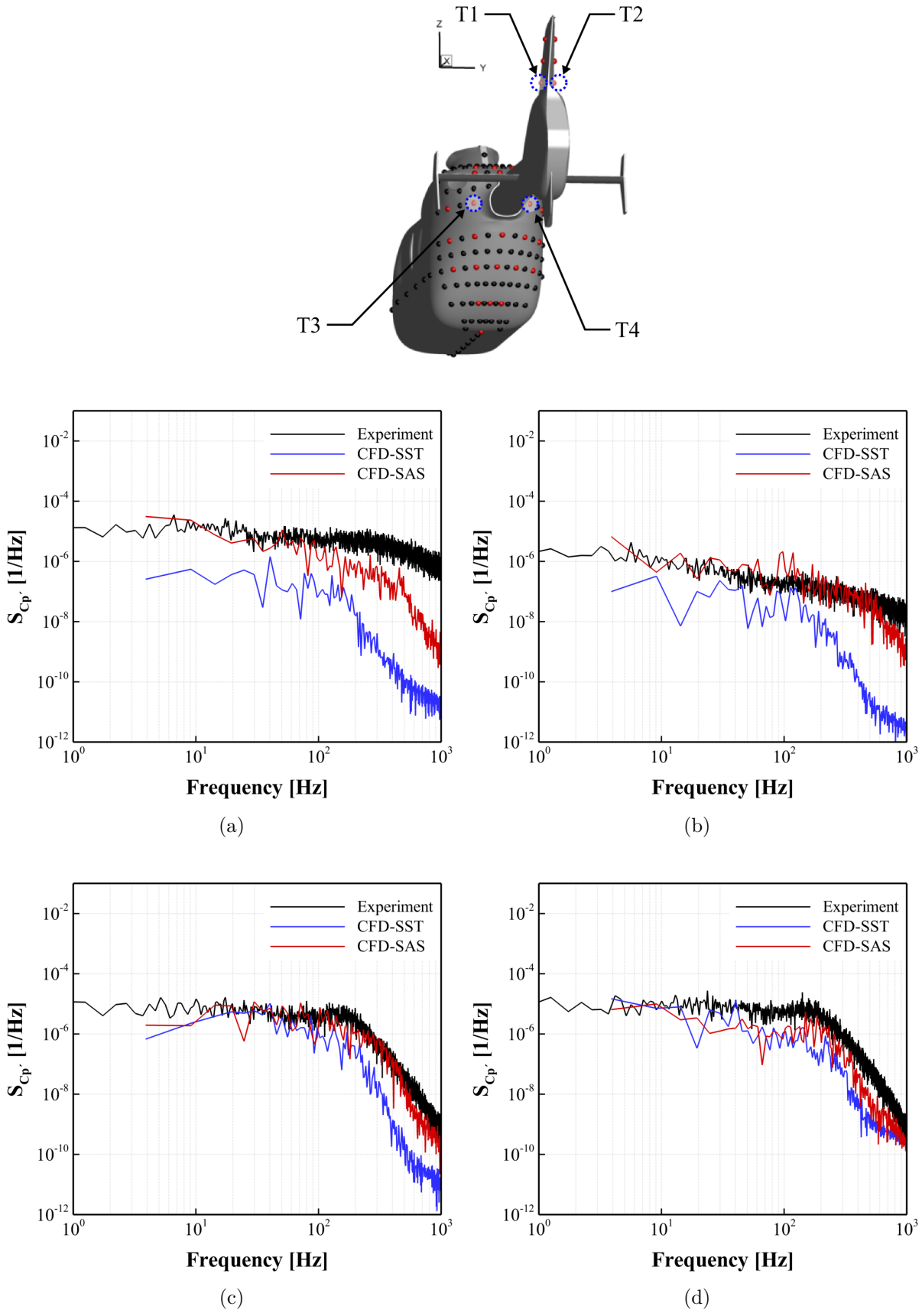

Figure 2.21: Power spectral density analysis of surface pressure coefficient fluctuations $S_{C_p'}$ at pressure tap positions (a) T1, (b) T2, (c) T3, and (d) T4.

Chapter 3

Numerical Methods for Far-Field Sound Prediction

This chapter focuses on the description of numerical methods and computation setups employed for the far-field sound prediction based on the Ffowcs Williams and Hawkings (FWH) method of the permeable integration surface. Moreover, the assessment of the predictive capability of the hybrid acoustic approach will be presented by comparing the computed far-field sound with the measured noise data for a fan-in-wing configuration.

3.1 Sound Prediction Tool – SPySI

In this thesis, the far-field sound radiating from the shrouded tail rotor is predicted by usage of the acoustic post-processing tool – Sound Prediction by Surface Integration (SPySI) [41, 85, 86], developed at the Institute of Process Machinery and Systems Engineering (iPAT), Friedrich-Alexander University Erlangen-Nürnberg (FAU). This tool is based on the modified version of the FWH analogy of the porous integration surface (Farassat Formulation I) [33] in combination with the advanced time algorithm [16].

Ffowcs Williams and Hawkings [104] derived a more general form of the Lighthill equation [60, 61] in order to take into account a solid surface in the fluid domain (see Fig. 3.1) by usage of the Heaviside function of a newly introduced function f, formulated as following:

$$f(x_i,t) = \begin{cases} < 0 : x_i \in V_s \\ = 0 : x_i \in S_s \\ > 0 : x_i \notin V_s \end{cases} \tag{3.1}$$

with V_s being the volume that is enclosed by the surface (control surface) S_s. Then, the Heaviside function of f has following properties:

$$H(f(x_i,t)) = \begin{cases} 0 : f(x_i,t) < 0 \\ 1 : f(x_i,t) > 0, \end{cases} \tag{3.2}$$

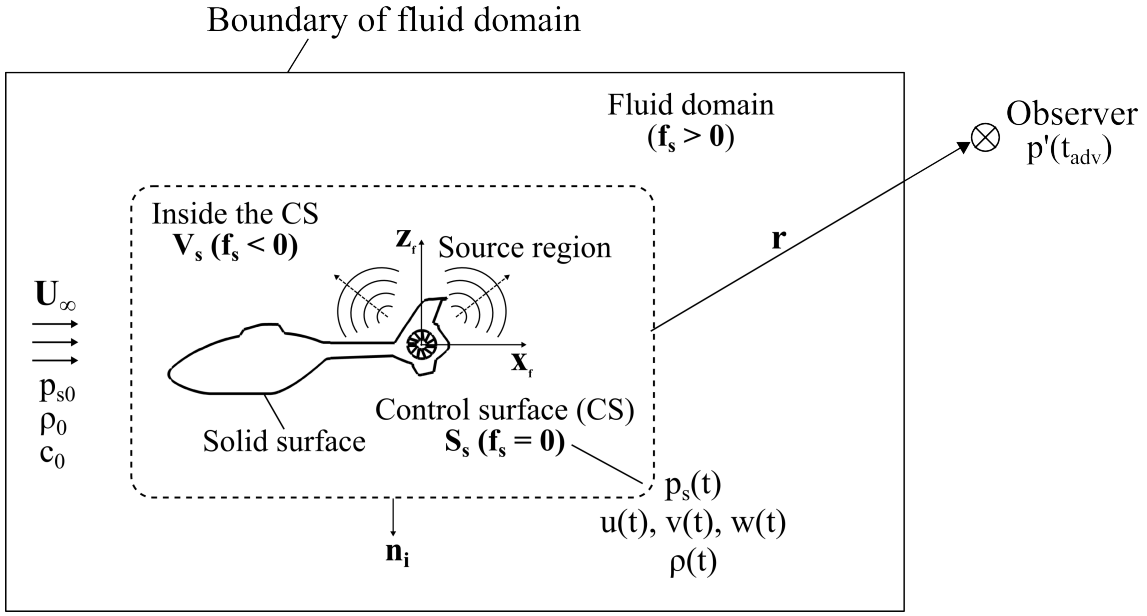

Figure 3.1: Schematic illustration of the FWH method of the permeable integration surface implemented in SPySI.

The idea using the Heaviside function is to neglect the region enclosed by the control surface in the calculation of sound, but to consider flow quantities, which are obtained immediately outside the control surface. In principal, the control surface can be any arbitrary surface immersed into the flow domain, and assume any shape of any size. In addition, it can be a non-permeable (e.g. solid surface of a rotor blade) or a permeable surface, and also be a moving or a non-moving surface. The acoustic far-field pressure is then calculated on the assumption that sound propagates linearly from the control surface to an observer located in the far-field. Thus, any acoustic nonlinearities occurring outside the control surface and any solid surfaces located on the propagation path are not taken into account in the calculation of the acoustic pressure. Using $H(f)$, the generalized form of the Lighthill equation can be defined as following:

$$\begin{aligned}\left(\frac{\partial^2}{\partial t^2} - c_0^2 \triangle\right)\{\rho' H(f)\} = \\ \frac{\partial^2}{\partial x_i \partial x_j}\{T_{ij} H(f)\} \\ + \frac{\partial}{\partial t}\left(\{\rho(u_i - v_i^s) + \rho_0 v_i^s\}\frac{\partial f}{\partial x_i}\delta(f)\right) \\ - \frac{\partial}{\partial x_i}\left(\{\rho u_i(u_j - v_j^s) + P_{ij}\}\frac{\partial f}{\partial x_i}\delta(f)\right),\end{aligned} \tag{3.3}$$

where $\rho' = \rho - \rho_0$ is the acoustic density fluctuation, c_0 is the speed of sound at given ambient air temperature, u_i is the flow velocity, $T_{ij} = \rho u_i u_j - \tau_{ij} + \delta_{ij}\{(p - p_0) - c_0\rho'\}$ is

the Lighthill stress tensor, $P_{ij} = (p - p_0)\delta_{ij} + \tau_{ij}$ is the compressible stress tensor, v_i^s is the velocity of the control surface and δ is the Dirac delta function. The equation of the acoustic density fluctuation, Eq. 3.3, is known as the differential form of the FWH equation and can be solved by using the free-space Green's function [33], which is defined as:

$$G(x_i, t : y_i, \tau) = \frac{\delta\left(t - \frac{r}{c_0} - \tau\right)}{4\pi r} \tag{3.4}$$

with t being the time at the observer position x_i, $r = |x_i - y_i|$ being the distance from the sound source y_i to the observer, and τ being the retarded time, describing the time which an acoustic signal needs to travel from a source (control surface) to the observer and defined as:

$$\tau = t - \frac{r}{c_0} \tag{3.5}$$

By the convolution with the free-space Green's function, the integral form of the generalized Lighthill equation of Eq. 3.3 is derived as following:

$$\begin{aligned} 4\pi c_0^2 \{\rho' H(f)\}(\overrightarrow{x}, t) = \\ \frac{\partial^2}{\partial x_i \partial x_j} \iiint_{R^3} \left[\frac{T_{ij} H(f)}{r}\right]_{ret} \mathrm{d}y_i^3 \\ + \frac{\partial}{\partial t} \iint_S \left[\frac{\rho(u_i - v_i^s) + \rho_0 v_i^s}{r} n_i\right]_{ret} \mathrm{d}S \\ - \frac{\partial}{\partial x_i} \iint_S \left[\frac{\rho u_i (u_j - v_j^s) + P_{ij}}{r} n_i\right]_{ret} \mathrm{d}S, \end{aligned} \tag{3.6}$$

where n_i is the outward normal vector of the surface element and the subscript ret denotes that the integrands are evaluated at the retarded time. The first term on the right hand side of Eq. 3.6 is usually assigned as quadrupole noise, while the second and the last term represent the thickness and loading noise term, respectively. However, this physical interpretation is only relevant if a solid surface, such as the surface of a rotor blade, is considered as the integration surface. Contrary to this, if a permeable control surface is used, which is the case of this thesis, the terms lose these physical meanings. The integral form of the FWH equation of Eq. 3.6 can be further simplified for a stationary control surface ($u_i - v_i^s = 0$), and if the control surface is enclosing all relevant source regions, thus allowing to neglect the quadrupole term of Eq. 3.6. In addition, by using algebraic transformations, the divergence expression at the loading noise term in Eq. 3.6 can be replaced by temporal derivatives, as explained in [28, 41]. Finally, the simplified FWH

equation implemented in SPySI can be given as:

$$\begin{aligned} 4\pi\rho'(\overrightarrow{x},t) = \\ \frac{\partial}{\partial t}\iint\limits_S \left[\frac{\rho_0 v_i^s}{r} n_i\right]_{ret} \mathrm{d}S \\ + \frac{\partial}{\partial t}\iint\limits_S \left[\frac{P_{ij}}{c_0 r}\right]_{ret} \mathrm{d}S + \iint\limits_S \left[\frac{P_{ij}}{r^2}\right]_{ret} \mathrm{d}S \end{aligned} \tag{3.7}$$

The SPySI was initially developed for the application of non-moving sources, such as for cooling fan and/or helicopter in hovering. Thus, the code does not take into account any influence of the convective amplification, which arises if the sound source is in moving motion and leads to a higher sound pressure level in the moving direction than in the opposite direction. For all acoustic calculations in this thesis, fixed observer points are used, which indicates that the relative velocity of observer points with respect to the helicopter is zero. Moreover, broadband noise issues are not part of this work as on the one hand, the acoustic code does not contain the quadrupole noise term of Eq. 3.6, and on the other hand, the URANS approach used herein is limited to the prediction of tonal noise components due to its averaging manner. Generally, evaluating the quadrupole noise requires a volume integration, which is, however, impractical for such a three-dimensional, complex flow problem. Nevertheless, the contribution of the quadrupole sources to the overall noise level can be implicitly considered in such a way as to take an appropriate control surface, which is positioned sufficiently far from the source region, and thus enclosing all relevant quadrupole (volumetric) noise sources (see Sec. 3.2).

The SpySI adopts the advanced time approach of Casalino [16], indicating that the integrands in Eq. 3.7 are evaluated at the current time t_e (emission time), and the sound signal at an observer is then provided at the advanced time t_{adv} (arrival time at observer in future, see Eq. 3.8). By using the retarded time algorithm, the integrands of Eq. 3.7 are evaluated with flow quantities in the past to calculate an acoustic signal at an observer in the present (see Eq. 3.5). As a result of this, the retarded time algorithm requires storing the CFD data over several simulation periods to calculate the sound pressure at a certain observer time [86]. On the contrary, using the advanced time algorithm, the sound prediction is performed only based on the data of the current time step and therefore computationally more efficient.

$$t_{\mathrm{adv}} = t_e + \frac{r}{c_0} \tag{3.8}$$

3.2 Influence of Control Surfaces and Computational Parameters

This section deals with the evaluation of the influence of both control surfaces and computational parameters on the far-field noise extraction.

3.2.1 Influence of Control Surfaces

The acoustic post-processing using the FWH method of porous integration surface needs a control surface that includes the information about acoustic perturbations. Generally, it is known that the FWH method is less sensitive to both the placement and the shape of the control surface [15]. An appropriate choice of the control surface is, however, still important to ensure a certain degree of accuracy of the calculated noise. The control surface should surround all relevant acoustic source regions, thus covering all significant flow phenomena and flow non-linearities linked to the noise generation. In this thesis, two disconnected control surfaces enclosing the STR inlet and outlet opening, respectively, are employed for all acoustic calculations (see Fig. 3.2). The control surfaces employed enclose not only the monopole (fluid displacement by moving blade) and the dipole noise sources, such as the unsteady blade load fluctuations as result of the interaction between the inlet flow distortion and the rotor blade (see Sec. 5.4), but also the entire quadrupole noise sources being present inside the duct fairing. In this way, the contribution of the quadrupole sources to the overall noise characteristics of the STR is implicitly taken into account, although the SPySI does not consider the quadrupole noise term of Eq. 3.6. Diffraction and reflection of sound occurring inside the duct fairing are also implicitly taken into account by using this type of control surfaces. A similar approach to the control surface can be found in Refs. [32, 37]. All permeable control surfaces used are meshed with the grid generator ANSYS ICEM CFD and resolved by rectangular elements.

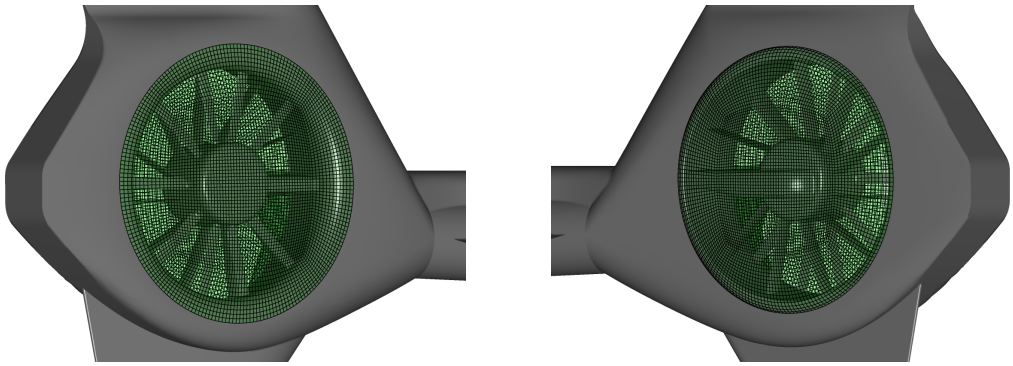

(a) (b)

Figure 3.2: Permeable control surfaces D1 placed in the vicinity of the (a) fan inlet and (b) fan outlet opening (reference grid resolution with $d_{\mathrm{CFD}} : d_{\mathrm{CAA}} = 1 : 1$).

3.2.1.1 Control surface placement

The influence of the control surface placement on the calculated STR far-field noise is assessed for the forward flight case (based on URANS-SST) [111]. Figs. 3.3(a) and 3.3(b) show the comparison of the computed far-field sound pressure $p'(t_{\text{adv}})$ and sound pressure level (SPL) of different permeable surfaces D1 and D2, respectively (see Fig. 3.3(b)). The control surface D2 consists of two disconnected hemispheres with a diameter of $d_{D2} = 1.2\, l_{\text{ref}}$. Hence, the surface D2 reveals a relatively lager distance to the source region, compared to the control surface D1. The observer point of this analysis is located on the fan inlet side with a distance of $d/l_{\text{ref}} = 39$ from the axis of rotation. Note that the calculated far-field sound pressure p' at the observer point in Fig. 3.3(a) is given for the period of arrival time (t_{adv}) that corresponds to the time requirement for one fan revolution. According to Fig. 3.3(a), both control surfaces provide a very similar acoustic pressure at the observer point considered. Slight differences are, however, observed. The control surface D1 predicts a more significant peak-to-peak amplitude compared to D2. Furthermore, some peak amplitudes (indicated by circles in Fig. 3.3(a)) are not clearly predicted by the surface D2. The reason for these differences lies in the fact that in the CFD simulation, the acoustic perturbations lose their strength with increasing distance from the rotor plane as the CFD grid resolution becomes also coarser. Regarding the sound spectrum in Fig. 3.3(b), both surfaces predict noticeable tonal components at the blade passing frequency (BPF, $f/f_{\text{BPF}} = 1$) and its high-order harmonics ($f/f_{\text{BPF}} = m$; $m = 2,3$) and, as result of the uneven blade spacing, at their lower ($f/f_{\text{BPF}} = m - 0.2n$; $m = 1,2,3$; $n = 1,2$) and

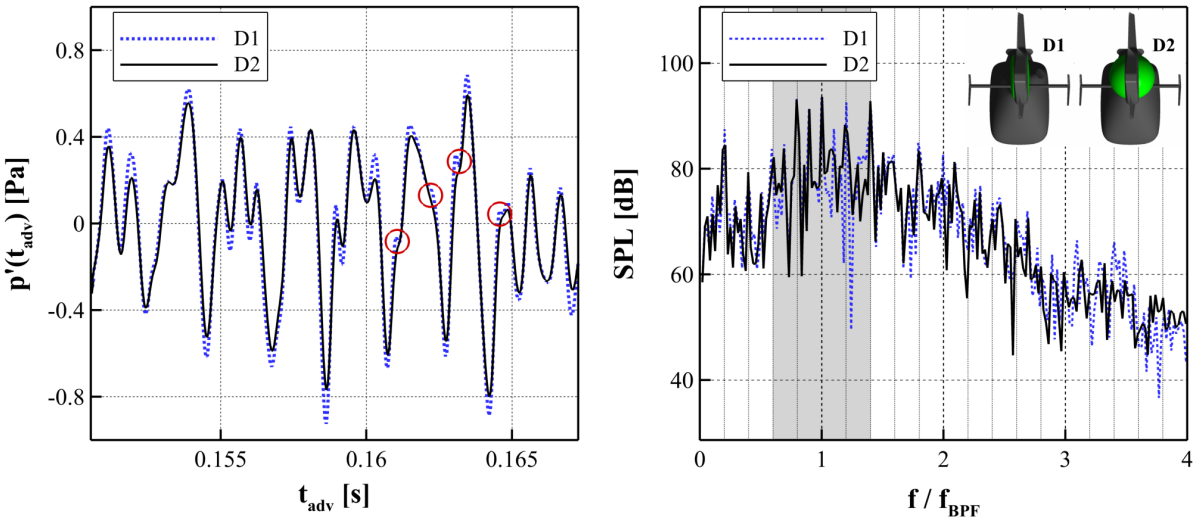

(a) (b)

Figure 3.3: Influence of control surface placement: comparison of (a) far-field acoustic pressure $p'(t_{adv})$ and (b) sound pressure level (SPL) between the control surface D1 and D2, computed for five fan revolutions with the reference acoustic time step of $\Delta t_{\text{CAA}} = 4.7 \times 10^{-5}$ s.

upper sideband frequencies ($f/f_{\mathrm{BPF}} = m + 0.2n;\ m = 1,2,3;\ n = 1,2$). Considering the relevant peaks at the BPF and its lower as well as upper sideband frequencies, it is found that both control surfaces D1 and D2 reveal nearly identical sound pressure levels. The influence of the control surface placement on the far-field sound spectrum, however, becomes relevant at higher frequencies, particularly beyond $f/f_{\mathrm{BPF}} = 3$ as the high-frequency sound attenuates more significantly with increasing distance from the sources than the low-frequency sound.

Apart from the relatively stronger numerical dissipation, the control surface D2 is also subjected to interactions with the fuselage wake due to its spatial extension. The flow field analysis indicates that in the forward flight condition, vortical structures formed at the fuselage aft-body are convected downstream towards the STR by the main flow and consequently, pass through the permeable control surfaces, as illustrated in Fig. 3.4(a). It is already known that such an interaction can generate undesirable, non-physical sound [62]. To evaluate the influence of the interaction between the highly turbulent vortical structures and the permeable control surface D2 on the acoustic prediction, a further unsteady flow simulation (based on URANS-SST) is performed based on the helicopter configuration with sealed STR inlet and outlet opening [106]. As presented in Fig. 3.4(b), the interaction results in significant velocity field disturbances on the control surface D2. The velocity field distribution bears a clear correlation with passing vortical structures, such as the upper fuselage vortex and the lower fuselage vortex (see also Sec. 5.1). As a result, the hybrid approach yields an artificial far-field sound pressure as presented in Fig. 3.5(b). The spectrum of this sound signal, however, indicates that the artificial noise is relevant only in a limited frequency range below $f/f_{\mathrm{BPF}} = 0.2$. Therefore, it can

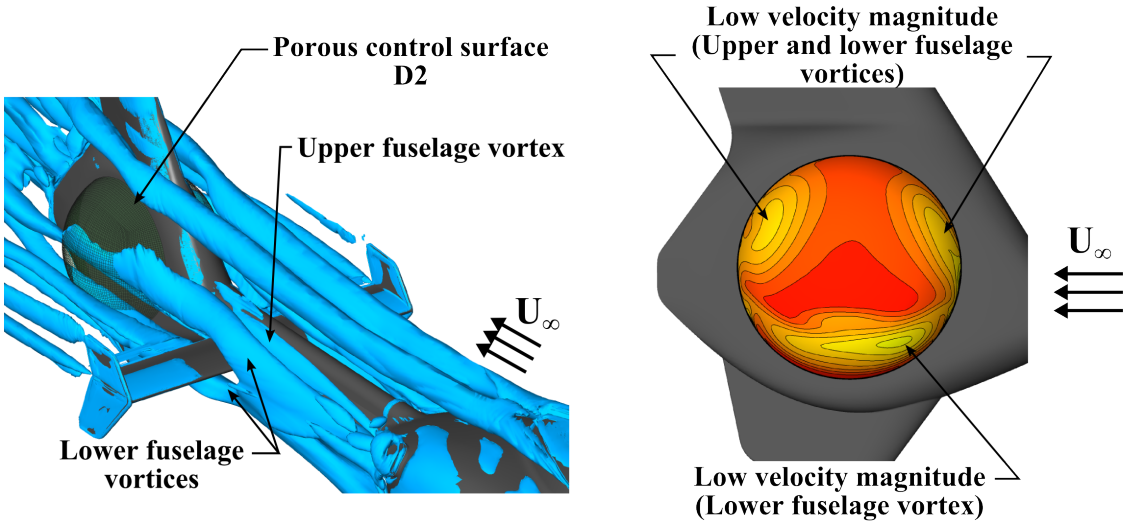

(a) (b)

Figure 3.4: Vortical-structure/preamble-control-surface interaction: (a) instantaneous vortical structures visualized by isosurface of Q-criterion ($Q = 3000\ 1/s^2$) and (b) velocity magnitude distribution on the control surface D2 (fan inlet side).

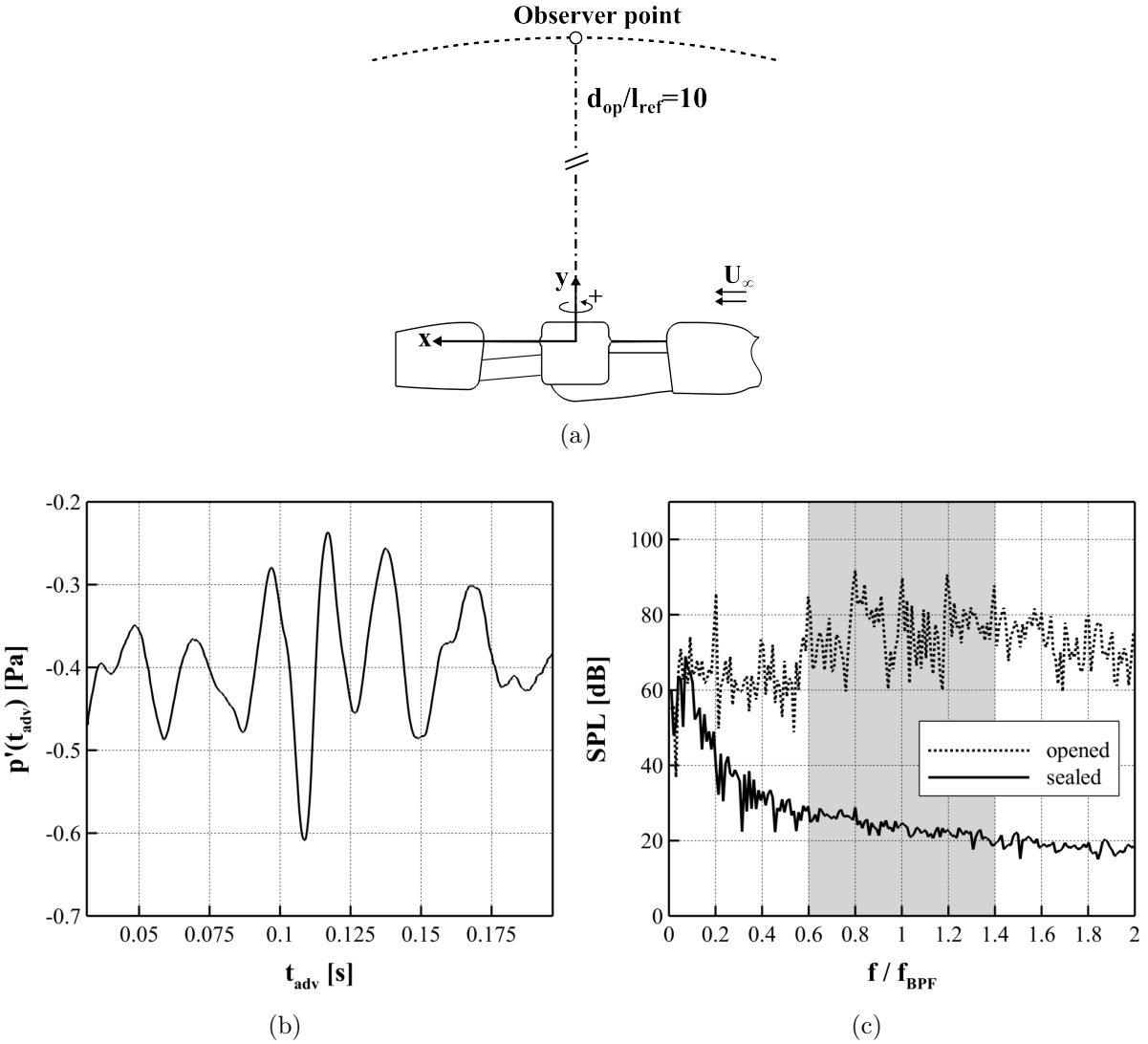

Figure 3.5: Influence of the fuselage wake interaction on the sound prediction using the control surface D2: (a) observer position, (b) calculated sound pressure $p'(t_{\mathrm{adv}})$ for the sealed STR case, and (c) comparison of sound pressure level between the sealed and opened STR. The sound prediction is performed for ten fan revolutions with a coarse acoustic time step ($\Delta t_{\mathrm{CAA}} = 1.41 \times 10^{-4}$ s).

be concluded that the tonal noise components at the fundamental frequency of the STR and its high-order harmonics as well as their corresponding sideband frequencies are not significantly affected by this kind of interaction. The control surface D1, selected for all acoustic computations in the present work, does not have any noticeable interactions with the fuselage wake.

3.2.1.2 Sensitivity study of acoustic grid

Based on the control surface D1, a grid sensitivity study of the porous control surface is performed [111]. The grid spacing of the reference porous surface is approximately identical to that of the CFD simulation ($d_{\mathrm{CFD}} : d_{\mathrm{CAA}} = 1 : 1$) at the position where the

control surface is inserted. Note that in this analysis, only the coarsening of the grid density is considered, as given in Table 3.1. In Fig. 3.6(a), the calculated sound pressure $p'(t_{\text{adv}})$ is given as a function of the arrival time t_{adv} at the observer point, described in Fig. 3.5(a). Recall that the given time range in Fig. 3.6(a) corresponds to one fan revolution. According to the figure, the resulting sound pressure is less sensitive to the grid coarsening up to a grid ratio of $d_{\text{CFD}} : d_{\text{CAA}} = 1 : 3$. On the contrary, the predicted sound signal using the coarsest grid ($d_{\text{CFD}} : d_{\text{CAA}} = 1 : 5$) significantly differs from that of the other grid ratios. Regarding the sound spectrum given in Fig. 3.6(b), the FWH result does not indicate any strong sensitivities to the grid resolution in the frequency range between $f/f_{\text{BPF}} = 0.8$ and $f/f_{\text{BPF}} = 3$. Indeed, the coarsest grid ($d_{\text{CFD}} : d_{\text{CAA}} = 1 : 5$) still provides nearly identical spectral characteristics as well as sound pressure levels compared to the other grid ratios at these frequencies. Considerable deviations are, however, observed at low frequencies $f/f_{\text{BPF}} \leq 0.6$ as well as at high frequencies $f/f_{\text{BPF}} \geq 3$. There, the coarsening of grid density leads to an overestimation of the sound pressure level. In the present work, the surface D1 with the reference grid resolution ($d_{\text{CFD}} : d_{\text{CAA}} = 1 : 1$) is used throughout all acoustic computations for both the hovering and forward flight condition due to the significant overprediction of the low frequency noise of the coarse grids.

$d_{\text{CFD}} : d_{\text{CAA}}$	1:1	1:2	1:3	1:5
Total number of nodes	10,804	2587	1100	415

Table 3.1: Details of grid coarsening for the control surface D1.

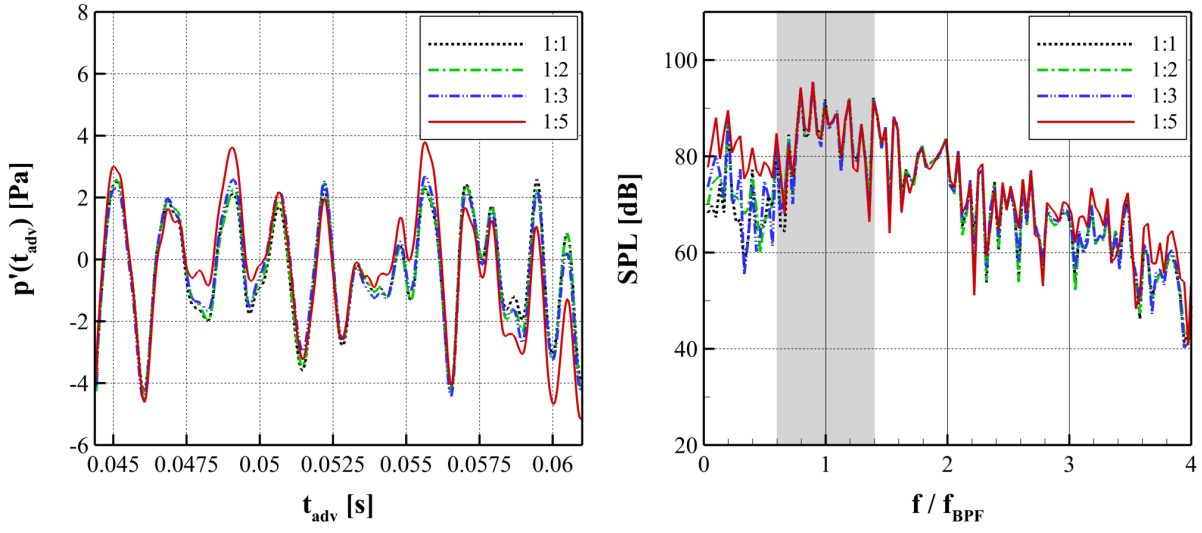

(a) (b)

Figure 3.6: Grid density study of the control surface D1: (a) sound pressure $p'(t_{\text{adv}})$ and (b) sound pressure level, computed for three fan revolutions with the reference acoustic time step of $\Delta t_{\text{CAA}} = 4.7 \times 10^{-5}$ s.

3.2.2 Influence of Computational Parameters

In the hovering flight, the flow field of the STR exhibits a rather periodic behavior that mainly depends on the rotor dynamics. Contrary to it, the flow field characteristics both around and inside the duct fairing in the forward flight is strongly affected by the fuselage wake and the inlet flow distortion provoked by the collector lip boundary layer separation (see Sec. 5.4). Thus, the fan parameters exhibit considerable variations of the mean value over the entire time range computed, as already shown in Fig. 2.12. For this reason, parameter studies with respect to the number of fan revolutions and the acoustic time step Δt_{CAA} are required for the forward flight case to ensure the accuracy of the resulting sound pressure.

3.2.2.1 Influence of number of fan revolutions

In Fig. 3.7(a), the sound pressure $p'(t_{\mathrm{adv}})$ predicted for seven rotor revolutions is given for the observer point described in Fig. 3.5(a). Because of the complex flow phenomena, subjected to the STR under cross-flow condition, the resulting acoustic signal in the far field does not reveal any clear periodic behavior over seven fan revolutions computed. Thus, repeating one and/or two periodic acoustic signals, which can drastically reduce the computational efforts of the hybrid approach, is difficult to apply for the forward flight case. Consequently, it is necessary to compute more fan revolutions to ensure a certain degree of accuracy of the acoustic result. To assess the sufficient length of the sound signal, the SPL spectrum is calculated with different number of fan revolutions. Then, the relative difference of the SPL (ΔSPL) with respect to the case of seven fan revolutions is given in Fig. 3.7(b). According to the figure, ΔSPL at frequencies being relevant with respect to the uneven blade spacing become significant, as the number of fan revolutions decreases. In the present study, all acoustic computations are performed for five fan revolutions. This decision was made based on the fact that this number of fan revolutions corresponds to the traveling time of the fuselage wake to the STR. For this number of fan revolutions, the relative difference with respect to the seven revolution case is less than 1% (approximately 1 dB) at the BPF ($f/f_{\mathrm{BPF}} = 1$) and 1.5% at the lower sideband frequency $f/f_{\mathrm{BPF}} = 0.8$.

3.2.2.2 Sensitivity study of acoustic time step

A sensitivity study on the acoustic time step size Δt_{CAA} is also performed based on the surface D1 (reference grid density). The number of fan revolutions considered is five. In Fig. 3.8, the predicted far-field sound pressure $p'(t_{\mathrm{adv}})$ and corresponding sound spectra are given for five different acoustic time steps. Note that Δt_{CAA} is given as the blade rotation angle $\Delta\psi_f$ per time step (see Table 3.2). The reference acoustic time step size is identical to the time step size of the numerical flow simulation ($\Delta t_{\mathrm{CAA}} = \Delta t_{\mathrm{CFD}} = 4.75 \times 10^{-5}$ s corresponding to approximately $\Delta\psi_f = 1°$). Hence, only coarsening of Δt_{CAA} is considered in this analysis. With respect to $p'(t_{\mathrm{adv}})$ and the sound pressure level, the FWH result does not indicate any strong sensitivities to Δt_{CAA} up to the time step size

corresponding to $\Delta\psi_f = 3°$, while the time step sizes corresponding to $\Delta\psi_f = 5°$ and $\Delta\psi_f = 10°$ yield a noticeable underestimation in the high frequency range. In the present thesis, the reference time step size ($\Delta t_{\mathrm{CAA}} = 4.75 \times 10^{-5}$ s) is used throughout all acoustic computations for both the hovering and forward flight condition.

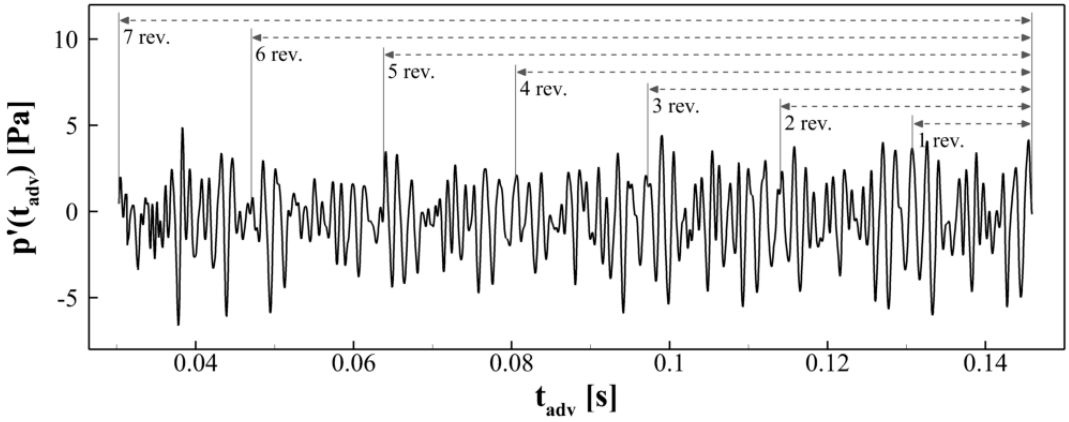

(a)

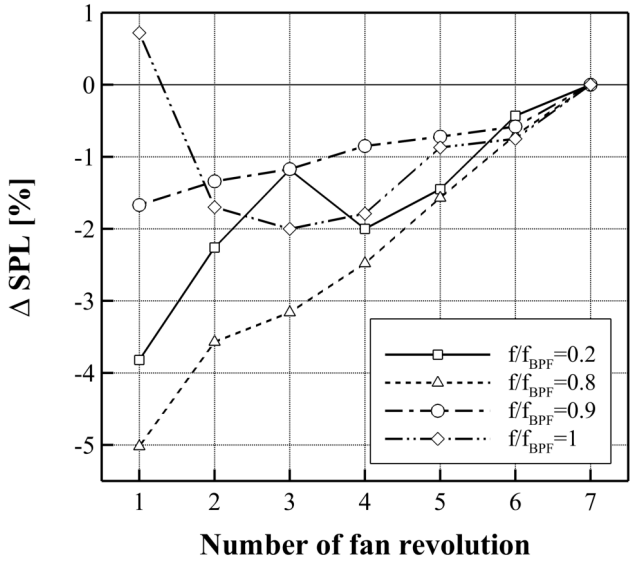

(b)

Figure 3.7: Influence of the number of fan revolutions: (a) sound pressure $p(t_{\mathrm{adv}})$ over seven fan revolutions computed with $\Delta t_{\mathrm{CAA}} = 4.75 \times 10^{-5}$ s and (b) relative differences of the sound pressure level (ΔSPL) with respect to the case of seven fan revolutions.

$\Delta t_{\mathrm{CAA}} \times 10^{-5}$ s	4.7	9.4	14.1	23.5	47
$\Delta\psi_f$	1°	2°	3°	5°	10°

Table 3.2: Correlation between the acoustic time step and the blade rotation.

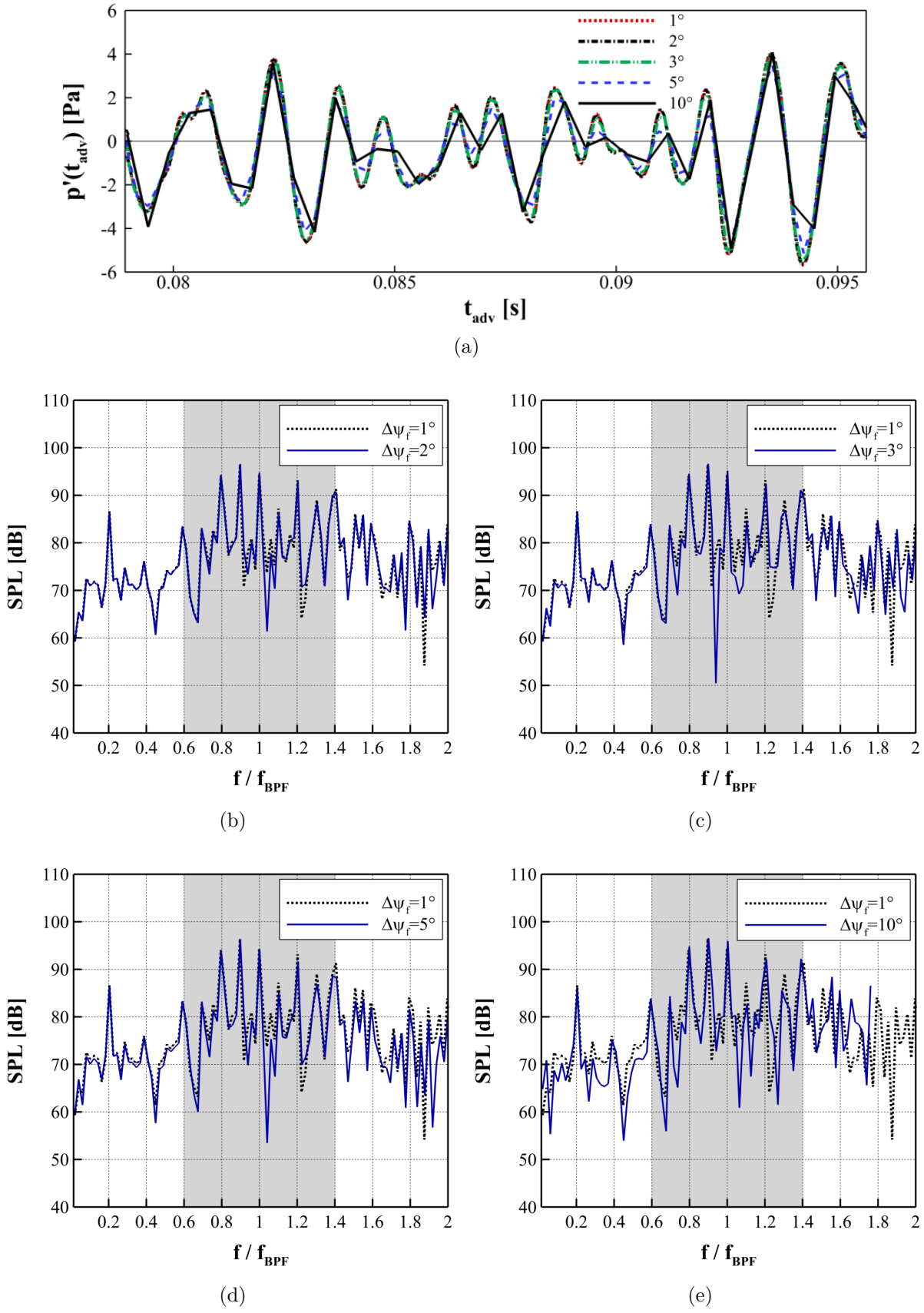

Figure 3.8: Sensitivity study on the acoustic time step size Δt_{CAA} (given as $\Delta\psi_f$) based on the surface D1 (reference grid density) and for five fan revolutions.

3.3 Validation of Hybrid Approach

The predictive capability of the hybrid approach employed in this thesis was assessed in a related work [98, 99] for a generic fan-in-wing (FIW) configuration. The FIW is a wing-embedded four-bladed lift fan (Fig. 3.9), and regarding flow phenomenology, it bears strong similarities with the STR. For instance, under cross-flow condition, the FIW configuration is also subjected to significant boundary layer separation in the vicinity of the fan inlet. Thereby, a separation bubble is generated on the rotor plane and interacts with the rotor blade as indicated in Fig. 3.9(c) with spot e. Consequently, the inlet distortion results in a significant dynamic blade loading, thus affecting the FIW acoustic characteristics negatively. The aerodynamic characteristics of the FIW configuration has been expensively studied through computational simulations (URANS-SST) as well as wind tunnel experiments in the previous research [95].

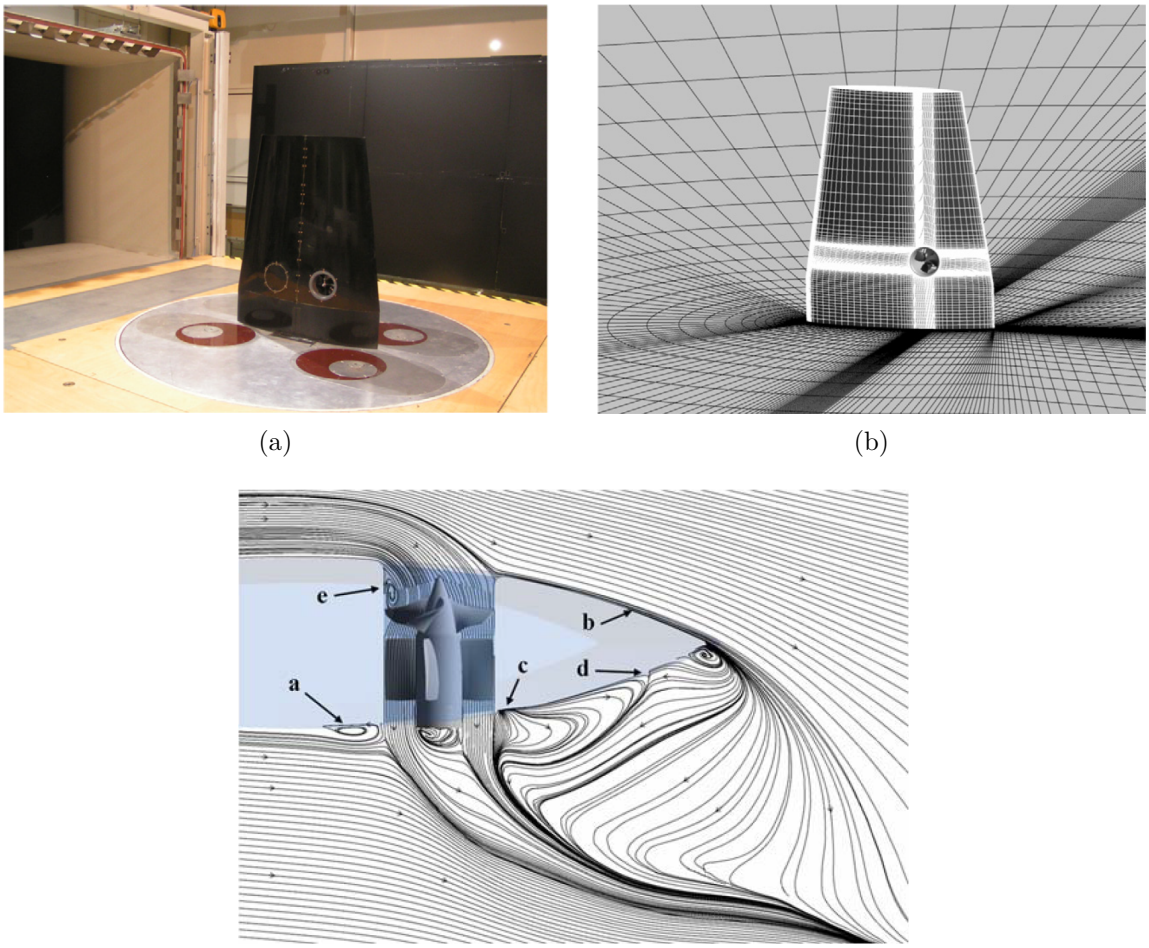

(a) (b)

(c)

Figure 3.9: Fan-in-wing configuration [95]: (a) wind tunnel model, (b) grid topology of numerical simulations, and (c) flow topology based on time-averaged velocities obtained from URANS simulation using the SST turbulence model.

Following the aerodynamic study, comprehensive aeroacoustic investigations of the FIW configuration were performed by means of both numerical and experimental methods [98, 99]. For the numerical investigation, an identical hybrid approach (URANS-SST simulations using ANSYS CFX flow solver and acoustic post-processing by using SPySI) is employed to predict the FIW far-field sound radiation. A wing-like porous control surface, which was extruded from the solid surface of the wing and encloses all flow non-linearities including inlet flow distortion, is used. The predicted sound radiation into the far field is then compared with experimental data obtained from the microphone measurement in the acoustic wind tunnel of BMW in Munich [51]. The model installation in the acoustic wind tunnel and the microphone positions considered are given in Figs. 3.10(a) and 3.10(b), respectively.

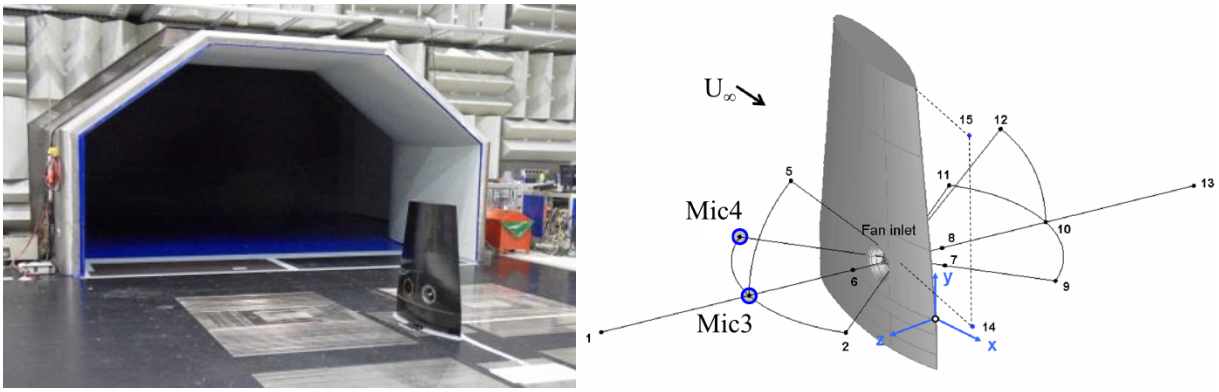

(a) (b)

Figure 3.10: Acoustic investigation of fan-in-wing configuration [98, 99]: (a) microphone measurement in BMW acoustic wind tunnel and (b) microphone positions.

In Figs. 3.11(a) and 3.11(b), the far-field sound pressure level (SPL) calculated by the hybrid approach (computed for 15 fan revolutions) is compared to the measured SPL for microphone positions Mic3 and Mic4, receptively. Both microphone positions are located on the fan inlet side with the identical distance from the wing middle plane, corresponding to a half of the wing root chord ($0.5\,c_r$). Both the predicted and measured SPL spectra indicate significant tonal components at frequencies related to the BPF and its high-order harmonics. Considering the discrete noise component at the fundamental frequency of the FIW noise (BPF) and its first harmonic (second BPF), a fairly good agreement is found between the numerical prediction and the measurement for both microphone positions regarded. Differences in SPL at these frequencies are approximately ± 2 dB. Particularly at the microphone Mic4, located upstream of the fan inlet (45° to the fan axis), the acoustic prediction using the FWH method matches well the measurement not only at the discrete noise components (first, second, and third BPF) but also in-between (see Fig. 3.11(b)). The hybrid method, however, significantly underestimates high-frequency noise, particularly beyond third BPF, at both microphone positions. This noticeable discrepancy is due to the fact that the URANS simulation using the classical turbulence model (e.g.

SST turbulence model) is incapable to accurately capture spectral contents of turbulent flows, particularly at the high frequency range [35]. The hybrid method also yields underestimation of sound pressure levels at low frequencies below the BPF. Nevertheless, the investigation demonstrates the predictive capability of the combined CFD-CAA in the application of the noise prediction of the ducted fan under superimposed cross flow with high accuracy regarding both the sound pressure level and the frequency distribution of the dominant tonal noise components.

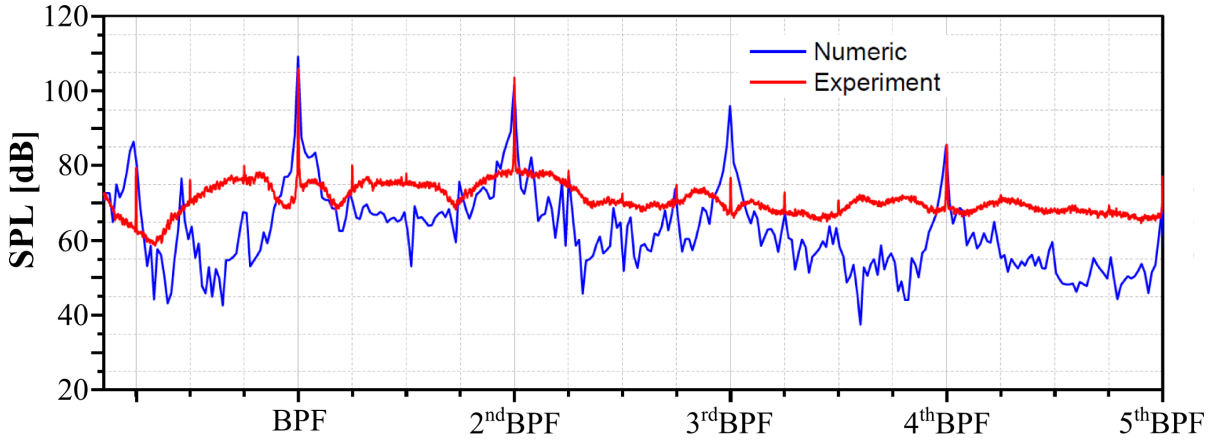

(a)

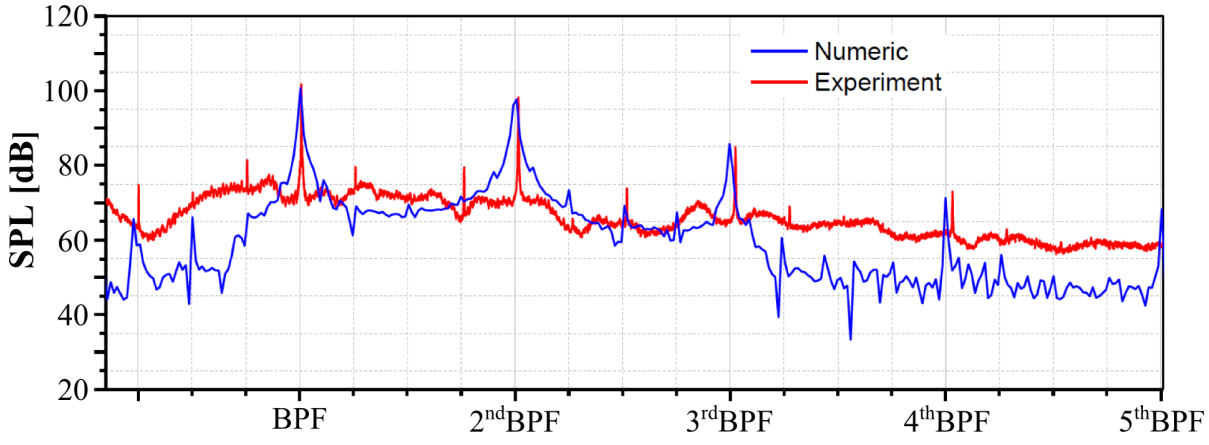

(b)

Figure 3.11: Comparison of calculated and measured fan-in-wing far-field sound pressure level (SPL) for microphone positions (a) Mic3 and (b) Mic4 (Jithendra Tirakala, private communication, 2014 / see [109]).

Chapter 4

Aerodynamic and Aeroacoustic Analysis of Hovering Condition

This chapter deals with the analysis of both the near-field aerodynamics and the far-field acoustic characteristics of the shrouded helicopter tail rotor (STR) in an ideal hovering condition ($U_\infty = 0\ m/s,\ \alpha_\infty = 0°,$ and $\beta_\infty = 0°$). Firstly, the near-field aerodynamic properties of the STR are analyzed by means of both the instantaneous and time-averaged flow quantities, obtained from the CFD simulations using the SST turbulence model. Subsequently, the far-field acoustic properties are analyzed by usage of the FWH porous surface integration method. The predicted far-field sound is compared with the flight test data, supported by Airbus Helicopters Deutschland.

4.1 Aerodynamic Characteristics

In this section, the aerodynamic characteristics of the STR in the hovering condition are presented to give an in-depth understanding of the flow physics linked to the noise generation in a uniform inflow [109–111, 113].

4.1.1 Anti-torque Thrust

In the ideal hovering condition, the STR is the only part generating the necessary anti-torque thrust among other helicopter subsystems. In Fig. 4.1(a), the breakdown of the lateral force coefficient C_y in the hovering condition is presented for respective components of the STR. Regarding the direction of the thrust vector, there are two groups among the STR components. The first group including the shroud fairing, the collector (divided into the collector lip and the rotor casing), the rotor hub, and the ten-bladed rotor produces a positive anti-torque thrust, whereas another group involving the ten stator vanes, the drive shaft fairing, the diffuser, and the gear box provides a negative C_y. The URANS-SST simulation of the present study yields a similar result as previous researches [21, 102], so that in the hovering condition the entire rotor blades (50%) and the collector (40%) provide together more than 90% of the overall anti-torque thrust. The substantially high contribution of the collector part to the overall anti-torque thrust is associated with the

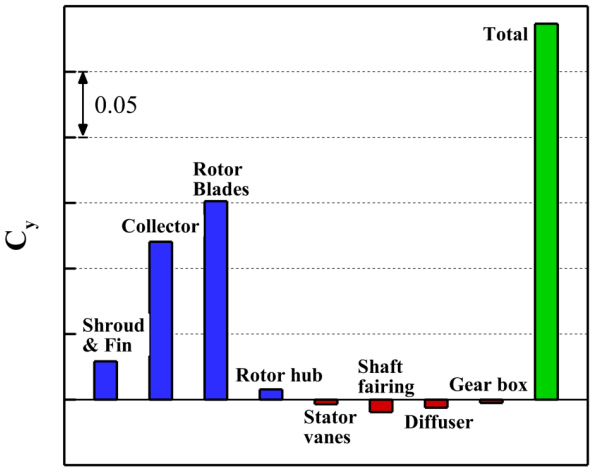

(a)

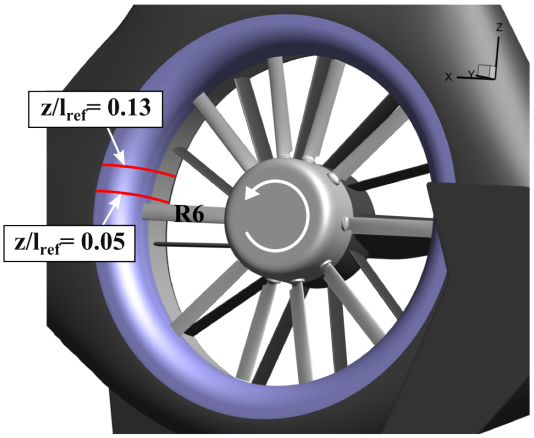

(b)

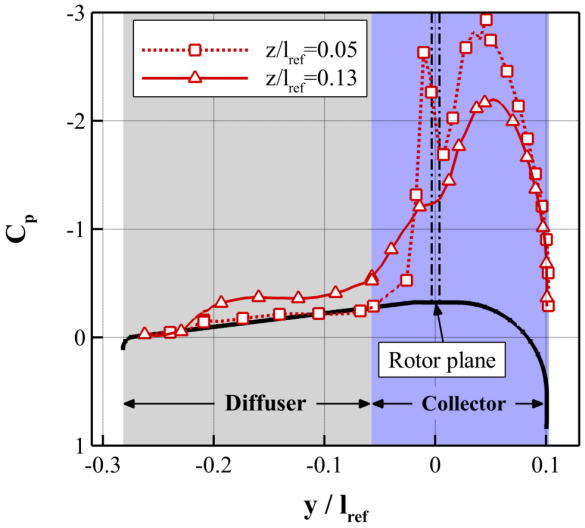

(c)

Figure 4.1: Anti-torque thrust in the hovering condition: (a) breakdown of lateral force coefficient C_y for respective components of the STR, (b) cross-sectional lines regarded, and (c) streamwise surface pressure coefficient C_p along the inner surface of the duct fairing (from collector lip to diffuser).

significant suction peak present on the collector lip, as indicated in Fig. 4.1(c). In this figure, the streamwise distribution of the instantaneous surface pressure coefficient C_p is presented along the inner surface of the duct casing (from the collector lip to the diffuser) for two different cross-sectional lines $z/l_{\text{ref}} = 0.05$ and $z/l_{\text{ref}} = 0.13$. At $z/l_{\text{ref}} = 0.05$, where the cross-sectional line is located directly behind the trailing edge of the blade R6 at the current simulation time step (see Fig. 4.1(b)), a noticeable high level of $|C_p|$ is detected on the collector lip, highlighting a strong acceleration of the local fluid flow (suction peak). The positive C_y of the shroud, as seen in Fig. 4.1(a), is also related to the acceleration of the local fluid flow provoked by the collector lip. Downstream of the suction peak, the

pressure level begins to recover streamwise, thereby resulting in a strong adverse pressure gradient ($dp/dy > 0$) directly upstream of the rotor plane. Immediately downstream of the rotor plane, an abrupt increase in $|C_p|$ is observed, which is caused by the tip-leakage vortex. The tip-leakage vortex is convected downstream and occurs an increase in $|C_p|$ on the surface of the diffuser due to its strong cross velocity. Comparably higher levels of $-C_p$ observed in the diffuser part at $z/l_{\mathrm{ref}} = 0.13$, located further away from the blade trailing edge of R6, confirms it. The pressure recovery in the diffuser part is more gentle than in the collector part and does not indicate any noticeable flow separation.

4.1.2 Overview on Flow Field Characteristics

In Fig. 4.2, the most relevant flow phenomena occurring in the rotor and stator row in the hovering condition are visualized by means of an isosurface of the entropy rise ΔS. These involve the tip-leakage vortex, the blade wake interaction, the blade root wake, and

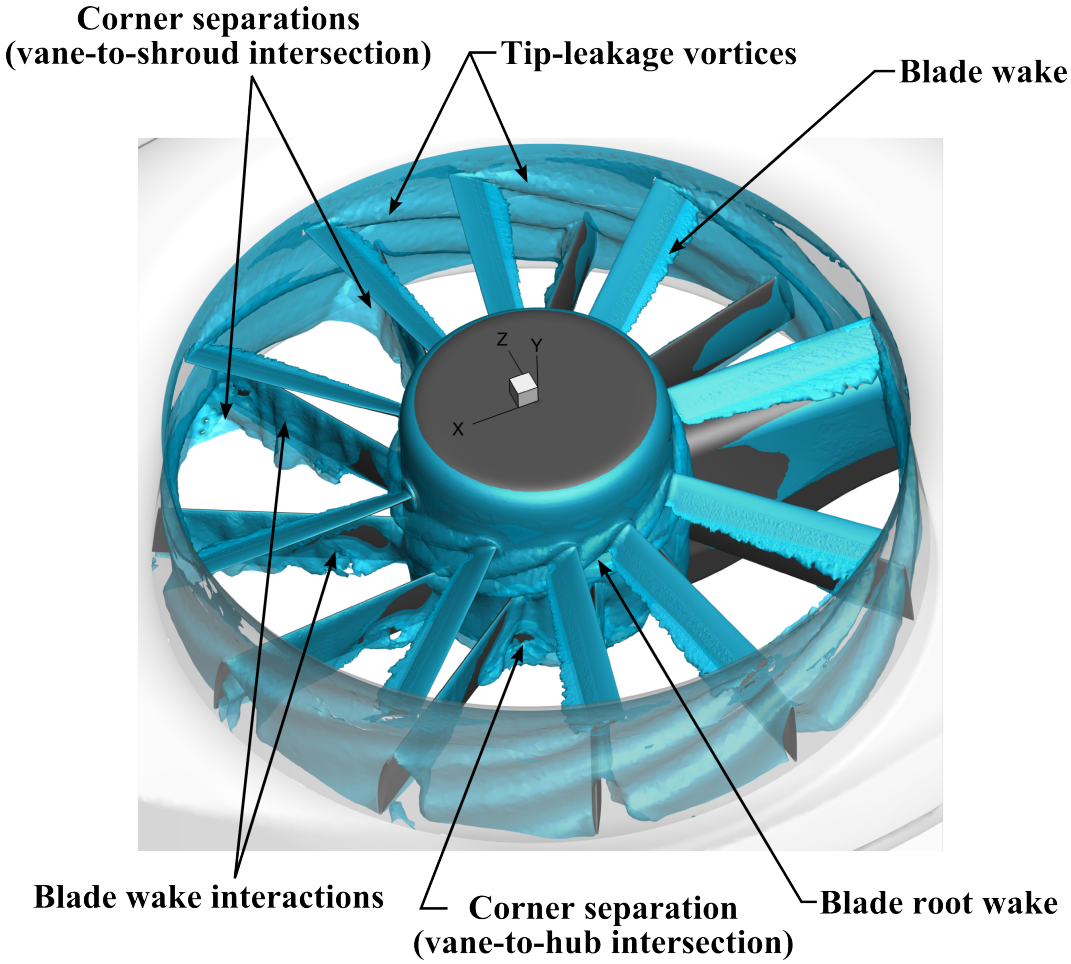

Figure 4.2: Isosurface of the entropy rise $\Delta S = 4\,\mathrm{J/K}$ highlighting unsteady flow phenomena occurring inside the duct fairing of the STR in the hovering condition, based on the URANS simulation using the SST turbulence model (the anti-torque rotor rotates counterclockwise).

the corner separation in the vicinity of the vane-to-shroud intersection as well as of the vane-to-hub intersection. In Fig. 4.3, these flow phenomena are analyzed in more detail by means of the instantaneous total pressure ratio $p_t/p_{t,max}$ and the instantaneous fan axial velocity ratio $u_a/U_{70\%}$ at different cross-sectional planes located inside the duct fairing. The total pressure and the axial velocity are made non-dimensional by the maximum total pressure $p_{t,max}$ observed inside the duct fairing and the tangential component of the local velocity measured at 70% of the fan radius, respectively. The rotor blades rotate in counterclockwise direction viewed from the inlet side of the STR.

Regarding the cross-sectional plane located immediately downstream of the rotor plane ($y/l_{\text{ref}} = -0.0175$), $p_t/p_{t,max}$ rises with increasing radial distance from the rotor hub. This is because of the radially increasing sectional blade load, resulting from the radially increasing circumferential speed, and the presence of the rotor casing. Consequently, the induced axial velocity also rises with increasing radial distance from the axis of the anti-torque rotor. Generally, the spatial distribution of $p_t/p_{t,max}$ is more significant on the blade pressure side (PS) than on the suction side (SS). The distribution of $p_t/p_{t,max}$ is more pronounced at the azimuth angle of $\psi_f = 0°$, where the rotor blade (R1) is located immediately above the drive shaft fairing at the current CFD time step. This is because of the interaction occurring between the potential field of the upstream rotor blade and the downstream drive shaft fairing (discussed in Sec. 4.1.3.1 in more detail). Further flow regimes of low levels of $p_t/p_{t,max}$ are found in the vicinity of the rotor hub and the rotor casing. The former is due to the boundary layer separation at the rotor hub as well as the cylindrical blade root wake including horseshoe vortices, while the latter is associated with the tip-leakage vortices. Blade wake impingement on the flow field can be identified by velocity deficits observed near the blade trailing edge.

On the plane located in the stator row ($y/l_{\text{ref}} = -0.13$), a significant velocity distortion is visible near the stator vane, particularly on the outgoing blade side (OG). A wake, shed from the upstream blade, periodically hits the stator vanes, thus provoking a strongly distorted flow field on the outgoing blade side (also see Fig. 4.13 and Fig. 4.14). Further flow regimes characterized by a recirculating flow are found at the vane-to-shroud intersection (corner separation) and near the gear box (blade root wake, hub separation, and corner separation).

Considering the $u_a/U_{70\%}$ distribution in the vicinity of the fan exit ($y/l_{\text{ref}} = -0.34$), a strong mixing process is observed at the boundary between the jet region and its surrounding flow field (Kelvin-Helmholtz instability). Furthermore, velocity deficits caused by the stator vane wake are also visible. Both the gear box and the drive shaft fairing result in a significantly large recirculating flow zone at the fan exit.

In the following, the most relevant flow phenomena linked to the noise generation in the hovering condition, such as the rotor/stator interactions (both potential field and viscous wake interaction) and the uneven blade spacing, are discussed in more detail.

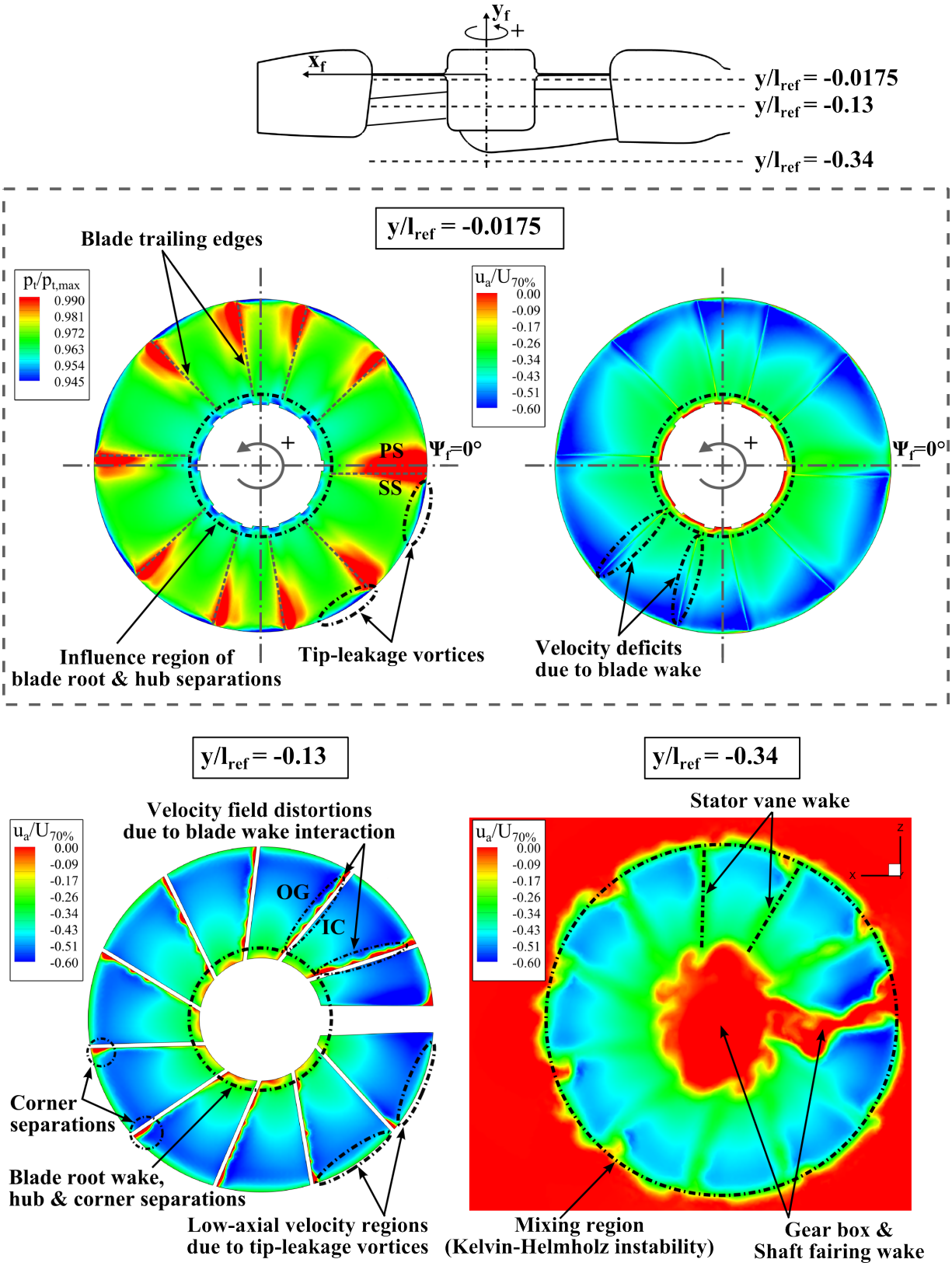

Figure 4.3: Instantaneous distributions of the total pressure ratio $p_t/p_{t,max}$ and the fan axial velocity ratio $u_a/U_{70\%}$ on cross-sectional planes located at $y/l_{\text{ref}} = -0.0175$, $y/l_{\text{ref}} = -0.13$, and $y/l_{\text{ref}} = -0.34$.

4.1.3 Rotor/Stator Interaction

Numerous studies [20, 40, 50, 88] indicate that the unsteady interaction occurring between the rotor and stator row is one of the major mechanism responsible for the fan noise emission. Four interaction mechanisms linked to the noise generation are noted in the literature [40]:

- Interaction between the potential (pressure) field of the rotor blade and the downstream obstacle (e.g. stator vanes, struts, pylons): a rotor blade experiences unsteady lift fluctuations, when it is moving above a stator vane and therefore influenced by the potential field of the stator (SPF-R, see Fig. 4.4). Likewise, the stator vane undergoes unsteady force fluctuations, when the rotor potential field passes through the downstream stator row (RPF-S)
- Vortex shedding is triggered as result of the SPF-R. The vortices are then convected downstream, causing strong velocity fluctuations in the stator row, which in turn leads to the unsteady force fluctuations on the stator vanes. In this case, both the blade and the stator vane emit sound (RV-S).
- Noise emission because of the force fluctuations on the stator vanes as a result of the periodic impingement of the viscous wake shed from the blades (RW-S).

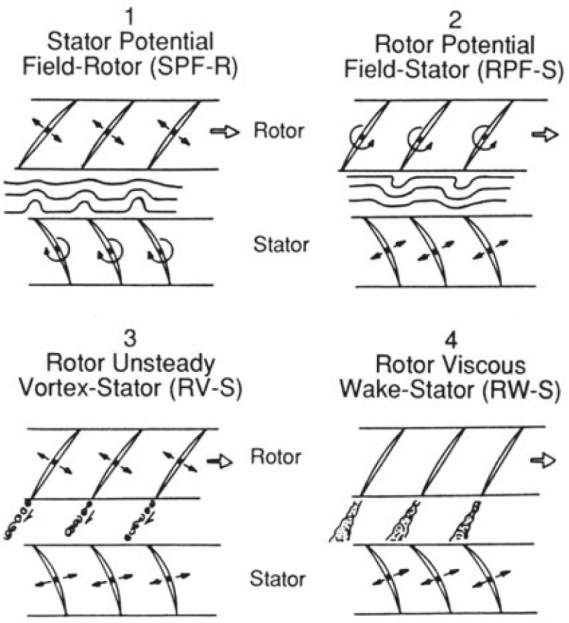

Figure 4.4: Noise generation mechanisms by rotor/stator interaction [40].

4.1.3.1 Potential field interaction

In this thesis, the interaction occurring between the potential field of the rotor blade and the stator vane is assessed by means of comparison of the reference simulation case to

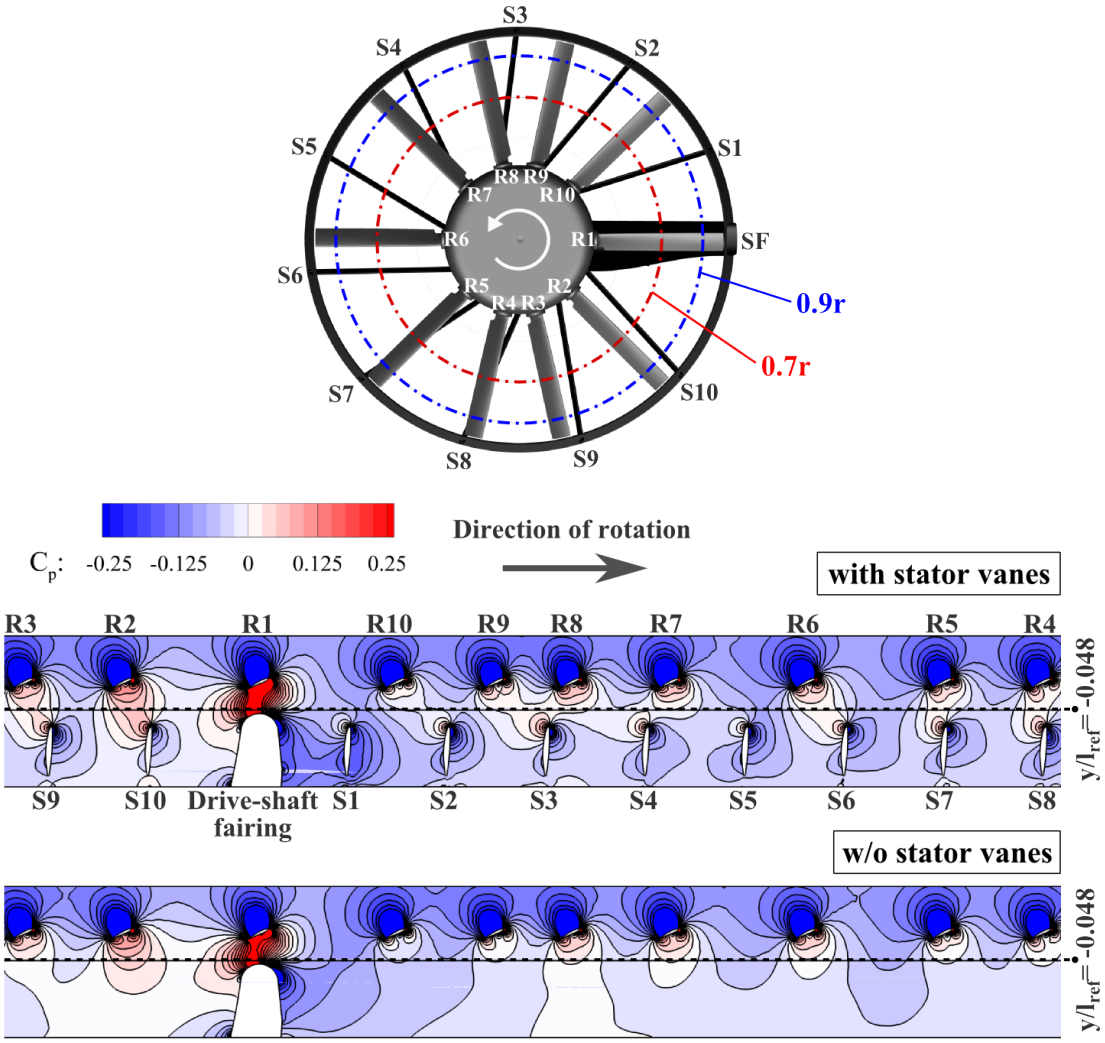

Figure 4.5: Blade-to-blade contours of pressure coefficient C_p at 70% of the fan radius for the simulation cases with and without stator vanes.

an additional simulation case where the stator vanes, except the drive shaft fairing, are removed. Both the flight parameters and the simulation setups used for the simulation case without stator vanes are identical to that for the reference case for a consistent evaluation.

To visualize the potential field interaction, instantaneous blade-to-blade contours of the pressure coefficient C_p are given in Fig. 4.5 for the reference case and the case without stator vanes. The contour plots represent the flow field that is projected on a coaxial-plane located at 70% of the fan radius. According to the figure, the reference case reveals a noticeable distribution of C_p between the blade lower surface (pressure side) and the leading edge of the stator vane. When the blade is located directly upstream of the stator vane, it instantly blocks and deflects the incoming flow of the stator vane. In addition, the rotor pressure field interacts with the stator potential field. It consequently causes an increase in the pressure level between the rotor and stator row. A most significant interaction occurs, when the blade is moving immediately above the drive shaft fairing (SF) as the SF features a larger front surface than the stator vane.

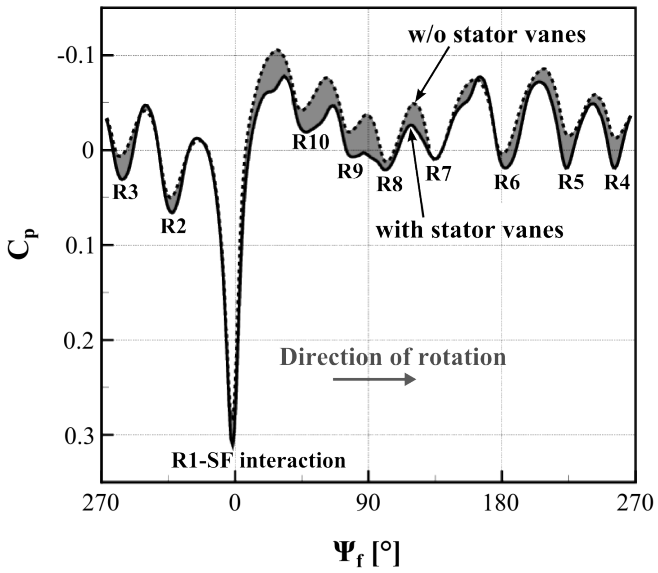

Figure 4.6: Comparison of the instantaneous pressure coefficient C_p observed on a cross-sectional line located at 70% of the fan radius and $y/l_{\text{ref}} = -0.048$.

Fig. 4.6 shows the instantaneous distribution of C_p obtained from monitor points located between the rotor and stator row ($y/l_{\text{ref}} = -0.048$ at $0.7r$) to quantify the influence of the stator being installed downstream. In this figure, the dotted line reveals pressure levels of the case without stator vanes. Hence, the pressure levels represent a net influence of the rotor potential field propagating downstream, except at the fan azimuth angle of $\psi_f = 0°$ where the potential field of the blade R1 strongly interacts with that of the drive shaft fairing for the current simulation time step (see also Fig. 4.5). In contrast to that, the solid line in Fig. 4.6 indicates the pressure levels obtained from the simulation of the reference case. Therefore, the difference between both lines indicates the pressure increase caused by the potential field interaction. The significant pressure difference found at $\psi_f = 90°$ is due to the comparably close angular distance between the blade R8 and R9. The potential field of both blades interacts together with the pressure field of the stator vane S3 at the current CFD time step (see also Fig. 4.5).

Rotor/shaft-fairing interaction. As pointed out by previous studies [47, 73, 82] and already observed in Fig. 4.5 and Fig. 4.6, the drive shaft fairing (SF) has a strong impact on the aerodynamic properties of the STR due to its comparably large front surface and the relatively close distance to the blade lower surface. The rotor/shaft-fairing (RSF) interaction leads to a drastic increase in C_p between the blade pressure side (PS) and the upper surface of the SF, as shown in Fig. 4.7 (b). Consequently, it alters the aerodynamic characteristics of the blade significantly. To show it more clearly, the chordwise distribution of C_p at $0.7r$ and $0.9r$ are given in Fig. 4.7 (a) for three interaction cases: non-interaction (R–No), interaction with the SF (R–SF), and interaction with the stator vane S2 (R–S2). Compared to the non-interaction case, both interaction cases (R–SF and R–S2) reveal a

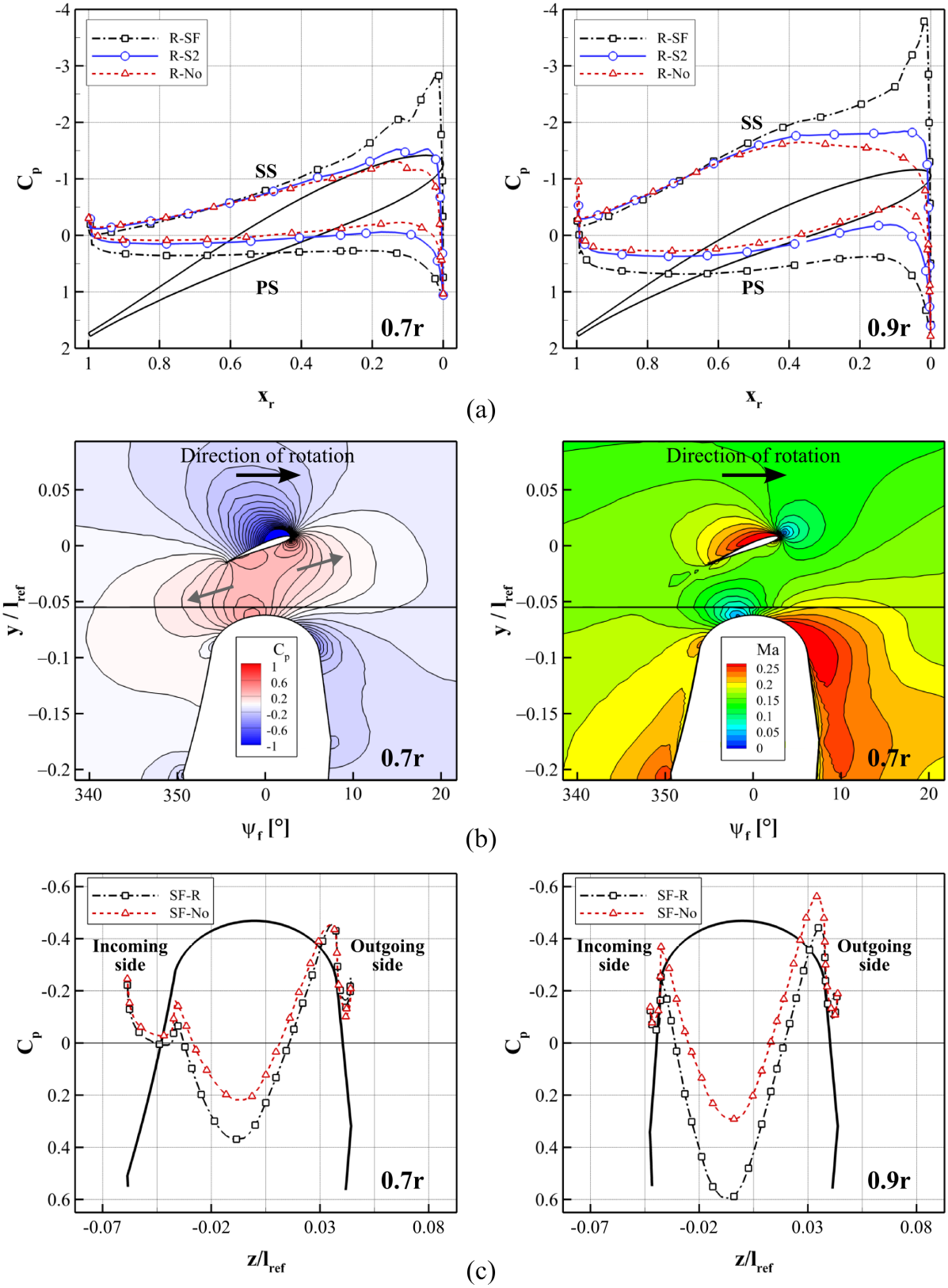

Figure 4.7: Rotor/shaft-fairing interaction: (a) chordwise distributions of C_p of the rotor blade R1 at $0.7r$ and $0.9r$, (b) C_p and Mach number distributions on the coaxial isoplane at $0.7r$, and (c) streamwise distributions of C_p of the shaft fairing at $0.7r$ and $0.9r$.

noticeable increase in C_p on the blade pressure side (PS) at 70% of the fan radius ($0.7r$). As expected, the pressure increase is more significant when the blade is encountering the interaction with the shaft fairing (relative $|C_p|$ increase of 670% for R–SF and 180% for R–S2 with respect to R–No at 40% blade chord ($x_r = 0.4$)).

The RSF Interaction also has an impact on the blade incidence angle. In the case of the interaction, the stagnation point (SP_w in Fig. 4.8) is located more downstream compared to the non-interaction case ($SP_{w/o}$). Accordingly, the flow acceleration around the blade leading edge is more stronger in the interaction case, as indicated in Fig. 4.8 using the $u_a/U_{70\%}$ distribution. Consequently, it causes a more significant suction peak on the blade suction side (SS) in the vicinity of the leading edge (relative $|C_p|$ increase of 150% with respect to R–No). The influence of the RSF interaction on the pressure distribution reaches up to 60% blade chord on the blade upper surface. As a result of the RSF interaction, the blade experiences an abrupt increase in the overall blade load, obtained from the spanwise integral of the sectional blade load (see also Fig. 4.15(b)). At 90% of the fan radius ($0.9r$), a similar analysis can be made, whereas the increase in $|C_p|$ on both the PS and SS is more significant than at $0.7r$ due to the presence of the rotor casing and the blade tip-leakage (relative $|C_p|$ increase of 34% with respect to $0.7r$ at the suction peak).

In Fig. 4.7 (c), the streamwise C_p distribution of the shaft fairing in the interaction case (SF–R) is compared with that of the non-interaction case (SF–No). As expected, the RSF interaction leads to an increase in pressure levels, mostly on the frontal surface of the SF at the current simulation time step. The relative increase in C_p with respect to the non-interaction case in the vicinity of the stagnation point on the frontal surface amounts to approximately 100% and 200%, at 70% and 90% of the fan radius, respectively. As a consequence of this, the shaft fairing also bears an abrupt change of the aerodynamic forces when the blade is moving above the SF.

The RSF interaction also has an effect on the tip-leakage vortex formation. In the

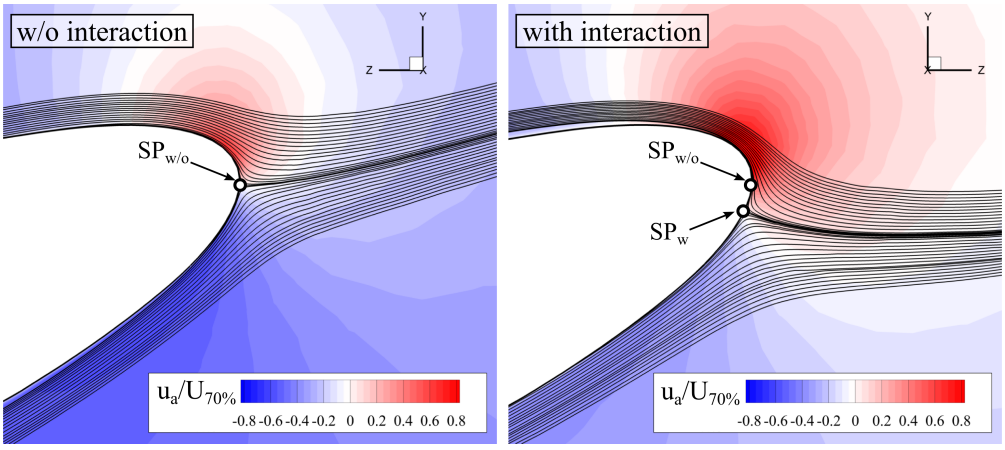

Figure 4.8: Effect of the RSF interaction on the stagnation point (SP) and fan axial velocity ratio $u_a/U_{70\%}$ presented on the coaxial isoplane located at 70% of the fan radius.

interaction case (R–SF), the pressure difference between the blade lower (pressure side) and upper side (suction side) is more stronger than in the non-interaction case (R–No) and thus inducing a stronger jet-like flow in the gap between the blade tip-face and the rotor casing, as provided in Figs. 4.9(a) and 4.9(b). Indeed, the relative increase of the fan axial velocity ratio $u_a/U_{70\%}$ amounts to approx. 400% with respect to the non-interaction case. Note that the reverse flow zone observed on the blade tip face close to the blade lower side is due to the separation bubble. As a consequence of the RSF interaction, the tip-vortex formation becomes more significant, as shown in Fig. 4.10 where the instantaneous C_p distribution on the blade suction side and isosurface of the entropy rise ΔS are presented.

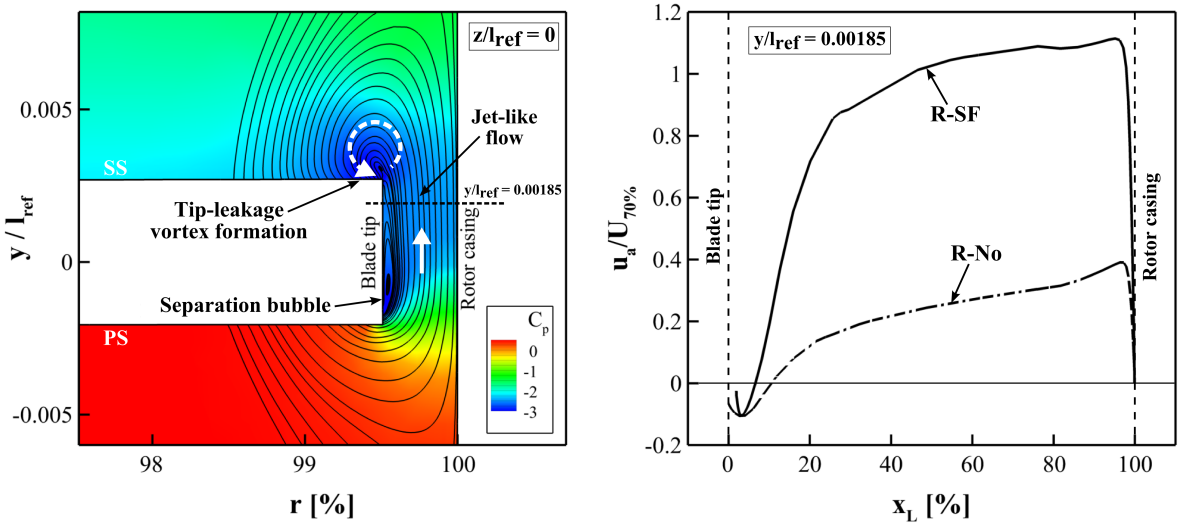

Figure 4.9: Tip-leakage vortex: (a) instantaneous C_p distribution and (b) fan axial velocity $u_a/U_{70\%}$ profile in the vicinity of the tip leakage ($z/l_{ref} = 0$).

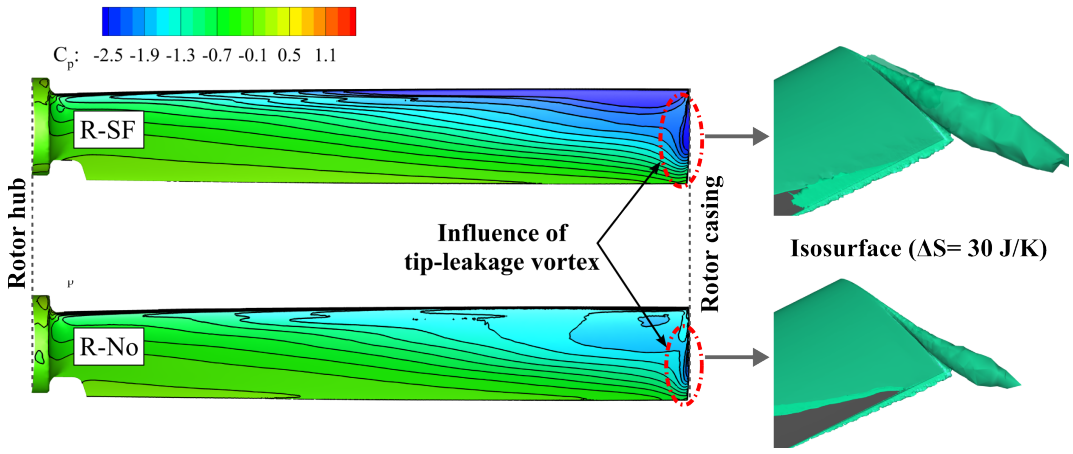

Figure 4.10: Instantaneous C_p distributions on the blade suction side and isosurface of $\Delta S = 30$ J/K for the interaction (R–SF) and non-interaction case (R–No).

Rotor/stator-vane interaction. Similar to the shaft fairing, the stator vane also undergoes a pressure fluctuation, if it encounters an interaction with the upstream blade. However, the interaction (S2–R) is less significant than the RSF interaction and mostly affects the flow field on the incoming and outgoing blade side, as shown in Fig. 4.11(a) and Fig. 4.11(b). The pressure levels on the outgoing blade side also results from the blade wake impinging (cf. Fig. 4.13).

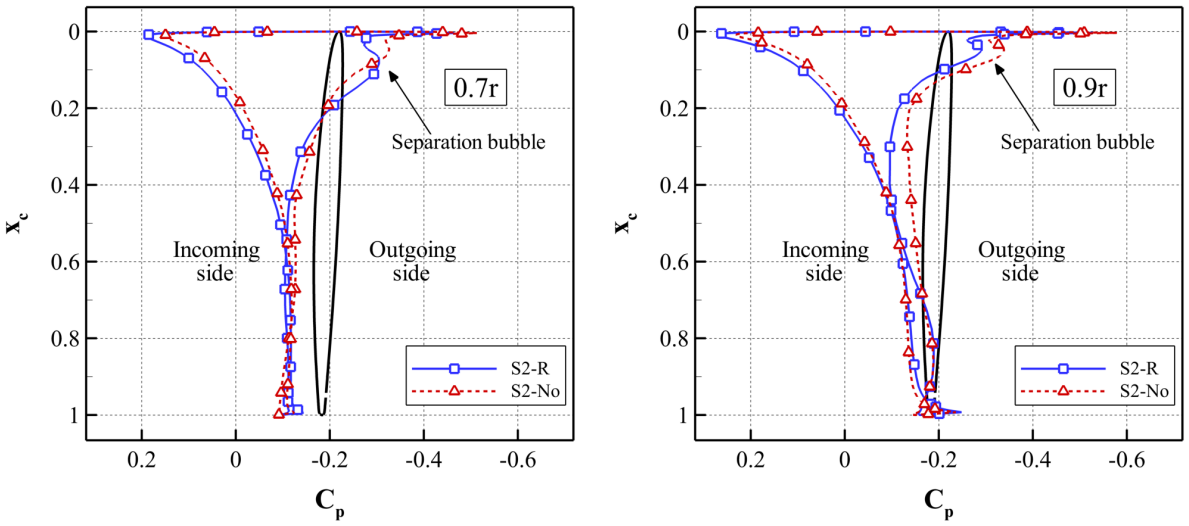

(a) (b)

Figure 4.11: Blade/stator-vane interaction: chordwise C_p distributions of the stator vane S2 at (a) 70% and (b) 90% of the fan radius.

4.1.3.2 Blade-wake/stator-vane interaction

A wake is shed from the upstream blade that excites the stator vane periodically. Thus, the vane experiences a fluctuating load. In Fig. 4.12, the instantaneous wake interaction is visualized by using the turbulence intensity Tu. Here, the blade wake is indicated by high levels of the turbulence intensity. The wake interaction leads to a fluctuating velocity field on the outgoing blade side, as indicated in Fig. 4.13(a) using the root mean square value of the fan axial velocity $u_{a,\mathrm{rms}}$. Because of the direction of the fan rotation, the wake impingement is more significant on the outgoing blade side, as highlighted in Fig. 4.13(b). Note that the profile of $u_{a,\mathrm{rms}}$ is obtained immediately upstream of the stator vane S2 ($y/l_{\mathrm{ref}} = -0.0983$) at 70% of the fan radius. The noticeable high levels of $u_{a,\mathrm{rms}}$ in Fig. 4.13(a), observed on the outgoing side of the stator in the vicinity of the leading edge, is due to the separation bubble (see also Figs. 4.11(a) and 4.11(b)).

As a result of the wake impingement, the stator vane undergoes a strong surface pressure fluctuation, as indicated in Fig. 4.14. As expected, the outgoing blade side exhibits a strongly disturbed pattern of C_p', while the distribution of the surface pressure fluctuation on the incoming side is rather continuous. The significant pressure fluctuation

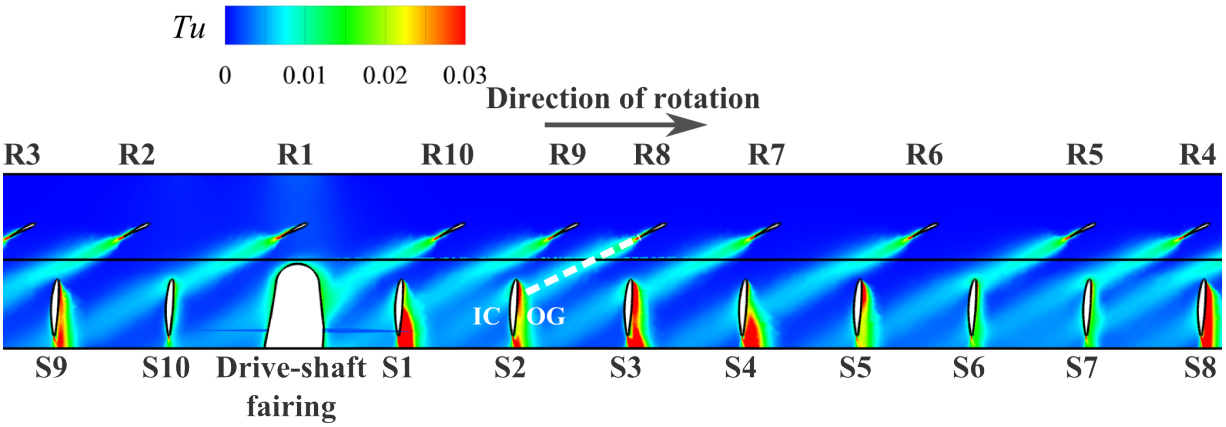

Figure 4.12: Blade-to-blade contour of turbulence intensity Tu at 70% of the fan radius.

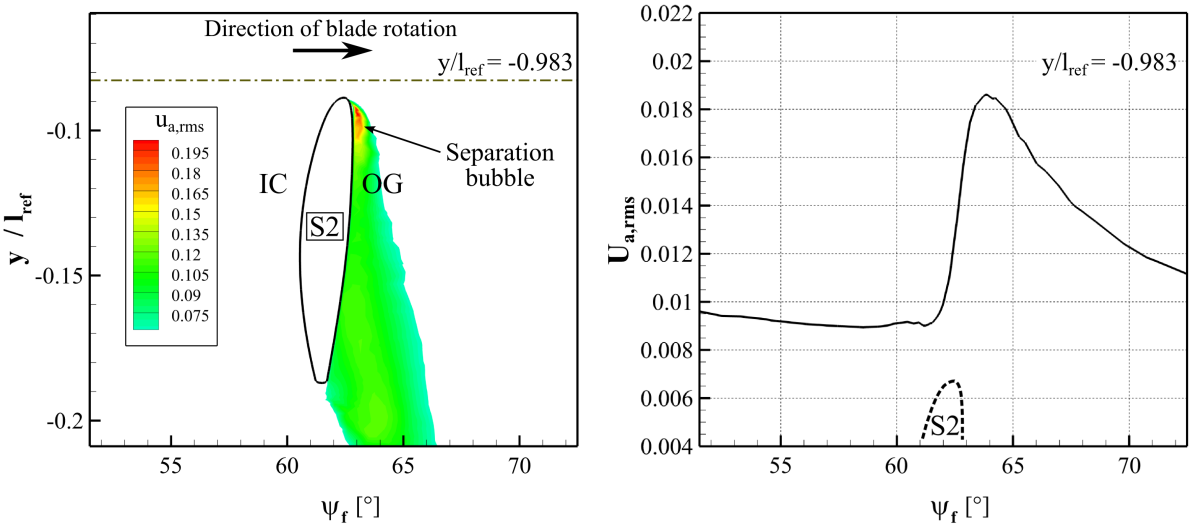

Figure 4.13: (a) Contour of root mean square value of the fan axial velocity v_{rms} at the stator vane S2 and (b) profile of $u_{a,\mathrm{rms}}$ observed at $y/l_{\mathrm{ref}} = -0.0983$.

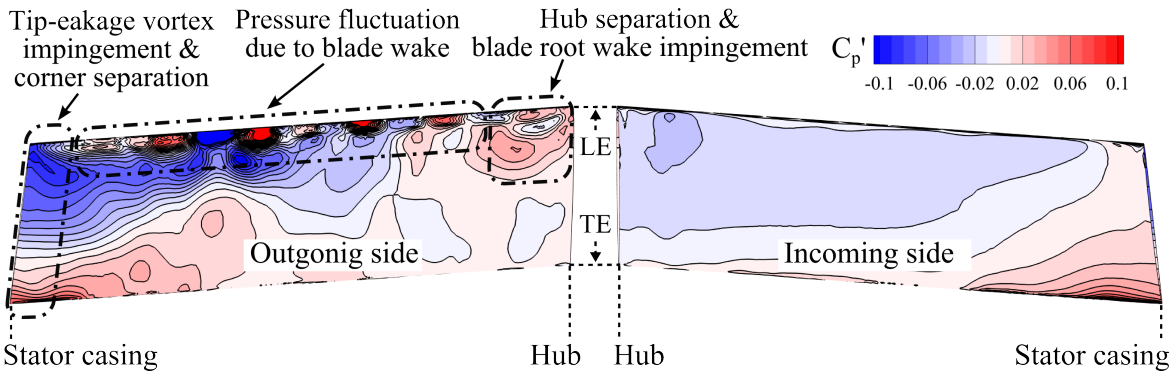

Figure 4.14: Distributions of the surface pressure coefficient fluctuation C_p' on the stator vane S2.

observed on the outgoing side in the vicinity of the leading edge is due to the separation bubble, resulting from the direct impact of the viscous blade wake. Further regions of significant C_p' are found in the vicinity of the vane-to-shroud intersection and vane-to-hub intersection. The former is associated with the tip-leakage vortex and the corner separation, while the latter is caused by the interaction with the blade root wake and the hub separation.

4.1.3.3 Unsteady force fluctuations

Fluctuating blade load. Fig. 4.15(b) reveals the time dependent behavior of blade load C_y of a single rotor blade (R1) as a function of the blade passing period (BPP). Note that at the starting point (BPP = 0), the blade R1 is located immediately upstream of the shaft fairing ($\psi_f = 0°$). In the reference case (solid line in Fig. 4.15(b)), the blade experiences significant fluctuations of C_y over one blade passing period. It is because of the interaction between the potential field of the blade and the stator vane, which results in an instantaneous increase in the blade load. Hence, in the case without stator vanes, this kind of load fluctuation is not observed, except the high level of C_y at BPP = 1 and BPP = 2 indicating the RSF interaction. The relative increase in C_y by the RSF interaction amounts to approximately 63% in comparison to the rotor/stator-vane interaction.

The time dependent behavior of the entire ten blades is given in Fig. 4.15(b) as a function of the BPP of the blade R1. As expected, all blades indicate a similar pattern of the load fluctuations, but different levels of the blade load depending on the angular spacing to adjacent blades. Considerably high levels are predicted on the blade R1 and R2 as well as on R6 and R7. These blades feature the largest angular spacing (θ_1, see Fig. 4.15(a)) to preceding blades (R10 and R1 as well as R5 and R6, respectively) in the direction of rotation. On the contrary, the lowest blade load is observed for the blade R4 and R9, which have the smallest angular distance (θ_3), therefore having a stronger impact from the neighboring blades (R3 and R8). As provided in Fig. 4.16, the comparison of the instantaneous streamlines and the stagnation point (SP) between the blade R2 (θ_1) and R4 (θ_3) indicate that the blade spacing alters the local blade incidence angle and therefore the position of the stagnation point, which consequently leads to a different pressure field around the blade leading edge. The stagnation point of the blade R2 (SP_{R2} in Fig. 4.16) is located more downstream than that of R4, highlighting that the blade R2 experiences a higher blade incidence angle. Indeed, the blade incidence angle of R4 amounts only 20% of that of R2, as indicated in Fig. 4.17 where the blade incidence angle ratio α/α_{R2} is given for the blade R1 to R5. The individual blade load of the blade R1 to R5 in Fig. 4.15(c) has a very high correlation with α/α_{R2} in Fig. 4.17.

Because of the unequal blade spacing, the overall blade load (sum of all individual blade loads) $C_{y,\text{total}}$ exhibits a distributed pattern over a half fan revolution, as plotted in Fig. 4.15(d). High levels of $C_{y,\text{total}}$ occur when interactions arise simultaneously and thus being superimposed. For instance, the blade R2 interacts with the stator vane S1, while R3 is influenced by the shaft fairing at the same time (BPP = 1.24 in Fig. 4.15(c)).

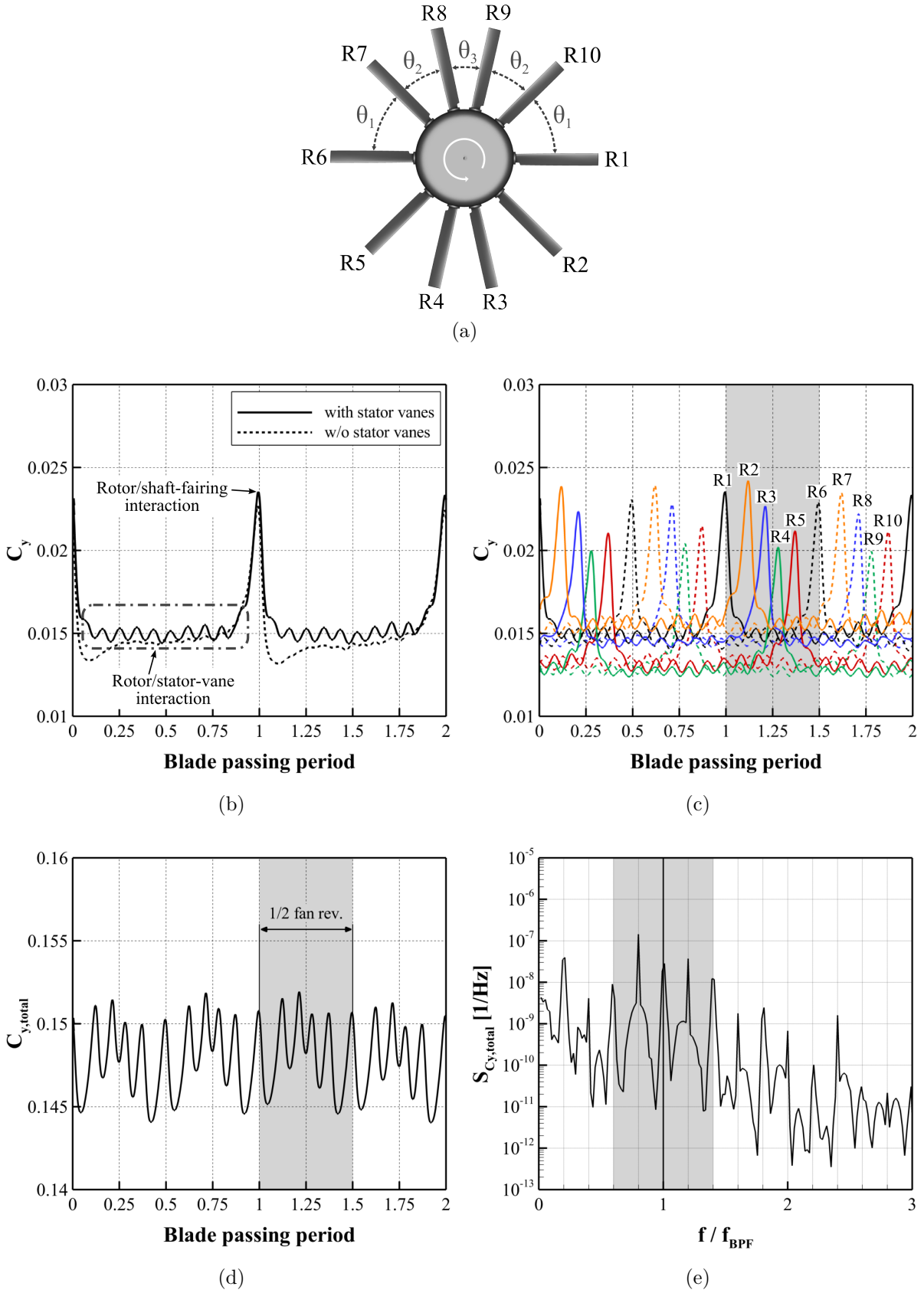

Figure 4.15: Fluctuating blade load: (a) uneven blade spacing, (b) time dependent behavior of single blade (R1) load C_y, (c) time dependent behavior of entire blades, (d) overall blade load $C_{y,\text{total}}$, and (c) power spectral density of the overall blade load $S_{C_{y,\text{total}}}$.

Fig. 4.15(e) depicts the power spectral density analysis of the overall blade load $S_{C_{y,\text{total}}}$. The analysis indicates a close similarity to the spectrum obtained from the analytic solution of the sinusoidal phase modulation (see Fig. 1.9(e)). As a result of the uneven blade spacing, the discrete component at the frequency $f/f_{\text{BPF}} = 0.8$ features a higher $S_{C_{y,\text{total}}}$ than at the blade passing frequency ($f/f_{\text{BPF}} = 1$), which is generally the most dominant one by a fan configuration with equally spaced blades. Further increased levels of $S_{C_{y,\text{total}}}$ are observed at $f/f_{\text{BPF}} = 1 \pm 0.2m$ with $m = 1, 2$, indicating upper and lower sideband frequencies. Since the rotor is designed as two-fold rotational symmetry ($\Delta\psi_f = 180°$), a noticeable increase in $S_{C_{y,\text{total}}}$ is found at $f_{\text{BPF}} = 0.2$, corresponding to twice of the fan rotational frequency.

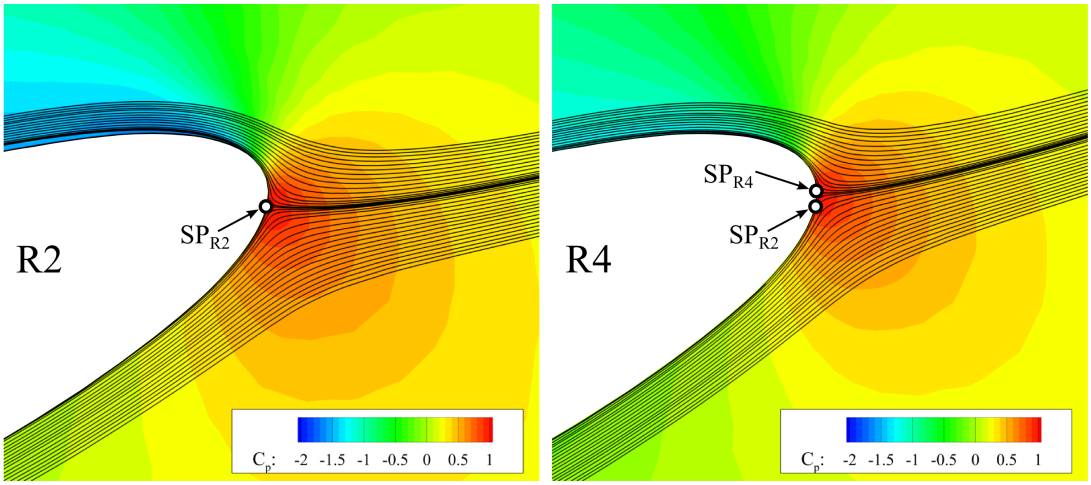

Figure 4.16: Time-averaged distributions of $\overline{C}_p$ and streamlines around the leading edge of the blade R2 and R4 on the coaxial-plane at 70% of the fan radius.

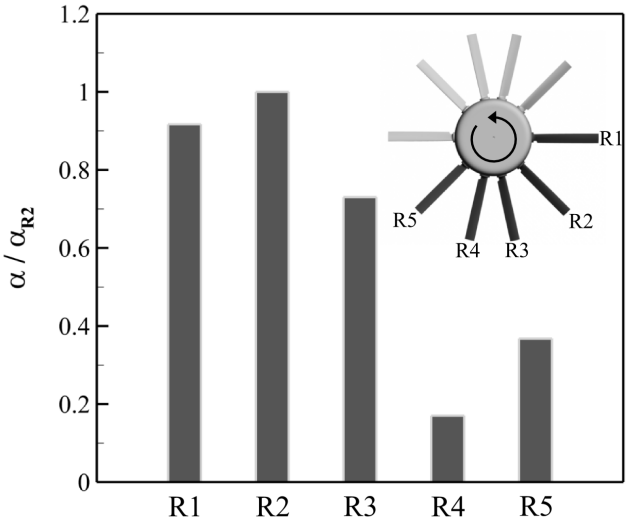

Figure 4.17: Local blade incidence angle ratio $\alpha/\alpha_{\text{R2}}$ for the blade R1(θ_1), R2(θ_1), R3(θ_2), R4(θ_3), and R5(θ_2).

Fluctuating stator vane load. Because of the phase-modulated excitation by the blade potential field and the viscous blade wake, the stator vane (including the shaft fairing) bears strongly fluctuating aerodynamic forces. It is visualized in Fig. 4.18(a) for the shaft fairing. Both the fan axial C_y and the circumferential component C_z of the shaft fairing load show a strong dependency on the blade spacing. Since the lateral surface is larger than the frontal surface, the circumferential force (F_z) reveals a higher magnitude than the axial one. The spectral analysis of C_z in Fig. 4.18(b) shows very similar spectral characteristics as the power spectral density of the overall blade load $S_{C_{y,\text{total}}}$ observed in Fig. 4.15(b)): a broadband-like spectrum and a higher level of S_{C_z} at $f/f_{\text{BPF}} = 0.8$ than at $f/f_{\text{BPF}} = 1$.

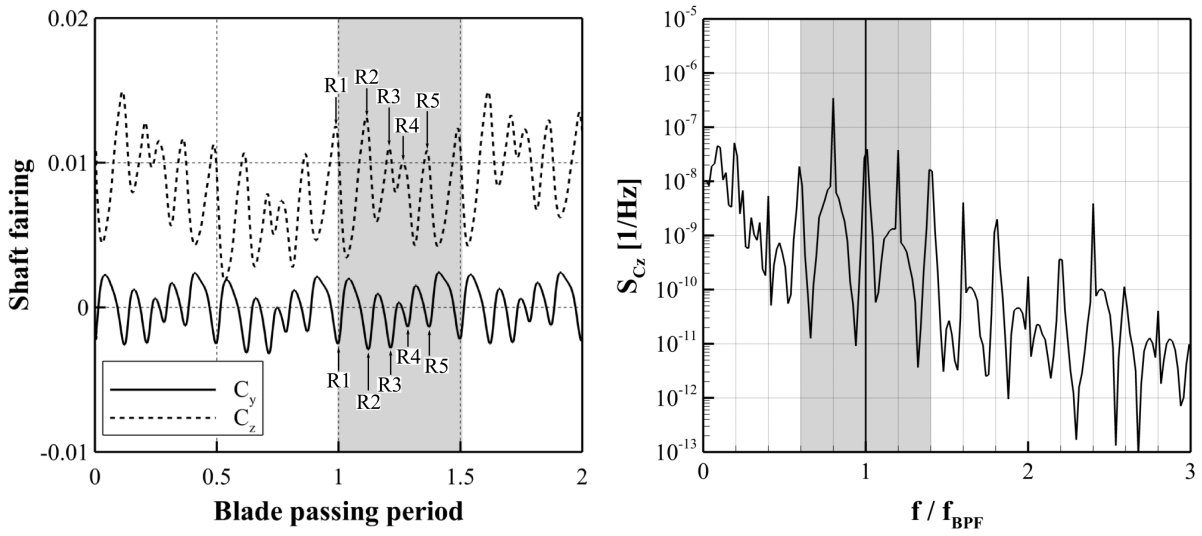

Figure 4.18: Fluctuating shaft fairing load: (a) time dependent behavior of the fan axial C_y and circumferential force coefficient C_z of the shaft fairing and (b) power spectral density of the circumferential force coefficient S_{C_z}.

4.1.3.4 Pressure field disturbance outside the duct fairing

In Figs. 4.19(a) and 4.19(b), the pressure coefficient fluctuation C_p' are given on the fan outlet side for the simulation case with and without stator vanes, respectively. The fluctuating pressure field outside the duct fairing is visualized on the coaxial isoplane located at 99.9% of the fan radius. The effect of the stator being installed downstream of the rotor is clearly visible: a strongly distorted and complex pattern of C_p' as result of the interaction of the tip-leakage vortex with the stator vane (see Fig. 4.19(a)). On the contrary, in the case without stator vanes, the traces of the tip-leakage vortex are still visible far from the fan exit as the tip-leakage vortex is convected downstream without any significant interactions (see Fig. 4.19(b)).

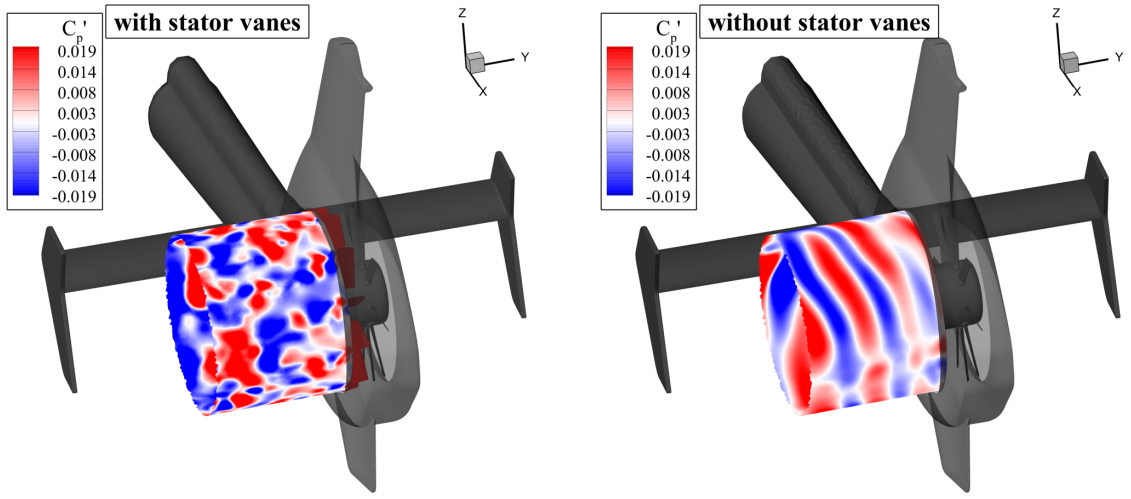

(a) (b)

Figure 4.19: Instantaneous distributions of C'_p for (a) the reference simulation case and (b) the case without stator vanes on a coaxial-plane (99.9% of the fan radius) located on the fan outlet.

Fig. 4.20(a) presents the isosurfaces of $C'_p = 7.57 \times 10^{-3}$ and $C'_p = -7.57 \times 10^{-3}$ in the vicinity of the STR inlet. The isosurface of $C'_p = -7.57 \times 10^{-3}$ represents the upstream propagating pressure disturbance occurred by the blade potential field. It is more significant, where the blade features the smallest spacing (θ_3), such as on the blade R3 and R4 as well as on R8 and R9. This is because the pressure disturbances of the individual blade are superimposed due to the relatively close angular spacing to the adjacent blade. On the other hand, the isosurface of $C'_p = 7.57 \times 10^{-3}$ indicates the pressure fluctuations

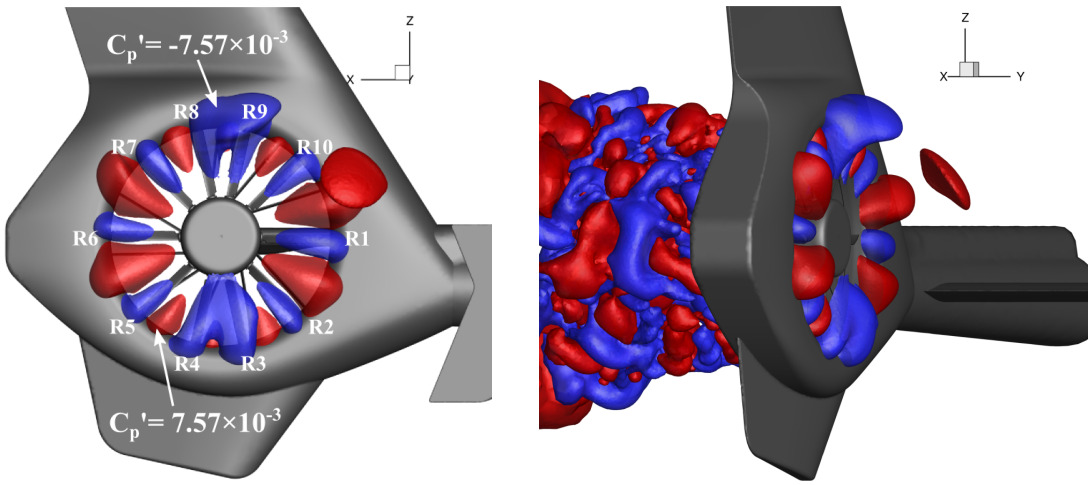

(a) (b)

Figure 4.20: Instantaneous isosurfaces of pressure fluctuations $C'_p = 7.57 \times 10^{-3}$ and $C'_p = -7.57 \times 10^{-3}$ for the reference simulation case.

provoked by the suction of the fluid flow occurring between the blades. These are more pronounced where the blade spacing is large (θ_1, between the blade R1 and R2, R1 and R10 as well as R5 and R6, R6 and R7). The significant isosurface of $C_p' = -7.57 \times 10^{-3}$ observed between the blade R1 and R10 is because of the RSF interaction and features a specific direction of propagation (see Fig. 4.20(b)).

Fig. 4.21(a) also shows the outward propagation of the pressure fluctuations caused by the RSF interaction by using instantaneous distributions of C_p' on the cross-sectional plane at $z/l_{\text{ref}} = 0$. Furthermore, the acoustic shielding effect of the STR shroud, the tailboom and the end plate are indicated. In addition, the acoustic shielding effect resulting from the upper fin and the bumper is indicated on the plane at $x/l_{\text{ref}} = 0$ (see Fig. 4.21(b)). This kind of shielding effect is, however, not considered in the prediction of the far-field noise, as the FWH method does not take into account any geometries in the propagating path of sound (between integral surfaces and observer points).

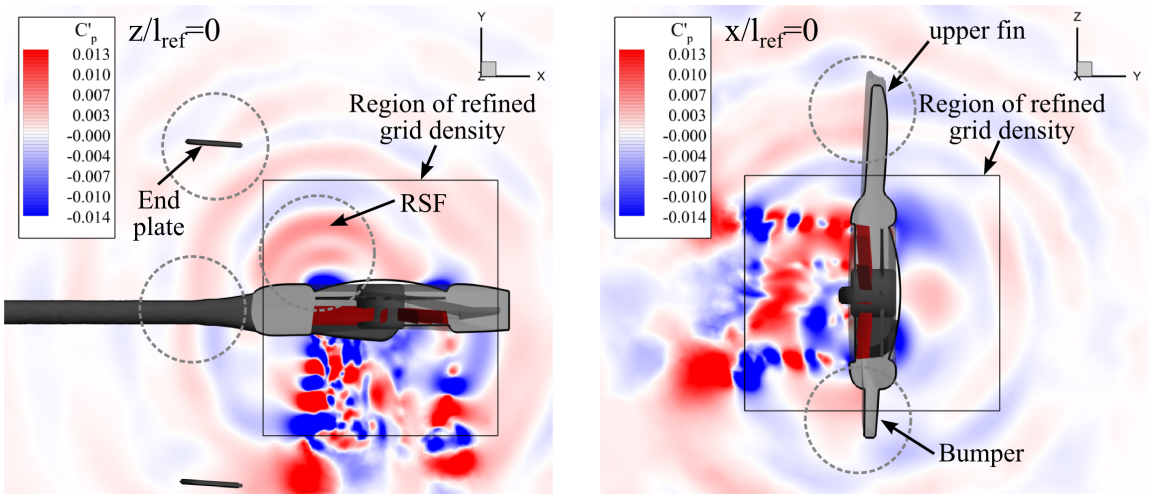

(a) (b)

Figure 4.21: Instantaneous distributions of C_p' on cross-sectional planes at (a) $z/l_{\text{ref}} = 0$ and (b) $x/l_{\text{ref}} = 0$ for the reference simulation case.

4.2 Far-Field Sound Characteristics

In this section, results of the acoustic post-processing based on the FWH porous surface integration method are presented. Firstly, the calculated far-field sound are compared with the measured sound obtained from the flight test to evaluate the predictive capability of the hybrid method applied herein. And then, the acoustic result of the reference case will be compared with that of the case without stator vanes to figure out the influence of the presence of the stator vanes on the far-field noise characteristics of the STR.

4.2.1 Evaluation of Predictive Capability

4.2.1.1 Overview of flight test campaign

The noise spectra predicted by the FWH method are compared with the measured sound spectra provided by AHD. The sound data were collected by ground microphones in a flight test campaign (see Fig. 4.22). In total, six microphones, distributed on the ground with increasing distance (maximum distance $D_{\max} = 200\ m$) from the axis of the main rotor, were used. The microphones were installed on the runway, which is acoustically hard. Possible reflections of the sound on the ground is, however, not taken into account in the acoustic post-processing. The helicopter was hovering approximately $H = 30.5\ m$ above the ground level during the measurements. In order to determine directional characteristics of noise radiation, the test helicopter was turned 45° counterclockwise (viewed on the top side of the helicopter) around the axis of the main rotor at each subsequent measurement. Hence, there are differences in the distance between the helicopter and the microphone positions: a smaller distance (approx. $\Delta D = -5\ m$) when the fuselage nose is directed

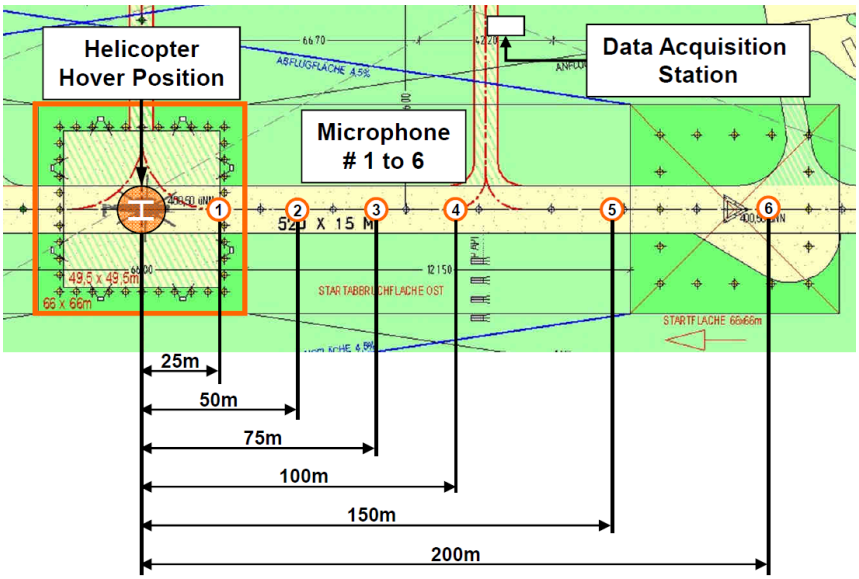

Figure 4.22: Position of microphones in the flight test measurement (figure from Airbus Helicopters Deutschland).

towards the microphone line ($\psi_h = 0°$, see also Fig. 4.23(a)) and a lager distance (approx. $\Delta D = +5\,m$) when the STR is facing the microphone ($\psi_h = 180°$, see also Fig. 4.23(a)). This circumstance has been taken into account in the acoustic computation.

The recorded sound signal contains all noise components originating from diverse noise sources at the helicopter, such as the main rotor, the gas turbine, the transmission shaft and the shrouded tail rotor. The tonal distribution of the shrouded tail rotor was extracted from the overall noise by use of the sound extraction tool Rotational Noise Source Identification (ROSI), developed by Airbus Group Innovations and validated by AHD. ROSI is a MATLAB based software and performs the acoustics post-processing based on a recorded pressure time signal. This tool enables the identification and extraction of the particular noise contributions of rotational noise sources from an acoustic input signal [116].

4.2.1.2 Sound directivity

In Figs. 4.23(a) and 4.23(b), the directivity contour plot of the hybrid method (URANS-FWH) and the flight test are presented. The acoustic prediction is performed based on the data set of the flow quantities obtained over five blade passing periods of the blade R1. The center of the directivity plane does not coincide with the midpoint of the STR, but it is located on the main rotor axis. Comparing the directivity, a fairly good agreement is found between the prediction and the measurement. The directivity of the URANS-FWH and the flight test reveal a significant noise radiation on the port side (fan outlet side) towards the aft part of the STR ($\psi_h = 135°$). The difference in overall sound pressure level (OSPL) between the hybrid method and the flight test ($\Delta\text{OSPL} = \text{OSPL}_{\text{FWH}} - \text{OSPL}_{\text{Flight}}$) at this azimuth angle is approximately 1.4 dB for the microphone at $D = 25\,m$ and 0 dB for the microphone at $D = 50\,m$.

The relatively low noise level on the bow side of the helicopter represents the acoustic shielding effect caused, on the one hand, by the duct fairing and the STR shroud, and on the other hand, by the helicopter fuselage. In the FWH computations, the effect of the duct fairing of the STR is implicitly considered by using the two-disconnected integral surfaces (see Fig. 3.2), while the masking effects of the fuselage and the STR shroud are not taken into account. As a result of neglecting the fuselage effect, the sound level is slightly overestimated on the bow side of the STR. The overestimation of OSPL at $\psi_h = 0°$ (bow side) and $D = 200\,m$ is around 4 dB, whereas ΔOSPL at $\Psi_h = 180°$ (stern side) and $D = 200\,m$ is approximately -1.5 dB.

4.2.1.3 Narrowband spectra

In Fig. 4.24 and Fig. 4.25, the narrowband spectrum of the calculated noise is compared with that of the flight test measurements at the microphones located at $D = 25\,m$ and $D = 100\,m$, respectively. Both the calculated and the measured sound spectra indicate significant discrete noise components. As a result of the uneven blade spacing, the tonal components are distributed over a wide rage of frequencies. As expected, the spectra show

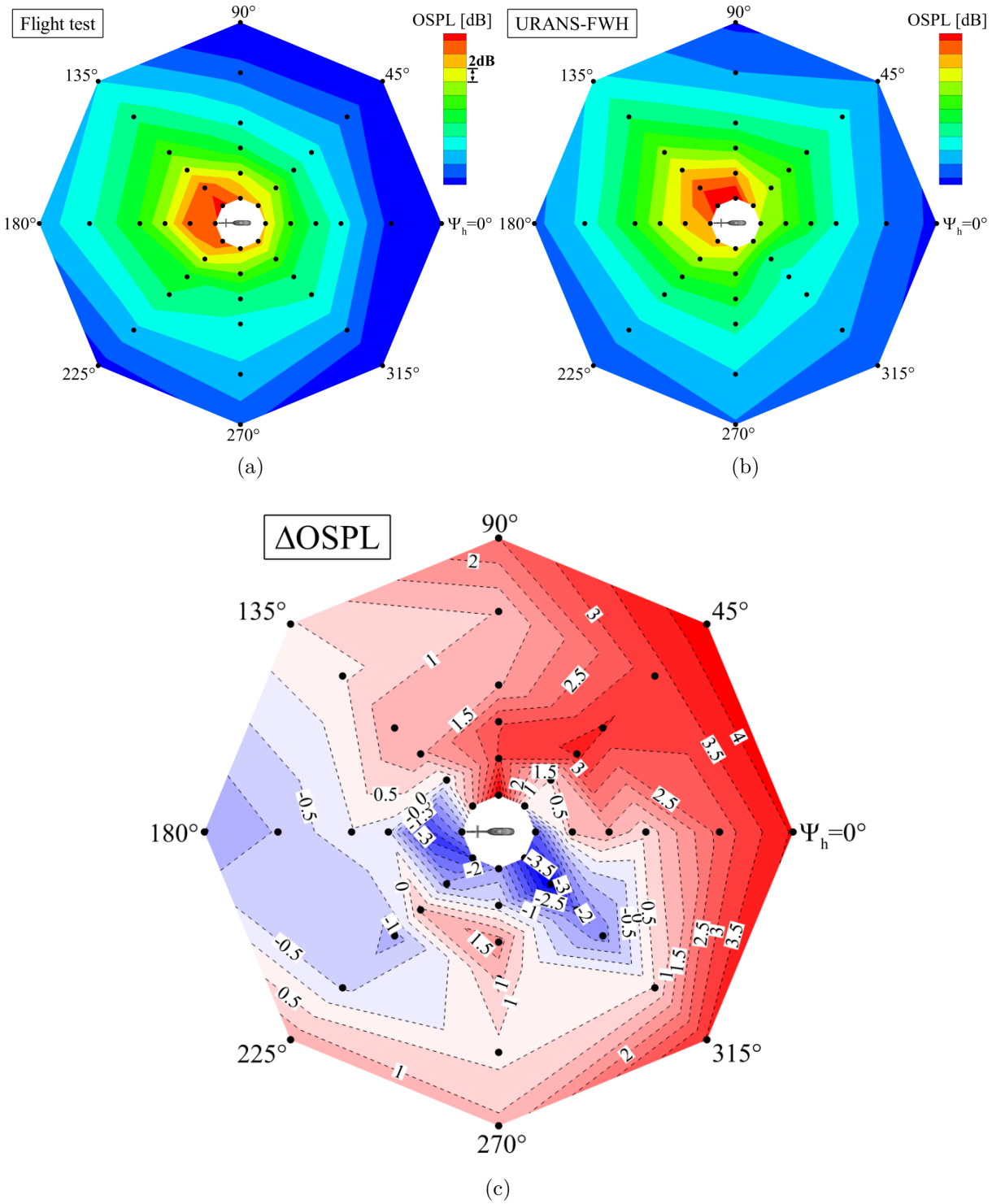

Figure 4.23: Comparison of noise directivities: (a) flight test and (b) URANS-FWH, and (c) differences in OSPL ($\Delta\text{OSPL} = \text{OSPL}_{\text{FWH}} - \text{OSPL}_{\text{Flight}}$).

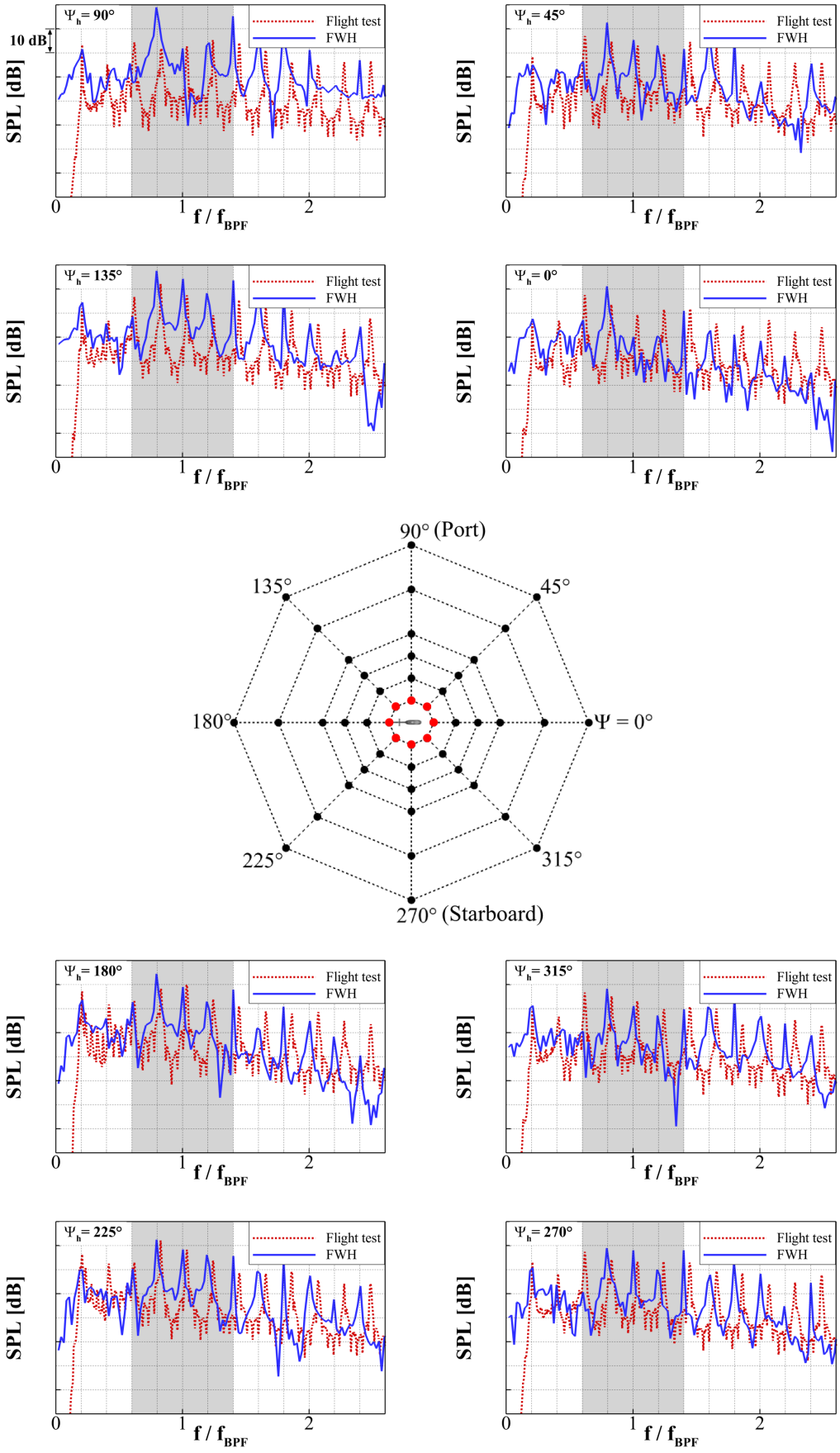

Figure 4.24: Comparison of narrowband spectra between hybrid method data and flight test measurements at microphones with $D = 25\,m$.

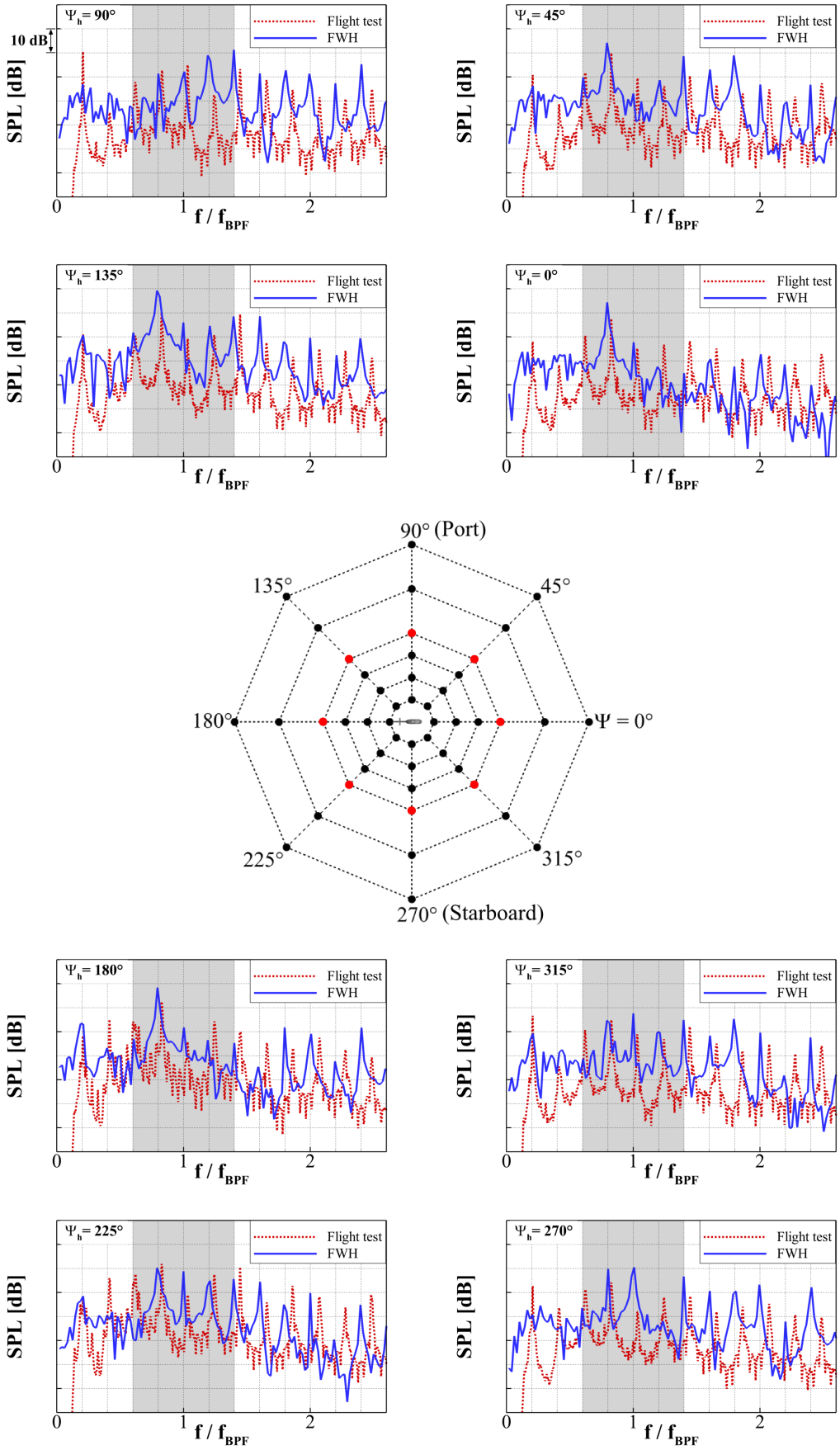

Figure 4.25: Comparison of narrowband spectra between hybrid method data and flight test measurements at microphones with $D = 100\,m$.

a very close similarity to the spectrum of the analytic solution of the sinusoidal modulation (cf. Fig. 1.9(e)) and to the power spectral density analysis of the overall blade load (cf. Fig. 4.15(e)) as well as of the shaft fairing load (cf. Fig. 4.18(b)). Hence, in addition to the BPF tone ($f/f_{\mathrm{BPF}} = 1$) and its high-order harmonic (e.g. $f/f_{\mathrm{BPF}} = 2$), significant tonal components are observed at $f/f_{\mathrm{BPF}} = n \pm 0.2m$ with $m, n = 1, 2$ in both the FWH prediction and the flight measurement.

Comparing the spectra for the microphones with $D = 25\,m$ (see Fig. 4.24), the calculated noise spectra are in good agreement with the measured spectra. The URANS-FWH provides all relevant tonal noise components in the frequency range between $0.2 < f/f_{\mathrm{BPF}} < 2$. The discrete noise component at $f/f_{\mathrm{BPF}} = 0.2$, corresponding to twice the fan rotational frequency, is due to the fact that the anti-torque rotor is designed as two-fold rotational symmetry (180°). The frequency offset observed at the discrete tonal component at $f/f_{\mathrm{BPF}} = 0.2$ is due to a deviation in the fan rotational frequency between the simulation ($f_{R,\mathrm{FWH}} = 100\%$) and the flight test ($f_{R,\mathrm{Flight}} = 103.6\%$), and is slightly amplified with increasing frequency (frequency offset for the blade passing frequency is $\Delta f/f_{\mathrm{BPF}} = 0.03$). Generally, the sound pressure levels are not only predicted well at the discrete components, such as at the BPF, its high-order harmonics, and corresponding sideband frequencies, but also for the frequency range in-between. Regarding the microphones with $D = 100\,m$, there are also good correlations between the calculations and the microphone measurements. However, the deviation is slightly higher than at the microphones with $D = 25\,m$.

4.2.2 Effect of Stator Vane

4.2.2.1 Directivity comparison

In Figs. 4.26(a) and 4.26(b), the directivity contour plot is presented for the case with and without stator vanes, respectively. Note that the directivity plane is located underneath of the STR with $H = 30.5\,m$ and features a higher density of the observer points ($\Delta\psi_h = 22.5°$) than that given in Fig. 4.23 ($\Delta\psi_h = 45°$). Comparing the directivity, it is found that the stator vanes have a significant impact on the far-field acoustic characteristics of the STR in the hovering condition. According to Fig. 4.26(c), the noise related to the stator vane and its interaction mostly propagates towards the port side and the bow side as well as the stern side of the STR. The maximum difference in OSPL between the cases without and with stator vane is $\Delta\mathrm{OSPL} = \mathrm{OSPL}_{\mathrm{w/o}} - \mathrm{OSPL}_{\mathrm{with}} = -6$ dB and observed at $\psi_h = 45°$ ((a) in Fig. 4.26(c)) and at $\psi_h = 135°$ ((b) in Fig. 4.26(c)). On the starboard side, particularly in the helicopter azimuth range between $225° < \psi_h < 315°$, the difference in OSPL between both simulation cases is negligible small, highlighting that the sound directivity in this area mainly depends on the sound emitting from the blades and their interactions. In this area, ΔOSPL is approximately ± 1 dB.

4.2.2.2 Narrowband spectra

In Fig. 4.27, the narrowband spectra of the cases with and without stator vanes are compared at the selected observer points for a more detailed analysis of the influence of the stator vane and its interaction on the far-field acoustics characteristics of the STR. Regarding the noise spectra at the observer points where noticeable deviations in OSPL have been observed in the directivity analysis ((a) and (b) in Fig.4.26(c)), significant decreases of sound levels are observed at the discrete components associated with $f/f_{\mathrm{BPF}} = 0.8$, $f/f_{\mathrm{BPF}} = 1.4$, $f/f_{\mathrm{BPF}} = 1.6$, $f/f_{\mathrm{BPF}} = 1.8$, and $f/f_{\mathrm{BPF}} = 2$, if the STR does not feature any stator vanes (see Fig. 4.27(a) and Fig. 4.27(b)). On the contrary, the sound pressure level at $f/f_{\mathrm{BPF}} = 1$ is increased in the case without stator vane. At both observer points, most significant decreases in SPL are found, particularly at the lower sideband frequencies of the BPF ($0.6 < f/f_{\mathrm{BPF}} < 1$) if no rotor/stator interaction occurs. At the observer points located on the fan inlet side ((c) and (d) in Fig.4.26(c)), the differences in the noise spectra between the cases with and without stator vanes are not significant, which highlights that the impact of the stator vane and its interaction on the far-field noise signature on the fan inlet side is small.

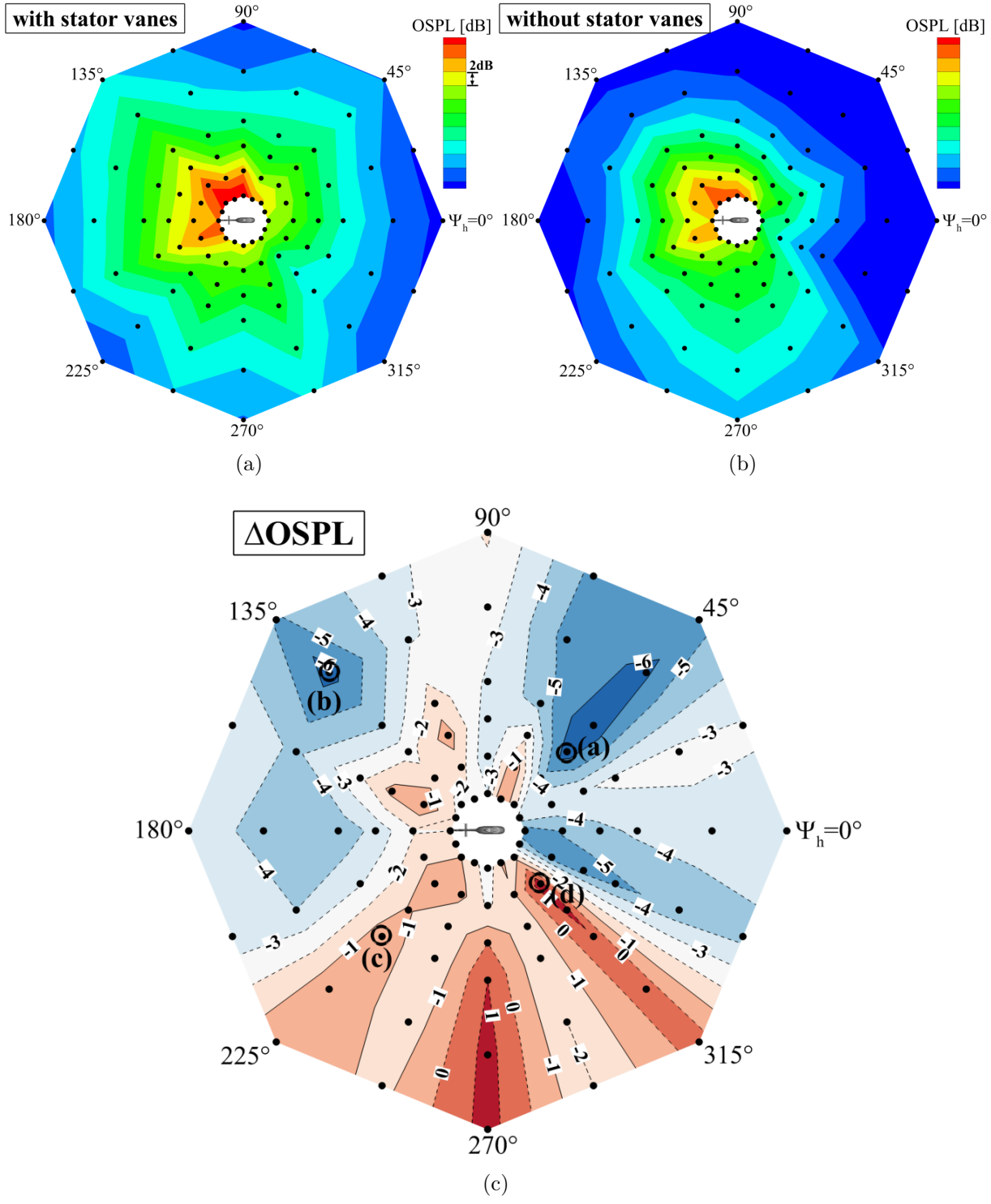

Figure 4.26: Influence of stator vanes on the STR noise directivity in the hovering condition: (a) reference simulation case, (b) case without stator vane, and (c) difference in OSPL ($\Delta\text{OSPL} = \text{OSPL}_{\text{w/o}} - \text{OSPL}_{\text{with}}$).

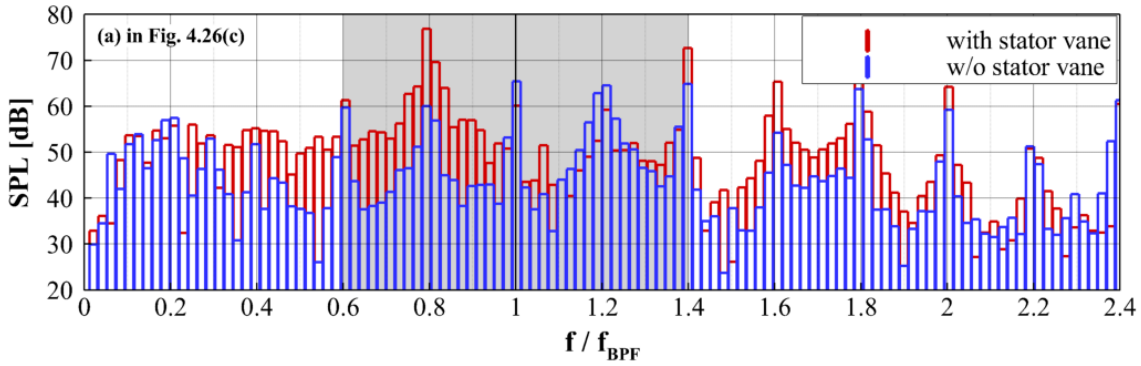

(a)

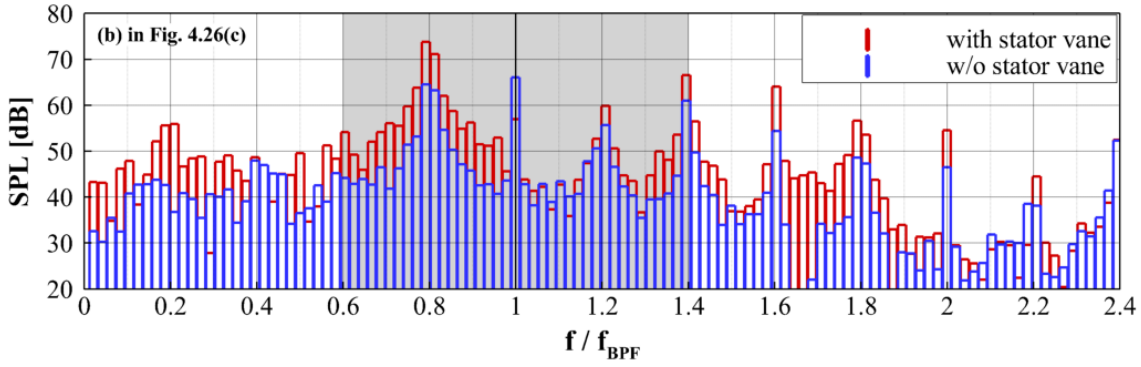

(b)

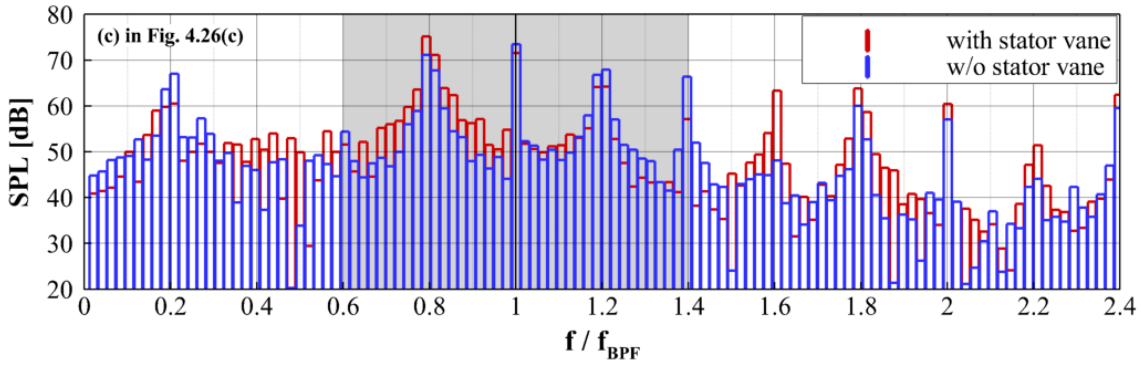

(c)

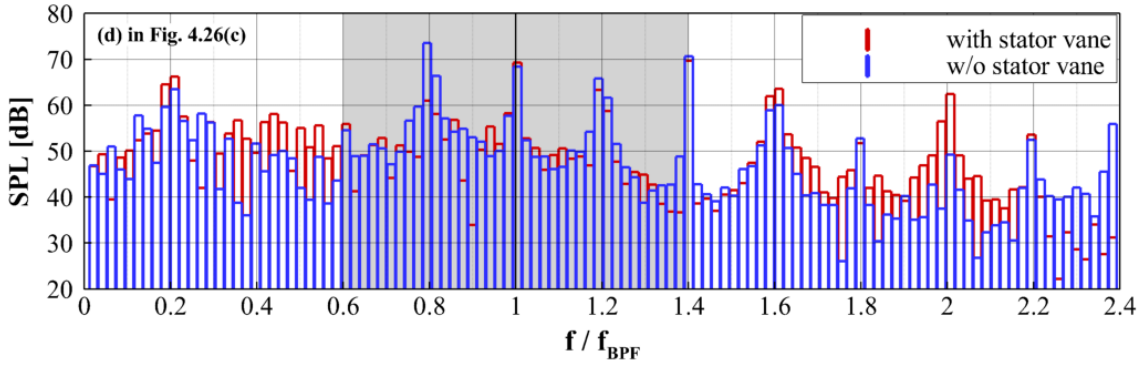

(d)

Figure 4.27: Comparison of narrowband spectra at (a) $\psi_h = 45°$, (b) $\psi_h = 135°$, (c) $\psi_h = 225°$, and (d) $\psi_h = 315°$.

4.3 Synthesis

In this chapter, a comprehensive aeroacoustic analysis of the shrouded tail rotor has been presented for a specific helicopter flight condition without any predominant inflow distortions as well as wake ingestion, namely the hovering flight. The numerical study has been conducted by means of the acoustic hybrid method combining the URANS-SST computation with the FWH porous integration surface method and in total for five fan revolutions. The employed acoustic time step size is identical to that of the CFD simulation and corresponds to the approx. $\psi_f = 1°$ per time step. The predictive capability of the employed hybrid method has also been assessed by comparing the calculated sound directivity and narrowband spectra with the measured data provided by AHD. The main findings of this chapter are as follows:

- The URANS-SST computation provides a detailed insight into the flow physics associated with the STR noise emission in the hovering condition. Among others, the rotor/stator interaction is identified as the most relevant noise generation mechanism that determines both the aerodynamic and acoustic characteristics of the anti-torque rotor in this STR operating condition. The rotor/stator interaction, in particular the rotor/shaft-faring (RSF) interaction leads to a noticeable change in surface pressure levels of the blade as well as of the shaft fairing. This consequently induces an abrupt increase in the blade load. The peak load by the RSF interaction strongly depends on the angular blade spacing to adjacent blades. Hence, the total thrust of the anti-torque rotor has distributed, rather broadband-like spectral characteristics. The temporal sequence of computed far-field sound pressure reveals a certain similarity to that of the total thrust. A significant tonal noise emission is found at the frequencies related to the uneven blade spacing.
- The influence of stator vanes on the far-field sound level is examined by comparing the reference simulation with the case where whole stator vanes, except the shaft fairing, are removed. The investigation shows that the stator vanes being installed downstream of the rotor plane significantly increase the sound pressure level of the rotational noise (max. 6 dB). This finding is, however, mainly relevant at the observer points on the fan outlet side.
- The computed and measured sound from the AHD flight test shows a satisfactory agreement. Regarding the narrowband sound spectrum, the hybrid method predicts the sound pressure level not only at relevant rotational noise but also in-between with a certain degree of accuracy. Comparing the directivity, deviations are observed between the computed and measure overall sound pressure level (OSPL). The hybrid method slightly overestimates the OSPL at the microphone potions located on the bow side of the helicopter. This is because the FWH method does not take into account the acoustic shielding effect resulting form the helicopter fuselage. There, the deviation between the computed and measured OSPL is, however, small (below 4 dB).

Chapter 5

Aerodynamic and Aeroacoustic Analysis of Forward Flight Condition

In this chapter, results of the CFD simulations and the acoustic post-processing for the high-speed flight case ($M_\infty = 0.184$) are presented and discussed. Firstly, a brief overview on both the aerodynamic and acoustic characteristics of the shrouded tail rotor (STR) under cross-flow condition will be given based on the results obtained through the reference URANS simulation using the SST turbulence model (URANS-SST). Afterwards, the impact of the main rotor downwash on the aeroacoustic properties of the STR in this flight condition will be assessed by means of the actuator disc approach. Furthermore, the influence of the turbulence model on the predictive capability of the hybrid method is evaluated by comparing the reference URANS-SST simulation to the advanced URANS formulation using the SAS method. Subsequently, extended analysis on the noise generation mechanism related to the superimposed cross flow, such as collector lip boundary layer separation and horizontal stabilizer interference, are performed. Based on the calculated sound pressure of the URANS-SST computation, a psychoacoustic investigation is also performed in the related work [34, 76], focusing on the sharpness and loudness pattern of the STR noise in the forward flight condition.

5.1 Overview on Aerodynamic and Acoustic Characteristics

5.1.1 Aerodynamic Features

The substantial difference of the aerodynamic and therefore the aeroacoustic properties of the STR in the high-speed forward flight condition compared to the hovering condition occurs due to the presence of cross flow. From the performance point of view, the cross flow is beneficial as all STR components having a certain angle of incidence to the incoming cross flow contribute to the generation of the anti-torque thrust. Indeed, the result of the URANS-SST simulation indicates that approximately 69% of the anti-torque thrust is provided by the upper vertical fin, featuring a cambered cross-sections, together with the lower bumper and the STR shroud fairing(indicated as DUC in Fig. 5.1). In addition

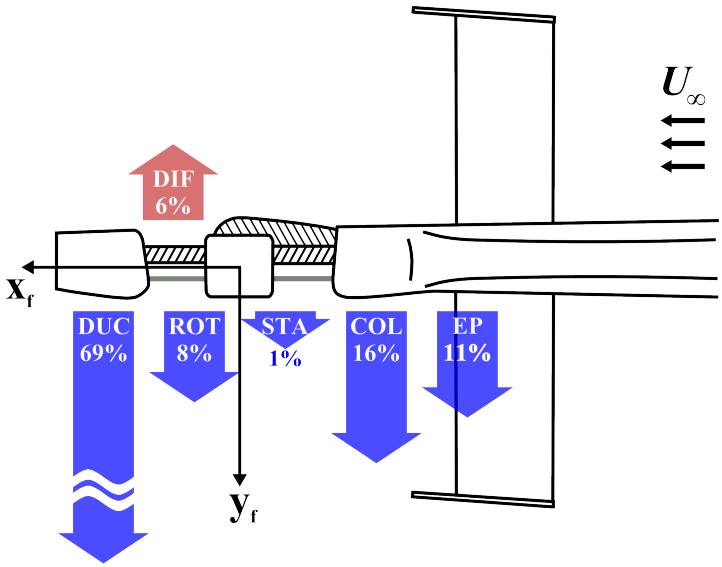

EP = End plate L + R
COL = Collector lip
STA = Stator vanes + shaft fairing + S_casing + gear box
ROT = Rotor blades + R_casing + R_hub
DUC = Shroud fairing + upper fin + bumper
DIF = Diffuser

Figure 5.1: Time-averaged lateral force $\overline{F}_y$ contribution of respective components of the shrouded tail rotor in the forward flight condition, based on the URANS simulation using the SST turbulence model.

to that, the end plates equipped at the left and right tip of the horizontal stabilizer (HS) provide around 11% of the overall anti-torque thrust (EP in Fig. 5.1). This fact allows the rotor to be markedly less loaded than in the hovering flight, and improves significantly the overall helicopter performance (less power requirement by the tail rotor). The rotor part including the rotor blades, the rotor casing and the rotor hub produces only 8% of the anti-torque thrust required in this flight condition (ROT in Fig. 5.1). Although the anti-torque rotor in the forward flight condition is comparably less loaded than in the hovering flight due to the above mentioned reasons, the noise signature of the STR in the forward flight is, however, not improved upon the hovering condition, as it will be shown in Fig. 5.7. The reason lies in the fact that in the forward flight condition, the anti-torque rotor operates under a highly complex and disturbed flow condition arising from the superimposed cross flow. Consequently, the strongly disturbed flow field both outside and inside the duct casing and their interactions with the rotating blades have a negative impact on the STR noise characteristics (see Sec. 5.4).

The flow field analysis based on the URANS-SST simulation identifies three significant flow phenomena in the forward flight condition [112, 114]: (1) the turbulent wake region of the helicopter fuselage and the horizontal stabilizer, (2) inflow distortions in the

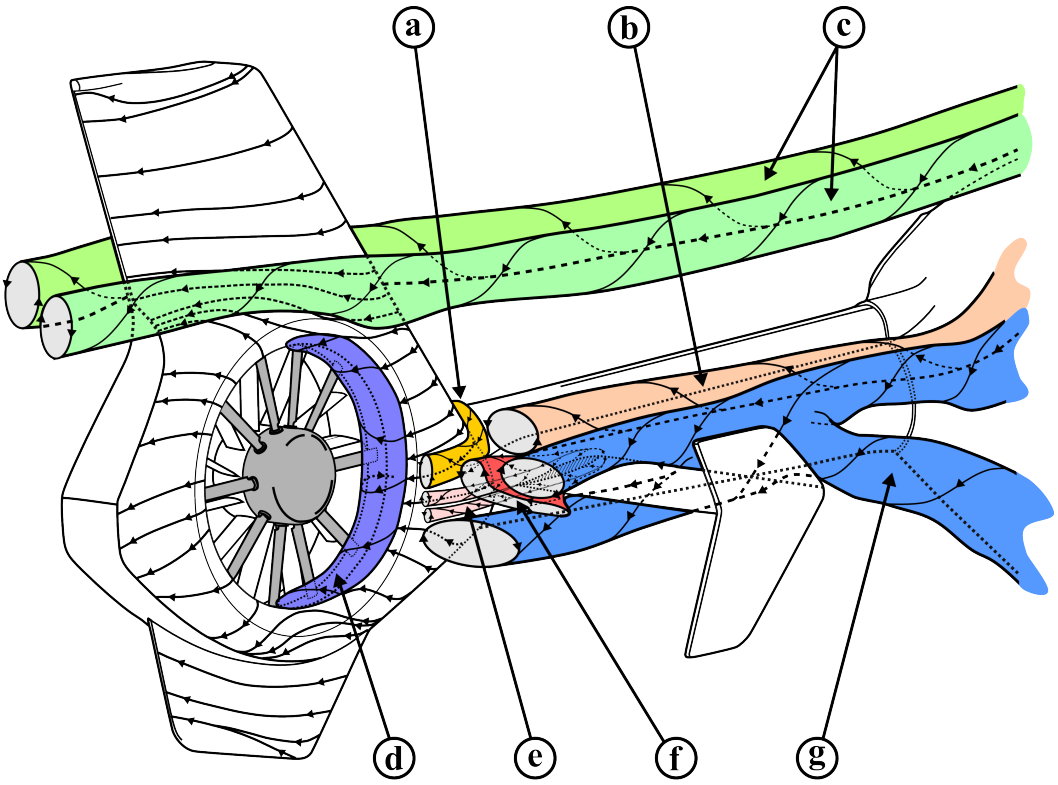

ⓐ **Horseshoe vortex (HSV)**
ⓑ **Upper fuselage vortex (UFV)**
ⓒ **Hub fairing vortex (HFV)**
ⓓ **Inlet separation bubble (ISB)**
ⓔ **Horseshoe vortex of HS (HSV-HS)**
ⓕ **HS wake + corner separation (HSW)**
ⓖ **Lower fuselage vortex (LFV)**

Figure 5.2: Sketch of flow phenomenology on the starboard side of the helicopter (STR inlet side) in the forward flight condition; the sketch is based on the time-averaged result of the URANS simulation using the SST turbulence model.

vicinity of the STR inlet, and (3) complex flow regimes inside the duct casing characterized by strongly recirculating flow fields. In the following, these phenomena will be briefly explained by means of flow phenomenology sketch, as given in Fig. 5.2.

5.1.1.1 Fuselage wake formation

The highly complex inflow to the anti-torque rotor is predominantly caused by the turbulent fuselage wake resulting from flow separation at diverse fuselage parts. The lower fuselage vortex (LFV, ⓖ in Fig. 5.2) pair resulting from the massive boundary layer separation at the lower fuselage aft-body is the most dominant counter rotating vortex pair (CVP) in the fuselage wake region. To explain the LFV formation, the time-averaged pressure coefficient $\overline{C}_p$ and time-averaged skin-friction lines on the fuselage are presented in Fig. 5.3(a). Since the lower part of the fuselage aft-body studied in this thesis features a strongly curved surface, a rapid increase in $\overline{C}_p$ is observed in the rear fuselage upsweep and

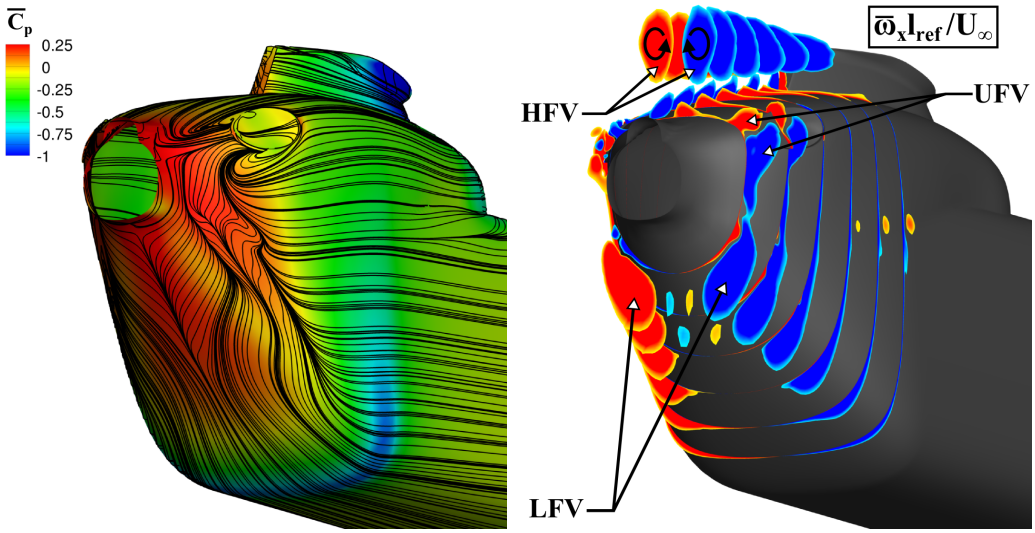

(a) (b)

Figure 5.3: Flow topology around the fuselage aft-body: (a) time-averaged pressure coefficient $\overline{C}_p$ along with time-averaged skin-friction lines, (b) time-averaged non-dimensional streamwise vorticity $\overline{\omega}_x l_{\text{ref}}/U_\infty$ on cross sectional planes downstream.

lateral tapering region. Therefore, massive boundary layer separation occurs, as clearly indicated by the pattern of the skin-friction lines in the region where the lateral tapering begins. Consequently, the detached shear layers form a counter rotating vortex pair (CVP), as indicated in Fig. 5.3(b) by means of the time-averaged non-dimensional steamwise vorticity $\overline{\omega}_x l_{\text{ref}}/U_\infty$. The LFV is convected downstream by the main flow along the tail boom and partly merged with a part of the upper fuselage vortex (UFV, (b) in Fig. 5.2). Directly upstream of the STR, the LFV interacts with the horizontal stabilizer, thus splitting into two discrete vortices on each STR side. In addition to the fuselage wake, the flow around front surface of the STR shroud (HSV, (a) in Fig. 5.2) and in the vicinity of stabilizer root (HSV-HS, (e) in Fig. 5.2) evoke horseshoe-like vortices. These vortices are ingested into the fan and lead to a significant interaction with the rotor blade (see also Sec. 5.5). The corner separation occurring at the tailboom-to-HS intersection also merges with the HS wake (HSW, (f) in Fig. 5.2) and it is ingested into the fan. Flow separation occurring at the sharp edge of the main rotor hub-fairing leads to a further CVP formation, namely the hub fairing vortex (HFV, (c) in Fig. 5.2). The HFV is also transported downstream towards the upper fin by the main flow, but it does not directly affect the inflow condition of the anti-torque rotor due to the installation position of the STR relative to the hub fairing.

5.1.1.2 Inlet flow distortions

Another noticeable flow phenomenon arising in the forward flight condition is the inlet flow distortion. In the superimposed cross-flow, the strongly curved collector lip contour leads

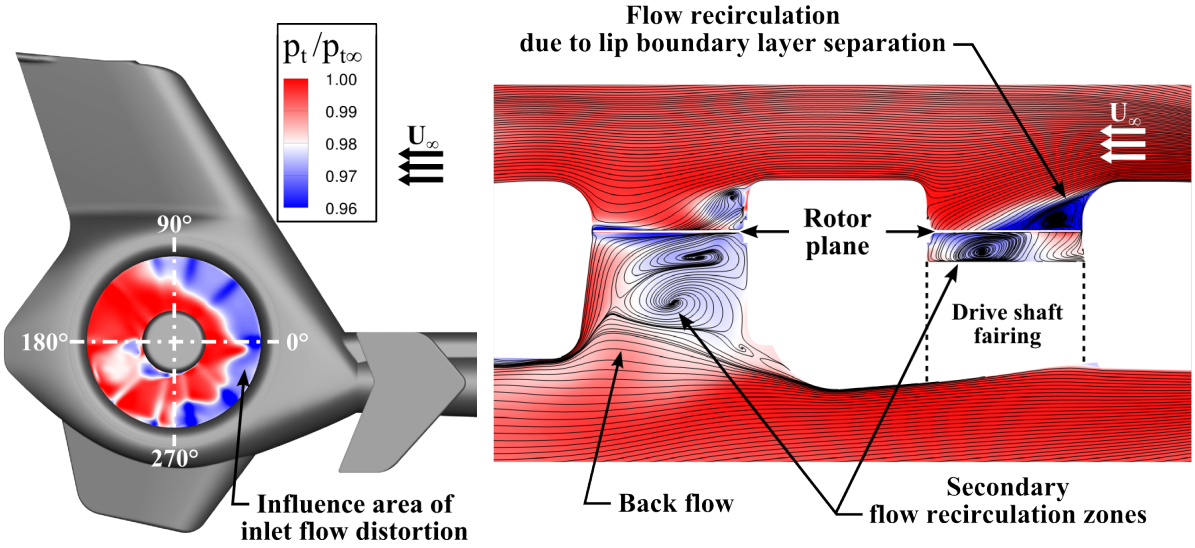

Figure 5.4: Instantaneous total pressure ratio $p_t/p_{t,\infty}$ distributions on cross-sectional planes located at (a) $y/l_{\text{ref}} = 0.04$ and (b) at $z/l_{\text{ref}} = 0$.

to an abrupt flow deflection and a boundary layer separation. Hence, a significant region of recirculating flow is provoked upstream of the rotor plane (inlet separation bubble, ISB, (d) in Fig. 5.2). To visualize it, the instantaneous distribution of total pressure ratio $p_t/p_{t,\infty}$ is presented in Fig. 5.4(a) on the plane located upstream of the rotor plane ($y/l_{\text{ref}} = 0.04$). Here, the ISB can be identified by significantly low levels of $p_t/p_{t,\infty}$. The spatial extension of the ISB along the inlet lip reaches from the advancing blade side ($270° < \Psi_f < 0°$) over the retreating blade side ($0° < \Psi_f < 120°$). This unsteady recirculating flow zone interacts with the rotating blade. Thereby, the rotor blades experience a strongly deflected incoming flow, as indicated in Fig. 5.4(b), and highly distorted blade loads. Furthermore, the interaction drives secondary flow recirculations, which are transported towards the stator row provoking there further unsteady phenomena.

5.1.1.3 Recirculating flow in the stator row

The flow field in the stator row is also characterized by a strongly recirculating flow field. It is visualized in Figs. 5.5(a) and 5.5(b) by means of the instantaneous distribution of the non-dimensional fan axial velocity $u_a/U_{70\%}$ on cross-sectional planes located downstream of the rotor plane ($y/l_{\text{ref}} = -0.057$) and in the stator row ($y/l_{\text{ref}} = -0.117$). Here, the positive y-axis is directed outward from the plane. Thus, regions with positive values are correlated with the reserve flow regions: (1) separation bubble transported from the rotor row and (2) secondary flow recirculation induced by the rotor/ISB interaction. In addition, the velocity field in the stator shows a strongly disturbed asymmetric feature. As a consequence of that, the stator vanes exhibit a strongly varying aerodynamic load depending on their azimuthal position.

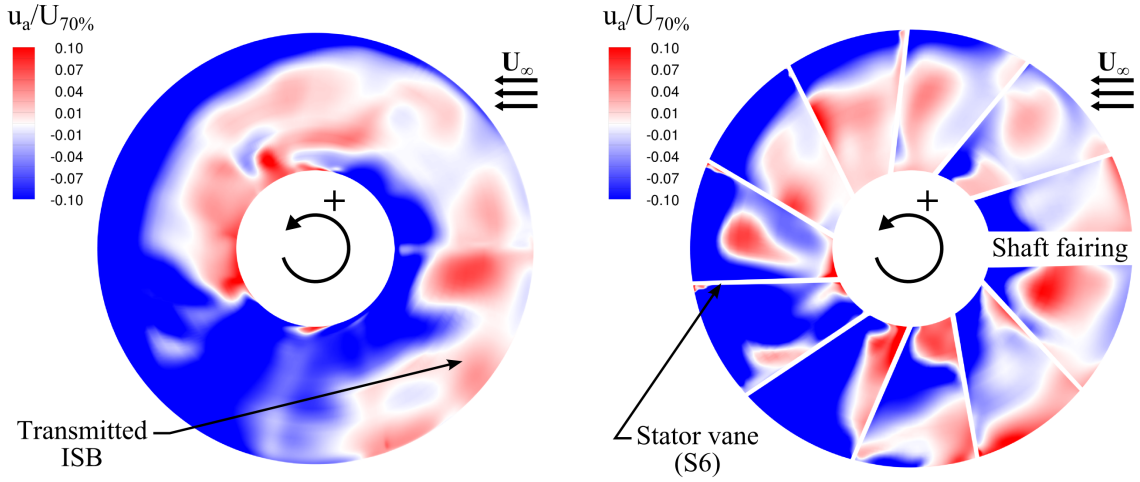

(a) (b)

Figure 5.5: Instantaneous distribution of the non-dimensional fan axial velocity $u_a/U_{70\%}$ on cross-sectional planes located (a) downstream of the rotor plane ($y/l_{\text{ref}} = -0.057$) and (b) in the stator row ($y/l_{\text{ref}} = -0.117$).

5.1.2 Acoustic Features

In Fig. 5.6, the computed far-field sound pressure $p'(t_{\text{adv}})$ of the STR in the forward flight condition is compared with that in the hovering condition. Here, both FWH results are based on the instantaneous flow quantities obtained through the URANS-SST simulations of five blade passing periods, corresponding to the time needed to reach the fluid from the fuselage aft-body to the STR by the mean velocity. The observer point is located on the inlet side of the STR with a distance of $d/l_{\text{ref}} = 10$. Note that the relative velocity of the observer point to the helicopter is zero in both flight conditions. The resulting sound pressure of the forward flight case exhibits a strong variation over five computed blade passing periods, whereas in the hovering case $p'(t_{\text{adv}})$ shows a more periodic characteristic. Likewise, the narrowband spectrum of the forward flight case differs considerably from that of the hovering case (see Fig. 5.7). Nevertheless, the tonal noise components at the dominant frequencies corresponding to the blade passing frequency ($f/f_{\text{BPF}} = 1$) and its high-order harmonics ($f/f_{\text{BPF}} = m$; $m = 2, 3$), as well as their sideband frequencies ($f/f_{\text{BPF}} = m \pm 0.2n$ with $m = 1, 2, 3$ and $n = 1, 2$) can be clearly identified in both flight conditions. Compared to the hovering case, the forward flight case yields a more broadband-like sound spectrum. This is due to the significant increase in the SPL at the frequencies within the lower and the upper sideband (e.g. $f/f_{\text{BPF}} = m \pm 0.1n$ with $m = 1, 2, 3$ and $n = 1, 3$). As it will be explained in Sec.5.4, this is mainly due to the interaction between the rotor blades and the inlet flow distortion. Moreover, the SPL at $f/f_{\text{BPF}} = 0.2$, which is the twice the rotational frequency of the anti-torque rotor, is more pronounced in the forward flight condition. Consequently, the overall SPL of the forward flight case is higher than that of the hovering case, although the anti-torque rotor is comparably less loaded than in the hovering flight.

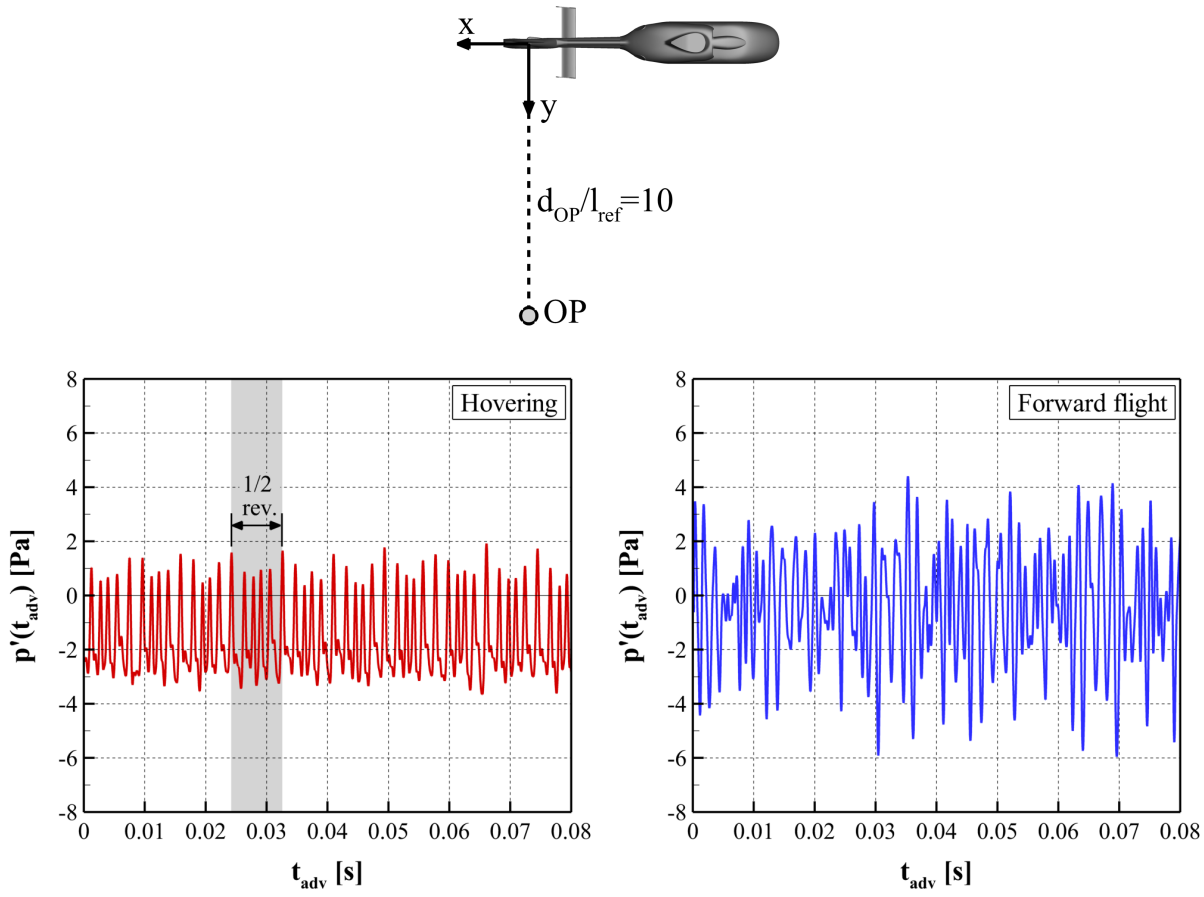

(a) (b)

Figure 5.6: Calculated sound pressure $p'(t_{\mathrm{adv}})$ for the (a) hovering and (b) forward flight case, based on the URANS simulation using the SST model. The observer point is located on the STR inlet side with a distance of $d_{\mathrm{OP}}/l_{\mathrm{ref}} = 10$.

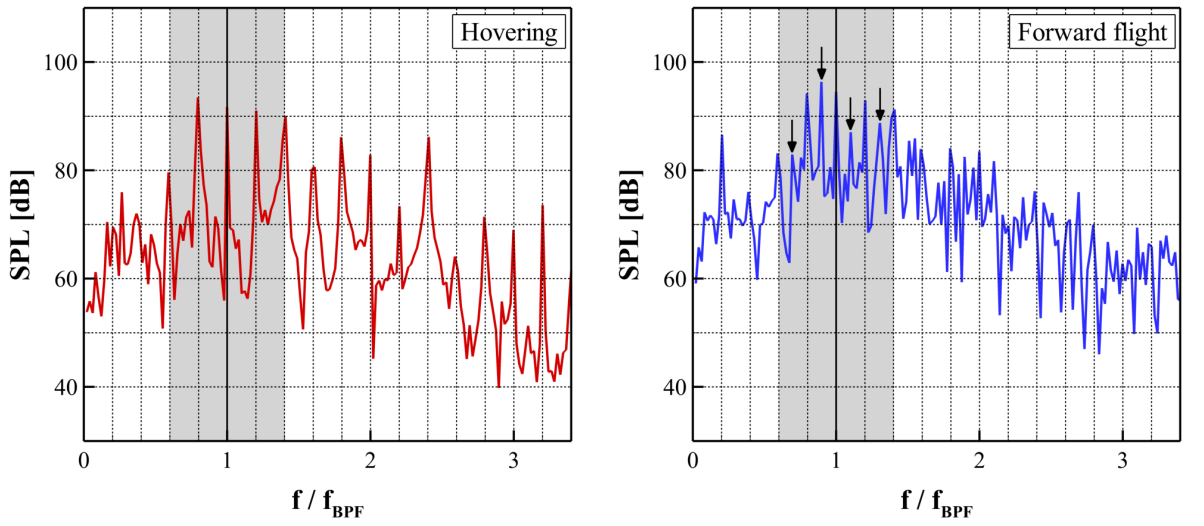

(a) (b)

Figure 5.7: Narrowband spectra for the (a) hovering and (b) forward flight case.

5.2 Assessment of Main Rotor Influence

As long as the analysis of the main rotor wake and its interaction with the helicopter components, such as the fuselage and/or the vertical tail fin, are not the main topic, the main rotor is often omitted in the CFD simulation. This is mainly due to the reason of computational costs and based on the assumption that the influence of the main rotor on the flow field around the fuselage and the shrouded tail rotor, particularly in the forward flight condition, is small. In order to confirm this assumption, this section presents the comparison between the reference simulation using the isolated fuselage including STR, but without any main rotor considerations (w/o AD), and the simulation with the main rotor effect modeled by the actuator disc approach (with AD, see Fig. 5.8).

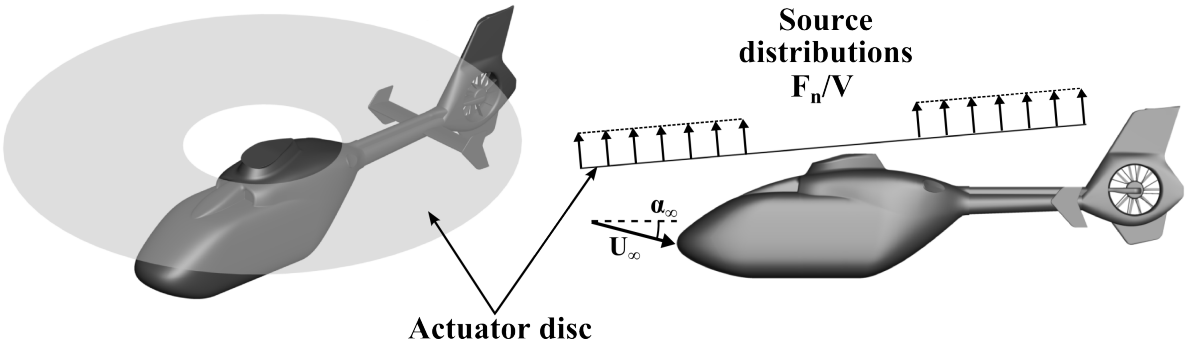

Figure 5.8: Actuator disc approach.

5.2.1 Numerical Details

In the field of helicopter aerodynamics, there are generally two approaches to model the helicopter main rotor and its impact on the surrounding flow field in the CFD simulation: (1) direct modeling of the main rotor blades and (2) approximation method of the main rotor influence by use of an actuator disc. The direct approach such as the sliding-mesh method, applied for the STR **ROTOR**–domain (see also Sec. 2.1.4.2), includes the real blade geometry to model the rotor system. This approach directly provides a comprehensive flow field around the blade by solving the Navier-Stokes equations and is thus able to provide an unsteady analysis of the blade load and the rotor wake. The direct modeling, however, increases the complexity of the CFD simulation enormously as it requires expensive grids and time-scale adaptions as well as special treatments of the interface lying between a stationary and rotating domain.

As an alternative to the direct modeling, the actuator disc method is widely used, such as for the study of rotor–fuselage interactions [22, 79]. This method employs an infinitesimally thin disc, which is inserted into the fluid domain and represents the rotor blades and their path around the helicopter main axis. On the disc, a steady-state disc load is specified, which in turn induces a steady-state velocity field underneath the disc. Because of the quasi-steady assumption and the absence of the blade geometry, the actuator disc approach can significantly reduce computational costs, compared to the direct

modeling approach. However, the drawback of the quasi-steady assumption is that the actuator disc approach can be only used as long as the accurate flow field around the blade as well as the unsteady behavior of the rotor wake are not needed to be resolved. Within the actuator disc method, there are different implementation approaches such as the boundary-condition approach and the source-term method [18]. In this thesis, the source-term method is used. Within this method, the steady-state load specified on the disc is regarded as an additional force term of the momentum equation and, in case of compressible flow, of the energy equation.

The following computational procedure is employed in this thesis, (Fig. 5.9). Firstly, the normal force component of disc load F_n is derived from the helicopter simulation code GenSim (Generic Simulation Tool) for the trimmed forward flight condition regarded in this thesis. GenSim is a helicopter aeromechanical simulation tool developed by Airbus Helicopters for the prediction of global steady and unsteady performance as well as for loads calculation. The tool is based on the blade element momentum (BEM) theory with simple analytical downwash models as well as the rigid rotor blade assumption [24]. After this step, the resulting disc load is converted to source terms S_v, defined as volumetric terms (force per unit volume), and stored in a shared library for further use in the CFD simulations (ANSYS CFX). The source terms are then invoked by the solver from the shared library at every iteration of the flow field calculations. Thereafter, the source terms are assigned by use of an in-house routine on the cell-vertices, lying within a predefined range that coincides with the range of the actuator disc ($r_1 < r < r_2$, see Fig. 5.10 and Fig. 5.11). Outside of the disc area, the source terms are set to zero. Due to the reason of numerical stability, the source strength is bisected, and the source terms

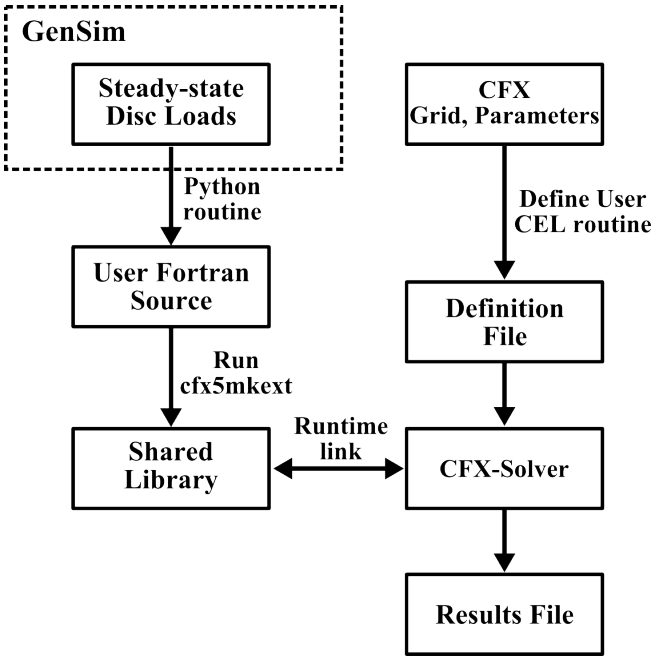

Figure 5.9: Computational procedure of the actuator disc simulation, figure modified from [8].

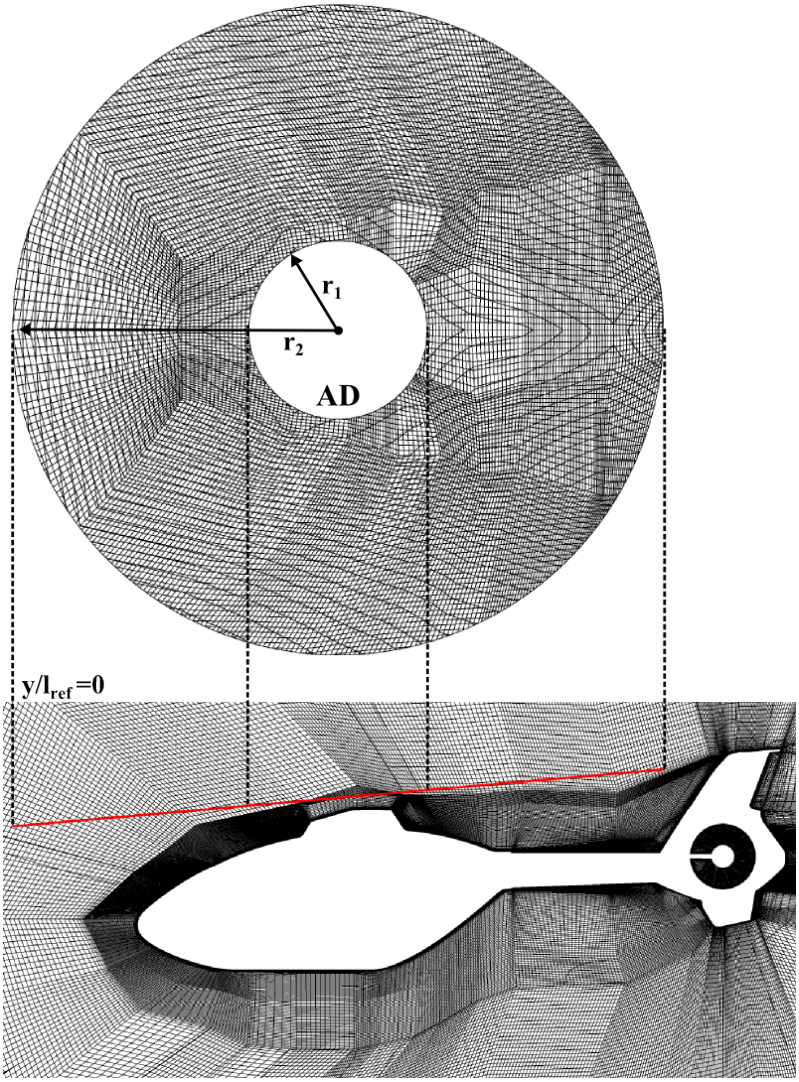

Figure 5.10: Grid topology in the vicinity of the actuator disc.

are specified on two connected cell-layers lying vertical to the helicopter main axis. The velocity field underneath the disc is then calculated by solving the momentum equation that involves the additional source terms. In Fig. 5.11, the distribution of the normal force coefficient C_n (defined in Eq. 5.1) derived by GenSim is compared with the C_n assigning on the cell-vertices. In this work, there is no feedback from the CFD solver into the aeromechanical tool GenSim (open-loop). Therefore, a possible repercussion of the fuselage flow on the inflow condition of the actuator disc is not taken into account, and thus the initial disc load is not changed during the CFD simulations. All other simulation parameters, domain boundary conditions, and numerical grids as well as flight parameters of the CFD simulation using the superimposed actuator disc are identical to those of the reference simulation case (SST turbulence model) to highlight only the effect of the main rotor.

$$C_n = \frac{F_n}{\frac{1}{2}\rho_\infty U_\infty^2 A_h} \tag{5.1}$$

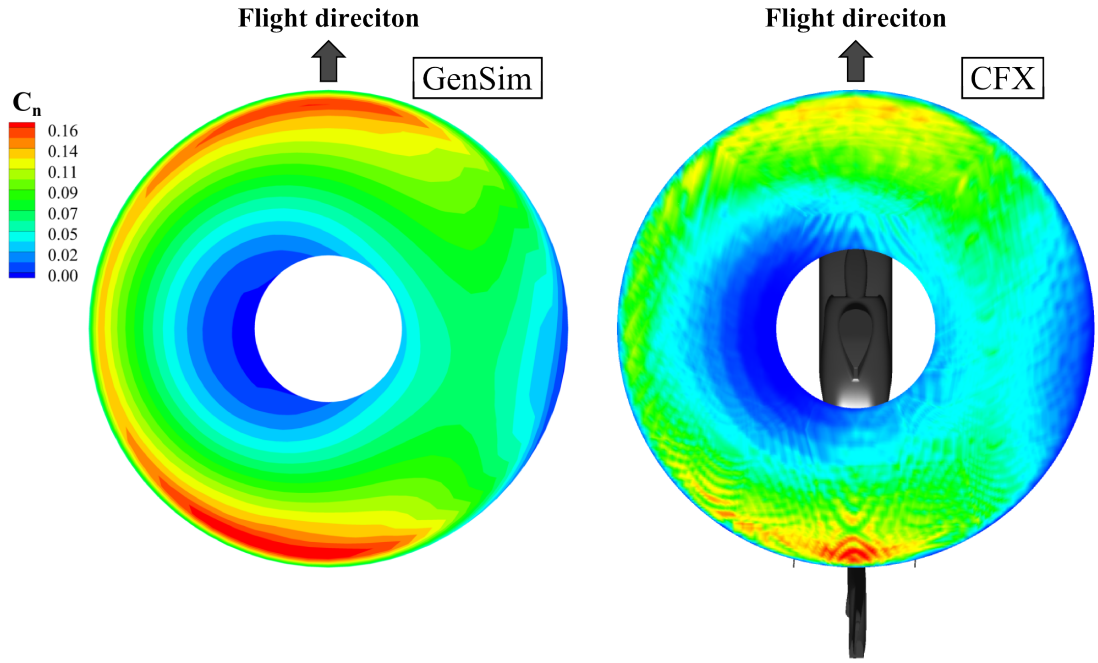

Figure 5.11: Normal distributions of force coefficient C_n of steady-state, non-uniform disc load calculated by GenSim and the source distribution in CFX.

5.2.2 Flow Field Characteristics

Global and local flow field characteristics of the reference (w/o AD) and actuator disc case (with AD) are compared by use of instantaneous and time-averaged flow quantities obtained through the URANS-SST simulations.

5.2.2.1 Fuselage wake

Figs. 5.12(a) and 5.12(b) depict time-averaged, space-filled streamlines that pass though both the rotor and stator row of the STR, for the reference and actuator disc case, respectively. The streamlines are colored by the time-averaged dimensionless velocity magnitude $\overline{U}/U_\infty$. In both cases, the streamlines around the helicopter fuselage are very similar. However, in the AD case, some streamlines, in particular the upper fuselage streamlines pass through the main rotor area and travel towards the upper part of the STR inlet. Unlike the upper streamlines, the lower fuselage streamlines, representing the lower fuselage vortex (LFV), indicate no significant influence of the downwash induced by the actuator disc.

In order to give an overview on the flow field characteristics near and far from the fuselage, Figs. 5.13(a) and 5.13(b) show the time-averaged downwash velocity $\overline{w}/U_\infty$ distribution and time-averaged streamlines at the symmetry plane ($y/l_{\text{ref}} = 0$) as well as at the cross-sectional planes located on the starboard side (STR inlet side) of the helicopter ($y/l_{\text{ref}} = 0.3$ and $y/l_{\text{ref}} = 3.6$). Considering the symmetry plane ($y/l_{\text{ref}} = 0$), both simulation cases yield a very similar flow field pattern, particularly on the lower side of the fuselage as well as in the vicinity of the STR. A slight difference in the $\overline{w}/U_\infty$ distribution is found in the front part of the upper fuselage section. In the AD case, the flow

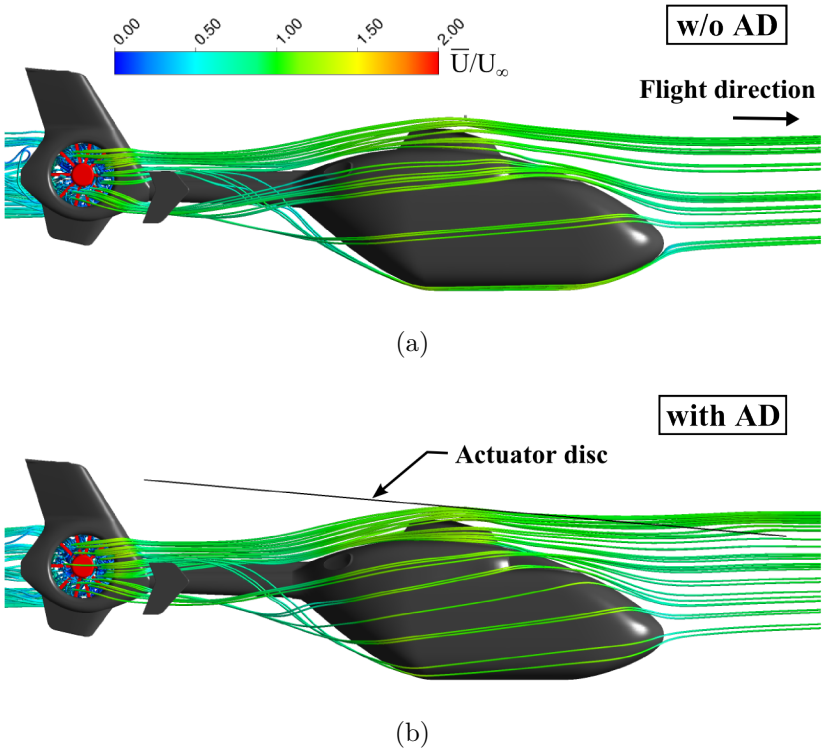

Figure 5.12: Time-averaged, space-filled streamlines colored by time-averaged dimensionless velocity magnitude $\overline{U}/U_\infty$ around the helicopter fuselage for the simulation (a) without (w/o AD) and (b) with actuator disc (with AD).

regime with positive $\overline{w}/U_\infty$ resulting from the upward deflection of the incoming flow around the fuselage nose is attenuated by the actuator disc. On the cross-sectional plane at $y/l_{\text{ref}} = 0.4$, both simulations cases show a certain similarity regarding the downwash distribution and the streamlines around the helicopter fuselage, while a slight difference is observed close to the STR. Because of the induced downwash velocity, the simulation case with AD yields a more significant distribution of the negative $\overline{w}/U_\infty$ in the vicinity of the STR inlet. On the plane at $y/l_{\text{ref}} = 3.6$, the differences in the $\overline{w}/U_\infty$ distribution and the streamlines are more pronounced than on the other planes because the actuator disc sectional load increases radially from the main rotor axis to this location (see also Fig. 5.11). However, the relatively strong downwash here has no significant impact on the STR flow field characteristics due to the large distance to the STR inlet.

Fig. 5.14 shows time-averaged skin-friction lines on the surface of the fuselage aft-body for both simulation cases to evaluate the influence of the main rotor downwash on the formation of the fuselage counter-rotating vortices. Generally, the overall pattern of the skin-friction lines is very similar in both simulation cases. Both simulation cases indicate diverse vortex formations (e.g. UFV and LFV), which result from a massive boundary layer separation at the fuselage aft-body. In the simulation case with AD, the separation foci located on the upper part (UFV) and lower part (LFV) of the aft-body close to the fuselage-tailboom-intersection are slightly shifted downward compared to the w/o AD case due to the induced downwash. The postponed vortex formation, however, does

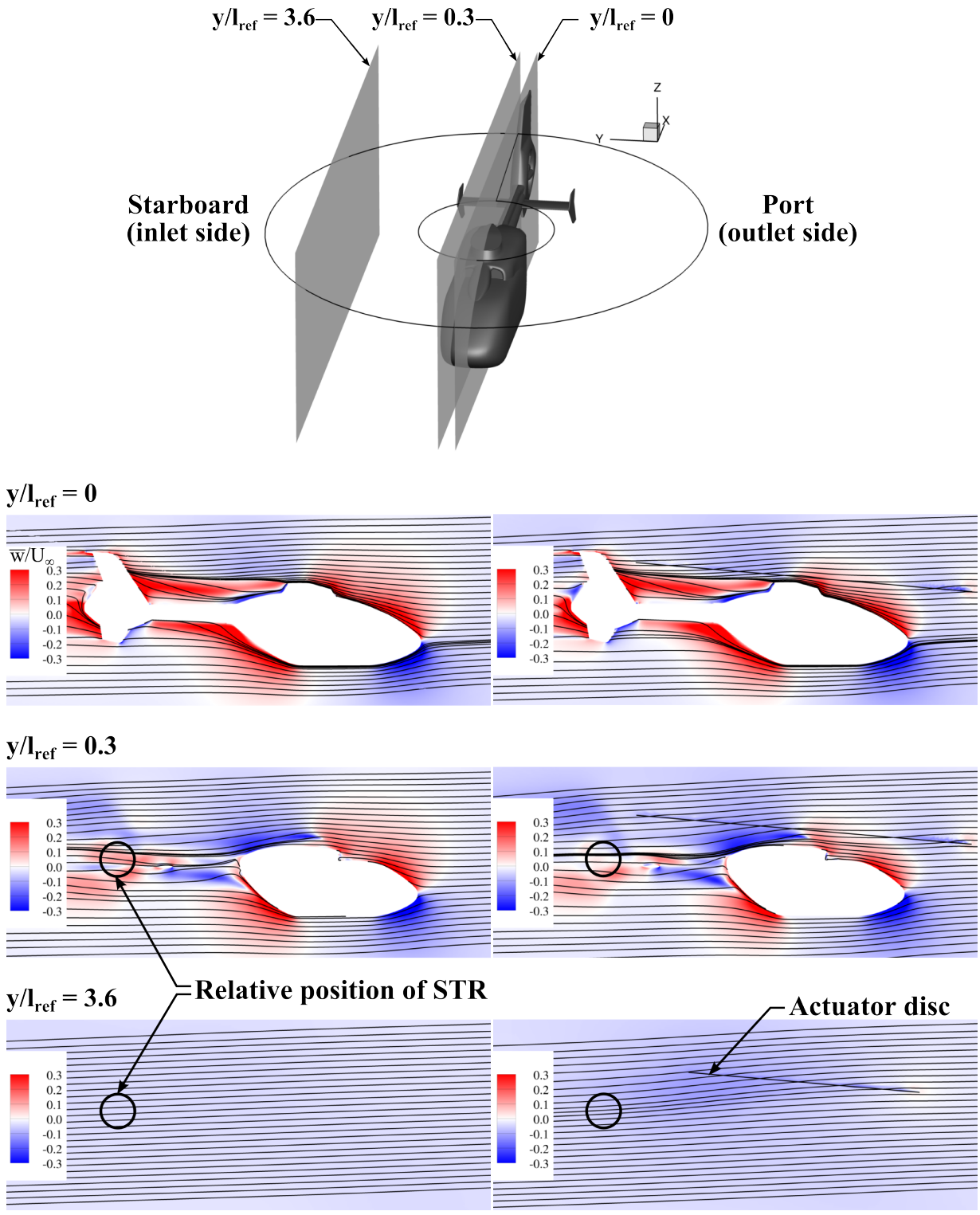

Figure 5.13: Time-averaged distributions of the downwash velocity $\overline{w}/U_\infty$ along with time-averaged streamlines at cross-sectional planes located at $y/l_{\text{ref}} = 0$, $y/l_{\text{ref}} = 0.3$, and $y/l_{\text{ref}} = 3.6$ for the simulation cases (a) without (w/o AD) and (b) with actuator disc (with AD).

not significantly change the fuselage wake topology, as indicated in Fig. 5.15 using the time-averaged distribution of non-dimensional streamwise vorticity $\overline{\omega}_x l_{\text{ref}}/U_\infty$ on diverse cross-sectional planes located downstream of the fuselage. The minor difference in the fuselage wake topology compared to the case w/o AD is that the UFV and the LFV are shifted slightly more downwards and outwards in the fuselage wake region due to the main rotor downwash (see also Fig. 5.16).

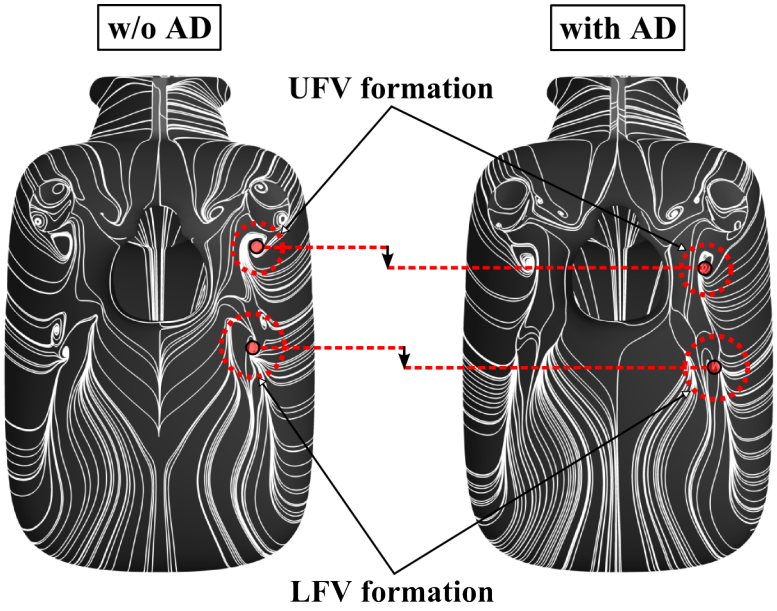

Figure 5.14: Comparison of the time-averaged skin-friction lines on the fuselage aft-part between the simulation cases without (w/o AD) and with actuator disc (with AD).

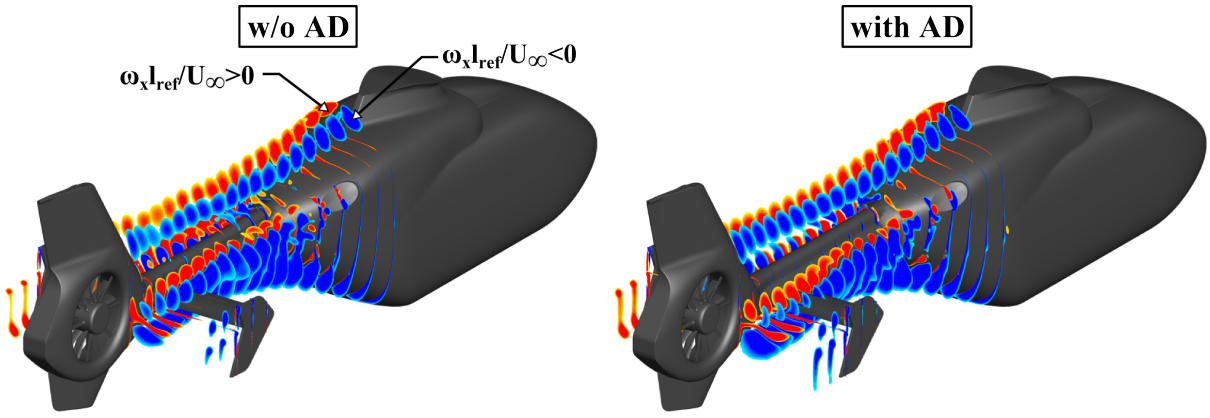

(a) (b)

Figure 5.15: Time-averaged, non-dimensional streamwise vorticity $\overline{\omega}_x l_{ref}/U_\infty$ distributions on cross-sectional planes downstream of the fuselage aft-body for the simulation cases (a) without (w/o AD) and (b) with actuator disc (with AD).

5.2.2.2 STR flow field characteristics

Both the fuselage wake and the horizontal stabilizer (HS) wake strongly influences the incoming flow to the STR, as highlighted in Figs. 5.16(a) and 5.16(b) for the w/o and with AD case, respectively. In these figures, the STR incoming flow condition is visualized by the $\overline{\omega}_x l_{\text{ref}}/U_\infty$ distribution on the plane located immediately upstream of the STR ($x/l_{\text{ref}} = -0.54$). In the AD case, the upper counter-rotating vortex pair (UFV) passes through this plane with a certain distance to the STR shroud as the induced downwash shifts these vortex tubes from the tailboom to the outside. Furthermore, the lower LFV (LLFV) is more pronounced than the upper LFV (ULFV) because the LFV is shifted more downwards by the main rotor downwash before it is split by the HS into LLFV and ULFV. In addition,further noticeable vorticity distributions are observed in the simulation case with actuator disc. These represent the main rotor tip vortices of the inner and outer edge of the actuator disc. They are formed due to the finite extension of the disc. These

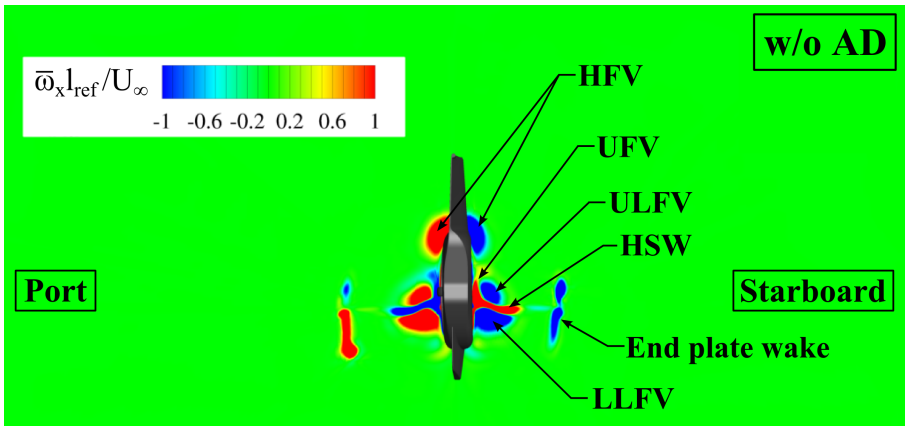

(a)

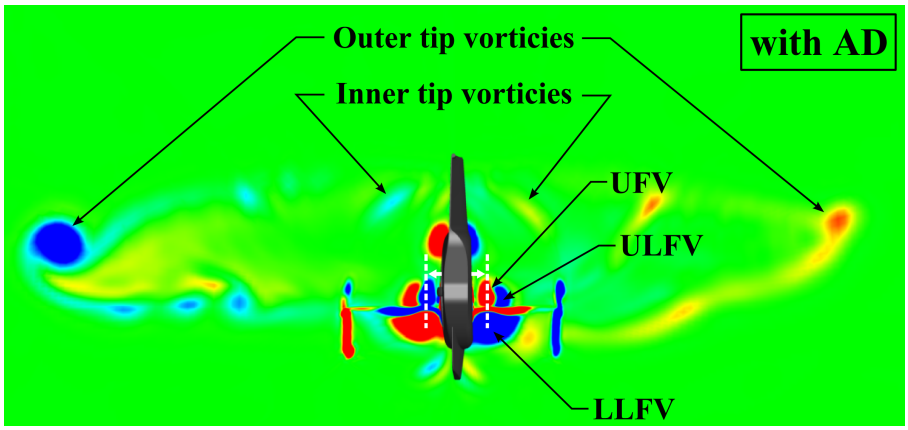

(b)

Figure 5.16: Time-averaged distributions of the non-dimensional streamwise vorticity $\overline{\omega}_x l_{\text{ref}}/U_\infty$ on the cross-sectional plane immediately upstream of the STR ($x/l_{\text{ref}} = 9.75$) for the simulation cases (a) without (w/o AD) and (b) with actuator disc (with AD).

vortices, however, have only a very limited impact on the STR flow field characteristics as the inner disc tip vortices dissipate relative rapidly in the wake region due to its low magnitude and the outer disc tip vortices are convected downstream by the main flow with a large distance to the STR.

Fig. 5.17 presents the inlet flow distortion by means of time-averaged distribution of the total pressure ratio $\overline{p}_t/p_{t,\infty}$ on the upper interface of the **ROTOR**–domain. Time-averaged skin-friction lines are also presented on the surface of the STR shroud. Regarding the skin-friction lines, there is no noticeable difference between the reference and actuator disc case. Considering $\overline{p}_t/p_{t,\infty}$, it is found that the influence region of the inlet separation bubble (ISB) provoked by the lip boundary layer separation is also similar in terms of the spatial distribution and the $\overline{p}_t/p_{t,\infty}$ magnitude in either simulation case. Apart from this region, the levels of $\overline{p}_t/p_{t,\infty}$ is slightly higher in the case with the actuator disc compared to the reference simulation case. It indicates that in the actuator disc case, the fan inflow is less disturbed by the fuselage wake as the main rotor downwash moves the LFV and UFV outwards, as already seen in Fig. 5.16(b). Nevertheless, both simulation cases yield similar rotor spectral characteristics, as indicated in Fig. 5.18 using the power spectral density analysis of load fluctuations $S_{C_y'}$ of a single blade. Both spectra clearly show the peaks, which are associated with the uneven blade spacing (e.g. $f/f_{\mathrm{BPF}} = 0.8$) and the interaction between the rotating blade and the recirculating flow zones (e.g. $0.8 < f/f_{\mathrm{BPF}} < 1$), with a similar amplitude.

According to the flow field analysis, it can be concluded that the actuator disc and the resulting downwash velocities have a relatively small impact on the fuselage as well as STR aerodynamic characteristics in the high-speed forward flight condition regarded in this thesis. The influence of the actuator disc might however be not negligible in

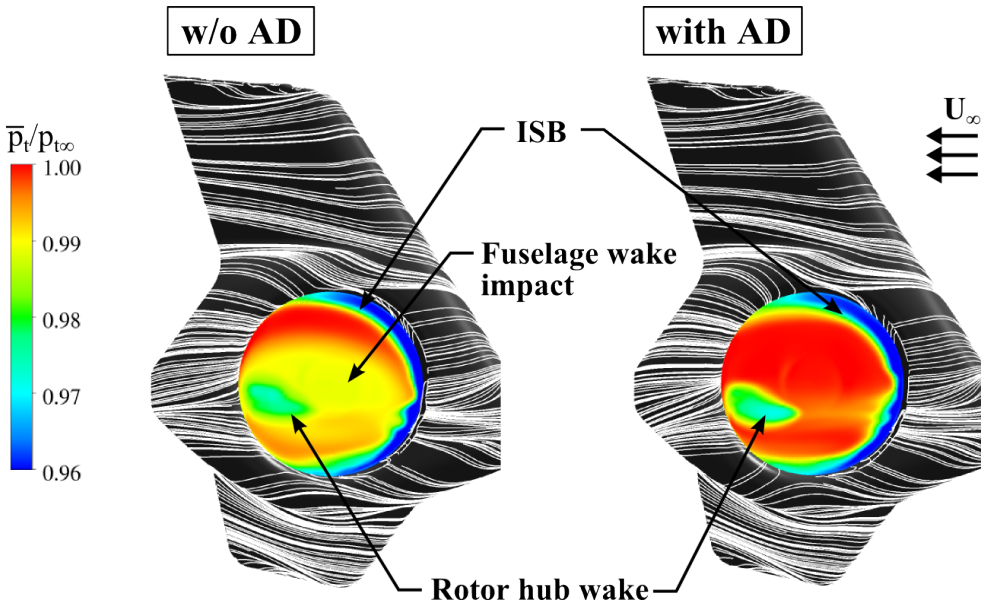

Figure 5.17: Comparison of time-averaged total pressure ratio $\overline{p}_t/p_{t,\infty}$ distributions, presented on the upper interface of the **ROTOR**–domain.

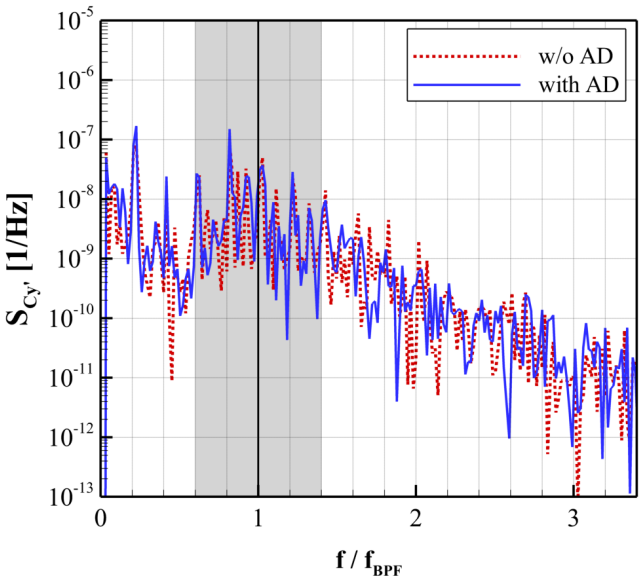

Figure 5.18: Comparison of power spectral densities of blade load fluctuations $S_{C_y'}$ between the simulation cases with and without AD.

specific flight conditions, such as the climb and approach flight, in which the rotor wake significantly interacts with other helicopter components [22, 36]

5.2.3 FWH Computations

Based on the near-field flow quantities obtained through the URANS-SST simulations, the FWH computations are performed for the isolated fuselage case (w/o AD) as well as for the actuator disc case (with AD). The acoustic time step size used is identical to the time step of the flow simulation ($\Delta t_{\mathrm{CAA}} = \Delta t_{\mathrm{CFD}} \approx \Delta\psi_f = 1°$), and the duration of the continuous time input signal corresponds to the time needed to complete computing five fan revolutions.

In Fig. 5.19, the calculated STR sound directivity of the reference case is compared with that of the case with AD. The directivity is obtained from a set of observer positions, which are located equidistantly with a radius of $d_{\mathrm{OP}}/l_{\mathrm{ref}} = 25$ from the axis of the anti-torque rotor and circumferentially distributed with an even angular distance of $\Delta\psi_h = 2.5°$. The directivity plane (xy-plane) is perpendicular to the rotor plane (yz-plane). Regarding the FWH result of the w/o AD case, the directivity of the STR exhibits a dipole-like pattern. The local maximum values of the overall sound pressure level (OSPL) are found on the port side (fan outlet side) at $\psi_h = 85°$ and starboard side (fan inlet side) at $\psi_h = 275°$ of the STR, respectively. The OSPL on the inlet side is slightly higher than on the outlet side (approx. 0.6 dB higher). The local minimum values of the OSPL are identified on the bow ($\psi_h = 20°$) and stern side ($\psi_h = 160°$) of the STR, respectively. As already mentioned in Sec. 4.23, this is due to the acoustic shielding of the STR noise, mainly caused by the STR duct casing. In this work, it is implicitly taken into account by applying two disconnected control surfaces located on the inlet and outlet opening of the STR. Generally,

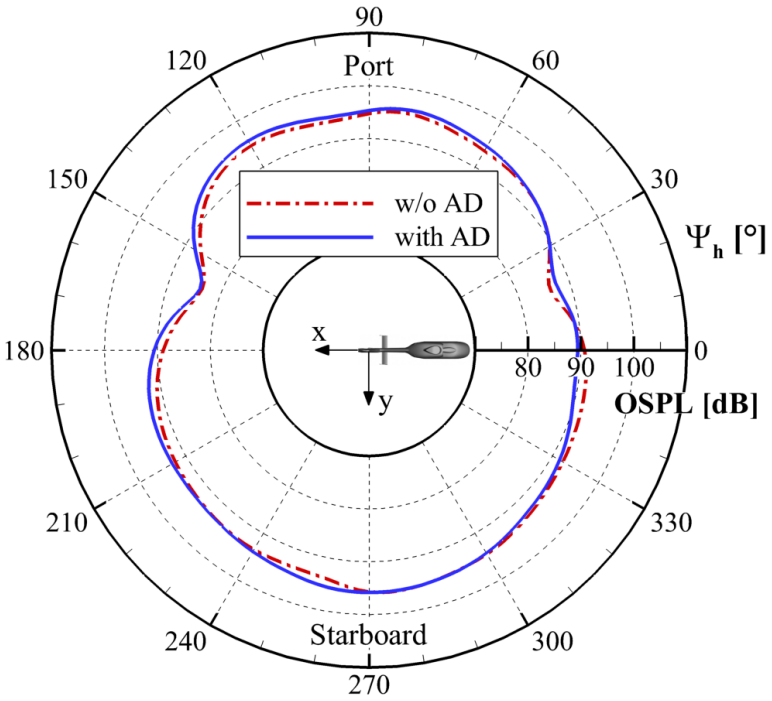

Figure 5.19: Comparison of the OSPL directivities pattern between the simulation cases w/o and with AD.

the AD case provides a nearly identical directivity pattern. The relative difference in the OSPL with respect to the reference case ($\Delta\text{OSPL} = \text{OSPL}_{\text{with}} - \text{OSPL}_{\text{w/o}}$) is 1.5 dB in the azimuth range of $140° < \psi_h < 150°$ (port side), 1.7 dB in the range of $175° < \psi_h < 190°$ (stern side), and 2 dB in the range of $345° < \psi_h < 355°$ (starboard side).

In Fig. 5.20, the narrowband spectra of both simulation cases are compared at four selected observer positions located on the port side at $\psi_h = 45°$ and $\psi_h = 135°$ as well as on the starboard side at $\psi_h = 225°$ and $\psi_h = 315°$. The comparison indicates that the isolated fuselage case and the actuator disc case predict very similar noise characteristics. As expected, both simulation cases yield significant tonal noise components at twice of the rotational frequency of the fan ($f/f_{\text{BPF}} = 0.2$), at the BPF ($f/f_{\text{BPF}} = 1$), and at its lower ($f/f_{\text{BPF}} = 1 - 0.2n$; $n = 1, 2$) as well as at upper sideband frequencies ($f/f_{\text{BPF}} = 1 + 0.2n$; $n = 1, 2$). Differences in the SPL at these dominant discrete components are relatively small. For instance, the SPL difference at $f/f_{\text{BPF}} = 0.6$, $f/f_{\text{BPF}} = 0.8$, and $f/f_{\text{BPF}} = 1$ for the observer point at $\psi_h = 45°$ is below 1 dB.

According to the analysis of the directivity as well as the narrowband spectra, it can be concluded that the induced downwash velocity of the main rotor, modeled by the actuator disc approach, has a very small impact on the acoustic characteristics of the STR in the high-speed forward flight condition. Therefore, the analysis in the following sections is performed based on the reference configuration, i.e. isolate fuselage with STR and without actuator disc, to reduce the modeling complexity of the CFD simulations.

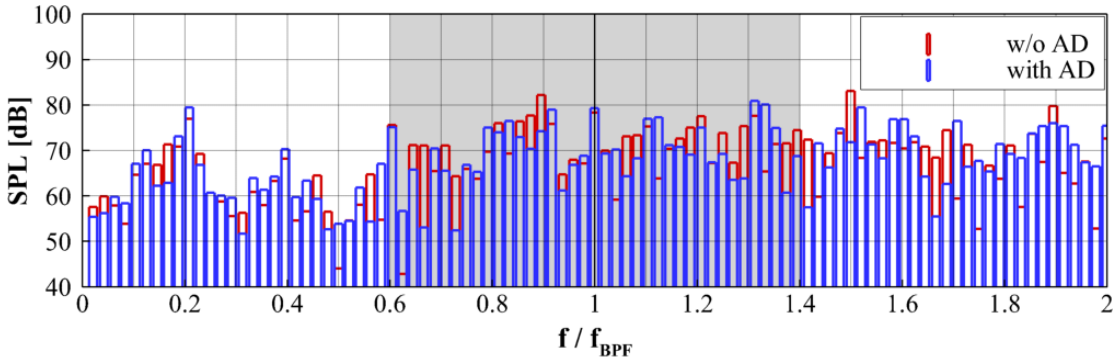

(a)

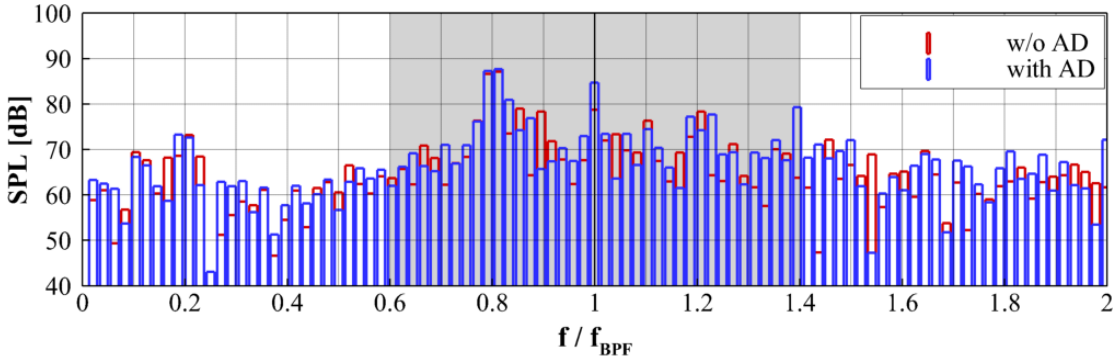

(b)

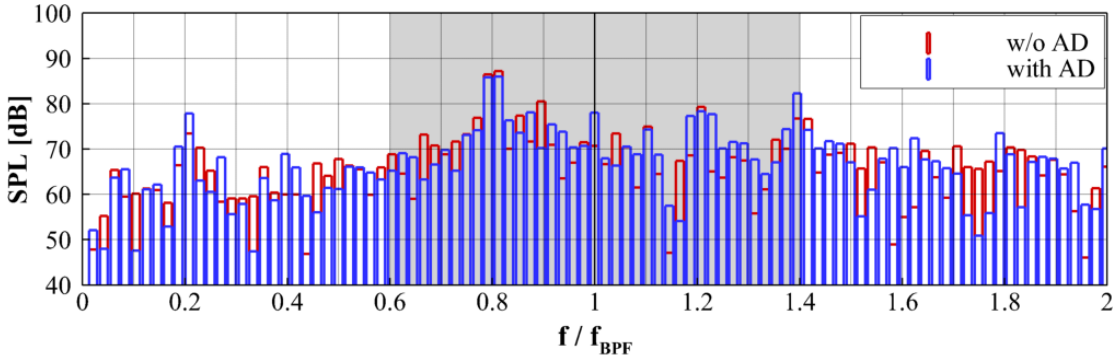

(c)

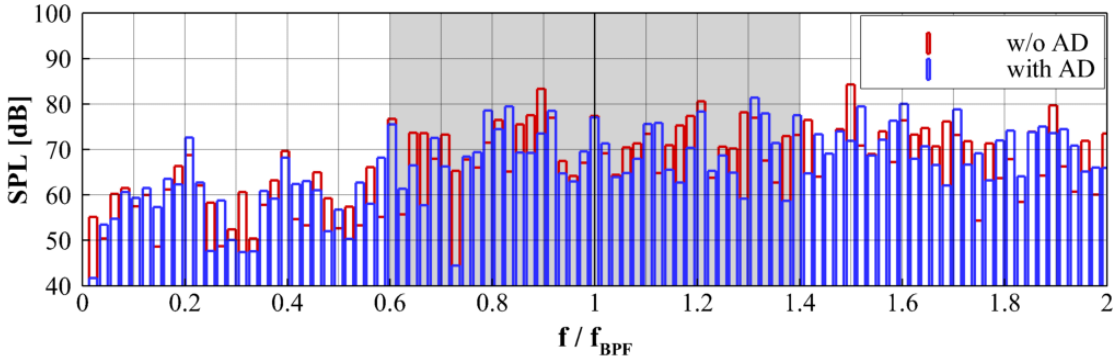

(d)

Figure 5.20: Comparison of the narrowband spectra at observer points located at (a) $\psi_h = 45°$, (b) $\psi_h = 135°$, (c) $\psi_h = 225°$, and (d) $\psi_h = 315°$ between the simulation cases w/o and with AD.

5.3 Influence of Turbulence Modeling

Regardless of which approach is employed to the far-field sound prediction (e.g. Direct Numerical Simulation (DNS) or hybrid method), an accurate capturing of all relevant acoustic sources is of overriding importance regarding the accuracy of the calculated far-field sound pressure. To achieve a high level of accuracy for computed sound levels, it is essential that the CFD has the capability to resolve as much as possible turbulent fluctuations in the acoustic source region. The unsteady RANS approach in combination with classical turbulence modeling such as the SST model, however, can provide only limited spectral contents of the unsteady flow because of its averaging manner and resulting highly dissipative nature. In order to overcome this problem and consequently to enhance the accuracy of the predicted far-field sound pressure, it is necessary to employ a less dissipative, high-order turbulence model such as the scale-adaptive simulation (SAS) method. The SAS method has the ability to capture flow-induced sound sources with an enhanced turbulence spectrum. In this context, this section focuses on the assessment of the influence of the scale-resolving capturing of the aerodynamic sound sources on the far-field noise prediction, particularly in the application of such complex configuration and the related flow field [106–108, 110, 111]. Both aerodynamic and acoustic results based on the URANS method using the SST turbulence model (URANS-SST) are compared with the findings from the scale-resolving computation using the SAS approach (URANS-SAS). Furthermore, the predictive capability of the hybrid approach is evaluated through comparison with the data obtained from the flight measurement campaigns conducted by the German Aerospace Center (Deutsches Zentrum für Luft- und Raumfahrt: DLR).

5.3.1 Flow Field Analysis

In the following, the resulting flow fields of the URANS-SST and URANS-SAS are compared by means of the unsteady and time-averaged flow quantities.

5.3.1.1 Fuselage wake

In Figs. 5.21(a) and 5.21(b), coherent vortical structures around the helicopter configuration are visualized by means of isosurfaces of the Q-criterion (defined in Eq. 5.2 with vorticity tensor Ω_{ij} and strain-rate tensor S_{ij} [42, 52]) for the URANS-SST and URANS-SAS, respectively. In addition, the isosurfaces are colored with the eddy viscosity ratio μ_t/μ. The eddy viscosity ratio denotes the ratio of the modeled turbulent viscosity μ_t, that is a measure of the numerical dissipation, to the molecular dynamic viscosity μ, keeping constant and identical in each simulation case. Hence, a lower value of μ_t/μ indicates that the computed flow field undergoes less numerical dissipation with respect to the turbulence modeling.

$$Q = \frac{1}{2}\left(|\Omega|^2 - |S|^2\right) > 0; \quad \Omega_{ij} = \frac{1}{2}\left(\frac{\partial u_i}{\partial x_j} - \frac{\partial u_j}{\partial x_i}\right); \quad S_{ij} = \frac{1}{2}\left(\frac{\partial u_i}{\partial x_j} + \frac{\partial u_j}{\partial x_i}\right) \tag{5.2}$$

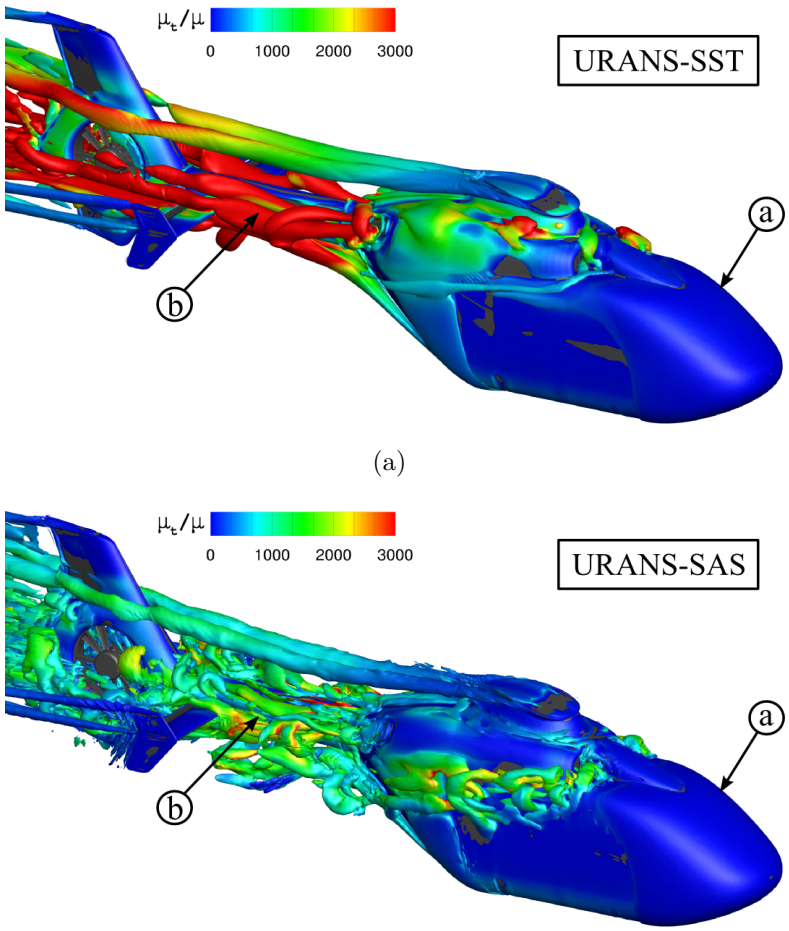

Figure 5.21: Instantaneous vortical structures around the helicopter configuration in the high-speed forward flight condition, visualized by isosurfaces of $Q = 2000$ $1/s^2$ for URANS simulations using (a) the SST turbulence model (URANS-SST) and (b) the SAS approach (URANS-SAS); the color of the isosurfaces represent the eddy viscosity ratio μ_t/μ.

Regarding the front part of the helicopter fuselage (ⓐ in Fig. 5.21), both the form of the isosurfaces and the level of μ_t/μ in the URNAS-SAS case are nearly identical to those in the URANS-SST case. This is attributed to the fact that in this relatively stable flow regime, characterized by an attached boundary layer, the solver activates the RANS mode in combination with the SST model instead of using the SAS formulation ($Q_{\mathrm{SAS}} = 0$, see Eq. 2.3). On the contrary, a noticeable dependency of the flow field on the turbulence model is observed in the region of the fuselage wake (ⓑ in Fig. 5.21), where the flow field exhibits strong unsteadiness resulting from the massive boundary layer separation at the fuselage aft-body. In this unstable flow regime, more small-scale vortices are observed in the case of URNAS-SAS since the solver switches to the unsteady mode using the SAS formulation. The URANS-SST predicts the same flow regime with comparably large-scale and smoothed turbulent structures. The difference between both turbulence models in the fuselage wake is referred to the significantly large difference in μ_t/μ, as indicated in Fig.

5.22(a) by means of the time-averaged μ_t/μ distribution. As mentioned in the previous section 2.1.4.1, the SAS approach diminishes the turbulent viscosity in a certain flow regime where sufficient flow unsteadiness is detected by using the von Kármán length scale $L_{\nu K}$. As a result, the SAS approach has the capability to provide a less dissipative flow field involving more small-scale vortices. To visualized it, the time-averaged, non-dimensional

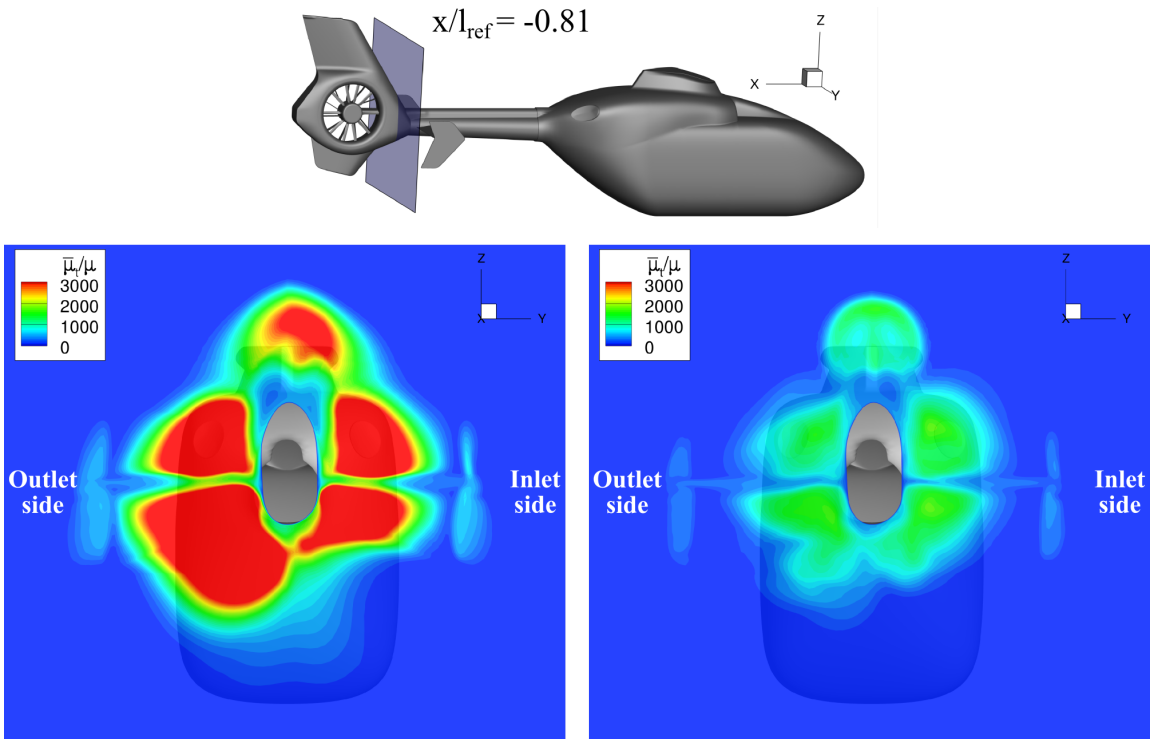

(a)

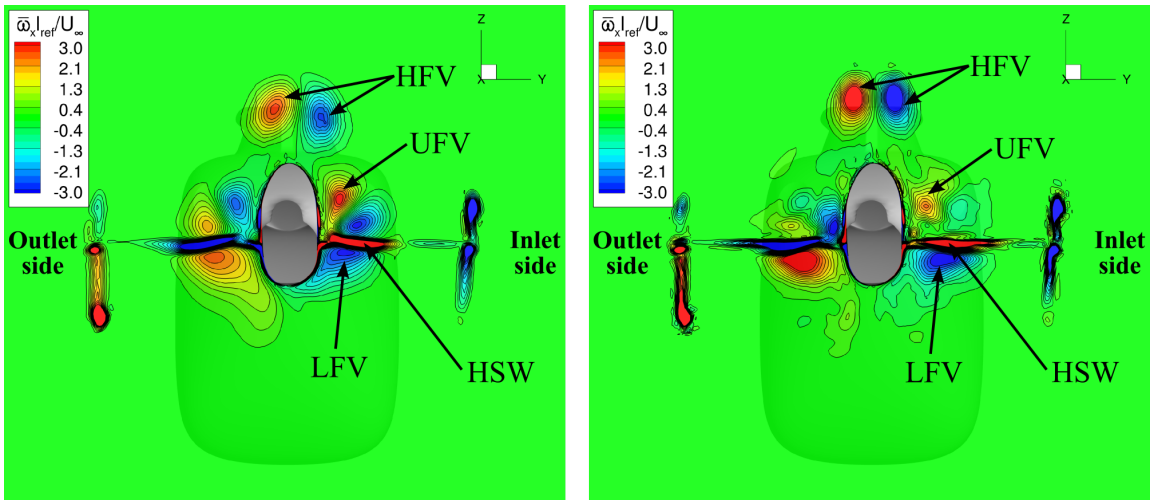

(b)

Figure 5.22: Comparison between URANS-SST and URNAS-SAS computations on the vertical cross-sectional plane ($x/l_{\text{ref}} = -0.81$): (a) time-averaged eddy viscosity ratio $\overline{\mu}_t/\mu$ and (b) time-averaged, non-dimensional streamwise vorticity $\overline{\omega}_x l_{\text{ref}}/U_\infty$.

streamwise vorticity $\overline{\omega}_x l_{\text{ref}}/U_\infty$ is given on the cross-sectional plane located upstream of the STR ($x/l_{\text{ref}} = -0.81$) (see Fig. 5.22(b)). Generally, the resulting flow field is similar to a certain extent for both turbulence models. It involves all relevant fuselage vortices (e.g. UFV and LFV) as well as the horizontal stabilizer wake (HSW). The URANS-SAS, however, reveals a more perturbed vorticity distribution as the SAS formulation splits the large-scale flow structures detected in the fuselage wake as well as in the HS wake into the small-scale eddies.

5.3.1.2 Rotor flow field characteristics

The effect of the turbulence model on the resulting flow field in the vicinity of the STR inlet is analyzed in Fig. 5.23(a) by means of isosurfaces of $Q = 1.2 \times 10^5$ 1/s^2. Here, a relatively

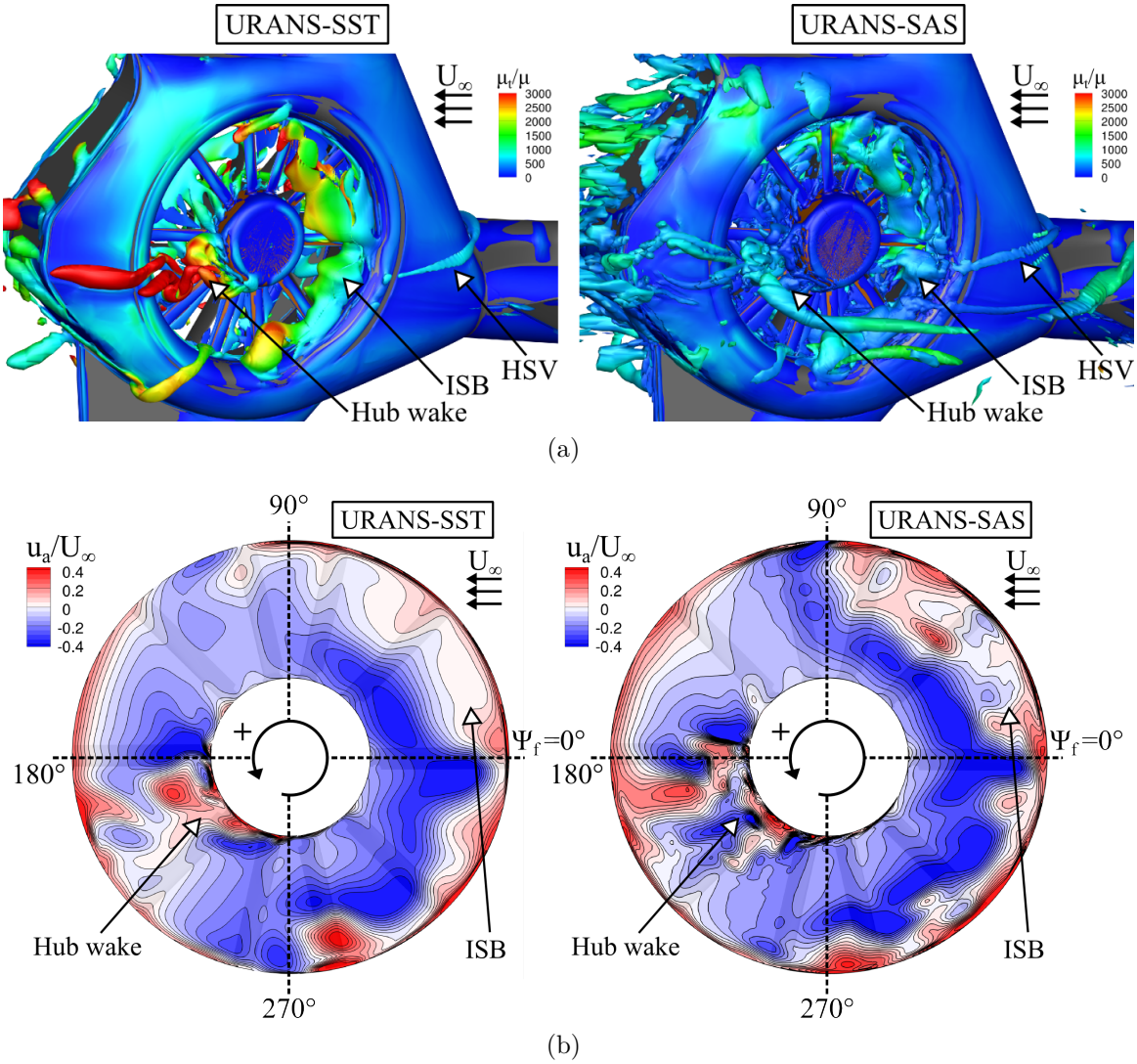

Figure 5.23: Comparison of (a) instantaneous vortical structures in the vicinity of the fan inlet visualized by isosurfaces of $Q = 1.2 \times 10^5$ 1/s^2 and (b) instantaneous fan axial velocity ratio u_a/U_∞ distribution at $y/l_{\text{ref}} = 0.04$ between URANS-SST and URANS-SAS computations.

high value of Q was chosen, so that the fuselage wake are preferably not visualized. Both the URANS-SST and URANS-SAS predict significant vortical structures in the vicinity of the STR inlet. These denote the inlet flow distortions caused by the flow separation at the collector lip as well as on the lateral surface of the rotor hub. As already observed in the fuselage wake, the SAS approach yields smaller vortices and remarkably lower values of μ_t/μ above the rotor plane, highlighting that the inflow to the anti-torque rotor has a more disturbed property. The instantaneous distribution of the fan axial velocity ratio u_a/U_∞ on the cross-sectional plane located above the rotor plane ($l_{\text{ref}} = 0.04$) supports this finding (Fig. 5.23(b)). Note that the positive y-axis is directed outward from the plane regarded here, and therefore, the region with positive values of u_a/U_∞ represents a reserve flow zone. Comparing the u_a/U_∞ distribution between URANS-SST and URANS-SAS, the general flow topology above the rotor plane is similar for both simulation cases. The URANS-SAS, however, indicates diverse small-scale recirculating flow zones within the inlet separation bubble (ISB). With the URANS-SST, it is predicted rather as a single continuous flow zone. The difference is more pronounced on the retreating blade side, particularly in the range of $0° < \psi_f < 90°$ (first quarter of the STR inlet). In addition to that, the ingested rotor-hub wake leads to a more perturbed u_a/U_∞ distribution with the scale-resolving turbulence model. Thus, a more complicated interaction with the rotor blade is expected at this fan azimuth range (see also Fig. 5.25(a)).

The inflow distortions considerably alter the blade aerodynamic characteristics, as it will be discussed in more detail in the following section (see Sec. 5.4). In Fig. 5.24, the surface pressure fluctuations p'_s at blade passing frequency ($f/f_{\text{BPF}} = 1$) are given on the blade upper surface for both turbulence models. The result of the URANS-SST shows that the blade surface experiences strong pressure fluctuations from 50% blade span to the blade tip. This is due to the interaction with the ISB (see also Fig. 5.53). With the

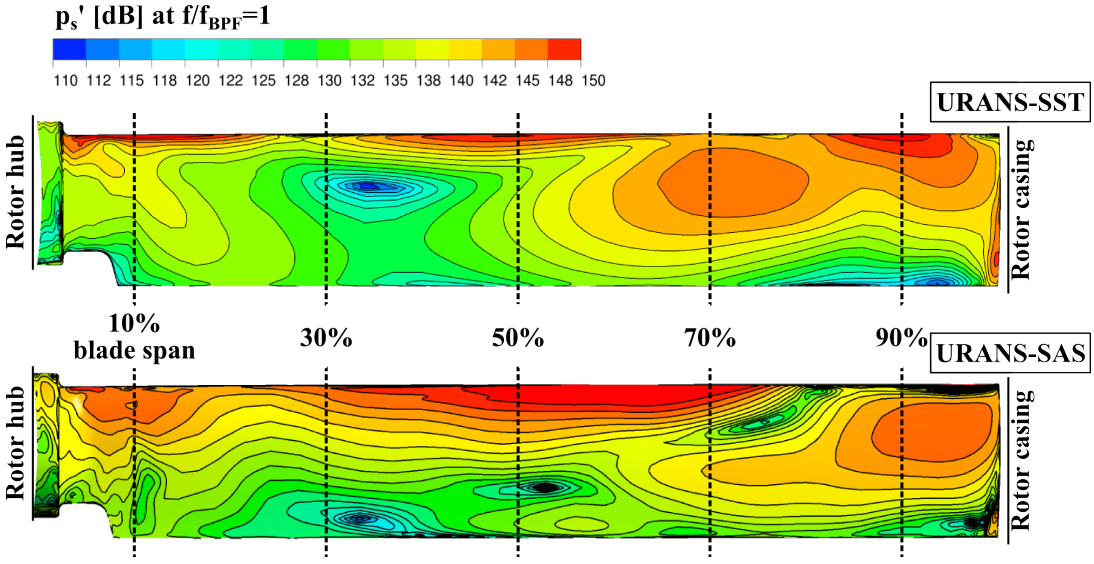

Figure 5.24: Surface pressure fluctuation p'_s at $f/f_{\text{BPF}} = 1$, presented on the blade upper surface for URANS-SST and URANS-SAS computations.

SAS approach, this region of strong p'_s is shifted more towards the blade tip region. In addition, the p'_s distribution in the vicinity of the blade leading edge between 30% and 50% blade span is more significant in the URANS-SAS case. The p'_s distribution in the vicinity of the blade root is due to the flow separation at the blade root as well as on the hub surface, and is more pronounced in the case of the SAS approach.

As expected from the surface pressure distribution, the blades experience a different load depending on the turbulence model applied. For this reason, the time dependent behavior of the blade load C_y is given in Fig. 5.25(a) as a function of the blade passing

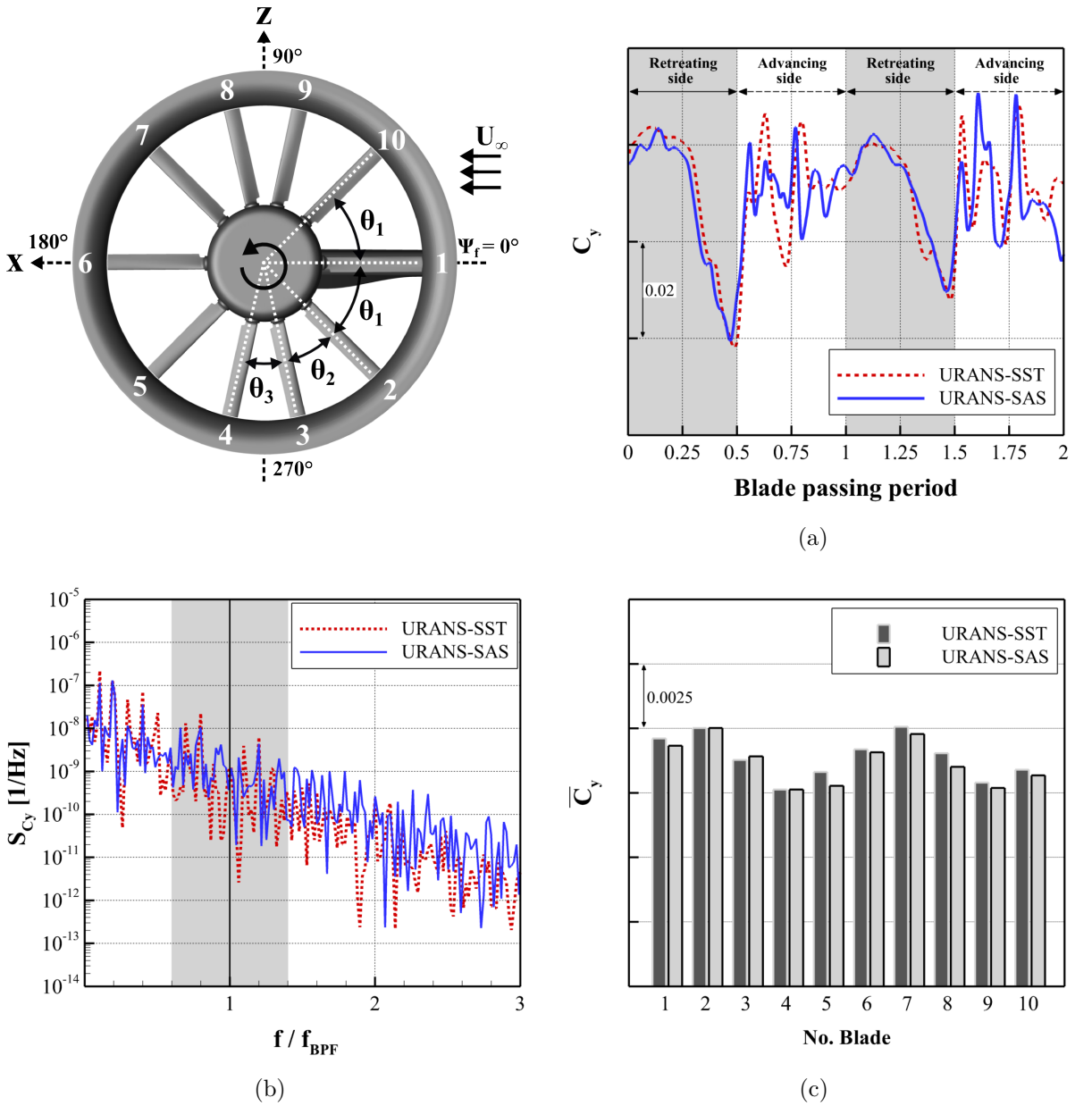

Figure 5.25: Comparison of (a) load history of the blade R2, (b) power spectral densities of blade load S_{C_y}, and (c) time-averaged blade load breakout $\overline{C}_y$ between URANS-SST and URANS-SAS computations.

period (BPP) of the blade R2 for both simulation cases. The blade R2 has the largest angular distance to adjacent blades and is therefore less influenced by the adjacent blades. The given blade load was obtained through summation of all chordwise sectional loads. As observed in Fig. 5.25(a), both simulation cases indicate that the blade R2 undergoes a highly fluctuating aerodynamic force within one blade passing period. This is caused, on the one hand, by the relative motion of the blade to the incoming flow (advancing and retreating blade), and on the other hand, by the interaction with the inflow distortions (see also Sec. 5.4) as well as with the ingested fuselage wake (see also Sec. 5.5). Generally, the unsteady blade load in the URANS-SAS case tends to provides more fluctuations when the blade passes through the lip separation bubble ($0 < \mathrm{BPP} < 0.25$ and $0.75 < \mathrm{BPP} < 1$) as well as the region of the rotor-hub wake ($0.5 < \mathrm{BPP} < 0.75$). As a result, the URANS-SAS yields a noticeable increase in the power spectral density of the blade load S_{C_y} at relatively high frequencies beyond $f/f_{\mathrm{BPF}} = 1.2$ (Fig. 5.25(b)). Since a blade experiencing fluctuations in the aerodynamic forces is known as one of the main noise sources of a fan configuration, the finding above can be interpreted in such a way that the SAS approach provide an enhanced far-field sound pressure level at these frequencies. The influence of the uneven blade spacing on the blade load is also well predicted by both turbulence models, as indicated in Fig. 5.25(c): blade R2 and R7 generate the highest time-averaged blade load $\overline{C}_y$, while blade R4 and R9 produces the lowest $\overline{C}_y$, as already observed in the hovering condition (cf. Fig. 4.15). Generally, higher $\overline{C}_y$ levels are observed in the case of URANS-SST compared to the URANS-SAS, but the differences are negligibly small (e.g. $\Delta\overline{C}_y = -3\%$ at blade R7).

In the following, the spectral characteristics of the pressure field above the rotor plane are studied (see Fig. 5.26). The input time signal of C_p' was acquired for five blade passing periods at stationary monitor points located above the rotor plane ($l_{\mathrm{ref}} = 0.04$) at 70% ($0.7r$) and 90% ($0.9r$) of the fan radius, respectively, and evenly distributed in the circumferential direction ($\Delta\psi_f = 10°$). The data obtained give valuable information about the pressure disturbances, which result not only from the periodic impingement of the rotor potential field but also from the inflow distortions and their interactions with the rotating blades. Therefore, both simulation cases yield a significant increase in the power spectral densities $S_{C_p'}$ at the frequencies related to the fan rotation as well as to the uneven blade spacing (e.g. $f/f_{\mathrm{BPF}} = 1 \pm 0.2n$ with $n = 1, 2$). Furthermore, this increase is more significant in the fan azimuth range coinciding with the circumferential stretching of the inlet separation bubble ($0° < \psi_f < 90°$: retreating blade side; $270° < \psi_f < 360°$: advancing blade side) as well as with the rotor wake ($180° < \psi_f < 225°$). Regarding both the monitor points at $0.7r$ and the frequency range of $0 < f/f_{\mathrm{BPF}} < 0.2$, there are discrepancies in $S_{C_p'}$. The SAS method results in a more spatially distributed characteristics over a wide fan azimuth range with a significant increase in $S_{C_p'}$ on the retreating blade side (e.g. $0° < \psi_f < 90°$). On the other hand, the SST model predicts a rather concentrated pressure disturbance on the advancing blade side (e.g. $270° < \psi_f < 360°$) (see Fig. 5.26(a)). The resulting pressure disturbance at this frequency range is

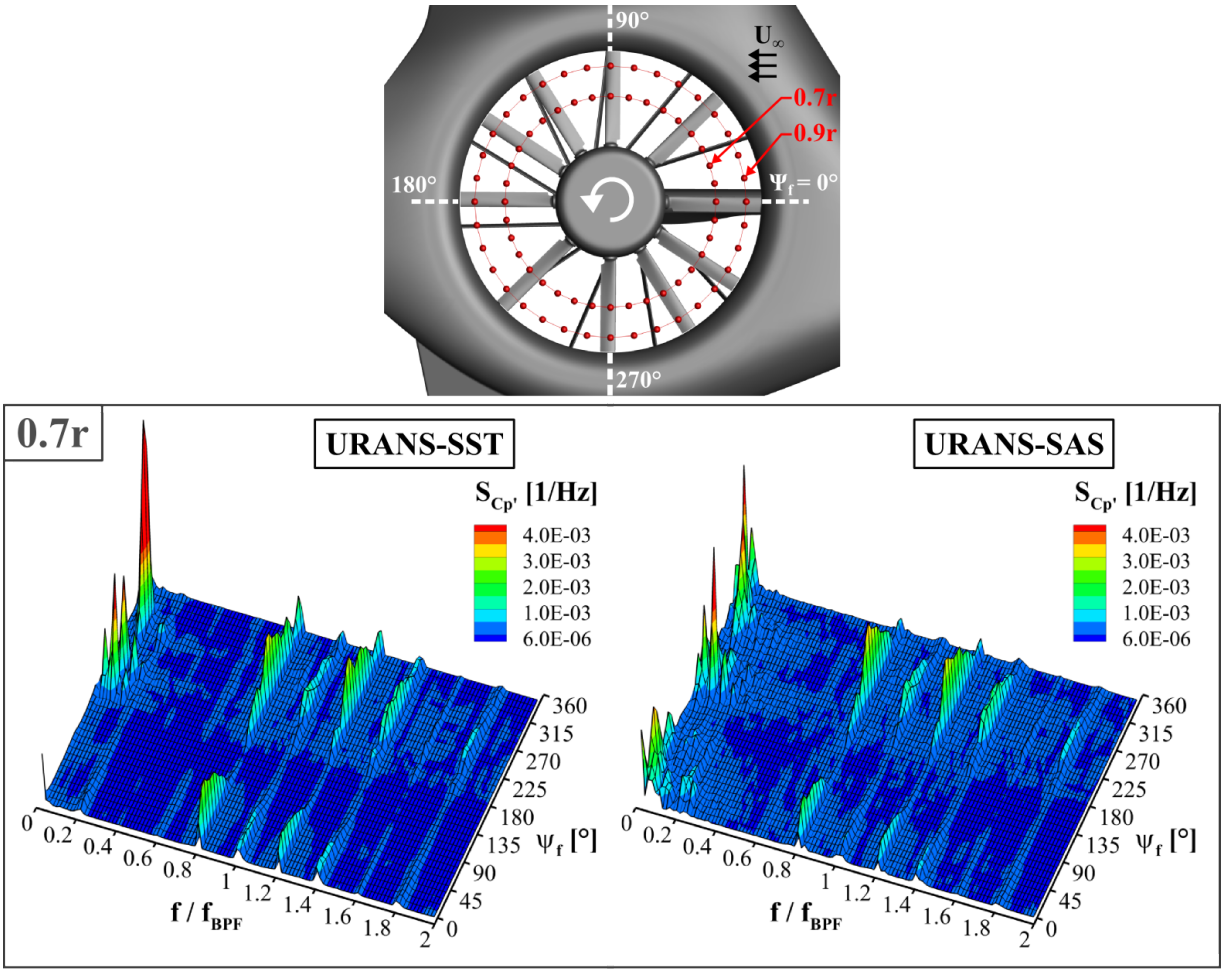

(a)

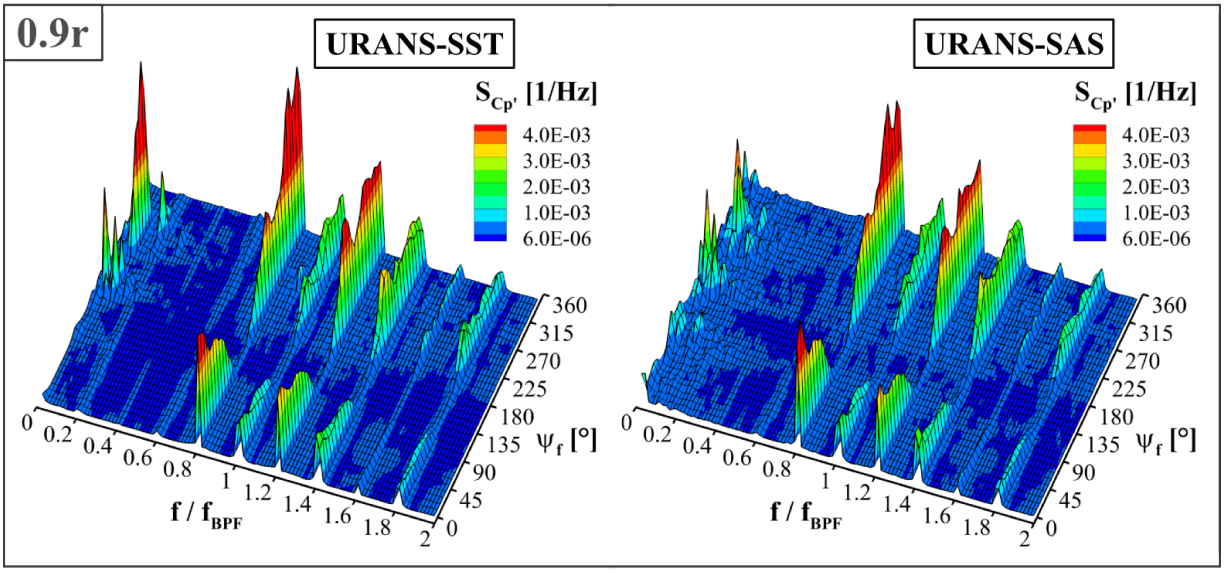

(b)

Figure 5.26: Power spectral densities of pressure fluctuations $S_{C_p'}$ at monitor points located above the rotor plane ($y/l_{\text{ref}} = 0.04$) at (a) 70% and (b) 90% of the fan radius for URANS-SST and URANS-SAS computations.

mainly attributed to the ingested vortical structures, such as the horseshoe vortex of the shroud fairing, the fuselage and HS wake, as well as their interactions with the blades (cf. Fig. 5.78). Therefore, it could be concluded that in the URANS-SAS case, the rotor blades experience a more significant interaction with small-scale vortical structures ingested, and the influence area is more circumferentially extended. Considering $S_{C_p'}$ at the frequencies of $f/f_{\mathrm{BPF}} = 1 \pm 0.2n$ $(n = 1, 2)$, there are no noticeable differences between both turbulence models. A similar observation about the spectral characteristics could be made at the monitor points located at $0.9r$ (see Fig. 5.26(b)).

5.3.1.3 Stator flow field characteristics

The inflow distortions are transmitted into the stator row and cause there further unsteady flow phenomena as indicated in Fig. 5.27. The figures show the instantaneous distributions of non-dimensional vorticity $\omega_z l_{\mathrm{ref}}/U_\infty$. The vorticity distribution of each simulation case indicates that there are diverse recirculating flow zones in the **STATOR**–domain. As expected, the vorticity field predicted by the URANS-SAS provides a more perturbed pattern compared to the URANS-SST.

To analyze the spectral characteristics in the **STATOR**–domain, the power spectral densities of the fan axial velocity fluctuations $S_{u_a'}$ are determined for two stationary monitor points, located underneath the rotor plane $(y/l_{\mathrm{ref}} = -0.025)$ and immediately upstream of the leading edge of the stator vane $(y/l_{\mathrm{ref}} = -0.057)$ at $\Psi_f = 180°$ and 60% of the fan radius. The analysis of $S_{u_a'}$ gives the information about the spectral contents of the velocity disturbances caused by the periodical impingement of the blade wake and hub wake convected downstream as well as by the secondary flow recirculation driven by the interaction with the blades. Considering $S_{u_a'}$ at the monitor point located downstream

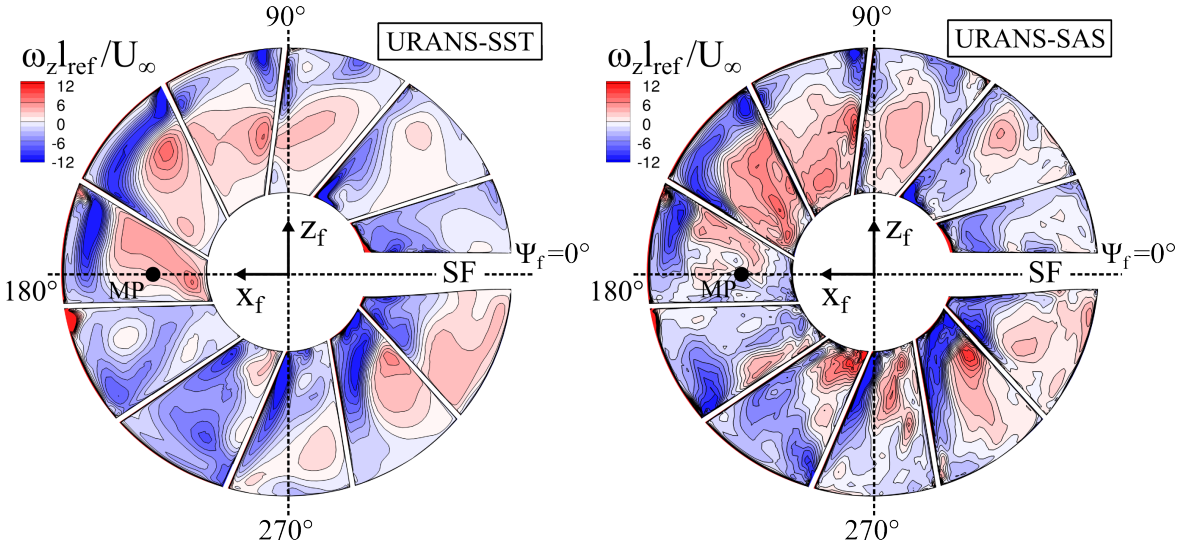

Figure 5.27: Instantaneous distributions of non-dimensional vorticity $\omega_z l_{\mathrm{ref}}/U_\infty$ on the cross-sectional plane located at $y/l_{\mathrm{ref}} = -0.148$ for URANS-SST and URANS-SAS computations.

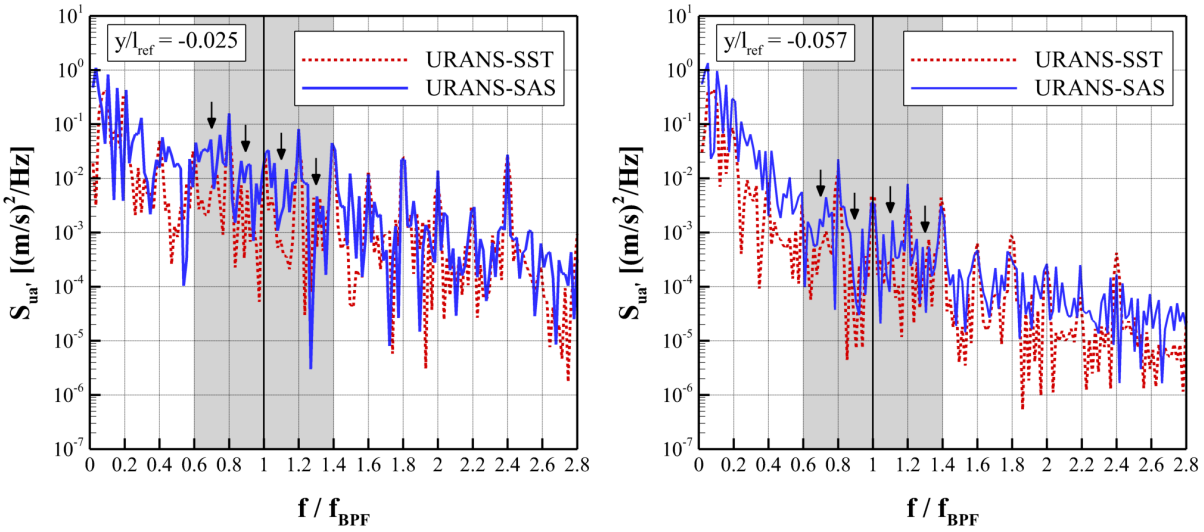

(a) (b)

Figure 5.28: Comparison of power spectral densities of fan axial velocity fluctuations $S_{u'_a}$ observed at monitor points located (a) downstream of the rotor plane ($y/l_{\text{ref}} = -0.025$) and upstream of the stator vane leading edge ($y/l_{\text{ref}} = -0.057$) between URANS-SST and URANS-SAS computations.

of the rotor plane (see Fig. 5.28(a)), the URANS-SAS provides higher levels of $S_{u'_a}$ over a relatively wide frequency range compared to the SST model. Here, a significant increase in $S_{u'_a}$ is observed in the case of URANS-SAS not only at the discrete components related to the fan rotation and uneven blade spacing, but also in-between (e.g. $0.8 < f/f_{\text{BPF}} < 1$ and $1 < f/f_{\text{BPF}} < 1.2$), resulting in a more broadband-like spectral distribution. As mentioned above, the increase at these frequencies is associated with the interaction between the rotor blades and the inflow distortions. At the monitor point positioned upstream of the stator row (see Fig. 5.28(b)), the spectral densities of both simulation cases are considerably decreased compared to those of the monitor point directly downstream of the rotor plane. This is due, on the one hand, to the information loss occurring across the domain interface, where the transfer of the flow quantities between **ROTOR**– and **STATOR**–domain is achieved by a trilinear interpolation method, and on the other hand, to the numerical diffusion caused by the comparably coarse grid spacing of the **STATOR**–domain. Nevertheless, the SAS method provides a higher $S_{u'_a}$ over the whole frequency range regarded.

Fig. 5.29 depicts the surface pressure fluctuations p'_s at $f/f_{\text{BPF}} = 0.8$ on the outgoing blade side of the stator vane S8 and on the incoming side of the drive shaft fairing as well as on the surface of the gear-box to visualize the scale-resolving capability of the URANS-SAS. Considering the distribution of p'_s on the gear-box, caused by the periodic detachment and attachment of the blade-root wake, a clear difference is found between the URANS-SST and URANS-SAS. The URANS-SAS predicts the surface pressure fluctuations on the gear box with an enhanced spatial resolution. A similar observation can

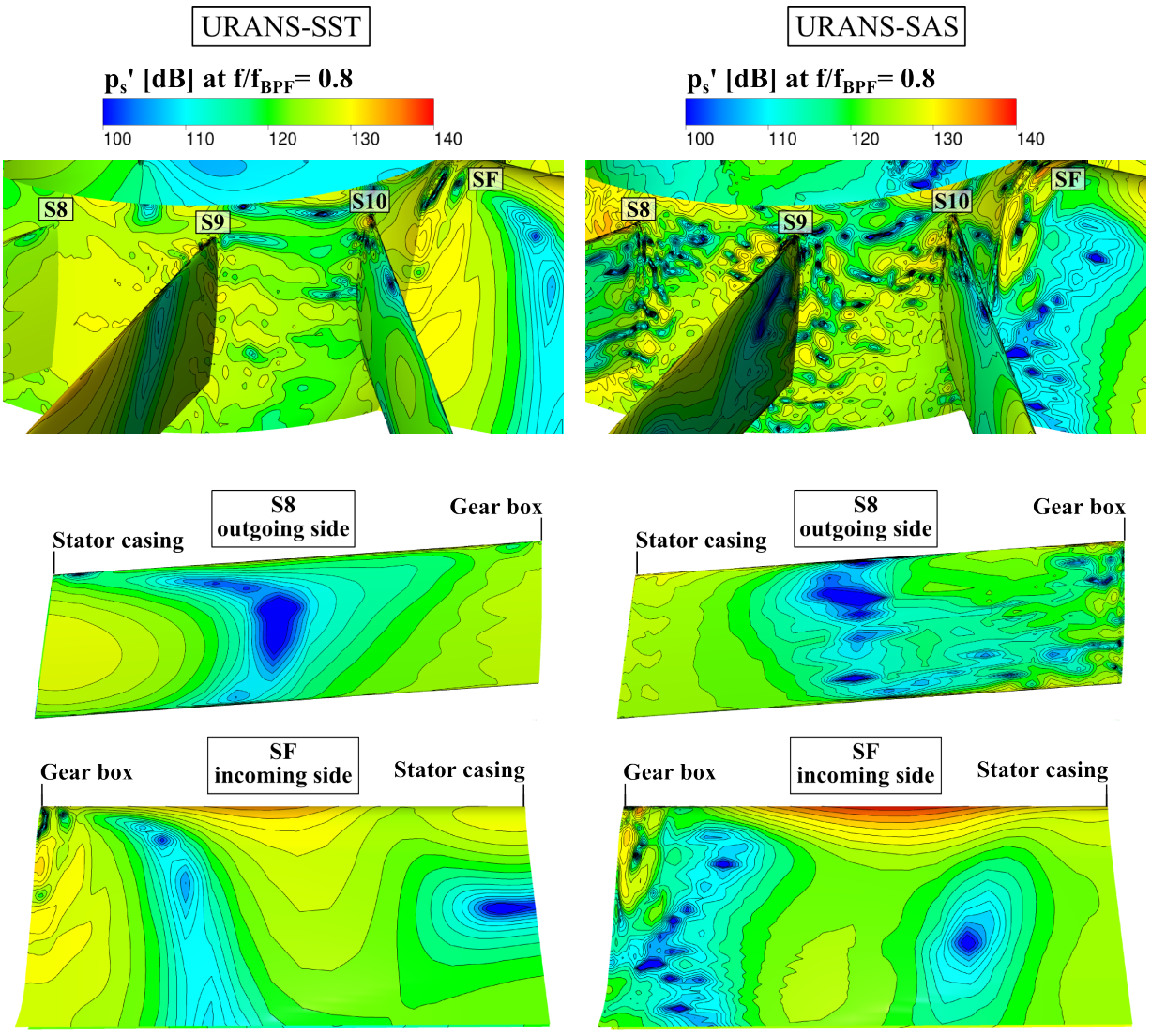

Figure 5.29: Comparison of surface pressure fluctuation p'_s at $f/f_{\mathrm{BPF}} = 0.8$ between computations with (a) URANS-SST and (b) URANS-SAS.

be made on the outgoing side of the stator vane S8 as well as on the incoming side of the drive shaft fairing: refined surface pressure fluctuations close to the vane(fairing)-to-hub intersection with the URANS-SAS. Since the grid spacing and the time scale employed are identical for both simulation cases, it is obvious that the resulting fine resolution of the blade-root wake is predominantly achieved by the specific formulation of the SAS method using the von Kármán length scale, along with the numerical schemes employed.

Since solid surfaces in the stator row can emit sound when they bear fluctuations in aerodynamic forces, the power spectral densities of the unsteady load of the drive shaft fairing is analyzed in Fig. 5.30. The spectral analysis of the fan axial C'_y and the circumferential components C'_z of the shaft fairing load fluctuations show that the URANS-SAS yields more broadband-like spectra. This is because that the SAS method results in a

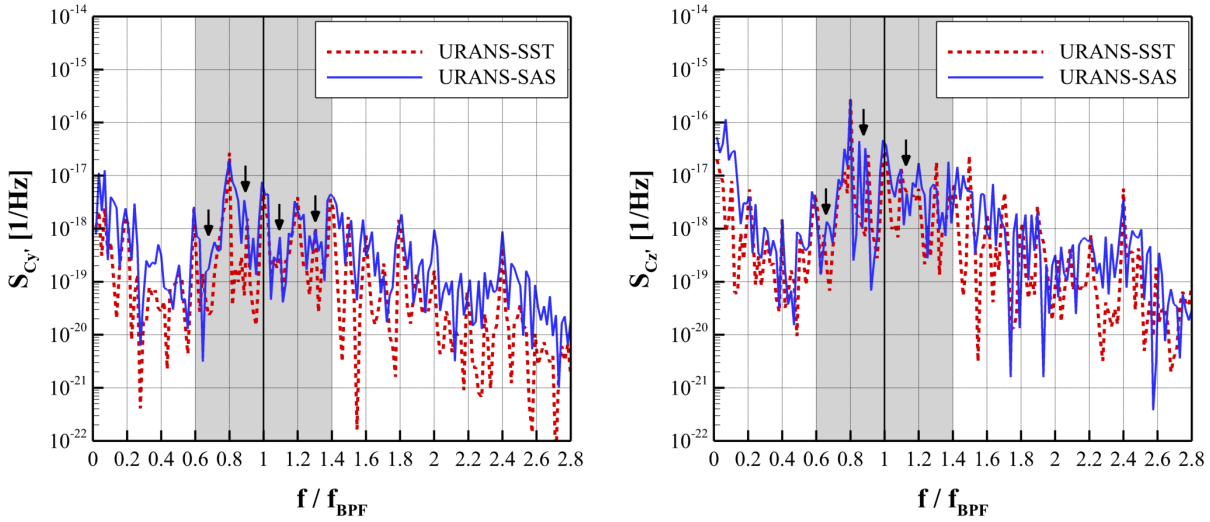

Figure 5.30: Power spectral density analysis of (a) C_y' and (b) C_z' of the drive shaft fairing for URANS-SST and URANS-SAS computations.

significant increase in $S_{C_y'}$ and $S_{C_z'}$ between the peaks at $0.8 < f/f_{\mathrm{BPF}} < 1$ as well as at $1 < f/f_{\mathrm{BPF}} < 1.2$, as already observed in Fig. 5.28.

Flow unsteadiness on the outlet side of the STR is presented in Fig. 5.31 by means of isosurfaces of $Q = 6.5 \times 10^4$ 1/s^2. It is clearly visible that the URANS-SAS provides more small-scales of vortical structures in this unstable flow regime, where the low-momentum fan exit flow interacts with the incoming flow of comparably high flow momentum ($\overline{u}_{exit,\mathrm{out}}/U_\infty \simeq 0.1$). Differences in the eddy viscosity ratio are also present. Similar to the analysis on the inlet side, the power spectral densities of the pressure coefficient fluctuations $S_{C_p'}$ of the monitor points located at the fan outlet (70% of the fan

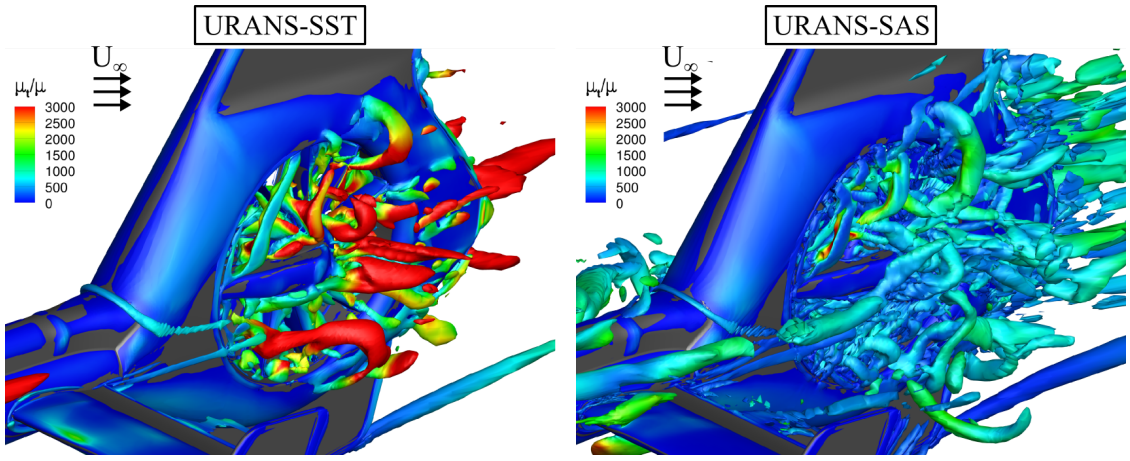

Figure 5.31: Instantaneous vortical structures in the vicinity of the fan outlet,visualized by isosurfaces of $Q = 6.5 \times 10^4$ 1/s^2 for URNAS-SST and URNAS-SAS computations; the color on the isosurfaces represent the eddy viscosity ratio μ_t/μ.

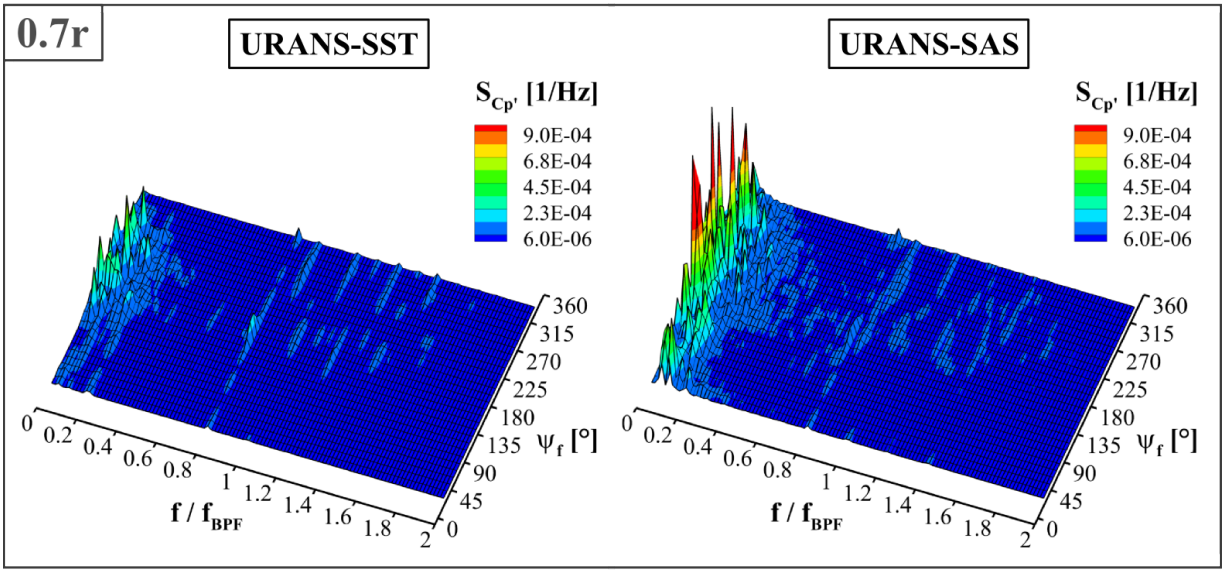

Figure 5.32: Comparison of power spectral densities of pressure fluctuations $S_{C_p'}$ at monitor points located at the fan outlet at 70% of the fan radius between URANS-SST and URANS-SAS computations.

radius) shows significant differences between both simulation cases (see Fig. 5.32). The URANS-SAS yields a clear increase in $S_{C_p'}$ at $0 < f/f_{\mathrm{BPF}} < 0.2$ over a wide fan azimuth range due to the more refined interaction between the fan exit flow and the incoming flow.

According to the flow field analysis performed for both outside and inside of the STR, the resulting flow field of the URANS-SAS exhibits a less disspative nature compared to the URANS-SST. Therefore, the URANS-SAS is able to include more resolved-scales of flow structures. Consequently, the URANS-SAS provides more spectral contents of acoustic sources, particularly at relatively high frequencies.

5.3.2 Far-Field Sound Characteristics

In the following, results of the acoustic post-processing of the URANS-SST and URANS-SAS are compared and analyzed. The emphasis is on the assessment of the influence of the scale-resolving prediction of the acoustic source region on the far-field sound radiation.

In Fig. 5.33(a), the computed directivity of the STR in the high-speed forward flight condition is presented for both turbulence models. The directivity is obtained from a set of observer points lying on the plane (xy-plane) perpendicular to the rotor plane (xz-plane) and located with an equivalent distance ($d_{\mathrm{op}}/l_{\mathrm{ref}} = 25$ and $\Delta\psi_f = 2.5°$) to the axis of the anti-torque rotor. The directivity of both turbulence models have a dipol-like radiation pattern with more pronounced values of the overall sound level (OSPL) on the starboard side (inlet side) of the helicopter. Generally, the hybrid approach in combination with the scale-resolving SAS method (FWH-SAS) predicts an increased OSPL. Most noticeable differences between the FWH-SST and FHW-SAS are observed downstream of the STR, particularly on the port side in the range of $95° < \psi_h < 125°$ with a difference in OSPL

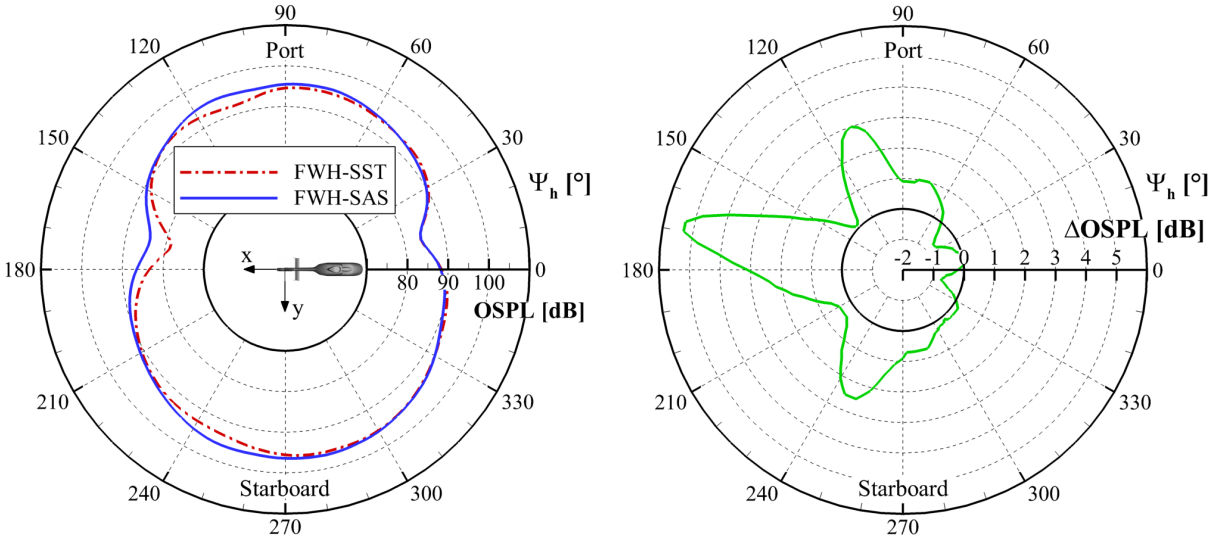

(a) (b)

Figure 5.33: Comparison of directivities between the FWH-SST and FWH-SAS: (a) directivity of OSPL and (b) relative difference $\Delta\text{OSPL} = \text{OSPL}_{\text{SAS}} - \text{OSPL}_{\text{SST}}$.

($\Delta\text{OSPL} = \text{OSPL}_{\text{SAS}} - \text{OSPL}_{\text{SST}}$) of 3 dB and on the stern side $150° < \psi_h < 190°$ with $\Delta\text{OSPL} = 5$ dB as well as on the starboard side of the helicopter $230° < \psi_h < 260°$ with $\Delta\text{OSPL} = 2.5$ dB (see Fig. 5.33(b)). Apart from these azimuth ranges, the difference in OSPL is small.

To clarify the reasons of the differences in the OSPL directivity, narrowband noise spectra are considered and presented in Fig. 5.34, for three selected observer points ($\psi_h = 110°$, $\psi_h = 167.5°$, and $\psi_h = 247.5°$). The SPL spectra of both simulation cases show broadband-like sound characteristics. They are attributed to the uneven blade spacing and further intensified by the inlet flow distortions as well as by the ingested wake of the fuselage and the horizontal stabilizer. The influence of the SAS turbulence model on the far-field sound characteristics of the STR is clearly visible at the observer points $\psi_h = 110°$ (Fig. 5.67(a)) and $\psi_h = 167.5°$ (Fig. 5.67(b)). Generally, the computed SPL of the FWH-SAS is higher than that of the FWH-SST over a wide frequency range. Furthermore, the far-field spectra of the FWH-SAS show a more broadband-like character than the FWH-SST as the increase of the SPL in the range of $0.8 < f/f_{\text{BPF}} < 1$ and $1 < f/f_{\text{BPF}} < 1.2$ is more perceivable, as already observed in the flow field analysis (cf. Fig. 5.30). Indeed, at $\psi_{\text{h}} = 110°$, the relative difference in the SPL ($\Delta\text{SPL} = \text{SPL}_{\text{SAS}} - \text{SPL}_{\text{SST}}$) at $f/f_{\text{BPF}} = 0.9$ is approximately 5 dB, while $\Delta\text{SPL} \simeq 2.5$ dB is observed at $f/f_{\text{BPF}} = 0.8$.

Consequently, it could be concluded that the FWH analogy in combination with the URANS-SAS provides an increased SPL, particularly at high frequencies because the acoustic sources captured by the URANS-SAS also contain enhanced spectral contents at these frequencies.

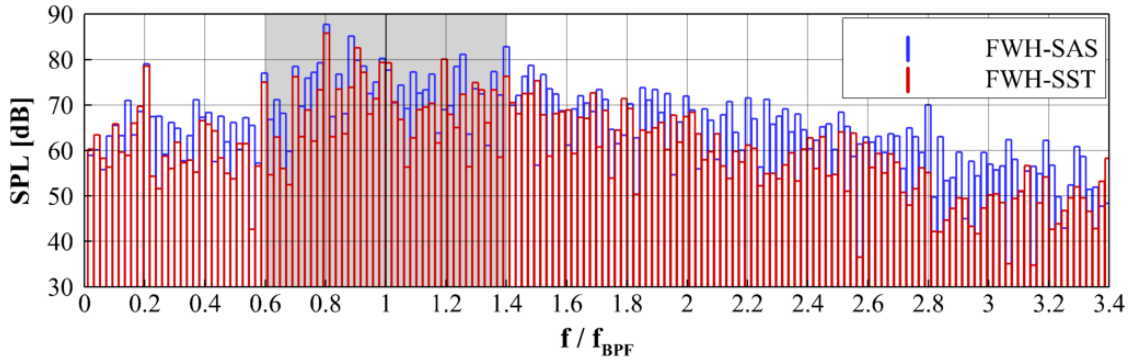

(a)

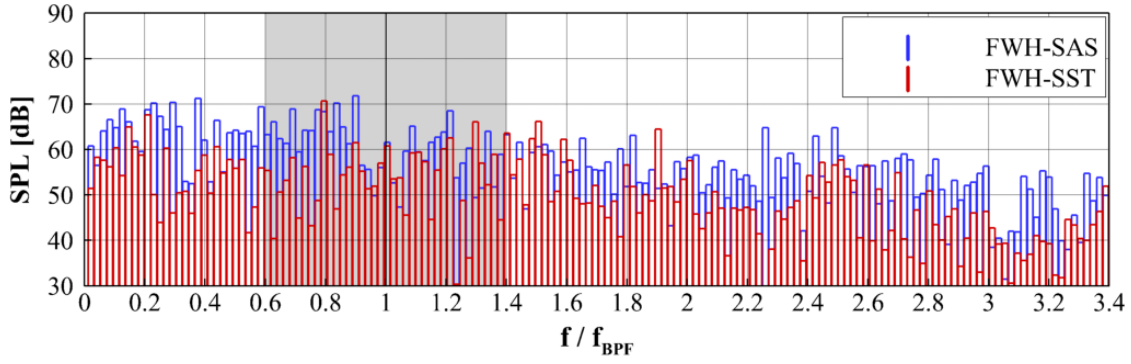

(b)

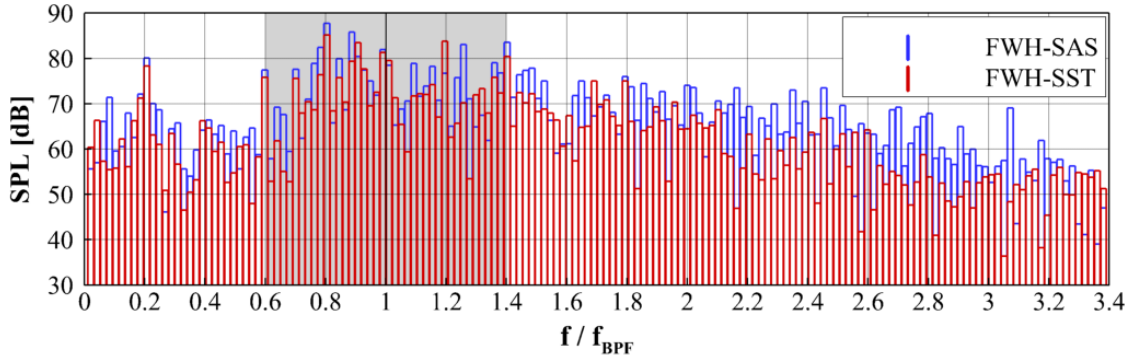

(c)

Figure 5.34: Narrowband spectra at observer points located at (a) $\psi_h = 110°$, (b) $\psi_h = 167.5°$, and (c) $\psi_h = 247.5°$ for the FWH-SST and FWH-SAS.

5.3.3 Comparison between Computations and Measurements

In order to asses the capability of the hybrid approach specifically in the application of the forward flight case, the computed STR noise is compared with the noise data obtained within flight measurement campaigns of DLR.

In the flight measurements, the emitted helicopter noise in the high-speed forward flight condition was measured by using 43 microphones, scattered on ground with a maximum distance of 800 m from the center position (see Fig. 5.35). This spatial distribution of the microphones was chosen to provide instantaneous sound directivities appropriately

Parameter	Flight test	FWH-URANS
Flight speed U_∞	67 m/s	62.5 m/s
Angle of attack α_∞	$-2°$	
Side slip angle β_∞	1°	0°
Blade pitch angle P_b	$-5°$	2°
Rotational speed of anti-torque rotor Ω	$\Omega_{\text{Flight}} = \Omega_{\text{FWH}}$	

Table 5.1: Flight parameters for the flight test and the numerical prediction.

when the test helicopter is flying over the center microphone [25]. For the flight test, the EC 135 FHS (Flying Helicopter Simulator) of DLR was used. The helicopter possesses a similar configuration of the fan-in-fin type anti-torque device as the STR regarded in this thesis. In Table 5.1, the parameters for the flight test as well as the numerical simulation are given. There is a noticeable difference in the blade pitch angle P_b. The analysis of DLR, however, shows that in this flight condition, the angle of attack and the side-slip angle, which are in good agreement, have a much greater influence on the STR noise emission than P_b [92]. Details about the microphone layout and test configurations as well as the measurement setups are given in references [91] and [25].

Likewise in the analysis of the hovering case, the tonal noise components of the STR were extracted from the recorded overall noise signal by the use of the ROSI program. After that process, the extracted tonal noise components are then propagated back to an imaginary hemispherical surface with a radius of 1 m to evaluate the STR sound di-

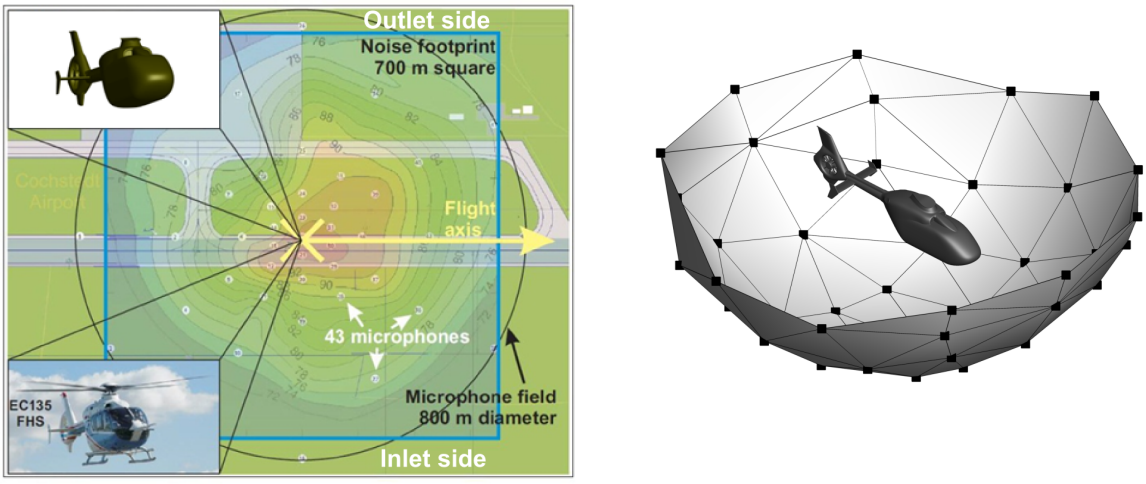

(a) (b)

Figure 5.35: (a) Microphone layout of DLR flight measurement campaigns [91] and (b) the directivity sphere (not true to scale).

rectivity. By the back propagation of the STR noise onto the hemispherical surface, the Doppler effect and the spherical spreading as well as the atmospheric absorption (based on the Sutherland law) of sound were taken into account [25]. Thus, for the comparison here, the relative velocity of microphones with respect to the helicopter can be considered as zero, which is also the case in the numerical prediction.

5.3.3.1 Directivity sphere

In Fig. 5.36, the sound directivity sphere ($R = 1$ m) of the flight test is compared with that of the hybrid method (FWH-SST and FWH-SAS). The directivity spheres in Fig. 5.36 are further projected onto the xy-plane. The directivity characteristics computed by

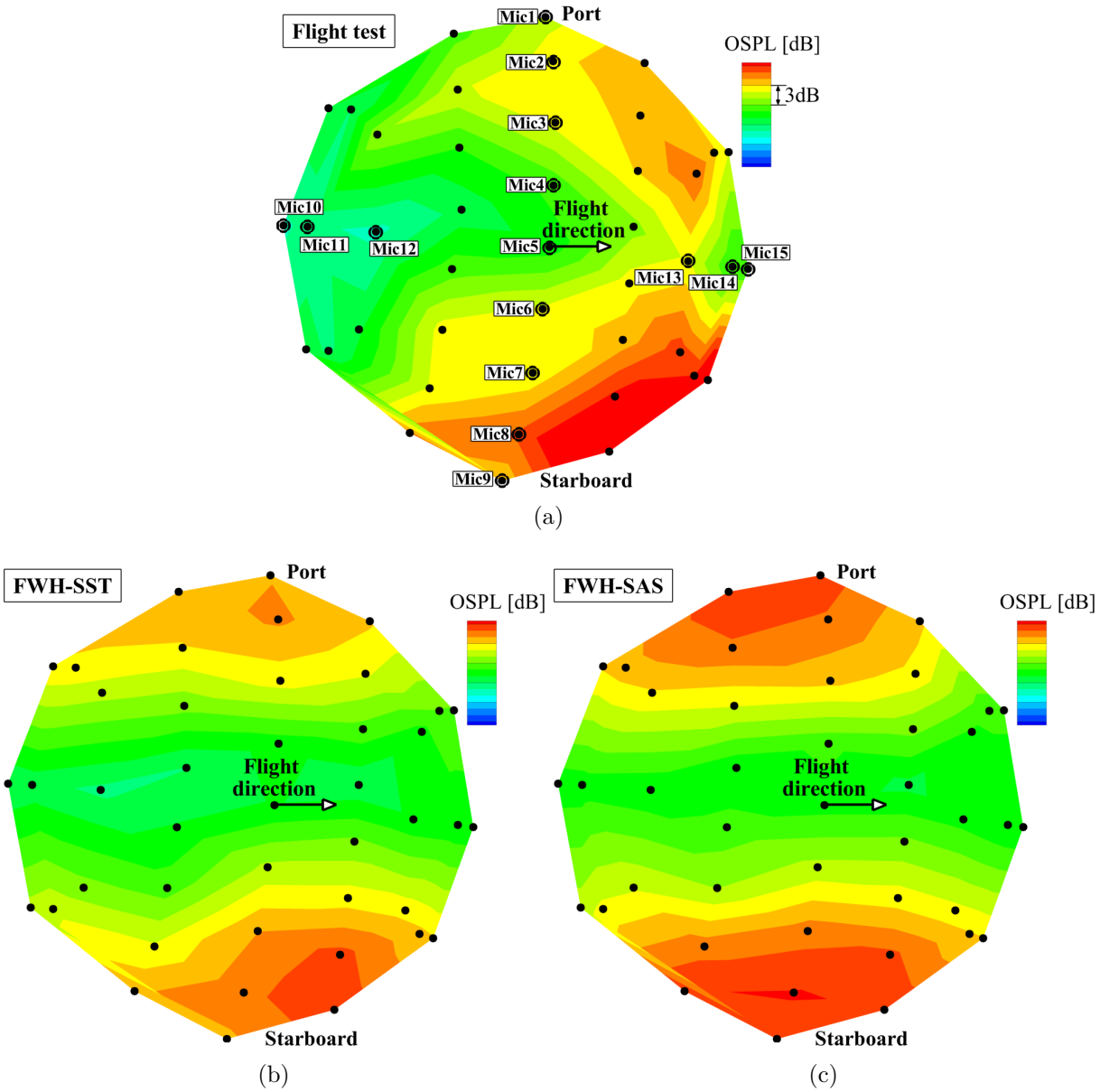

Figure 5.36: Comparison of noise directivities: (a) measured directivity, (b) directivity computed by the FWH-SST, and (d) the FWH-SAS.

the FWH-SST is similar to that of the flight test: a dipole-like directivity pattern with higher values of the OSPL on the starboard side (inlet side) of the helicopter. In the case of FWH-SST, however, the local maximum observed on both the starboard and port side are slightly shifted rearwards compared to the flight test. It is more pronounced on the port side of the STR. Both measured and computed directivities indicate significantly low values of the OSPL on the stern and bow side of the STR. This is due to the masking effect in the plane of the rotor, which is mainly achieved by the duct fairing. The directivity of the FWH-SAS is almost identical to that of the FWH-SST, whereas the FWH-SAS provides higher OSPL on the starboard and port side of the STR compared to the FWH-SST.

For a more quantitative analysis, a sectional distribution of the OSPL is made for the observer points Mic1 to Mic9, located perpendicular to the flight path (see Fig. 5.37(a)). At these microphone positions, the FWH results of both turbulence models indicate similar radiation characteristics to that of the flight test: a symmetric noise radiation with respect to Mic5 located directly underneath the STR. The best agreement regarding the OSPL is found for Mic5. Further good agreements are also found for Mic3 (port side) and Mic6 (starboard side), which are placed relatively close to the STR. At these microphone positions, the FWH-SAS provides slightly better results than the FWH-SST. Generally, the difference in the OSPL between the flight test and the numerical predictions tends to increase with increasing distance to the STR. The overprediction of the OSPL by the numerical simulations is attributed to the rearward shift of the local maximum, as seen in Figs. 5.36(b) and 5.36(c). However, the differences in the OSPL at these microphone positions are below 5 dB. Regarding the microphone positions underneath the flight path

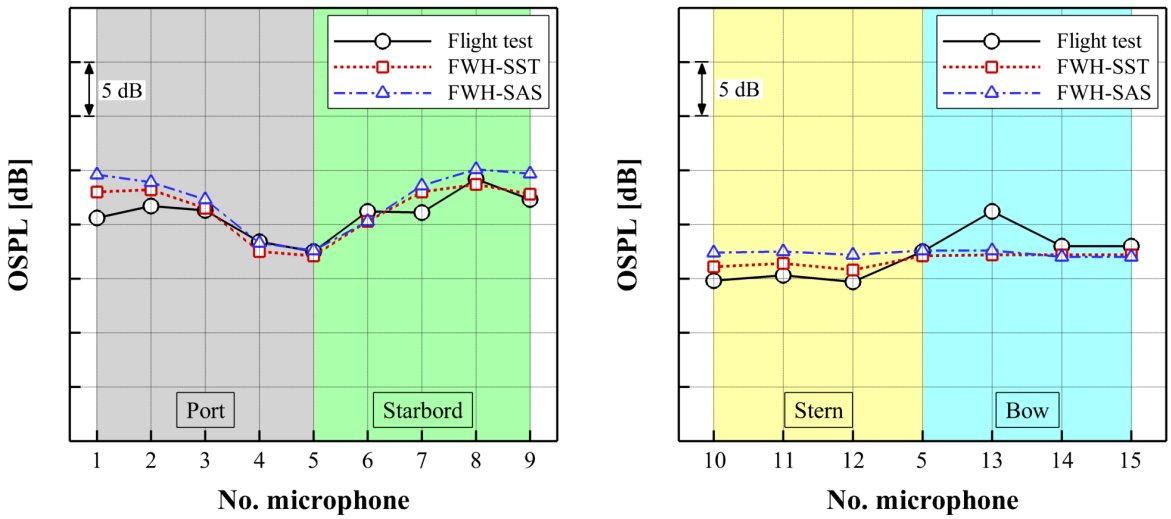

Figure 5.37: Comparison of directivities between the flight test and the FWH computations: microphone positions (a) perpendicular and (b) parallel to the flight path.

such as Mic10 to Mic15, the calculated directivity shows a fairly good agreement with that of the flight test data. Generally, the OSPL is overestimated on the stern side and slightly underestimated on the bow side of the helicopter. The discrepancies between the measured and computed OSPL are, however, below 5 dB, except at Mic13 located on the bow side. At Mic13, the sudden increase of the OSPL in the case of the flight test is somehow underpredicted by the numerical predictions.

5.3.3.2 Noise spectra

In the following, measured and calculated noise spectra are considered at the selected microphone positions. Note that, the given sound level is fitted with a 1/3-octave band filter. The calculated noise spectra correspond well with the measured one, particularly at Mic11 and Mic12, located on the stern side of the flight path. Both turbulence models predict well the sound pressure levels at the most dominant frequency at $(f/f_{\mathrm{BPF}})_{1/3} = 0.8$ as well as at $(f/f_{\mathrm{BPF}})_{1/3} = 1$. In general, the SAS results show a better agreement with the flight test data not only at low frequencies but also at the relatively high frequencies. Indeed, the FWH-SAS results show a better agreement with the flight test data for the frequency range up to $(f/f_{\mathrm{BPF}})_{1/3} = 2.4$, whereas the FWH-SST results show noticeable differences already from $(f/f_{\mathrm{BPF}})_{1/3} \geq 1.4$ on.

Comparing the noise spectra at Mic13, there are significant differences between the measured and computed SPL. Here, both FWH computations result in a significant underprediction at the frequencies below $(f/f_{\mathrm{BPF}})_{1/3} = 1.4$. It possibly explains the significant difference in the OSPL observed in Fig. 5.37(b). Nevertheless, the FWH-SAS indicates a better agreement with the measured one in the frequency range of $1.4 < (f/f_{\mathrm{BPF}})_{1/3} < 2.6$. In the case of microphone positions at Mic2, Mic5, and Mic8 located parallel to the axis of the anti-torque rotor and perpendicular to the flight path a similar observation can be made: good agreements with the flight test data at $(f/f_{\mathrm{BPF}})_{1/3} = 0.8$ and $(f/f_{\mathrm{BPF}})_{1/3} = 1$, and the FWH-SAS providing better results at relatively high frequencies.

According to the comparison with the flight test data, it can be concluded that the hybrid approach employed in this thesis provides a reasonable sound directivity. Concerning the noise spectra, the FWH results of both turbulence models show a very good agreement with the measured data at the frequencies $(f/f_{\mathrm{BPF}})_{1/3} = 0.8$ and $(f/f_{\mathrm{BPF}})_{1/3} = 1$. Generally, the FWH prediction in combination with the SAS method provides better results regarding the noise spectra. The enhancement is more pronounced at the frequencies up to $(f/f_{\mathrm{BPF}})_{1/3} = 2.6$. A further enhancement of the sound prediction beyond this frequency can be achieved by using a smaller CFD time step size and a finer grid spacing, which, however, result in a drastic increase in computational efforts. It is also investigated by AHD that the tonal extraction using ROSI in this high frequency range often yields overestimated results due to the presence of the high broadband noise. Concerning the dominant tonal noise components at $(f/f_{\mathrm{BPF}})_{1/3} = 0.8$ and $(f/f_{\mathrm{BPF}})_{1/3} = 1$, the FWH method combined with the SST turbulence model also provides good results with significantly less computational effort than the FWH-SAS.

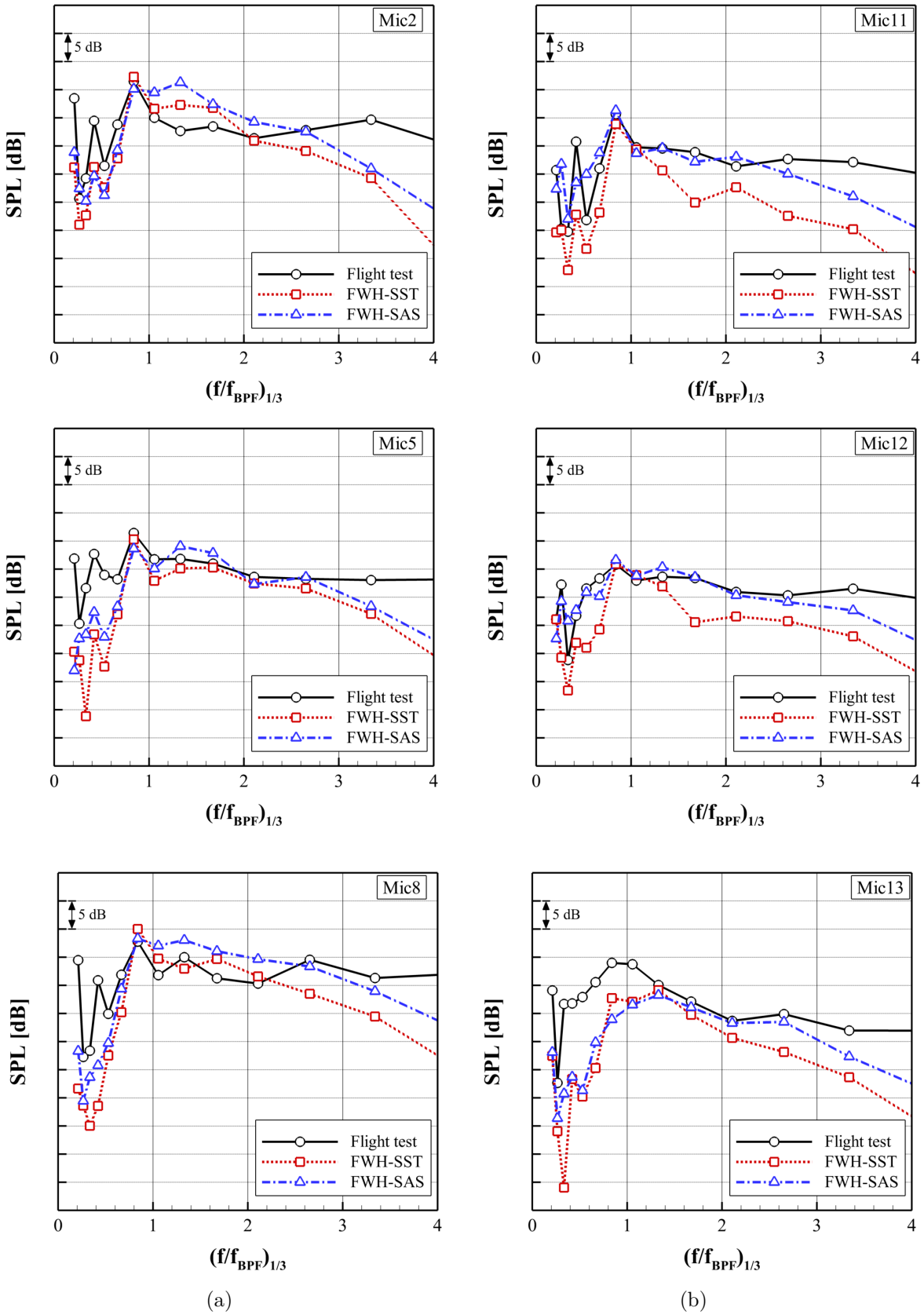

Figure 5.38: Comparison of narrowband spectra at microphone positions (a) perpendicular and (b) parallel to the flight path between the flight test and the hybrid method (FWH-SST and FWH-SAS).

5.4 Influence of Inlet Flow Distortion

This section focuses on the assessment of the aerodynamic and acoustic impact of the inlet flow distortions arising under cross-flow condition. Comprehensive aerodynamic and acoustic investigations are performed by comparing the reference STR configuration with a specific case where the inlet flow distortion is eliminated [107, 109]. Results of the aeroacoustic analysis indicate that the active flow control by lip boundary layer suction is an effective measure of noise reduction in the high-speed forward flight condition.

5.4.1 Choice of Flow Control Method

From both the aerodynamic and aeroacoustic point of view, the inlet flow distortion as a result of the boundary layer separation at the collector lip is the most critical flow phenomenon arising under cross-flow condition. The lip boundary layer separation substantially changes the flow topology, particularly in the vicinity of the rotor plane, and thus affecting the aerodynamic characteristics of the STR significantly. Consequently, the inlet flow distortion attenuates the acoustic benefits of the STR, resulting from shrouding of the rotor blades.

In order to estimate both the qualitative and quantitative contributions of the inlet flow distortion to the flow-induced noise, it is needed to compare the reference simulation case with the case of suppressed lip boundary layer separation. Suppression or delay of the separation onset on the collector lip, hence a preferably undisturbed flow field above the rotor plane, can be obtained by applying a passive and/or an active boundary layer control measure. For the choice of an appropriate and efficient flow control method, preliminary investigations are conducted by means of the steady-state simulation using the SST turbulence model for three specific cases: (1) reference configuration (fixed collector lip radius), (2) passive boundary layer control using modified inlet lip contours, and (3) active flow control via lip boundary layer suction. To reduce the computational costs of the steady-state simulations, the actuator disc approach is applied, as shown in Fig. 5.39. For this purpose, two domain interfaces are defined above the rotor plane ($y/l_{\mathrm{ref}} = 0.012$) and at the fan exit ($y/l_{\mathrm{ref}} = -0.209$), respectively. An Outlet boundary condition is used for the upper interface (fan inlet), and the Inlet boundary condition is defined on the lower interface (fan outlet). The non-dimensional mass flow rate through the STR (defined in Eq. 5.3) is determined for the interfaces and identical for all steady-state simulations ($\mu_f = 0.076$). The mass flow rate is obtained from the previous unsteady simulations of the reference case and averaged over the mid-interface.

$$\mu_f = \frac{\dot{m}_f}{\rho_\infty (\Omega/60)(D_f)^3} \tag{5.3}$$

In Fig. 5.40, results of the steady-state computations are presented. The total pressure ratio $p_t/p_{t,\infty}$ on the upper interface, skin-friction lines on the shroud fairing, the collector lip, and the rotor casing, as well as streamlines on the symmetry plane ($z/l_{\mathrm{ref}} = 0$) are

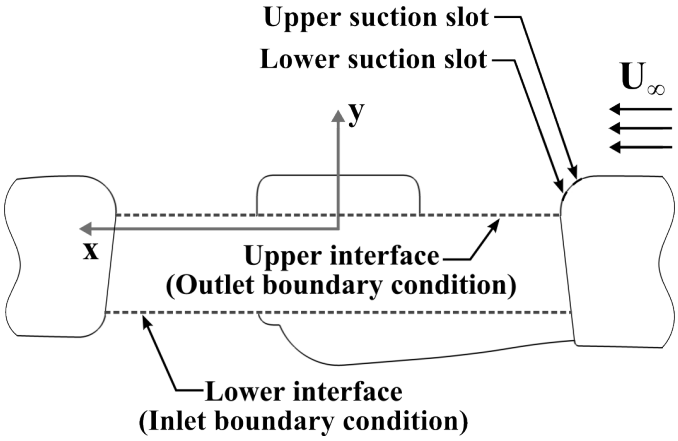

Figure 5.39: Actuator disc approach for steady-state simulations

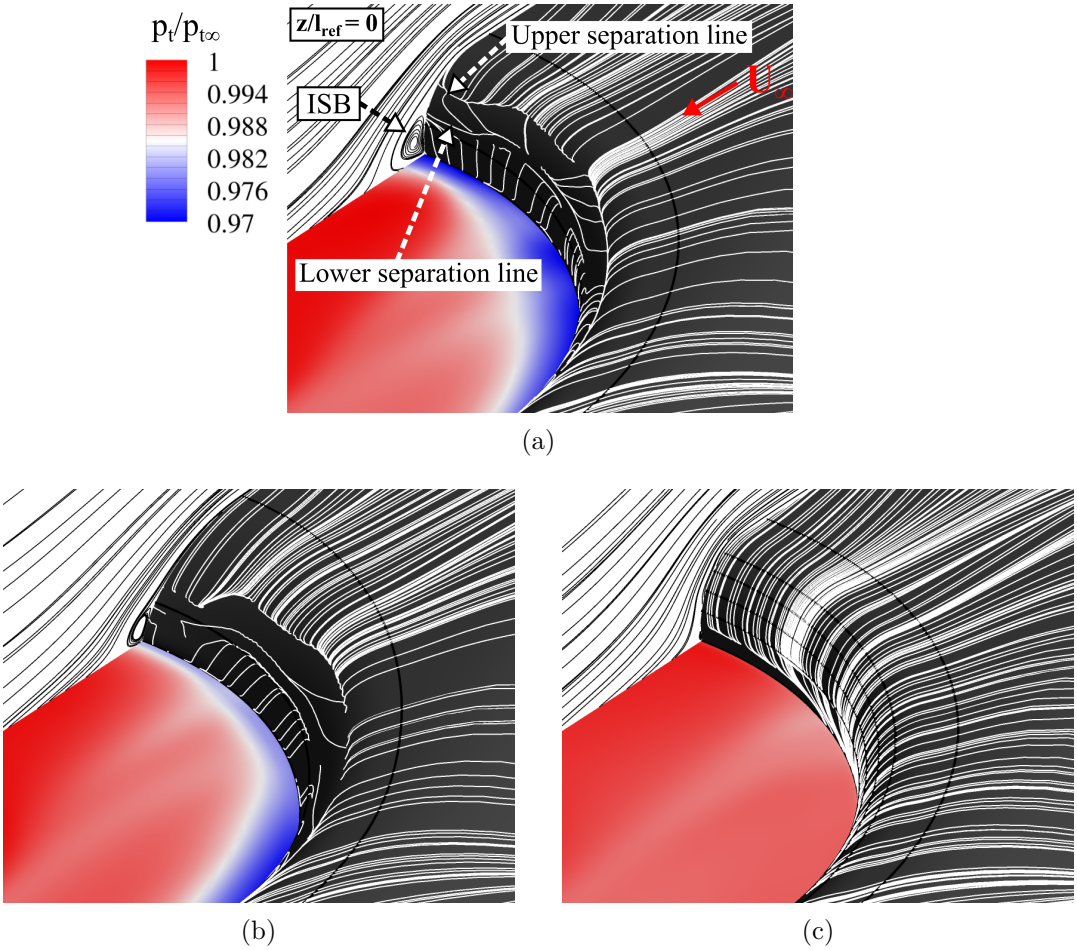

Figure 5.40: Total pressure ratio $p_t/p_{t\infty}$ on the upper interface ($y/l_{\text{ref}} = 0.012$) and skin-friction lines on the STR shroud, the collector lip, and the rotor casing as well as streamlines on the symmetry plane at $z/l_{\text{ref}} = 0$ for the (a) reference configuration, (b) modified inlet lip radius, and (c) boundary layer suction, based on steady-state simulations using the SST turbulence model.

visualized. The pattern of the skin-friction lines for the reference simulation case indicates two significant flow separation zones with an upper separation line and a lower separation line, as indicated in Fig. 5.40(a). On the collector lip (approximately 50% downstream), the boundary layer detaches from the collector lip (upper separation line). Then, the separated flow forms a recirculating flow zone, namely the inlet separation bubble (ISB), as shown by the streamlines on the symmetry plane ($y/l_{\mathrm{ref}} = 0$). Thereby, the fluid flow near the rotor casing reattaches to the surface, where after a short distance it separates again (lower separation line). The influence of the ISB on the upper interface can be identified by low levels of $p_t/p_{t,\infty}$ (total pressure distortion). Its circumferential stretching along the collector lip extends over almost a half of the STR inlet region ($0° < \psi_f < 110°$: retreating side and $260° < \psi_f < 360°$: advancing side).

5.4.1.1 Passive flow control

As a passive measure against the lip boundary layer separation, an increased collector lip radius is chosen, as shown in Fig. 5.41(b) and Fig. 5.42. Previous research on fan-in-wing aerodynamics [95] points out that increasing the ratio of the inlet-lip-radius-to-diameter r_{lip}/D_f can suppress a strong suction peak appearing on the collector lip and therefore alleviate an abrupt increase of the adverse pressure gradient downstream ($dp/dx > 0$). Thus, the boundary layer separation at the lip can be effectively prevented. In this thesis, not only the lip radius is increased but also the contour of the STR shroud as well as the rotor casing are modified to achieve an appropriate ratio of r_{lip}/D_f, at which the inflow distortion is suppressed as much as possible. The maximum value of r_{lip}/D_f is 0.126 at the fan azimuth of $\psi_f = 0°$ (see Fig. 5.41(b)). The ratio is gradually decreased from $\psi_f = 0°$ to $\psi_f = 90°$ (first quarter of the collector lip) and in the range of $270° < \psi_f < 0°$ (fourth quarter), as shown in Fig. 5.41(b). In the second and third quarter of the collector lip, the

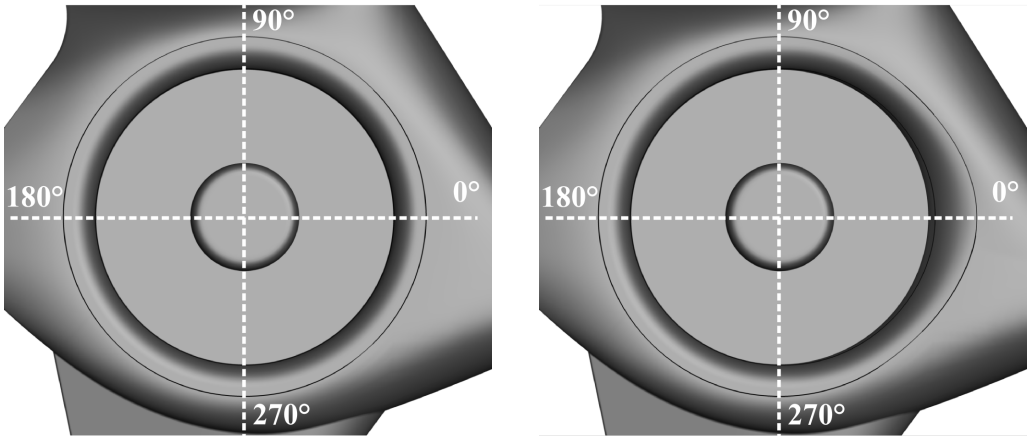

(a) (b)

Figure 5.41: Top view of the collector lip: (a) reference configuration and (b) increased lip radius.

lip radius is kept constant ($r_{\text{lip}}/D_f = 0.053$) and identical to the lip radius of the reference configuration.

As indicated in Fig. 5.40(b), the modified inlet lip contour reduces significantly the total pressure distortion: reduction of the ISB influence area on the upper interface. The skin-friction lines on the collector lip, particularly at $\psi_f = 0°$, also shows that the onset of boundary layer separation is noticeably delayed. Thus, the upper separation line is shifted more downstream compared to the reference case. To show it more clearly, the streamwise distribution of the surface pressure coefficient C_p ($z/l_{\text{ref}} = 0$ and $\psi_f = 0°$) is presented in Fig. 5.42. Comparing the case of the modified lip radius with the reference case, the suction peak is found more upstream, but the level of C_p is lower. The relative difference in the suction peak with respect to the reference case is $\Delta C_p = -34\%$. In addition, the streamwise pressure gradient (dp/dx) is smaller, and consequently, the separation onset is shifted further downstream in the case of increased lip radius. The abrupt increase of $|C_p|$ at $x/l_{\text{ref}} = -0.5$ is because of the remaining separation bubble.

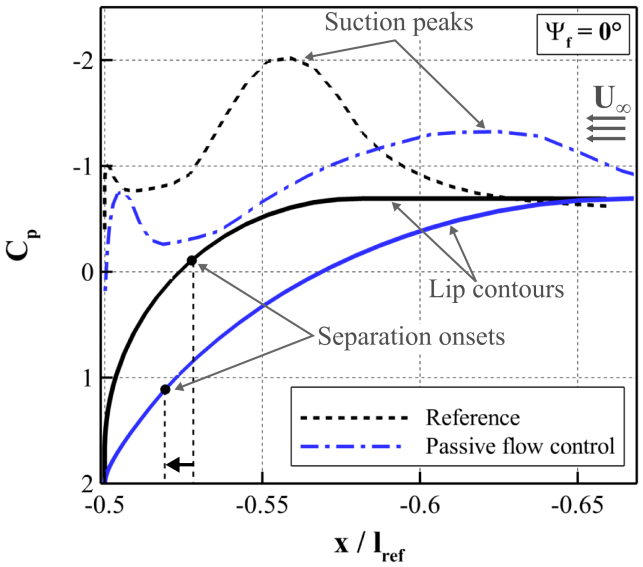

Figure 5.42: Streamwise distributions of the surface pressure coefficient C_p at $z/l_{\text{ref}} = 0$ and $\psi_f = 0°$ for the reference and modified lip contour.

Streamlines on the horizontal cross-section ($z/l_{\text{ref}} = 0$) indicate that a small region of recirculating flow remains above the upper interface (see Fig. 5.40(b)). This shows that the lip radius might to be increased further to prevent the flow separation completely. A further increase of the lip radius is, however, limited as the modification of the collector lip would possibly impact the overall tail rotor performance in other flight conditions. Indeed, approximately half of the anti-torque thrust required in the hovering flight is provided by the suction effect occurring on the collector lip (cf. Sec. 4.1.1). For the reasons mentioned above, the passive flow control by means of the increased lip radius does not fulfill the aim of keeping the flow completely attached.

5.4.1.2 Active flow control

For active flow control, boundary layer suction is considered. Another possible active flow control measure can be a blowing jet [17, 95]. It is, however, not considered within this thesis due to possible interactions occurring between the blowing high-momentum jet and the rotor blade. A preliminary study indicates that the use of a single suction slot directly downstream of the upper separation line is insufficient to eliminate the inlet separation bubble completely. Therefore, a further suction slot is introduced downstream of the first suction slot (see Fig. 5.39). Both suction slots are circumferentially extended form $\psi_f = 0°$ to the upper ($\psi_f = 90°$) and the lower part ($\psi_f = 270°$) of the collector lip. An outlet boundary condition is defined on the slot interfaces, and a circumferentially constant normal velocity profile is used for the upper ($C_\mu = 2.5 \times 10^{-4}$) and lower slot ($C_\mu = 1.4 \times 10^{-4}$), based on the momentum coefficient [17] defined as :

$$C_\mu = \frac{\dot{m}_s U_s}{0.5 \rho_\infty U_\infty^2 A_f} \tag{5.4}$$

Results of the RANS simulation indicate that the boundary layer suction is an effective method for suppressing flow separation on a strongly curved surface. As observed in Fig. 5.40(c), the boundary layer remains attached on the lip surface, and therefore, a fairly undisturbed flow topology is observed on the upper interface. According to the pattern of the skin-friction lines, the presence of the boundary layer separation is still detected on the rotor casing close to the upper interface. However, its impact on the rotor plane might be less significant than the recirculating flow observed in the case of passive flow control. Applying a further suction slot at this area is excluded because of the proximity to the rotor tip.

5.4.2 Overview on Inlet Flow Distortions

To analyze the aerodynamic and acoustic impact of the inlet flow distortion, further unsteady simulations are performed by means of the sliding mesh method and the active flow control using the boundary layer suction (BLS). The flight parameters (e.g. fan rotational frequency ω_f , blade pitch angle P_b) and the simulation setups are set identical to the reference simulation. Flow quantities are averaged over a total of five fan revolutions. Because of the comparably high computational efforts of the SAS method, the investigation is based on the SST turbulence model only.

In the following, the first insight to the inlet flow distortion is given by comparing data of the non-distortion case (BLS case) with the reference case before detailed analysis of its interaction with the rotating blades are performed in Sec 5.4.3.

5.4.2.1 Total pressure distribution

Fig. 5.43 depicts the instantaneous $p_t/p_{t,\infty}$ distribution on the vertical symmetry plan for the reference and BLS case. Here, the flow field characteristics inside the duct casing are compared. For the reference simulation case, recirculating flow zones provoked by the lip boundary layer separation are clearly identified by low values of the total pressure ratio ($p_t/p_{t,\infty} < 0.985$) in the vicinity of the collector lip both in the upper (retreating blade side) and lower part (advancing blade side) of the STR. The slightly disrupted $p_t/p_{t,\infty}$ distribution observed on the retreating blade side is due to the interaction between the separated flow field and the rotor blade at the current simulation time step. The recirculating flow zones and their interaction with the blades lead to further flow recirculations in the stator row.

In the BLS case, the active flow control using the lip boundary layer suction successfully removes the inlet separation bubble. A comparably low disturbed inflow is present upstream of the rotor plane. However, low levels of $p_t/p_{t,\infty}$ are still observed in the stator row. It is due to the flow separation occurring on the stator vanes as result of the low fan axial to circumferential velocity ratio u_a/u_c of the stator inflow at this STR operating point (see Sec. 5.4.2.4).

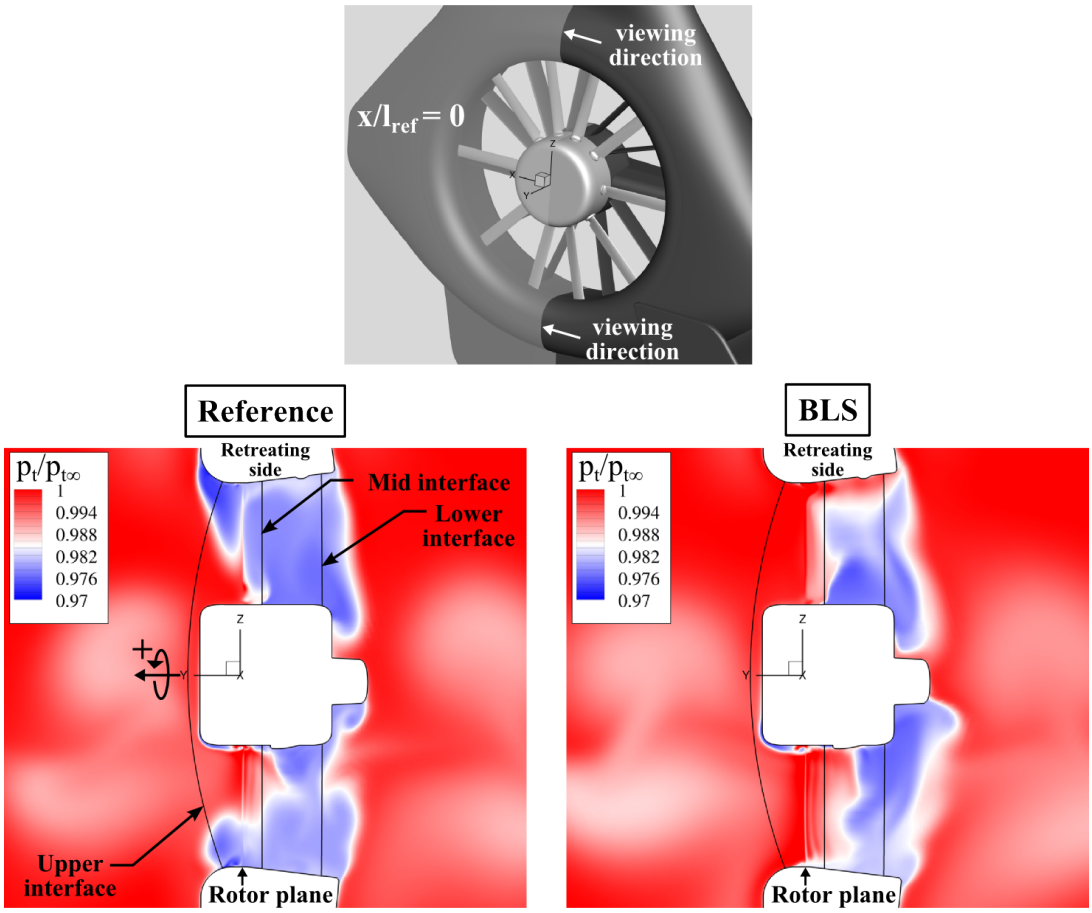

Figure 5.43: Instantaneous distributions of the total pressure ratio $p_t/p_{t,\infty}$ on the vertical symmetry plane ($x/l_{\text{ref}} = 0$) for the reference and BLS case.

5.4.2.2 Skin-friction lines and space-filling streamlines

In Fig. 5.44(a), the time-averaged skin-friction lines are presented on the STR shroud (inlet side) for the reference and BLS case. In the case where the massive lip flow separation is present, there are significant deflections of the skin-friction lines on both the upper and lower part of the STR. This is due to fact that the fluid flow into the fan is partly blocked by the inlet separation bubble. In the BLS case, where the blockage effect vanishes, more skin-friction lines are converged in the front part of the shroud. This finding is consistent with the distribution of the instantaneous space-filling streamlines, which are passing through the mid-interface and colored by the Mach number (see Fig. 5.44(b)). Considering the BLS case, more space-filling streamlines are ingested by the anti-torque rotor as the blockage effect vanishes. In addition, levels of Ma, in particular on the

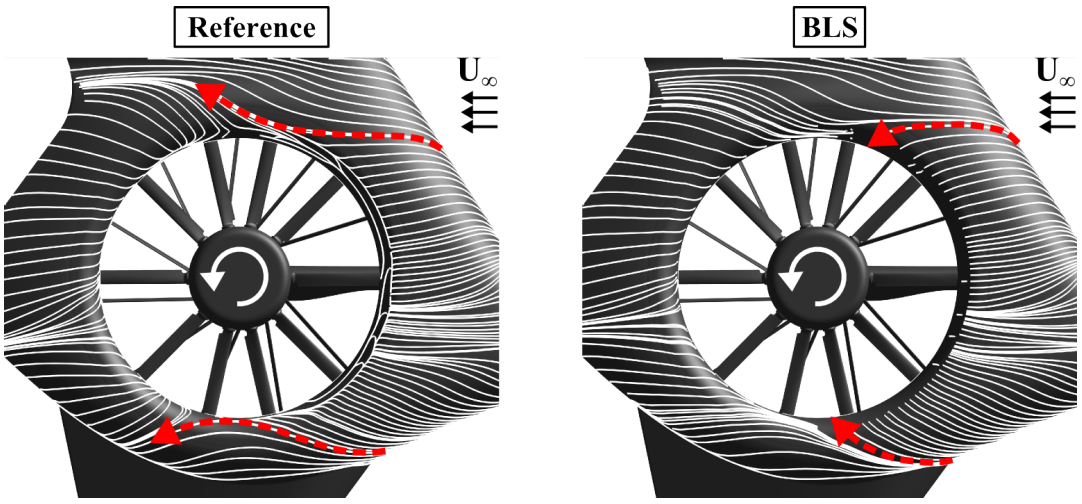

(a)

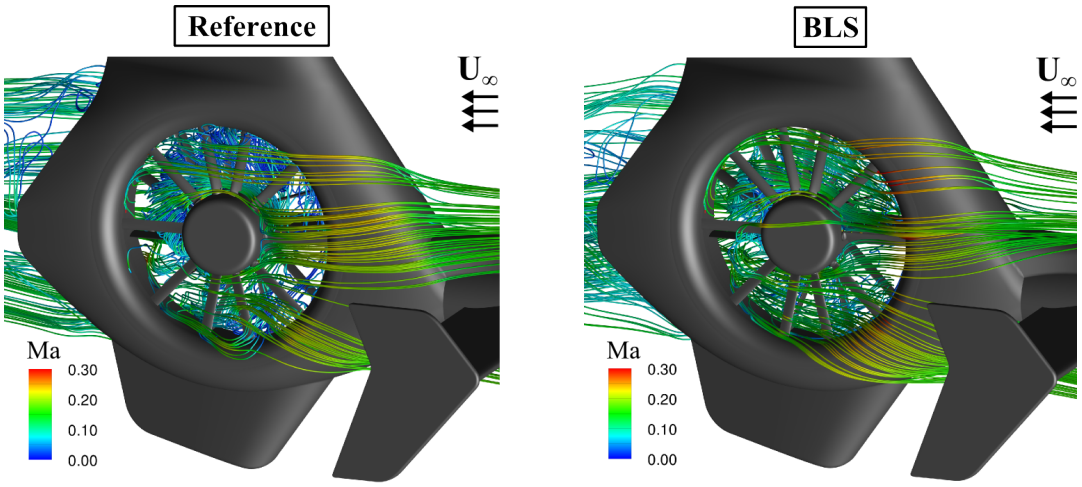

(b)

Figure 5.44: Comparison of (a) time-averaged skin-friction lines visualized on the STR shroud and (b) instantaneous space-filling streamlines colored by Ma between the reference and BLS case.

collector lip are higher in the BLS case as the effective contour gradient is recovered and thus a stronger flow acceleration occurs. Levels of Ma in the stator row are also higher in the case of non-inflow distortion (BLS case). As a consequence of the elimination of the blockage effect, the BLS case exhibits a higher value of the non-dimensional mass flow rate ($\mu_{f,\mathrm{BLS}} = 0.251$), averaged over the fan mid-interface, than the reference case ($\mu_{f,\mathrm{Ref}} = 0.157$).

5.4.2.3 Surface pressure distribution

Fig. 5.45(a) shows instantaneous distributions of C_p on the STR shroud for the reference and BLS case. Significant levels of negative C_p in the front part of the collector lip indicate

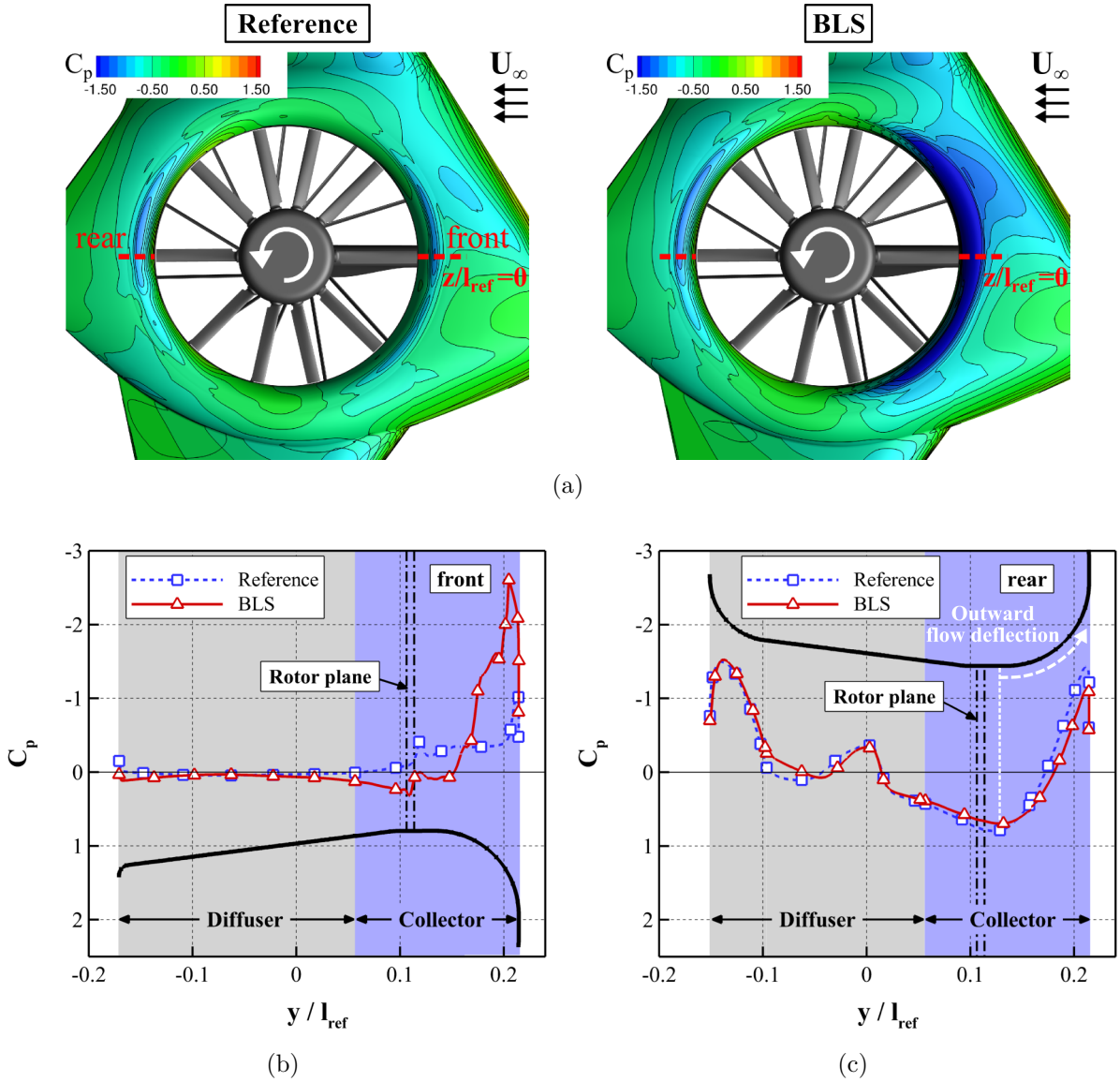

Figure 5.45: Comparison of surface pressure coefficient C_p between the reference and BLS case: (a) on the STR shroud, (b) streamwise distribution in the front part, and (c) in the rear part of the STR.

that the suction effect in the BLS case is substantial due to the stronger flow acceleration caused, on the on hand, by the recovered effective lip radius, and on the other hand, by the additional flow acceleration forced through the active flow control.

In Figs. 5.45(b) and 5.45(c), comparisons of the streamwise distribution of C_p are made between the reference and BLS case in the front part ($\psi_f = 0°$), and rear part of the STR ($\psi_f = 180°$), respectively. The BLS case yields a significant increase of the suction peak (147% higher compared to the reference case) in the front part of the collector lip. An abrupt change of C_p in the vicinity of the rotor plane is due to the presence of the tip-leakage vortex. In the BLS case, the impact of the tip-leakage vortex is observed further downstream than in the reference case as the blade generates a negative load, thus the tip-leakage vortex formation occurs on the blade lower side (see Sec. 5.4.3.6). In the rear part of the STR, the C_p distribution on the rotor and stator casing is quite similar for both simulation cases: (1) outward deflection of entering cross flow on the rotor casing, (2) disturbance of the streamwise pressure recovery in the stator row due to the secondary flow zones, and (3) accelerating flow on the curvature of the diffuser part. This clearly documents that the rear part is not affected by the inflow distortion of the collector lip flow separation.

Fig. 5.46 shows the time-averaged anti-torque thrust $\overline{C}_y$ of respective components of the STR in the high-speed forward flight condition. Compared to the reference case, the BLS case yields a higher $\overline{C}_y$ not only in the collector part but also on the STR shroud (mainly on the inlet side) as the recovered suction effect of the collector lip supports further flow acceleration on the STR shroud (see also Fig. 5.45(a)). Other components of

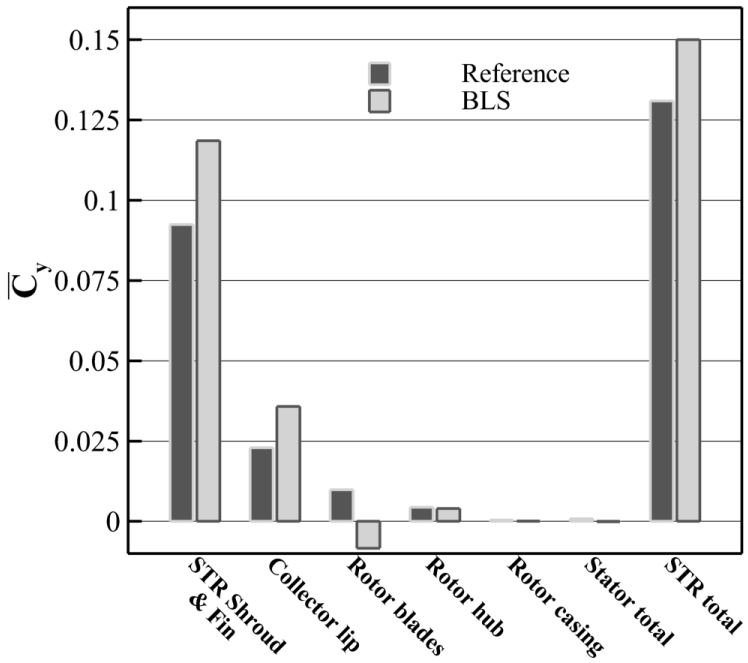

Figure 5.46: Time-averaged anti-torque thrust $\overline{C}_y$ of respective STR components in the high-speed forward flight condition for the reference and BLS case.

the STR do not indicate any significant differences in $\overline{C}_y$, except the rotor blades, which generate a negative thrust if the ISB is eliminated. It indicates that the inflow distortion alters the blade aerodynamic characteristics substantially (see Sec. 5.4.3.4).

5.4.2.4 Velocity distributions

In the following, the instantaneous distribution of the fan axial u_a/U_{tip}, circumferential u_c/U_{tip}, and radial velocity ratio u_r/U_{tip} are presented for diverse cross-sectional planes located in the **ROTOR**– and **STATOR**–domain (see Fig. 5.47) to give a more detailed insight into the flow field characteristics inside the duct fairing. Considering the reference case and the cross-sectional plane located upstream of the rotor plane ($y/l_{ref} = 0.04$), the influence area of the ISB can be identified with positive values of u_a/U_{tip} in the first and fourth quarter, indicating a velocity vector pointing outwards from the plane (see Fig. 5.48(a)). In front of the rotor hub ($\psi_f = 0°$), the reference case indicates higher $|u_a/U_{\text{tip}}|$ values than the BLS case. In the BLS case, $|u_a/U_{\text{tip}}|$ gradually decreases from the collector lip to the rotor hub. Both simulation cases indicate further reverse flow regions in the second and third quarter of the cross-sectional plane. These are related to the rotor-hub wake and the outward deflection of the entering cross flow on the rotor casing.

The ratio of u_c/U_{tip} is determined in the cylindrical coordinate system (counterclockwise is positive), therefore u_c/U_{tip} is positive on the retreating blade side and negative on the advancing side due to the direction of the incoming cross flow (from right to left in Fig. 5.48(b)). The distribution of $|u_c/U_{\text{tip}}|$ in the BLS case is homogeneous, while, in the reference case an abrupt sign change occurs in the influence area of the ISB (negative u_c/U_{tip} in the first quarter and positive in the fourth quarter). Similar to u_c/U_{tip}, the u_r/U_{tip} distribution exhibits a change in sign in the reverse flow regions. Comparing the magnitude of the velocity ratios, it is observed that u_c/U_{tip} is higher than u_a/U_{tip}, highlighting that the swirl angle above the rotor plane is significant in this flight condition.

On the plane located underneath the rotor plane and above the stator row ($y/l_{\text{ref}} = -0.025$), the velocity ratios exhibit a very similar distribution to that at $y/l_{\text{ref}} = 0.04$ (see Fig. 5.49). Particularly in the reference case, the convected ISB leads to a sign change of u_a/U_{tip}, u_c/U_{tip}, and u_r/U_{tip}. In both simulation cases, further reverse flow regions are observed in the vicinity of the blade root, which indicate the blade root flow separation. The blade wake is also identified by relatively low $|u_a/U_{tip}|$ values, and it is more pronounced in the BLS case.

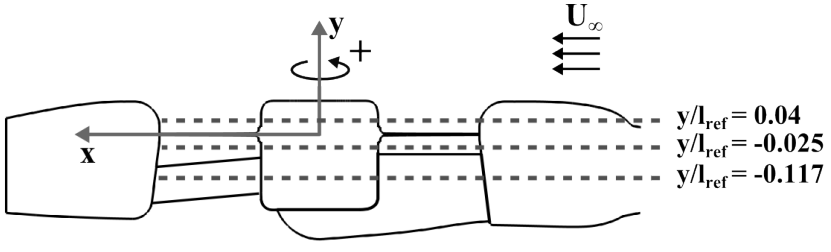

Figure 5.47: Position of cross-sectional planes.

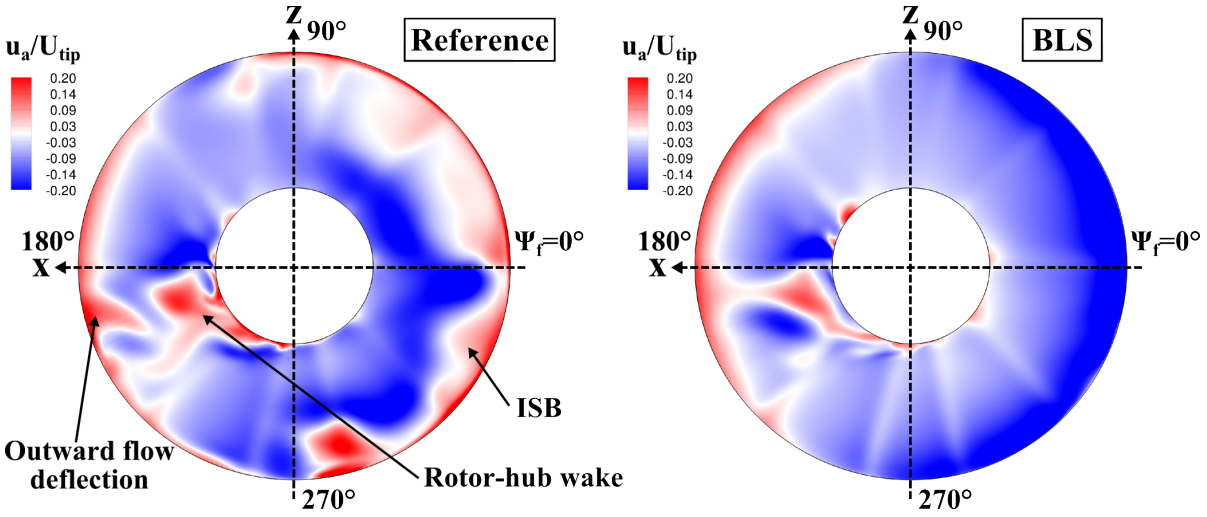

(a)

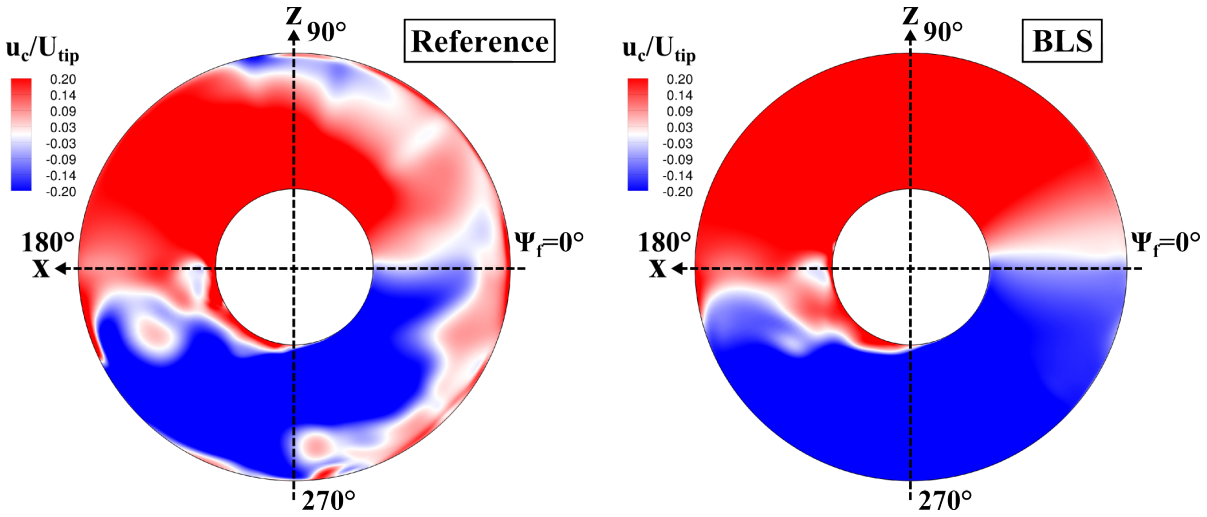

(b)

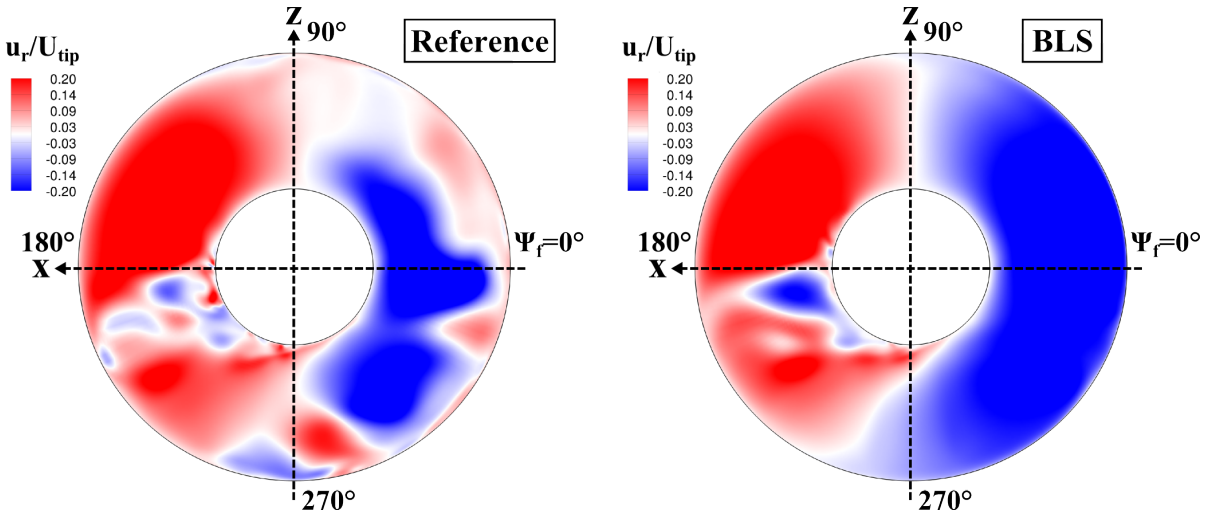

(c)

Figure 5.48: Comparison of non-dimensional velocity distributions on the cross-sectional plane at $y/l_{\text{ref}} = 0.04$ between the reference and BLS case: (a) axial velocity ratio u_a/U_{tip}, (b) circumferential velocity ratio u_c/U_{tip}, and (c) radial velocity ratio u_r/U_{tip}.

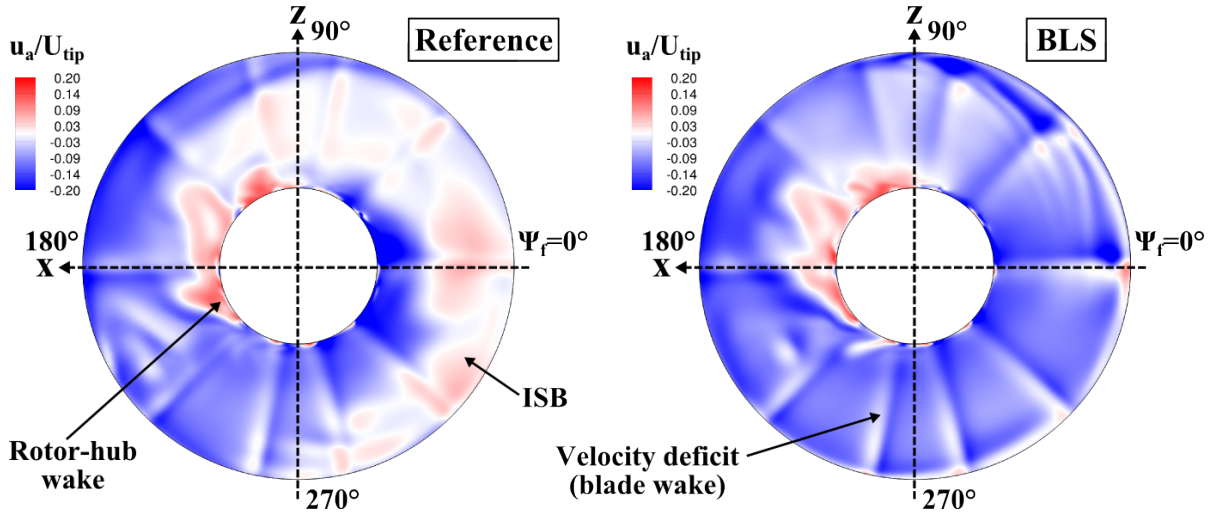

(a)

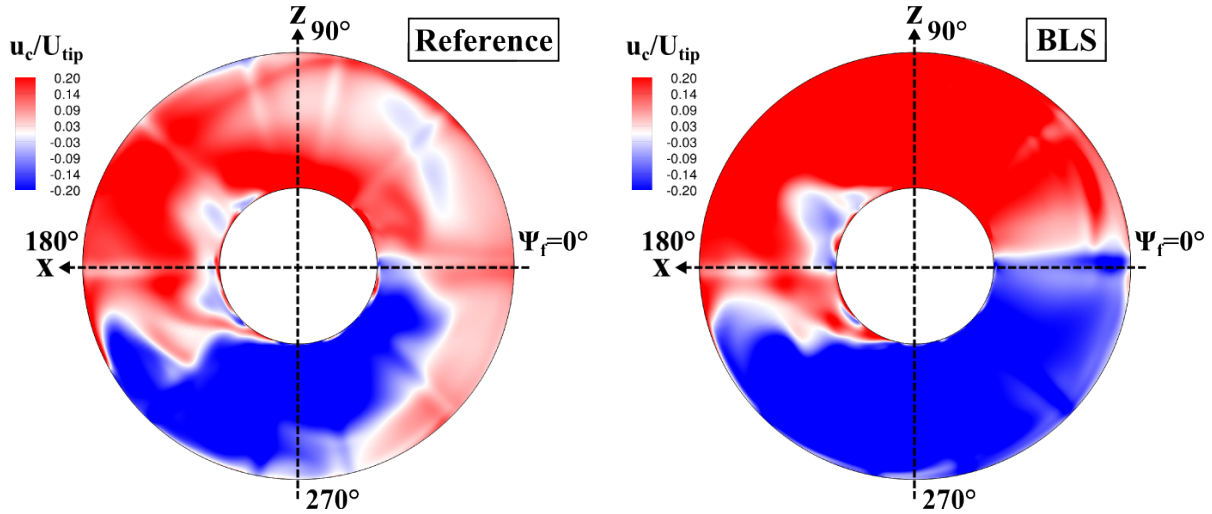

(b)

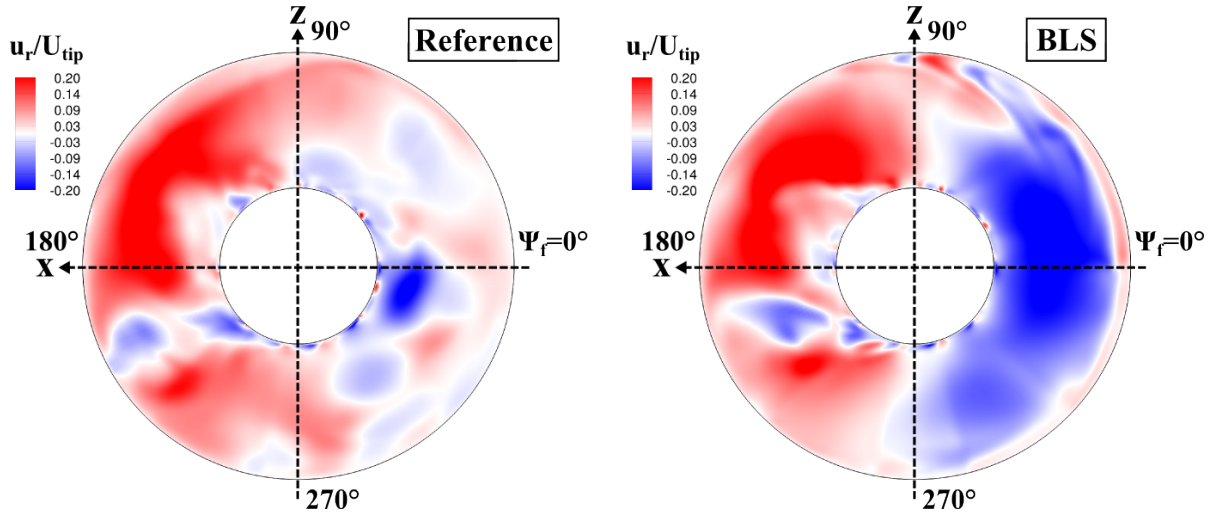

(c)

Figure 5.49: Comparison of non-dimensional velocity distributions on the cross-sectional plane at $y/l_{\text{ref}} = -0.025$ between the reference and BLS case: (a) axial velocity ratio u_a/U_{tip}, (b) circumferential velocity ratio u_c/U_{tip}, and (c) radial velocity ratio u_r/U_{tip}.

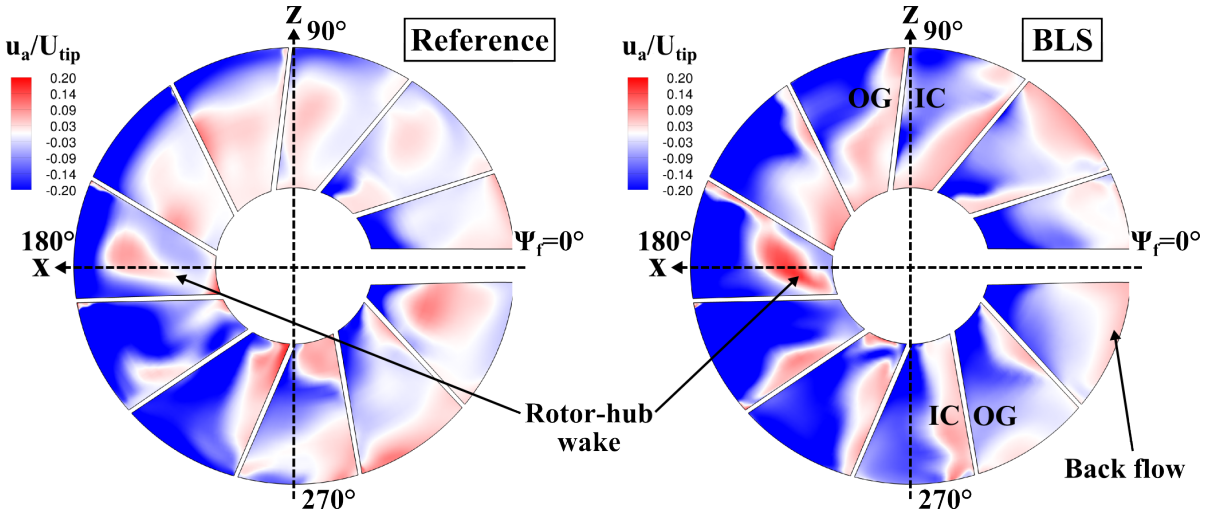

(a)

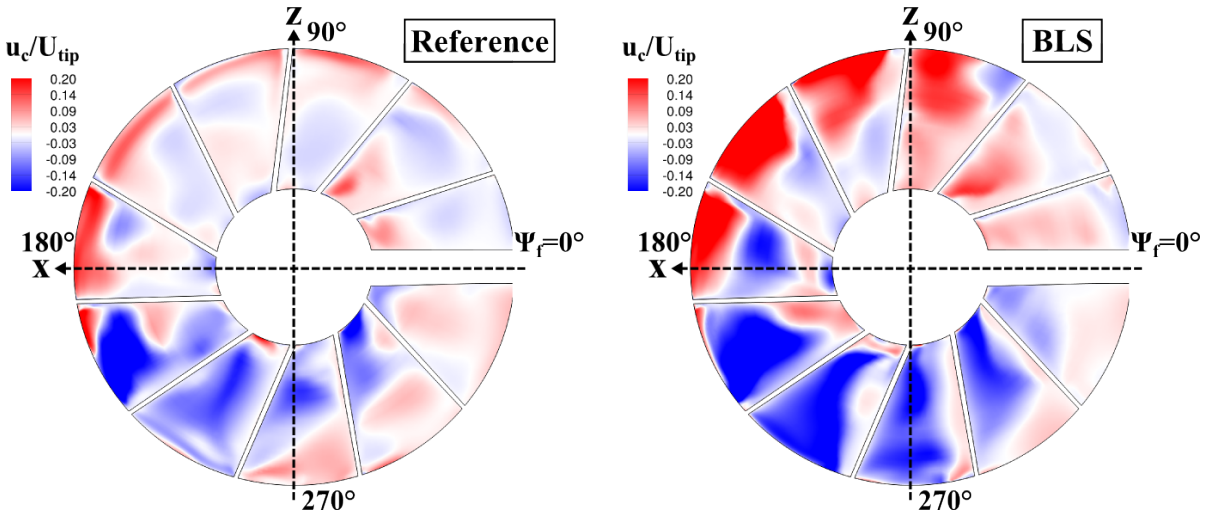

(b)

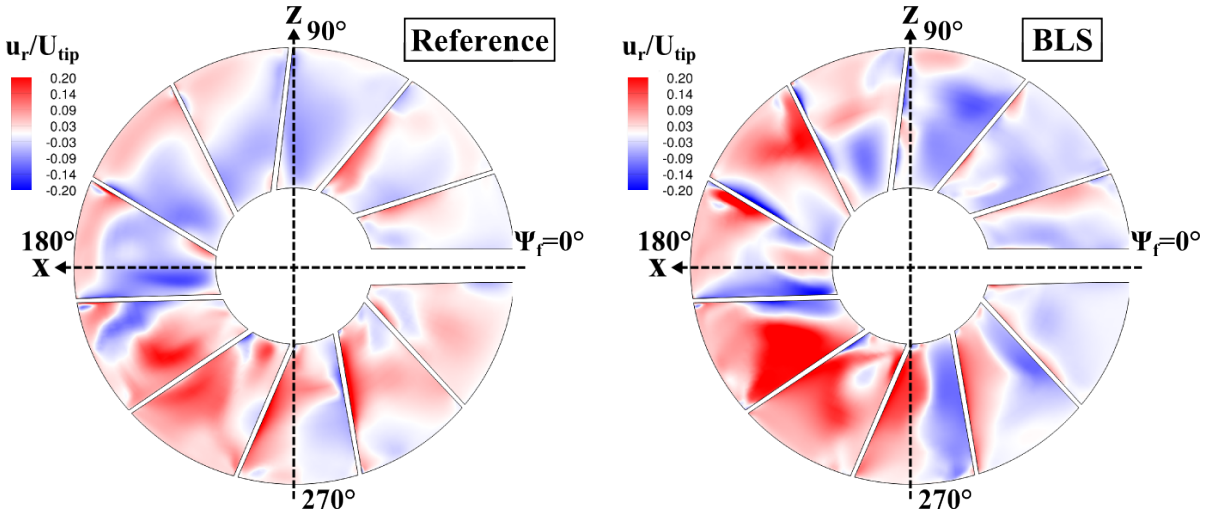

(c)

Figure 5.50: Comparison of non-dimensional velocity distributions on the cross-sectional plane at $y/l_{\text{ref}} = -0.117$ between the reference and BLS case: (a) axial velocity ratio u_a/U_{tip}, (b) circumferential velocity ratio u_c/U_{tip}, and (c) radial velocity ratio u_r/U_{tip}.

The flow field in the stator row is characterized by diverse reverse flow regions, as indicated in Fig. 5.50(a). In the reference case, it is due, on the one hand, to the transmitted inflow distortions (e.g. ISB, rotor-hub wake), and on the other hand, to the fact that under cross-flow condition, the stator vanes encounter a significantly increased incidence angle due to the low axial to circumferential velocity ratio (u_a/u_c) at the upstream area of the stator row. In addition, the high-momentum cross flow significantly blocks the low-momentum fan exit flow, and therefore, the flow recirculation in the stator row is further increased. On the contrary, the positive u_a/U_{tip} (reverse flow regions) observed in the BLS case is mainly due to the flow separation at the stator vanes (except the ingested hub wake at $\psi_f = 180°$ and the entering cross flow in the front part of the diffuser). It shows a strong correlation with the direction of u_c/U_{tip} at the upstream of the stator row. Hence, on the retreating blade side (first and second quarter), the reverse flow zone are observed on the outgoing blade (OG) side, while, on the advancing blade (third and fourth quarter) the flow separation occurs on the incoming blade (IC) side (see also Fig. 5.56).

5.4.3 Rotor/ISB Interaction

5.4.3.1 Total pressure distortion

In order to give an overview on the interaction between the rotating blades and the inlet separation bubble, instantaneous $p_t/p_{t,\infty}$ values are presented on the cross-sectional plane located upstream of the rotor plane ($y/l_{\text{ref}} = 0.04$) (see Fig. 5.51(a)). The position of the respective rotor blade at the current simulation time step is indicated by dashed lines. As already observed in Fig. 5.40 and Fig. 5.43, the ISB leads to a significant total pressure distortion above the rotor plane. The influence area of the inlet distortion is clearly identified by low levels of $p_t/p_{t\infty}$ along the collector lip ($0° < \psi_f < 120°$: retreating blade side, $260° < \psi_f < 360°$: advancing blade side). Considerably low levels of $p_t/p_{t\infty}$ are observed above the rotor blades R1 to R3 as well as R9 to R10, which are all passing through the ISB at the current simulation time step. The reason therefore is that an additional velocity magnitude is induced on the blade upper side by passing the recirculating flow zone, therefore resulting in noticeable levels of negative C_p (see also Fig. 5.52). The low levels of $p_t/p_{t\infty}$ are more pronounced on the blades R1 to R3, which are located on the advancing blade side. In the case of non inflow distortion (BLS case), the $p_t/p_{t\infty}$ distribution is mainly influenced by the blade pressure field. In both simulation cases, the rotor-hub wake is also clearly visible in the rear part of the STR (third quarter of the STR inlet).

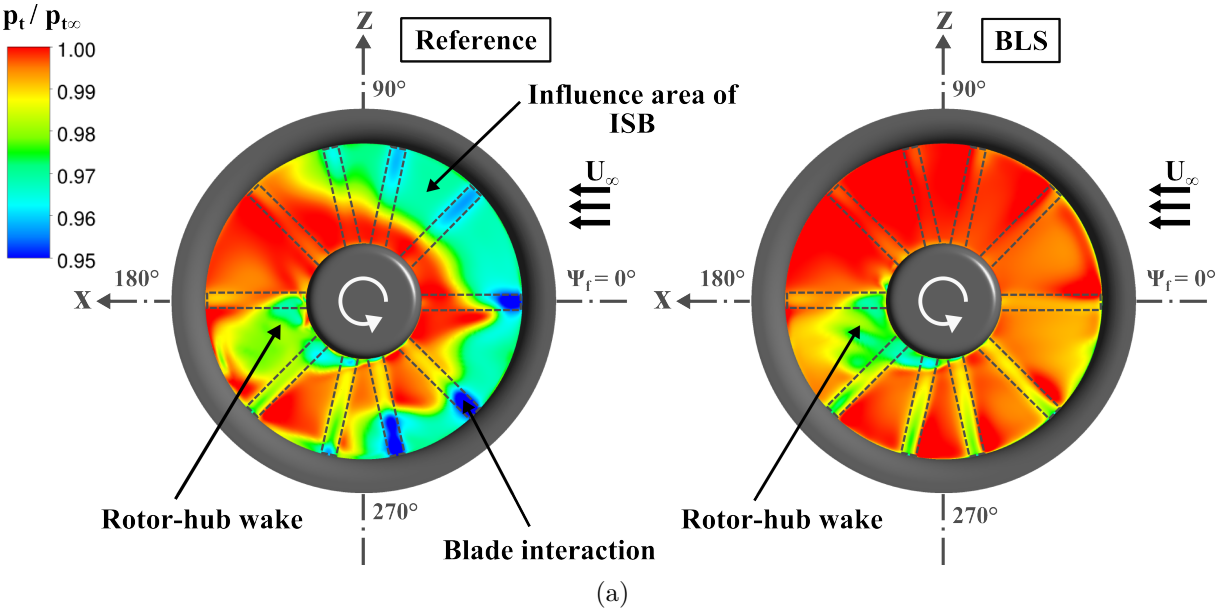

(a)

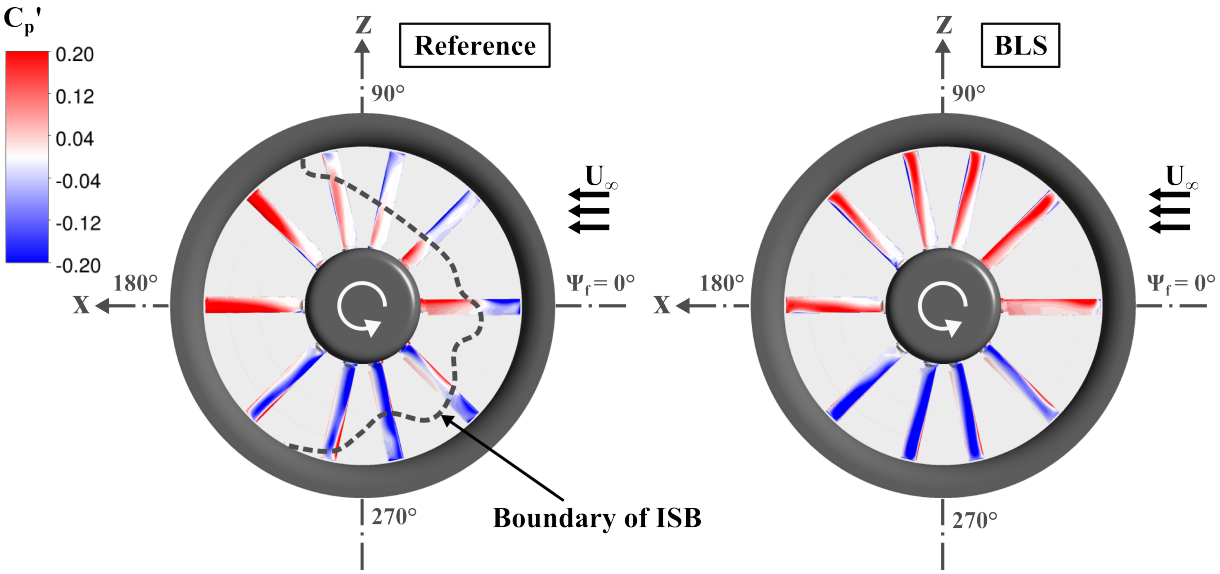

(b)

Figure 5.51: Inlet flow distortions: (a) instantaneous distributions of the total pressure ratio $p_t/p_{t,\infty}$ on the plane $y/l_{\text{ref}} = 0.04$ and (b) blade pressure coefficient fluctuations $C_p'(\psi_f) = C_p(\psi_f) - \overline{C}_p$.

5.4.3.2 Blade surface pressure

To investigate the impact of the ISB on the anti-torque rotor, the surface pressure coefficient fluctuations C_p' are considered (see Fig. 5.51(b)). Values of C_p' are determined by the subtraction of the surface pressure at the current azimuth $C_p(\psi_f)$ from the circumferentially averaged mean pressure $\overline{C}_p$ (averaged over five blade passing periods). As expected, the blade experiences an abrupt change in C_p' in the spanwise direction when the blade intersects with the ISB. Contrary to this, the C_p' distribution is more uniformly in the blade spanwise direction in the BLS case and indicates only the influence of the relative

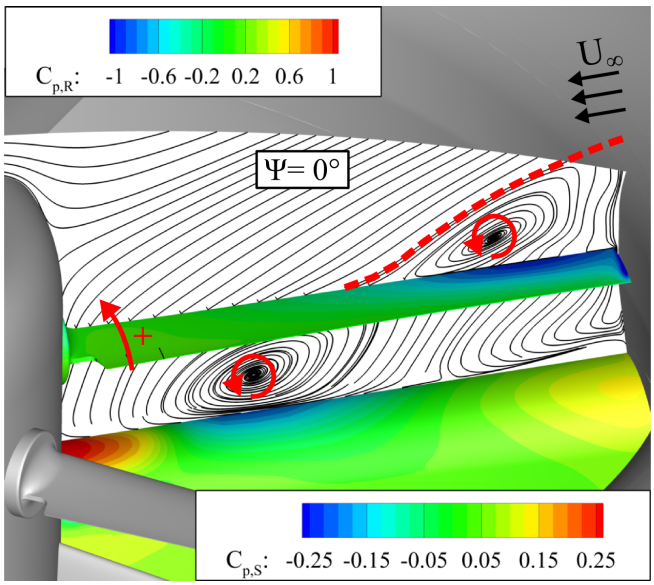

Figure 5.52: Rotor/ISB interaction visualized by instantaneous streamlines on the horizontal symmetry plane ($z/l_{\text{ref}} = 0$) and surface pressure coefficient on the blade R1, $C_{p,R}$, and the drive shaft fairing, $C_{p,S}$.

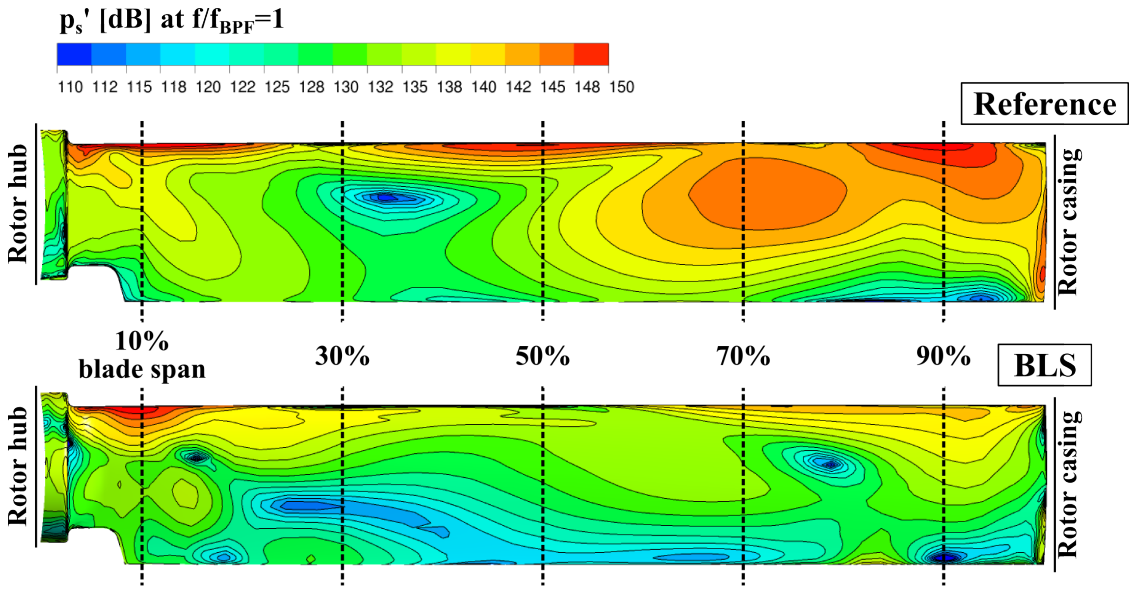

Figure 5.53: Comparison of surface pressure fluctuations p'_s of the blade R2 at $f/f_{\text{BPF}} = 1$ between the reference and BLS case.

motion between the blade and the incoming cross flow.

The findings above are further supported by the surface pressure fluctuations p'_s at $f/f_{\text{BPF}} = 1$, presented in Fig. 5.53 . In the reference case, a region with significant pressure disturbances is detected on the blade upper surface. The region of high p'_s is extended from approximately 50% blade span to the blade tip and consists with the influence area of the ISB. On the contrary, p'_s is distributed uniformly in the spannwise direction if the inflow distortion is not present. Since the blade generates sound if it experiences a

fluctuating load, the region exhibiting high pressure disturbances is the source region of noise emitting by the interaction. The relatively high pressure disturbance observed at the leading edge from 70% blade span to the blade tip in the BLS case is associated with the stagnation point that is shifted towards the blade upper side as the blade undergoes a negative incidence angle in this region (see also Sec. 5.4.3.3). Both simulation cases yield further regions with high p'_s in the vicinity of the blade root and the blade tip. The former is referred to the interaction with the the blade-root wake as well as of the rotor-hub wake, whereas the latter is associated with the tip-leakage vortex that is more weakly pronounced in the BLS case because of the negative effective incidence angle (see also Sec. 5.4.3.6).

5.4.3.3 Blade incidence angle variation

The inflow distortion, provoked by the lip flow separation, significantly change the blade incidence angle, as indicated in Fig. 5.54(a). In the plot, the effective incidence angle ratio $\alpha_{\text{eff}}/\alpha_{\text{eff,R2}}$ of respective rotor blades, obtained at the current simulation time step and at 90% of the fan radius ($0.9r$), is presented. A comparison between the distortion (reference case) and non-distortion case (BLS case) is made. According to the plot, there is a large difference in $|\alpha_{\text{eff}}/\alpha_{\text{eff,R2}}|$ between the reference and BLS case for the blades R1, R2, R3, R9, and R10. These blades are located under the influence of the ISB at the current simulation time step (see also Fig. 5.56). In particular, the blades R1, R2, R3 and R10 encounter a positive $\alpha_{\text{eff}}/\alpha_{\text{eff,R2}}$ in the recirculating flow region, while in the BLS

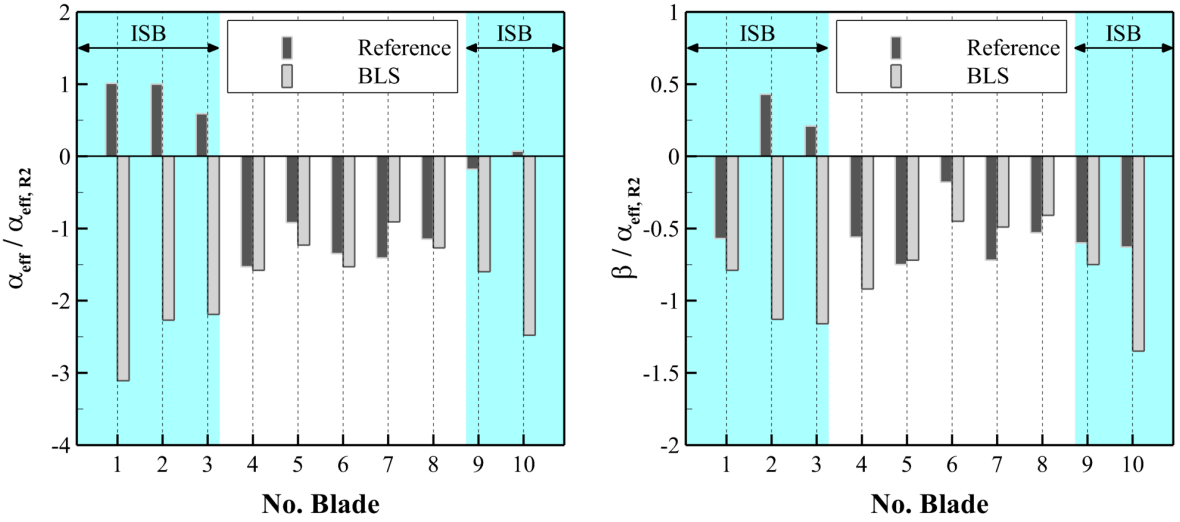

Figure 5.54: Comparison of (a) instantaneous effective blade incidence angle ratio $\alpha_{\text{eff}}/\alpha_{\text{eff,R2}}$ and downwash angle ratio $\beta/\alpha_{\text{eff,R2}}$ at 90% of the fan radius between the reference and BLS case; see Fig. 5.56 for the current position of blades.

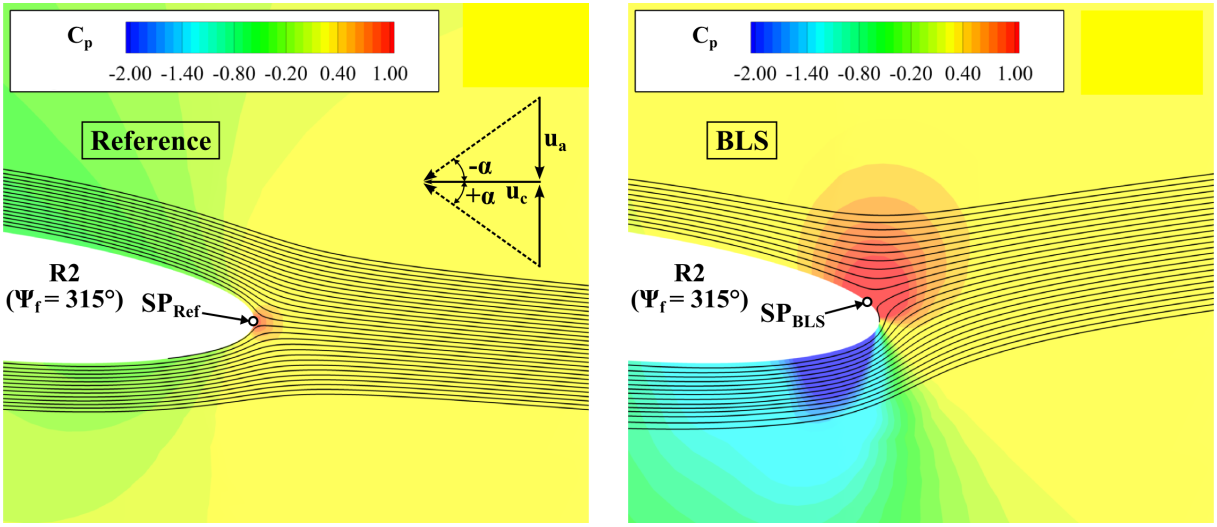

(a) (b)

Figure 5.55: Instantaneous streamlines and pressure coefficient C_p around the leading edge of the blade R2 at 90% of the fan radius for the (a) reference and (b) BLS case (for the current position see Fig. 5.56).

case, these blades experience a negative $\alpha_{\text{eff}}/\alpha_{\text{eff,R2}}$. In Figs. 5.55(a) and 5.55(b), the flow field around the leading edge of the blade R2 is visualized by means of instantaneous streamlines and pressure coefficient distributions at 90% of the fan radius for the reference and BLS case, respectively. The interaction clearly shifts the stagnation point (SP) being on the upper surface of the blade towards the leading edge. Continuing to $\alpha_{\text{eff}}/\alpha_{\text{eff,R2}}$ in Fig. 5.54(a), the remaining blades (R4 to R8), which do not interact with the ISB at the current simulation time step, experience a negative $\alpha_{\text{eff}}/\alpha_{\text{eff,R2}}$ at this fan radius ($0.9r$), and show a similar magnitude as in the BLS case.

The interaction with the ISB also alters the blade downwash angle ratio $\beta/\alpha_{\text{eff,R2}}$, as given in Fig. 5.54(b). Compared to the BLS case, $|\beta/\alpha_{\text{eff,R2}}|$ of the reference case is smaller in the influence area of the ISB, highlighting that the blade wake could have a more significant impact on the adjacent blade (see also Fig. 5.56).

5.4.3.4 Blade load distortion

As observed in the previous sections, the Rotor/ISB interaction leads to noticeable surface pressure fluctuations as well as the blade incidence variations. Therefore, a significant change of the blade load is expected, when the blade is passing through the ISB. To evaluate it, a comparison of the blade load history $C_{y,\text{R1}}(\psi_f)$ between the distortion and non-distortion case is made (see Fig. 5.57(a)). The overall blade load of the blade R1 is obtained by spanwise integration of the sectional blade load. The analysis of the blade load over one blade passing period indicates that the inflow distortion affects markedly the blade aerodynamic characteristics: positive values of $C_{y,\text{R1}}$ in the influence area of the ISB.

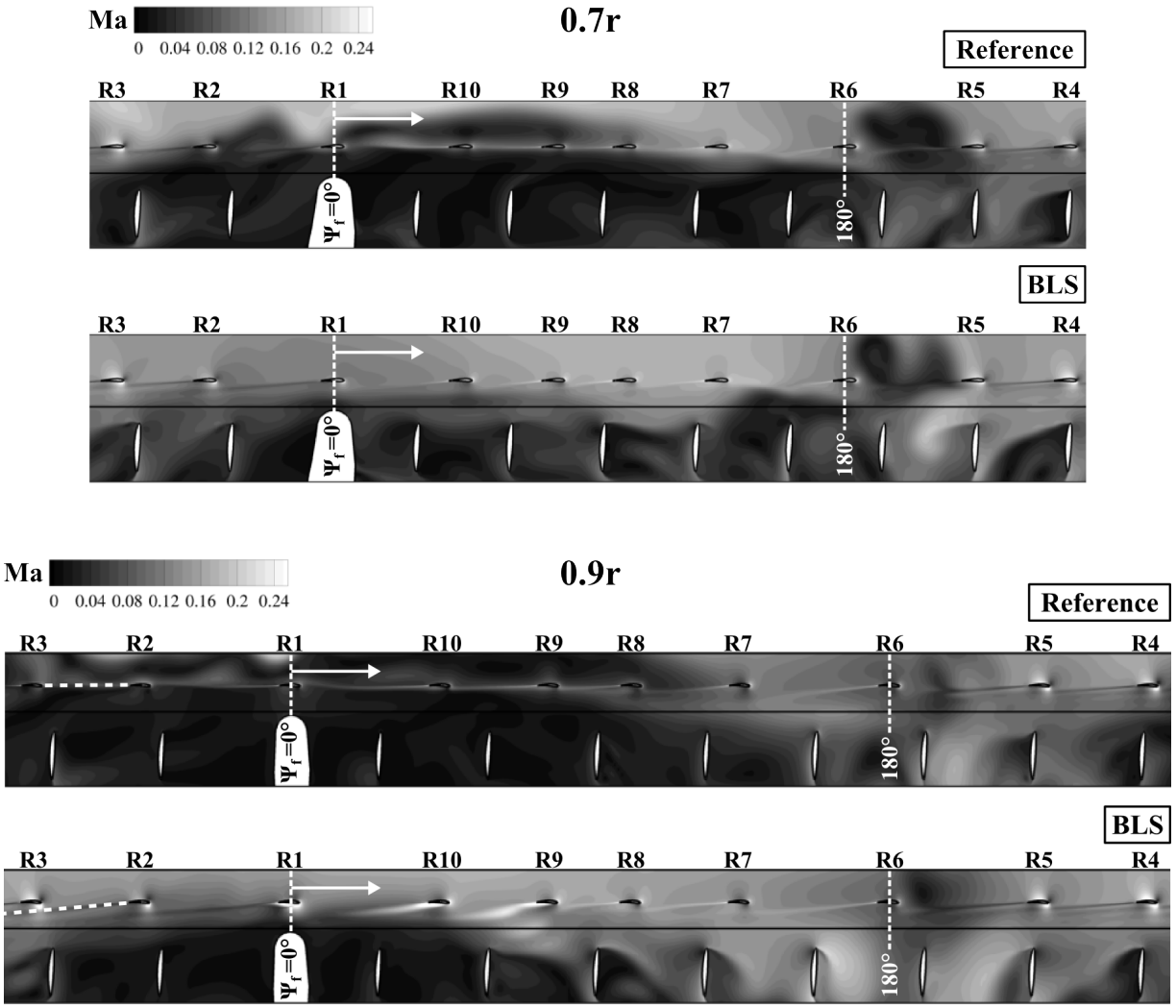

Figure 5.56: Instantaneous Ma distributions on coaxial planes located inside the fan at 70% and 90% of the fan radius for the reference and BLS case.

At the starting point, the rotor blade R1 is located directly upstream of the drive shaft fairing ($\psi_f = 0°$) for both simulation cases, thus the blade span coincides with the direction of the incoming cross flow. At this fan azimuth, the blade R1 generates a positive $C_{y,\mathrm{R1}}$ if the ISB is present. On the contrary, the blade load in the non-distortion case exhibits a negative $C_{y,\mathrm{R1}}$ with almost twice the magnitude.

The maximum difference in $C_{y,\mathrm{R1}}$ between the reference and BLS case appears at $\psi_f = 15°$ ((a) in Fig. 5.57(a)). Comparing the chordwise C_p distribution at this fan azimuthal position, as given in Fig. 5.58(a), significant differences are found between the reference and BLS case, particularly at the blade sections which are under the influence of the ISB ($0.7r$, $0.9r$, and $0.995r$). In the reference case, C_p is negative on the blade upper surface. This is due to the interaction with the ISB. As a consequence of this, the blade generates a positive $C_{y,\mathrm{R1}}$ at this fan azimuthal position ($\psi_f = 15°$). In the BLS case, the lower surface of the blade R1 at these blade sections undergoes a negative C_p up to 65% blade chord, and the stagnation point is located on the upper blade surface. It highlights

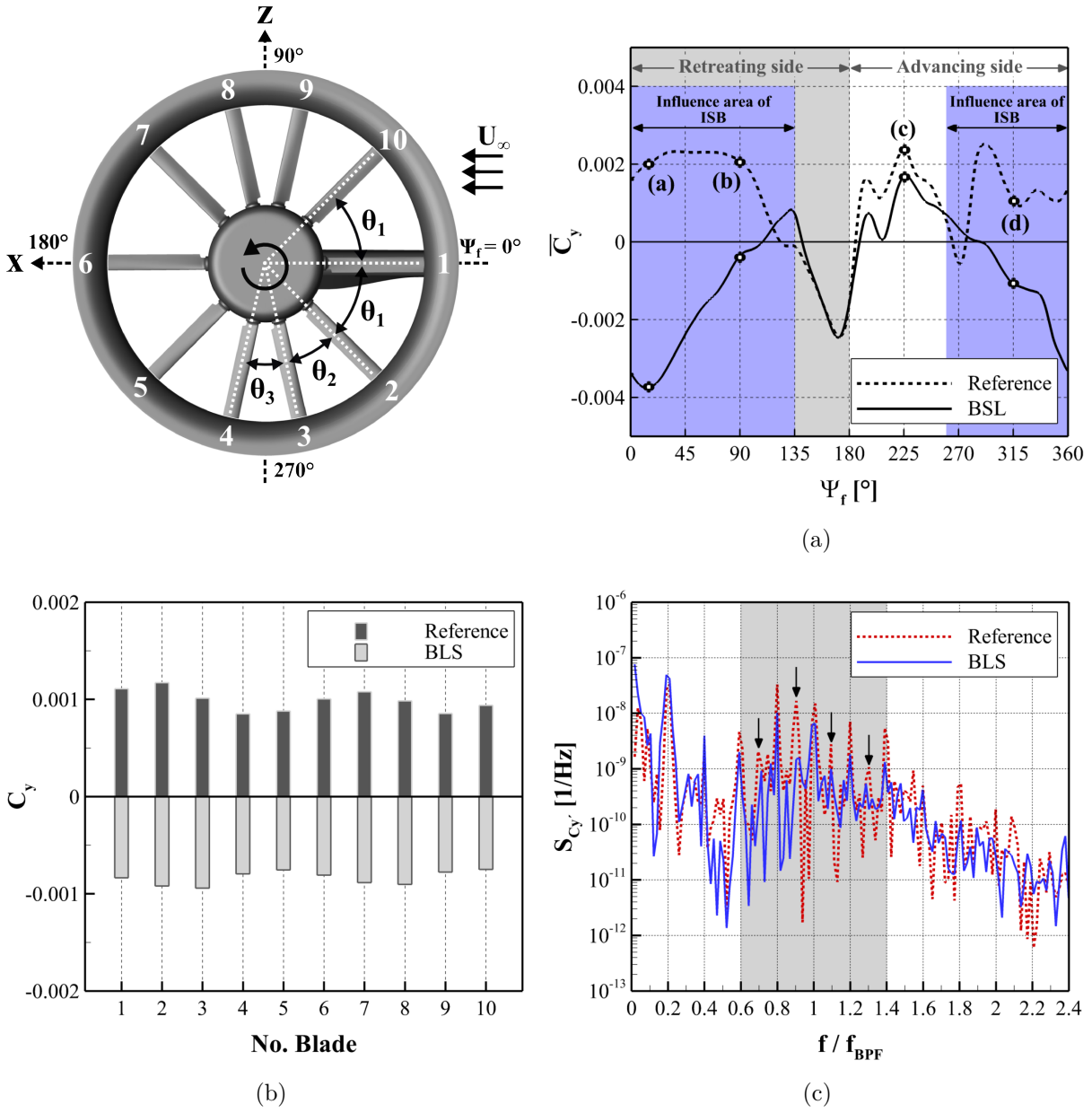

Figure 5.57: Blade load distortions: (a) load history $C_y(\psi_f)$ of the blade R1 over one blade passing period, (b) mean load $\overline{C}_y$ distributions of respective blades, and (c) power spectral densities of blade load fluctuations $S_{C_y'}$ for the reference and BLS case.

that the blade encounters a negative incidence angle, and explains the negative value of $C_{y,\mathrm{R1}}$ at this fan azimuthal position ($\psi_f = 15°$).

In the azimuth range of $15° < \psi_f < 135°$, which is consistent with the influence region of the ISB on the retreating blade side, the blade of the reference case generates a positive $C_{y,\mathrm{R1}}$. In contrast, the blade R1 in the BLS case generates a negative blade load in this azimuth range, and the curve of $C_{y,\mathrm{R1}}$ exhibits a positive slope. At $\psi_f = 90°$ ((b) in Fig. 5.57(a)), where the blade span is perpendicular to the direction of the incoming cross flow,

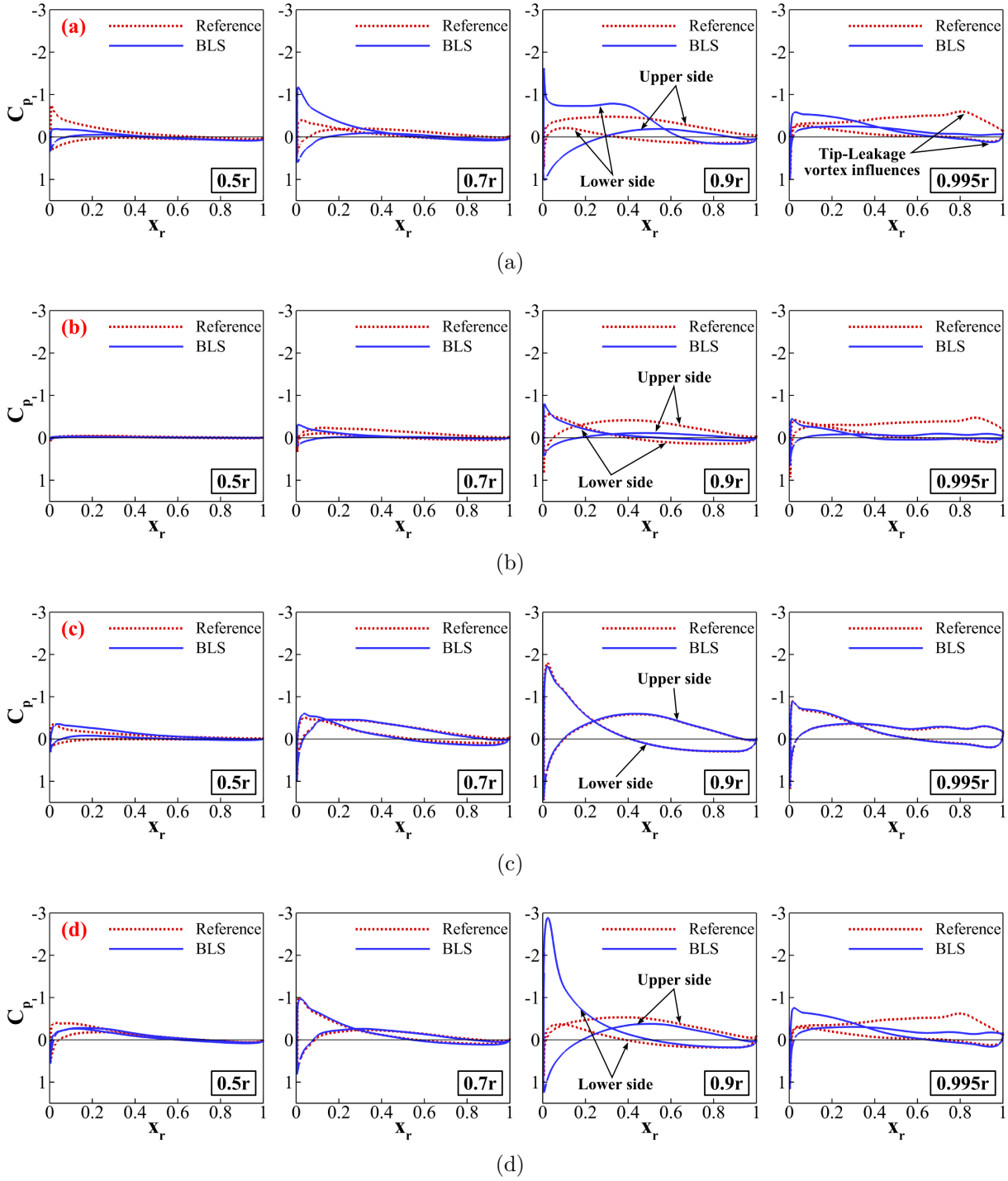

Figure 5.58: Chordwise distributions of the pressure coefficient C_p of the blade R1 at 50%, 70%, 90%, and 99.5% of the fan radius for (a) $\psi_f = 15°$, (b) $\psi_f = 90°$, (c) $\psi_f = 225°$, and (d) $\psi_f = 315°$ for the reference and BLS case.

the blade of the reference case still generates a significant level of $C_{y,\mathrm{R1}}$ due to the negative C_p distribution on the blade upper surface (see Fig. 5.58(b)). It is mostly induced by the ISB.

In the azimuth range of $135° < \psi_f < 180°$, in which the blade is not in the ISB, both simulation cases indicate almost an identical slope and values of $C_{y,\mathrm{R1}}$. Near $\psi_f = 180°$, where the blade span coincides with the direction of the incoming cross flow, both simulation cases reach local maxima of $|C_{y,\mathrm{R1}}|$ with a negative value. $|C_{y,\mathrm{R1}}|$ is, however, smaller than that at $\psi_f = 0°$ as the blade is under strong influence of the rotor hub. From this azimuth ($\psi_f = 180°$), $C_{y,\mathrm{R1}}$ of both simulation cases exhibits a positive slope because the blade is on the advancing side.

On the advancing side, a strong variation in the blade load is observed in both simulation cases in the azimuth range of $180° < \psi_f < 240°$. It is mostly related to the interaction with the rotor-hub wake. At $\psi_f = 225°$ ((c) in Fig. 5.57(a)), the slope of the $|C_{y,\mathrm{R2}}|$ curve of both simulation cases changes to negative. Regarding the chordwise C_p distribution at $\psi_f = 225°$ (see Fig. 5.58(c)), there are no differences between the reference and BLS case, indicating the blade is not affected by the ISB yet.

From $\psi_f = 260°$, the blade load starts to deviate from each other as the blade R1 is now in the recirculating flow region. At $\psi_f = 315°$ ((d) in Fig. 5.57(a)), the blade of the reference case generates a positive blade load due to the interaction with the ISB. On the contrary, $C_{y,\mathrm{R1}}$ for the non-distortion case is negative as the blade undergoes a significant suction peak on the blade lower side (see Fig. 5.58(d)). Consequently, in the reference case, all blades reveal a positive mean blade load, as indicated in Fig 5.57(b). On the contrary, $\overline{C}_y$ in the BLS case is negative for all blades. The influence of the uneven blade spacing on the blade load is also clearly observed for both simulation cases.

The comparison of the power spectral densities of the overall blade load fluctuations $S_{C'_y}$ between the distortion and non-distortion case is given in Fig. 5.57(c). Compared to the reference case, a significant decrease in $S_{C'_y}$ is observed in the BLS case not only at the frequencies associated with the fan rotation and the uneven circumferential blade

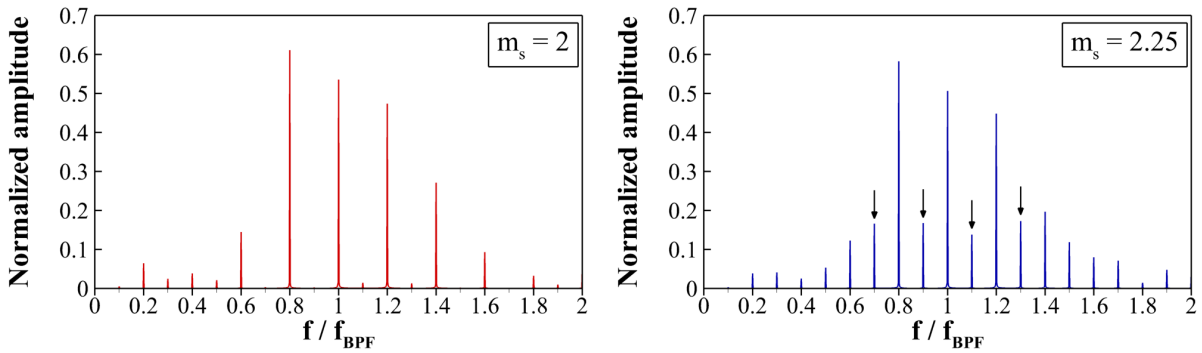

(a) (b)

Figure 5.59: Sinusoidal modulation effect of a ten-bladed generic fan configuration based on Eq. 1.3: (a) $m_s = 2$ and (b) $m_s = 2.25$.

spacing (e.g. $f/f_{\mathrm{BPF}} = 1 \pm 0.2n:\ n = 0,1,2$), but also at the frequencies in between (e.g. $f/f_{\mathrm{BPF}} = 0.7$, $f/f_{\mathrm{BPF}} = 0.9$, $f/f_{\mathrm{BPF}} = 1.1$, and $f/f_{\mathrm{BPF}} = 1.3$, indicated by arrows in Fig. 5.57(c)). The most pronounced increase with respect to the reference case is found at $f/f_{\mathrm{BPF}} = 0.9$. Thus, it is obvious that the rotor/ISB interaction is responsible for the increase in $S_{C'_y}$ at the frequencies corresponding to $f/f_{\mathrm{BPF}} = 1 \pm 0.1n$ with $n = 1,3$. As the aerodynamic characteristics of the blade is substantially and periodically changed in the recirculating flow region, it can be seen that the anti-torque rotor experiences a further sinusoidal phase modulation based on Eq. 1.3. In Figs. 5.59(a) and 5.59(b), the effect of the sinusoidal modulation of a ten-bladed generic fan configuration is presented for the case $m_s = 2$ (reference case) and $m_s = 2.25$ (further 0,25 modulation), respectively. In the case of $m_s = 2.25$, a significant increase in the pressure amplitude occurs at the frequencies $f/f_{\mathrm{BPF}} = 1 \pm 0.1n$ with $n = 1,3$, similar to the finding in Fig. 5.57(c).

5.4.3.5 Spectral analysis of pressure disturbances

In order to analyze the pressure disturbances resulting from the rotor/ISB interaction and propagating outwards, the power spectral densities of the pressure coefficient fluctuations $S_{C'_p}$ are determined for the inlet side of the STR (see Fig. 5.60). The pressure data is gathered over five blade passing periods at the stationary monitor points, located above the rotor plane ($y/l_{\mathrm{ref}} = 0.04$) and evenly distributed in the circumferential direction ($\Delta\psi_f = 10°$) at 70% and 90% of the fan radius, respectively. Regarding 90% of the fan radius, the BLS case indicates a noticeable decrease in $S_{C'_p}$ compared to the reference case. It is predominant at the frequencies related to the BPF ($f/f_{\mathrm{BPF}} = 1$) and its sidebands ($f/f_{\mathrm{BPF}} = 1 \pm 0.2n:\ n = 1,2$) at the fan azimuth range of $0° < \psi_f < 120°$ as well as of $260° < \psi_f < 360°$, which coincide with the influence area of the ISB. Since the recirculating flow region is periodically intersected by the blade, pressure disturbances appear at the frequencies related to the fan rotation and the uneven blade spacing, if they are measured at the stationary monitor points upstream of the rotor plane. The increased level of $S_{C'_p}$ on the retreating blade side in the reference case is only due to the rotor/ISB interaction. The $S_{C'_p}$ levels on the advancing blade side are the consequence of the superposition of the pressure disturbances provoked by the periodic impingement of the blade potential field, that is more significant on the advancing blade side due to the relative motion between the blade and the cross flow, and by the interaction with the ISB.

The noticeable levels of $S_{C'_p}$ at frequencies $0.1 < f/f_{\mathrm{BPF}} < 0.2$ on the advancing blade side ($270° < \psi_f < 360°$) in the reference case is due to the ingested vortical structures, such as the fuselage wake, horseshoe-like vortices of the shroud as well as of the horizontal stabilizer, and their interaction with the blades (see Sec. 5.5). It is, however, not observed in the BLS case as they are partly ingested into the suction slots. A further significant increase in $S_{C'_p}$ observed at $\psi_f = 0°$ in the BLS case is due to the rotor/shaft-fairing interaction, which is more pronounced, if the inflow distortion does not exist (see also Sec. 5.4.3.7). A similar analysis is also made for the monitor points located at 70% of the fan radius.

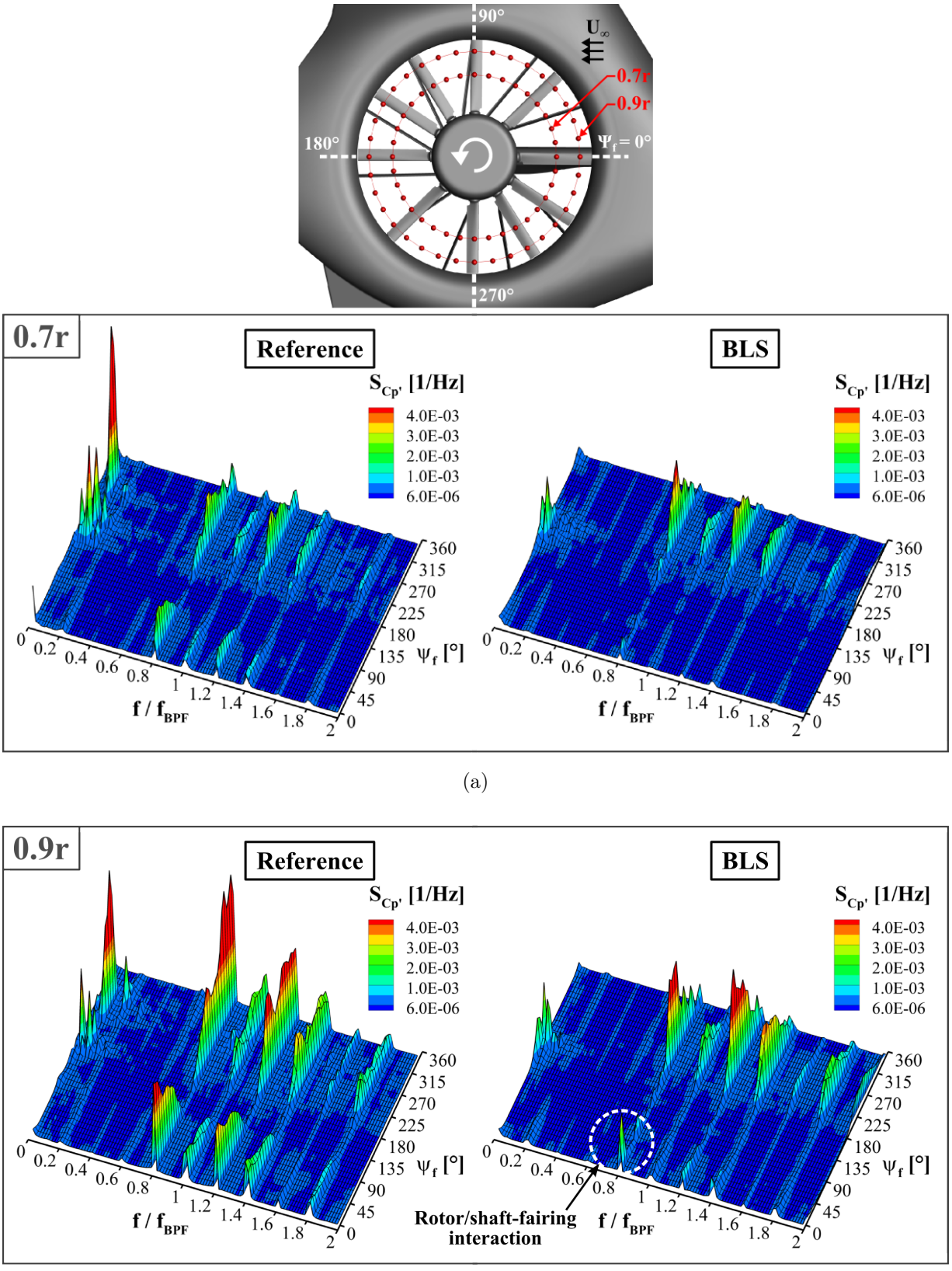

(a)

(b)

Figure 5.60: Power spectral densities of pressure coefficient fluctuations $S_{C_p'}$ at monitor points located above the rotor plane ($y/l_{\text{ref}} = 0.04$) at (a) 70% and (b) 90% of the fan radius for the reference and BLS case.

5.4.3.6 Tip-leakage vortex

In the analysis of the hovering condition, it has been identified that the drive shaft fairing substantially alters the flow characteristics in the region of the tip leakage (cf. Sec. 4.1.3.1). Thus, similar investigations are also performed for the high-speed forward flight condition.

In Figs. 5.61(a) and 5.61(b), the instantaneous C_p distribution are presented along with the instantaneous streamlines and the axial velocity ratio $u_a/U_{70\%}$ in the blade tip region for the reference and BLS case, respectively. In the reference case, the fan axial velocity ratio $u_a/U_{70\%}$ at $\psi_f = 0°$ is positive due to the pressure difference between the lower and upper surface of the blade. As a result, the tip-leakage vortex formation occurs

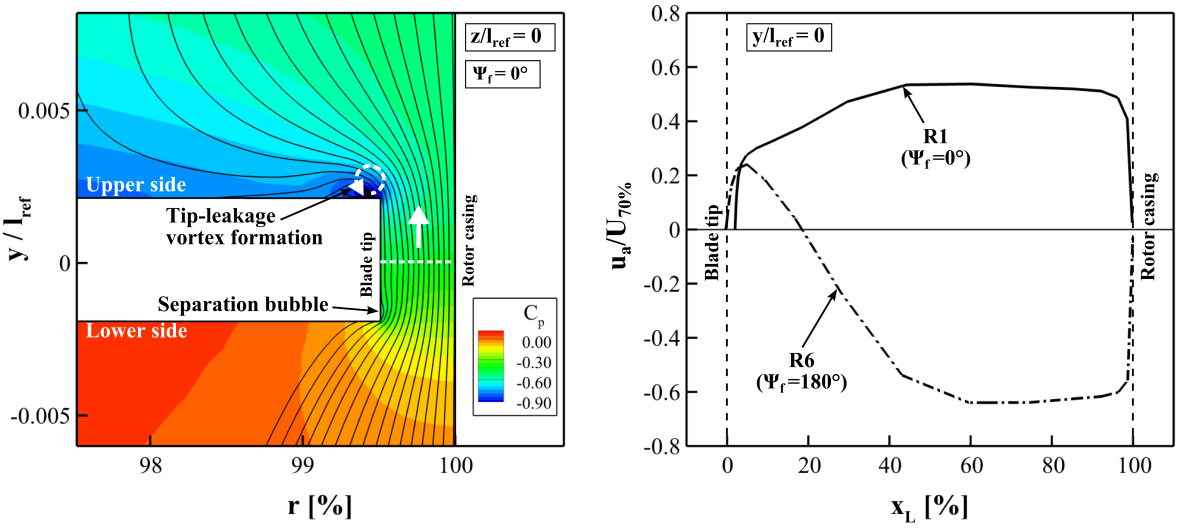

(a)

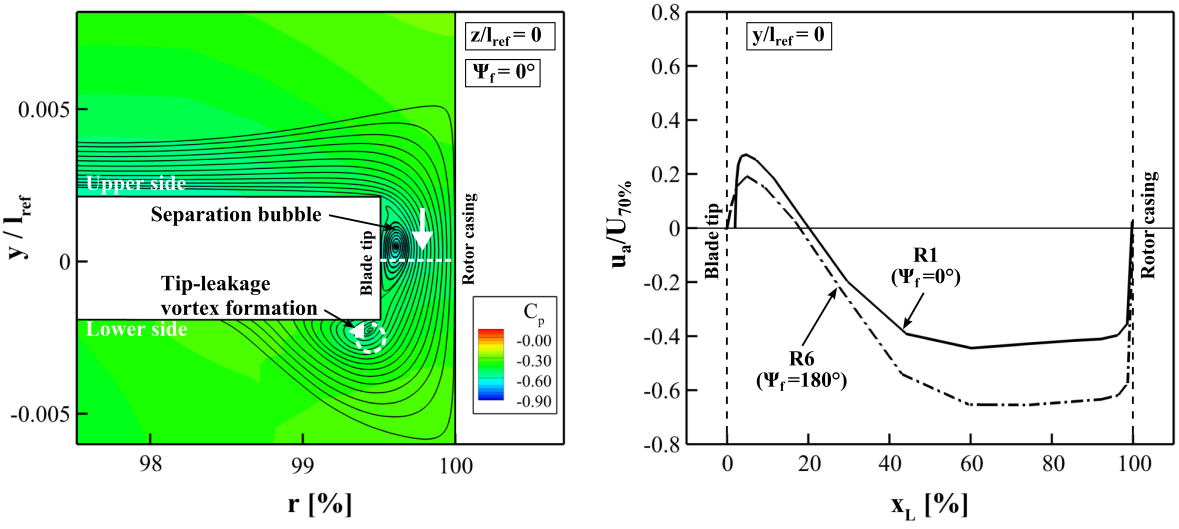

(b)

Figure 5.61: Instantaneous C_p distributions along with instantaneous streamlines and the fan-axial velocity ratio $u_a/U_{70\%}$ in the blade tip region for the (a) reference case and (b) BLS case.

on the upper surface of the blade. The vortex formation as well as $u_a/U_{70\%}$ levels are, however, less significant compared to the hovering condition as the pressure difference between the lower and upper side is relatively small. Unlike the hovering condition, the positive $u_a/U_{70\%}$ at $\psi_f = 0°$ (above the shaft fairing) in the forward flight condition is not the result of the interaction with the drive shaft fairing, but rather arises from the interaction with the ISB. The fan axial velocity ratio at $\psi_f = 180°$ is negative. The reverse flow region at the blade tip-face is due to a separation bubble.

In the non-distortion case, the fan axial velocity profile at $\psi_f = 0°$ is similar to that at $\psi_f = 180°$. Both at $\psi_f = 0°$ and $\psi_f = 180°$, the $u_a/U_{70\%}$ profiles exhibit negative values with the exception of the separation bubble (observed rather at the upper blade tip). The magnitude $|u_a/U_{70\%}|$, however, decreases, if the blade is influenced by the drive shaft faring. Unlike the reference case, in the BLS case, the tip-leakage vortex formation occurs always on the lower side of the blade. The impact of the tip-leakage vortex on the blade sectional pressure distribution is shown in Fig. 5.58.

5.4.3.7 Unsteady load of stator vane

The inlet flow distortion and its interaction with the rotating blade also strongly affects of the stator vane loads. In Fig. 5.62, the surface pressure fluctuations p'_s at $f/f_{\mathrm{BPF}} = 0.8$ are presented on the surface of the drive shaft fairing for both investigated cases. In the reference case, two significant regions with high pressure fluctuations are observed on the top surface. This is due, on the one hand, to the interaction with the ISB, and on the other hand, to the secondary flow zones, which occur if the ISB is divided by the blade into two parts and then the lower part is blocked by the shaft fairing, as observed in Fig. 5.52.

On the contrary, in the BLS case, the strong surface pressure disturbances are rather concentrated in the region near the stator casing, and decreases gradually towards the gear box. Generally, the levels of p'_s for the BLS case are higher than those for the reference case, highlighting that the shaft fairing noise might be more significant in the BLS case (cf. Sec. 5.4.4). Similar observations can be made for the stator vane S10 (see Fig. 5.63).

In Figs. 5.64(a) and 5.64(b), the fan axial and circumferential aerodynamic force coefficient, C_y and C_z, of the drive shaft fairing, respectively, are given as a function of the blade passing period for both simulation cases. As expected, the aerodynamics load is more significant in the BLS case than in the reference case. Furthermore, the effect of the uneven blade spacing is clearly visible. The comparison of the spectra of the aerodynamic load between the reference and BLS case indicate a clear tendency (see Fig. 5.65). In the reference case, additional peaks are observed at the frequencies $f/f_{\mathrm{BPF}} = 0.9$, $f/f_{\mathrm{BPF}} = 1.3$, and $f/f_{\mathrm{BPF}} = 1.5$ similar to the overall blade load (see Fig. 5.57(c)). In the BLS case, both $S_{C'_y}$ and $S_{C'_z}$ increase at the frequencies associated with the fan rotation and the uneven blade spacing due to the stronger rotor/shaft-fairing interaction.

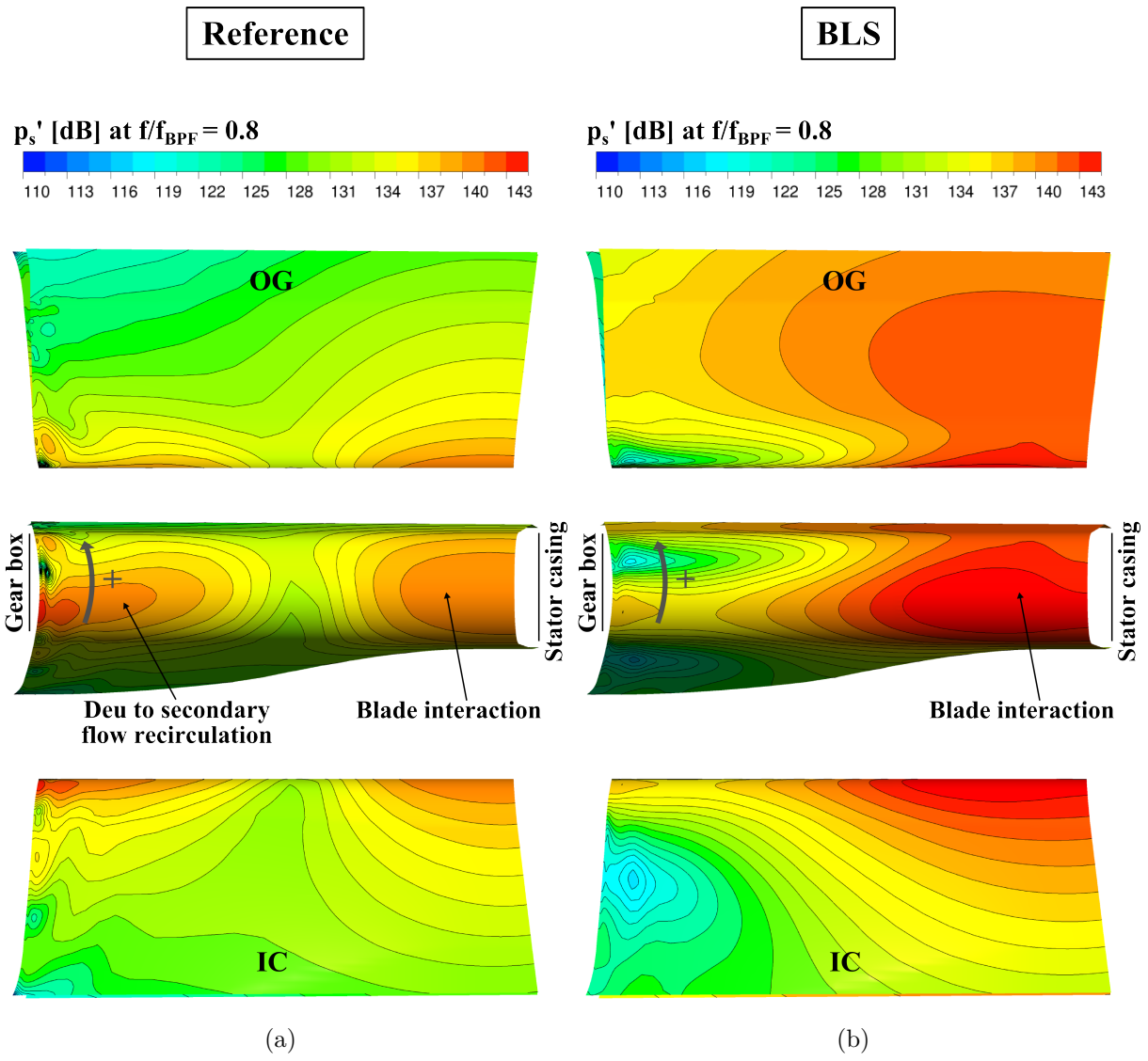

Figure 5.62: Surface pressure fluctuation p'_s on the drive shaft fairing at $f/f_{\mathrm{BPF}} = 0.8$ for the (a) reference and (b) BLS case.

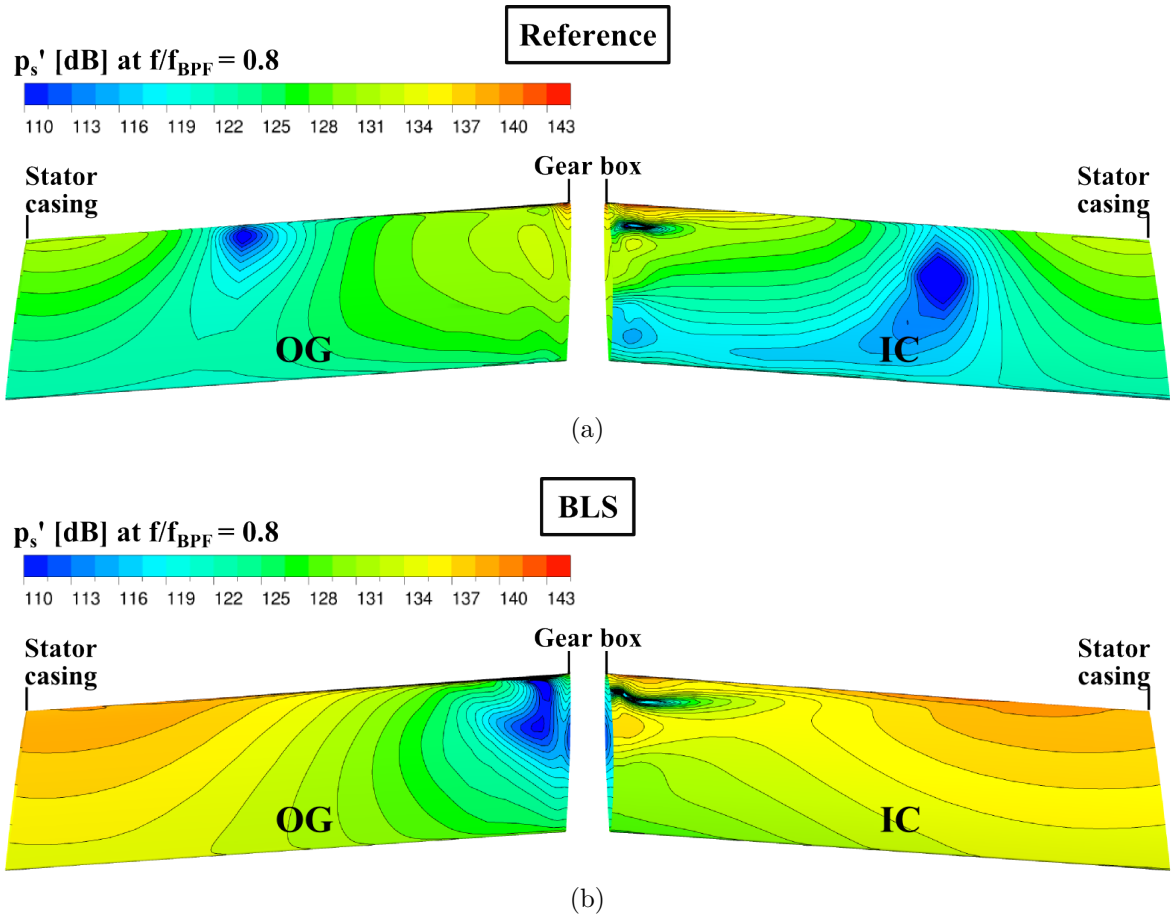

Figure 5.63: Surface pressure fluctuation p'_s on the stator vane S10 at $f/f_{\mathrm{BPF}} = 0.8$ for the (a) reference and (b) BLS case.

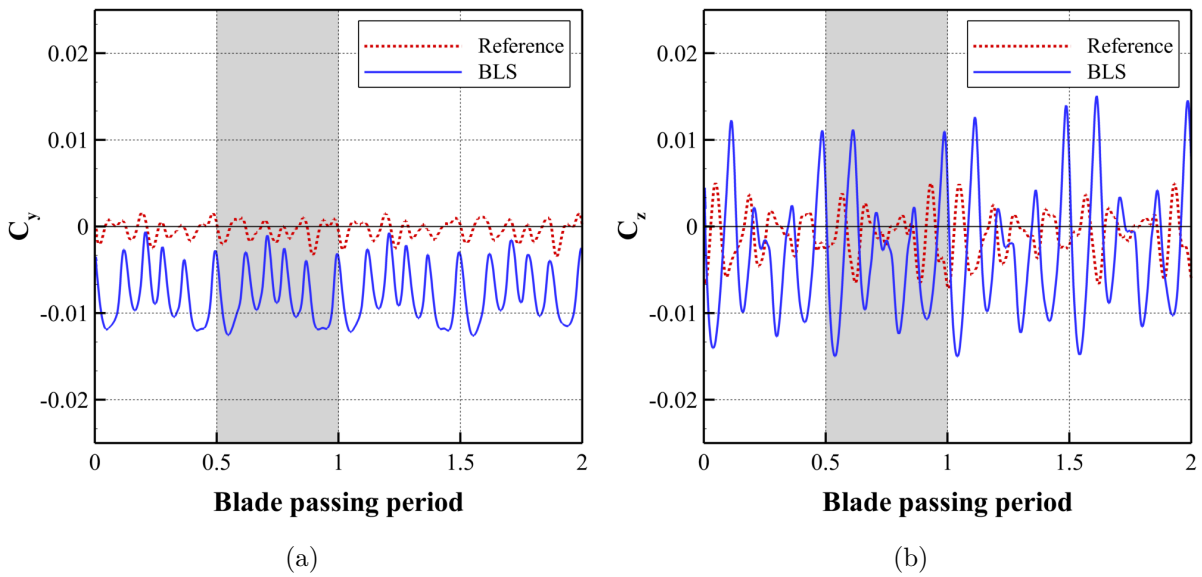

Figure 5.64: load history of the shaft fairing: (a) axial force C_y and (b) circumferential force coefficient C_z.

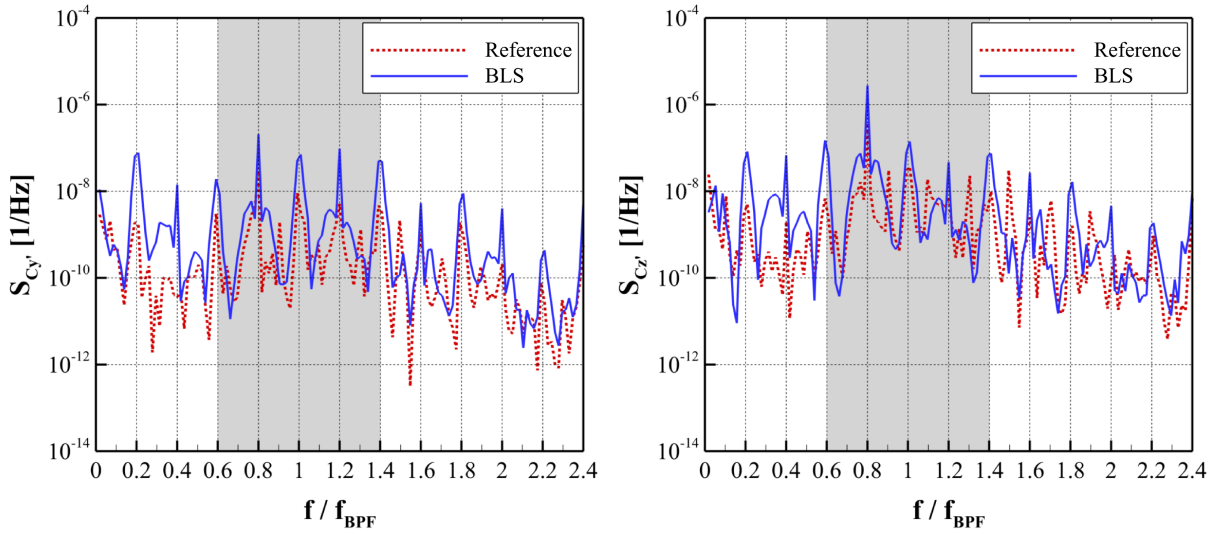

Figure 5.65: Power spectral density analysis of (a) axial force fluctuations $S_{C_y'}$ and (b) circumferential force fluctuations $S_{C_z'}$.

5.4.4 Acoustic Analysis of Inlet Flow Distortions

In Figs. 5.66(a) and 5.66(b), the directivity contour plots are presented on a plane ($400\,l_{\text{ref}} \times 400\,l_{\text{ref}}$, length $\times$ width), located below the helicopter flight path with a distance of $150\,l_{\text{ref}}$ (from the helicopter to the center of the directivity plane) for the reference and BLS case, respectively. In addition, the isosurfaces of the overall sound pressure level OSPL = 94 dB are given for both simulation cases. The relative velocity of the observer points to the helicopter is zero in this analysis. Regarding the isosurface, the directivity in the reference case has a dipole-like form with two rods, which are directed towards the starboard (inlet side) and port side (outlet side) of the STR, respectively. Hence, the directivity contour plot exhibits a similar pattern with two local maxima. The level of OSPL is more significant on the inlet side. In the non-distortion case, the isosurface reveals a more complex radiation pattern, as also observed on the directivity plane. In this case, three significant regions with relatively high OSPL are observed on the port side as well as on the starboard side of the STR. Furthermore, the highest OSPL value is found on the port side as opposed to the case with the inflow distortion. The difference in OSPL ($\Delta\text{OSPL} = \text{OSPL}_{\text{BLS}} - \text{OSPL}_{\text{Ref}}$) indicates that the elimination of the inflow distortion provides a noticeable reduction of the noise emission into the acoustic far field. The maximum noise reduction appears on the starboard side and upstream of the STR and amounts to $\Delta\text{OSPL} = -5.5$ dB, ((a) in Fig. 5.66(c)). A further significant reduction is found on the starboard side slightly downstream of the STR ((b) in Fig. 5.66(c)). In some regions, the OSPL is even increased in the BLS case. These regions ((c) and (d) in Fig. 5.66(c)) are, however, limited on the port side, and the increase in the OSPL ($\Delta\text{OSPL} < 2$ dB) is less significant than the decreased levels.

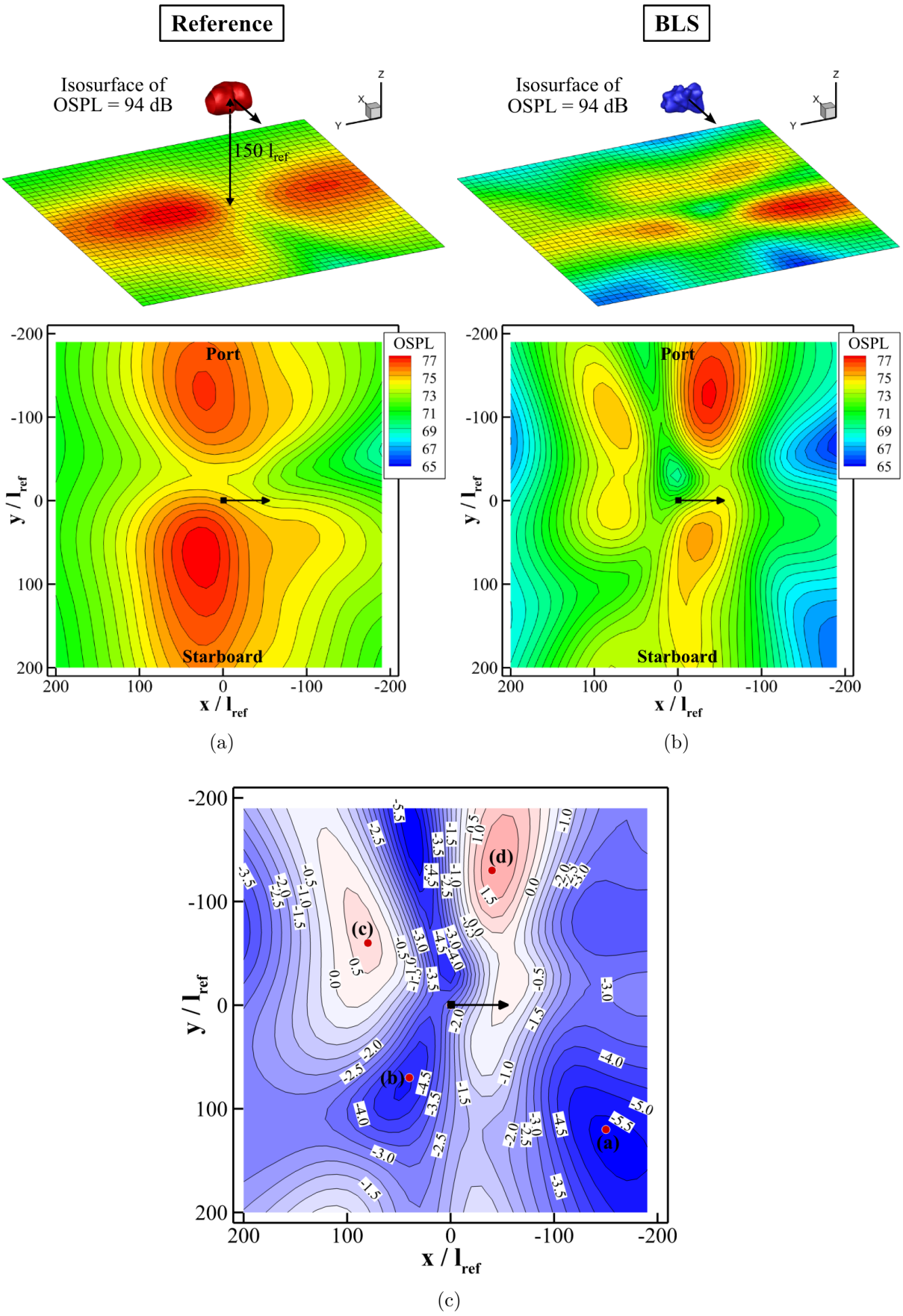

Figure 5.66: Comparison of directivity contour plots: (a) reference case, (b) BLS case, and (c) OSPL differences $\Delta\mathrm{OSPL} = \mathrm{OSPL}_{\mathrm{BLS}} - \mathrm{OSPL}_{\mathrm{Ref}}$.

The narrowband spectra of both simulation cases are also compared at the selected observer points for a more detailed analysis of the noise reduction. Concerning the monitor points ((a) and (b) in Fig. 5.66(c)), where the BLS case yields a noticeable decrease in the OSPL on the directivity plane, a significant decrease in the sound pressure level (SPL) is present, not only at the discrete noise components related to the fan rotation and the uneven blade spacing, but also at the frequencies in between (see Figs. 5.67(a) and 5.67(b)). It is similar to the finding of analysis of the blade load (cf. Fig. 5.57(c)) and the shaft fairing forces (cf. Fig. 5.65). As expected, the most pronounced SPL reduction occurs at $f/f_{\mathrm{BPF}} = 0.9$. The increase in OSPL, observed in the BLS case on the directivity plane at the observer position (c) and (d) in Fig. 5.66(c), is related to the considerable increase in SPL at $f/f_{\mathrm{BPF}} = 1 \pm 0.2n:\ n = 0,1,2$. It is because of the thrust inversion of the blades and the stronger rotor/stator-vane as well as rotor/shaft-fairing interaction in the non-distortion case. Thus, a significant increase in the discrete tone at the second harmonic of the BPF ($f/f_{\mathrm{BPF}} = 2$) is also found at these observer positions. At all observer points in the BLS case, a further decrease in SPL is found at $f/f_{\mathrm{BPF}} = 0.1$, corresponding to the fan rotational frequency.

In the following, the directivities of tonal components at the frequencies $f/f_{\mathrm{BPF}} = 0.8$ and $f/f_{\mathrm{BPF}} = 0.9$ are analyzed by means of the isosurface of SPL = 88 dB. In the reference case, the rods of the isosurface for the frequency $f/f_{\mathrm{BPF}} = 0.8$ is directed more towards the starboard (inlet side) and lower side of the STR (see Fig. 5.68). In contrary to this, the noise radiation at $f/f_{\mathrm{BPF}} = 0.8$ in the BLS case is more significant on the port side (outlet side) and both on the lower and upper side of the STR (see Fig. 5.69). Generally, the isosurfaces for the frequency $f/f_{\mathrm{BPF}} = 0.8$ are more significant in the BLS case because of the stronger rotor/stator-vane and rotor/shaft-faring interaction. Concerning the isosurfaces at $f/f_{\mathrm{BPF}} = 0.9$, it is found that the noise generated by the rotor/ISB interaction radiates rather towards the starboard side of the STR (see Fig. 5.70). As expected, the isosurfaces at $f/f_{\mathrm{BPF}} = 0.9$ in the BLS case are not significant anymore (see Fig. 5.71).

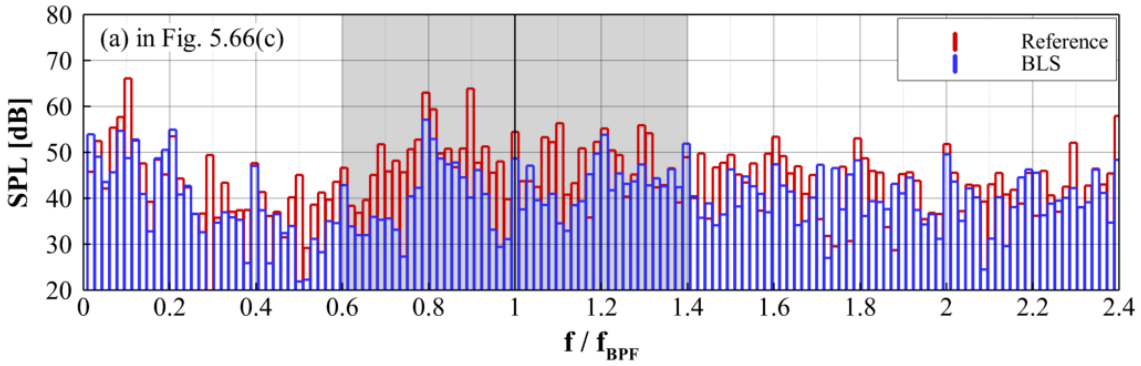

(a)

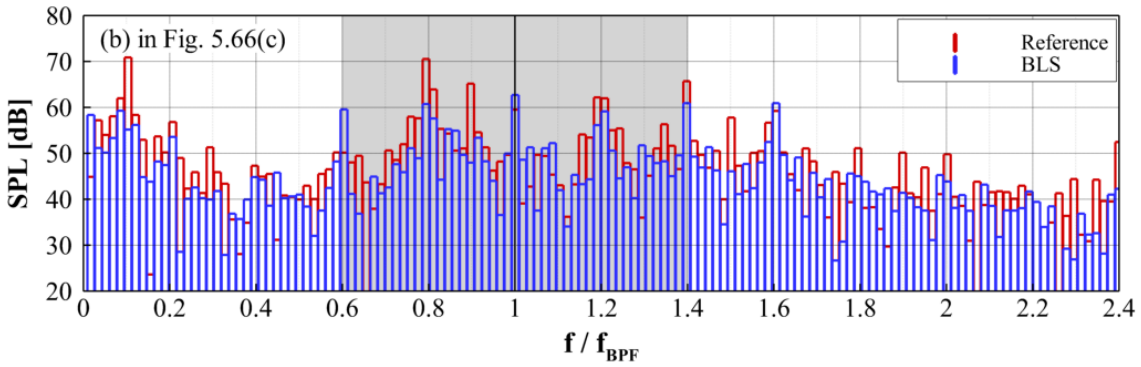

(b)

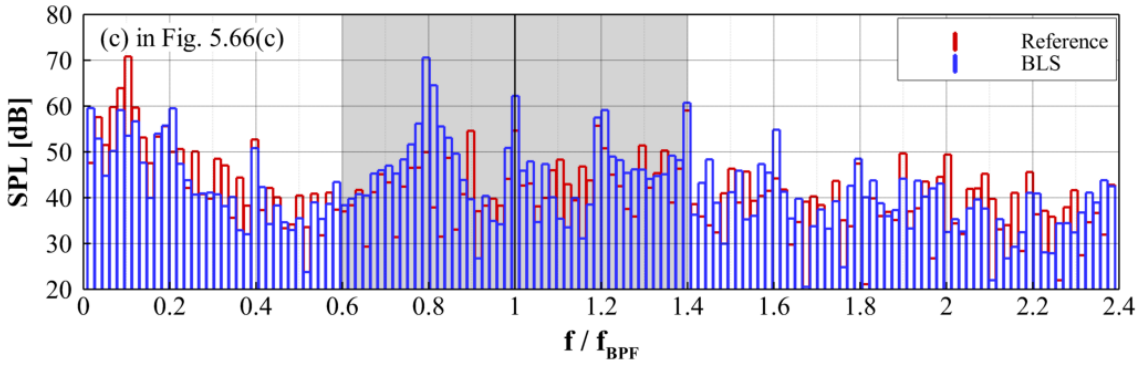

(c)

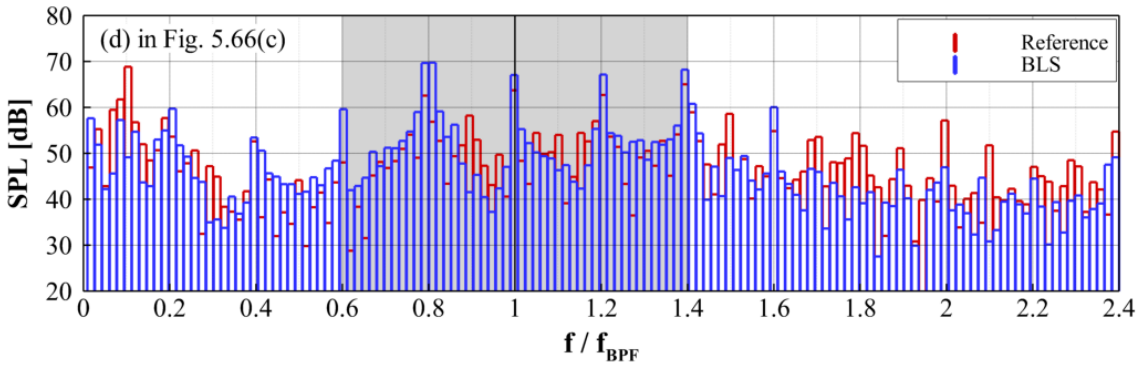

(d)

Figure 5.67: Narrowband spectra for (a) $\psi_h = 60°$, (b) $\psi_h = 135°$, (c) $\psi_h = 210°$, and (d) $\psi_h = 315°$ for the reference and BLS case.

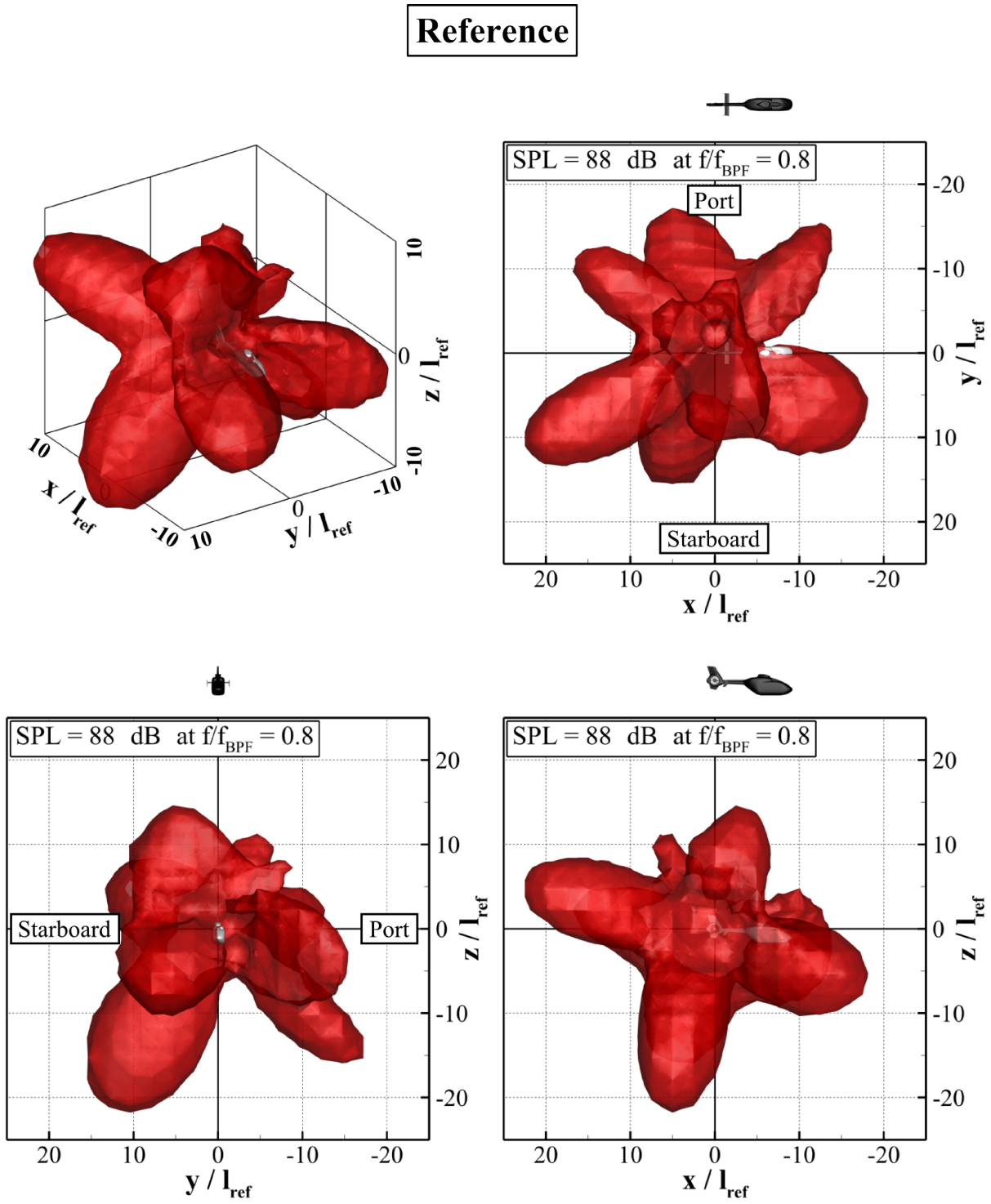

Figure 5.68: Isosurface of SPL = 88 dB for the frequency $f/f_{\mathrm{BPF}} = 0.8$ for the reference case.

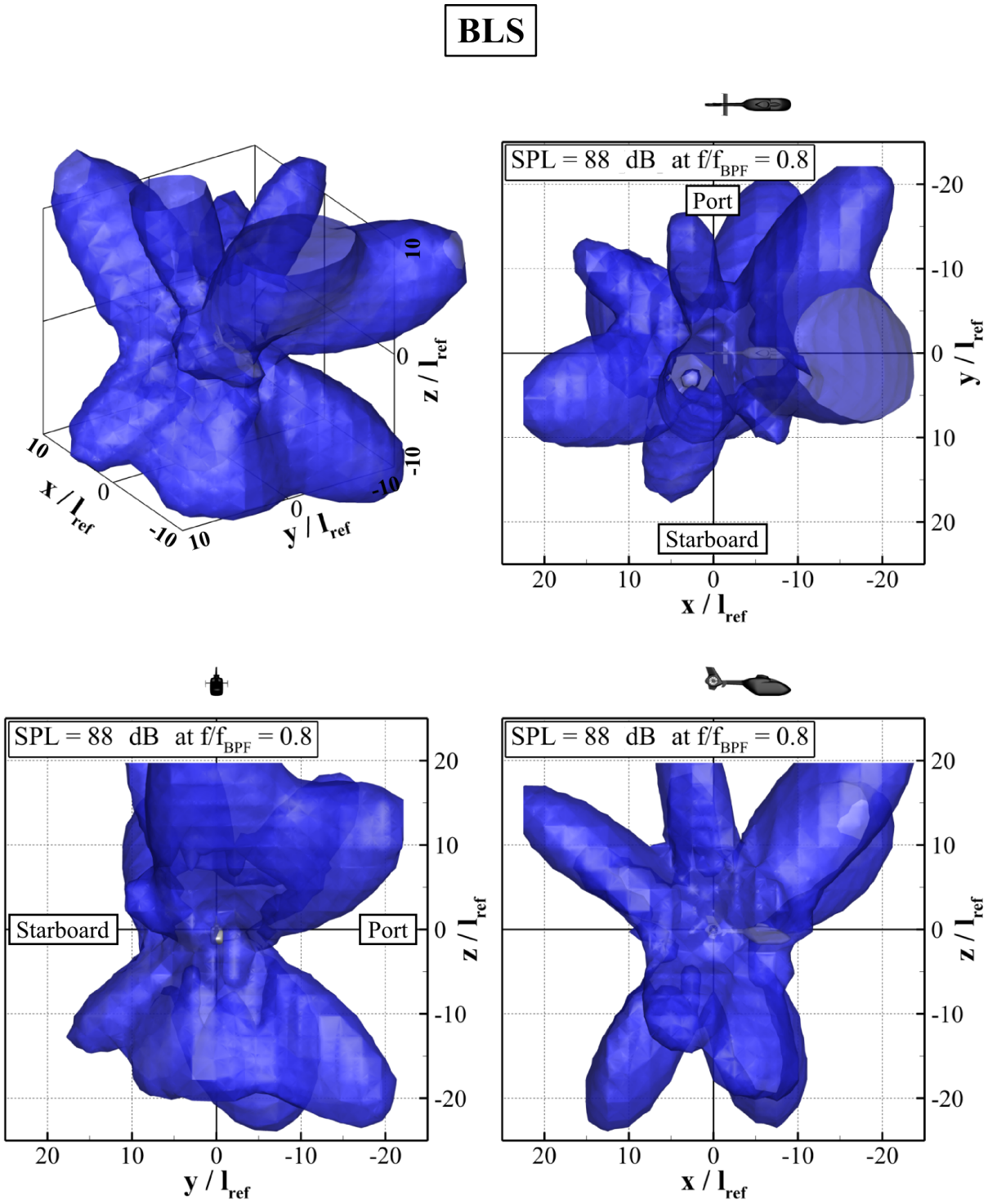

Figure 5.69: Isosurface of SPL = 88 dB for the frequency $f/f_{\mathrm{BPF}} = 0.8$ for the BLS case.

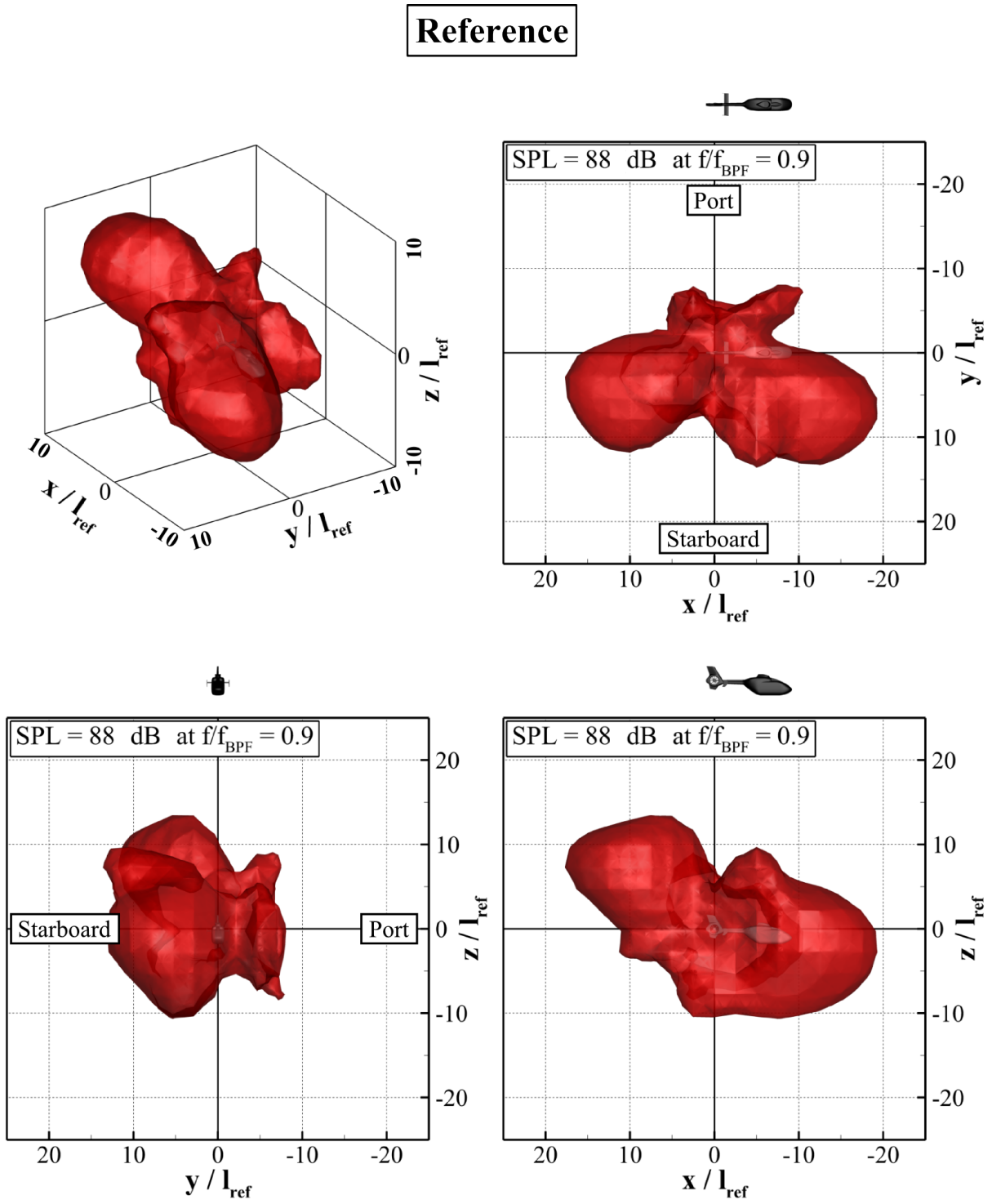

Figure 5.70: Isosurface of SPL = 88 dB for the frequency $f/f_{\mathrm{BPF}} = 0.9$ for the reference case.

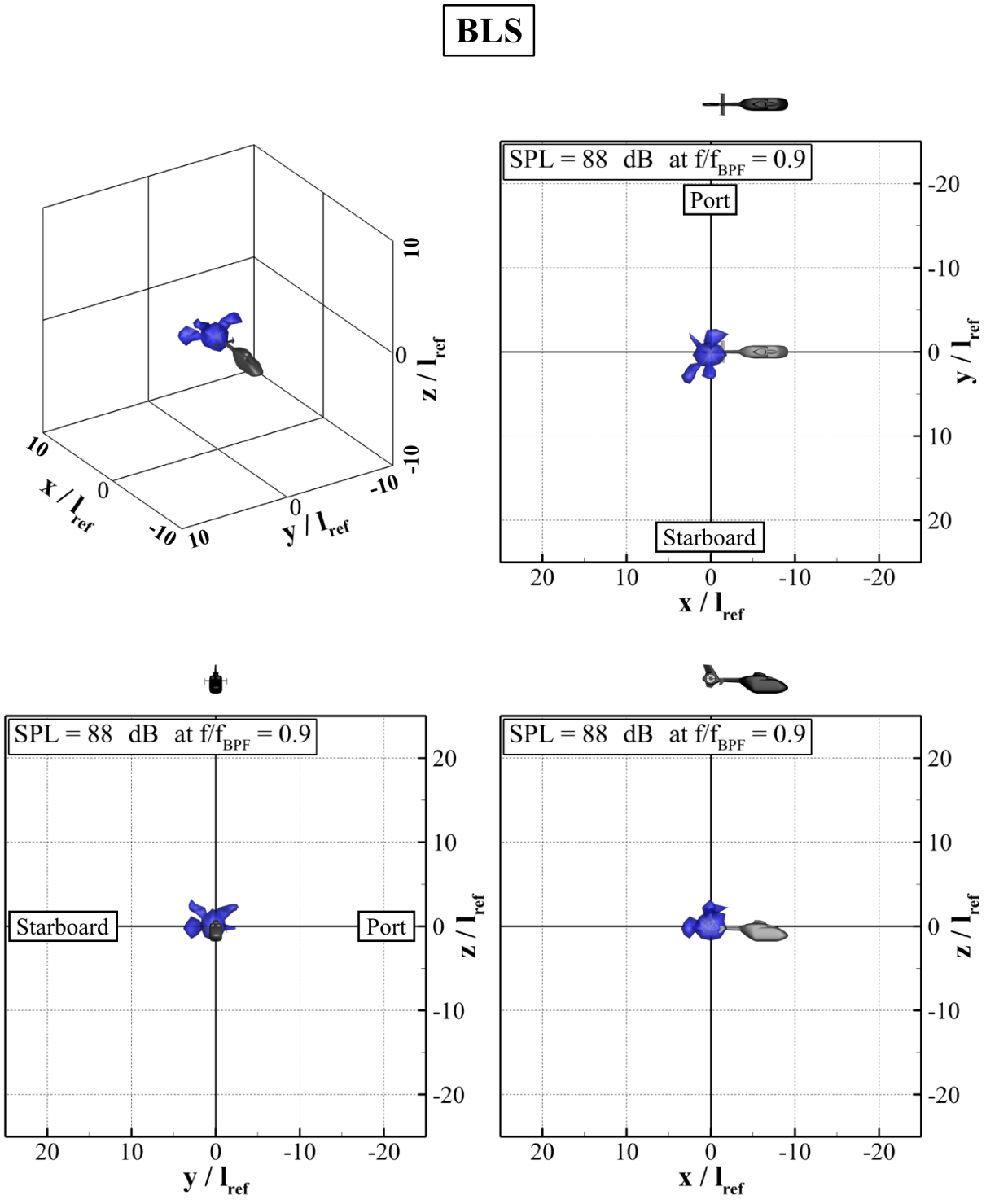

Figure 5.71: Isosurface of SPL = 88 dB for the frequency $f/f_{\mathrm{BPF}} = 0.9$ for the BLS case.

5.5 Influence of Horizontal Stabilizer

The influence of the horizontal stabilizer (HS) on the tonal noise generation of the STR in the high-speed forward flight condition will be discussed. The analysis is carried out by comparing the reference helicopter configuration (with HS, in Fig. 5.72(a)) with the case where the horizontal stabilizer is removed (w/o HS, in Fig. 5.72(b)). For this purpose, further unsteady RANS simulations are performed based on the configuration without horizontal stabilizer and its end-plates and by using the SST turbulence model. As mentioned in the previous section (see Sec. 5.1.1), both end-plates installed at the tips of the stabilizer contribute to approximately 11 % of the overall anti-torque thrust required in the forward flight. This indicates that in the case w/o HS, the anti-torque rotor has to be more loaded to compensate the loss of the anti-torque thrust, which, however, might increase the far-field noise level of the STR. In the following study, it is therefore assumed that the operating point of the anti-torque rotor (e.g. blade pitch angle P_b and fan rotational speed Ω) is identical in both simulation cases. In addition, the grid node distributions in the vicinity of the STR and the simulation parameters of the case w/o HS are identical to those of the reference case. Generation and subsequent far-field radiation of the HS-airfoil self-noise are not part of this analysis.

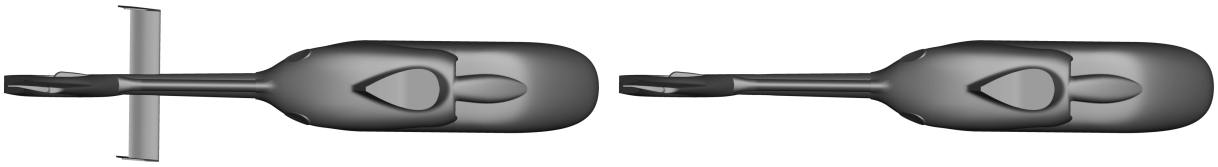

(a) (b)

Figure 5.72: Top view of the studied configurations (a) with HS and (b) w/o HS.

5.5.1 Flow Field Analysis

The analysis focuses on the influence of the horizontal stabilizer being installed upstream of the STR on the aerodynamic characteristics of the anti-torque rotor in the high-speed forward flight condition.

5.5.1.1 HS/fuselage-wake interaction

To give a first insight into the HS/fuselage-wake interaction, instantaneous spaced-filled streamlines on the starboard side of the helicopter configuration (STR inlet side) are given in Figs. 5.73(a) and 5.73(b) for the cases with HS and w/o HS, respectively. The streamlines in Fig. 5.73(a) indicate that the HS divides the fuselage wake, in particular the lower fuselage vortex (LFV) into two discrete vortices, namely the upper LFV (ULFV) and the lower LFV (LLFV). Thereby, the LLFV is shifted towards the STR shroud, whereas

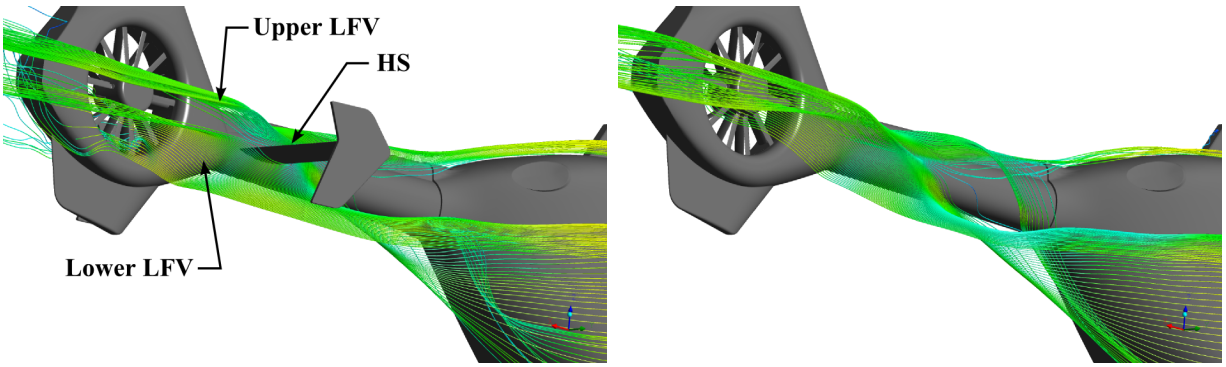

(a) (b)

Figure 5.73: Instantaneous space-filled streamlines on the starboard side of the helicopter (STR inlet side): (a) with HS and (b) w/o HS.

the ULFV is rather pushed away from the STR (see also Fig. 5.75). Consequently, a part of the LLFV is ingested into the lower area of the anti-torque rotor (advancing blade side). Therefore, an interaction between the rotating blades and the wake ingested are expected in the case with HS (see Sec. 5.5.1.2). On the contrary, streamlines in the case w/o HS case do not show any significant interaction with the STR as well as any ingestion into the fan due to the relatively low fan load in this flight condition.

In Fig. 5.74(a), instantaneous skin-friction lines are presented on the upper surface of the HS (starboard side of the helicopter). According to the figure, the influence region of the fuselage wake is limited to the inboard area of the HS. In the region of the wake impingement, the skin-friction lines are deflected towards the root of the HS. Comparing the chordwise distribution of the time-averaged surface pressure coefficient $\overline{C}_p$ at $y/l_{\text{ref}} = 0.23$ (inboard) with that at $y/l_{\text{ref}} = 0.64$ (outboard), the impact of the wake impingement on the HS aerodynamic characteristics is clearly visible (see Figs. 5.74(c) and 5.74(d)). The completely different $\overline{C}_p$ distribution highlights that the wake impingement substantially changes the effective incidence angle of the HS. In the region where the HS interacts with the wake, the stagnation point is located on the lower surface of the HS indicating that the local incidence angle is positive. On the outboard area, the stagnation point is found on the upper surface of the HS because the global angle of attack of the helicopter is negative ($\alpha_\infty = -2°$). Continuing to Fig. 5.74(a), a significant pattern of the skin-friction lines is observed in the root region. This refers to the corner separation and it interacts with the horseshoe vortex of the HS-tailboom intersection (HSV-HS, (5) in Fig. 5.74(e)), and forms a further vortex system (HSW, (6) in Fig. 5.74(e)) together with the secondary vortex system, generated on both the upper and lower surface of the HS. The spanwise range of the vortex system is extended from the root region to approximately 50% span of the stabilizer. The boundary layer on the outboard area remains attached, thus indicating no noticeable flow separation and wake formation. A further horseshoe vortex formation is observed on the frontal surface of the STR shroud (HSV, (4) in Fig. 5.74(e)). As a result, the anti-torque rotor encounters a very complex inflow condition in the high-speed

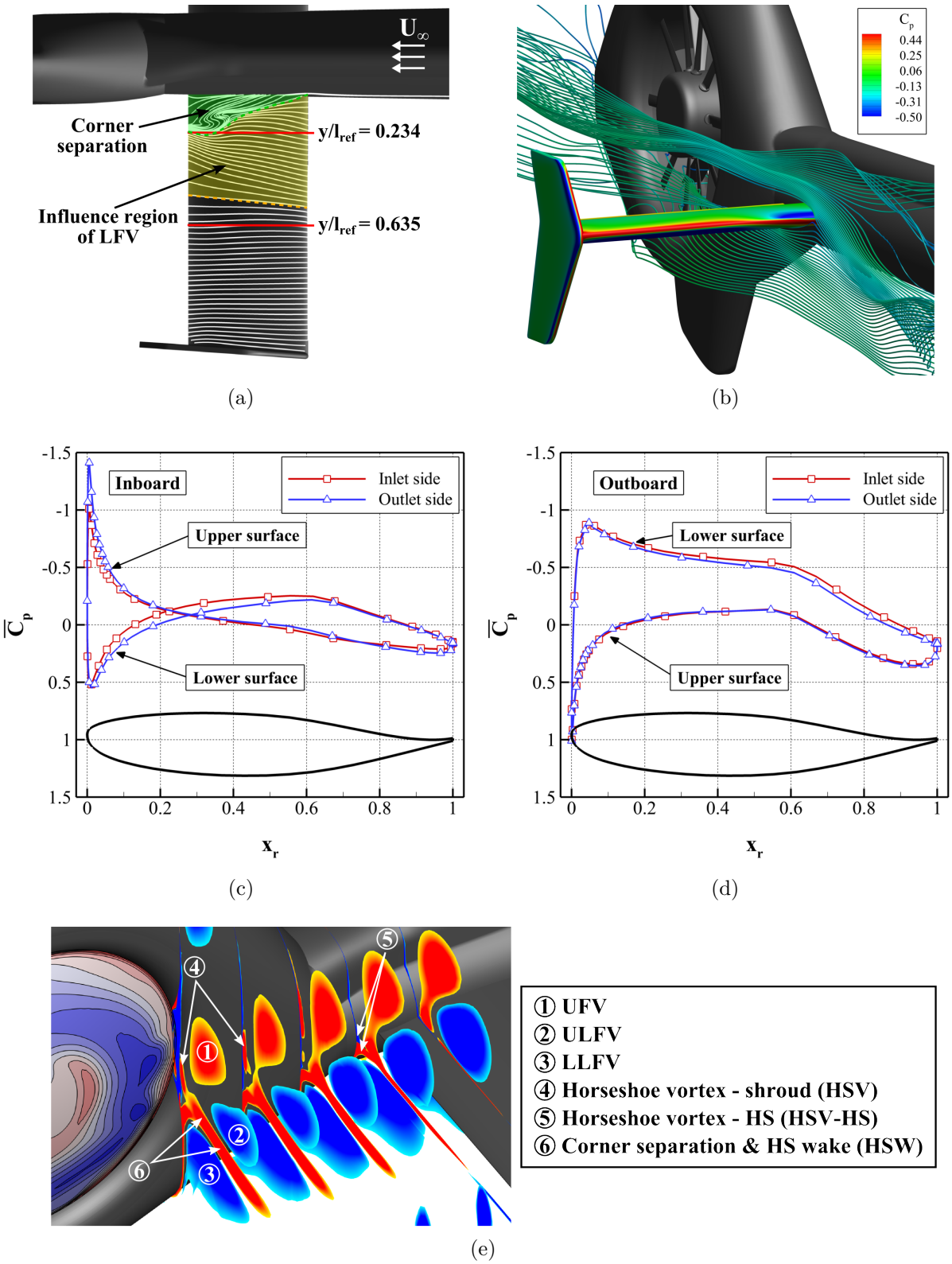

Figure 5.74: HS/fuselage-wake interaction and HS vortex formation: (a) instantaneous skin-friction lines on the upper surface of the HS (inlet side), (b) instantaneous C_p distribution on the HS, (c) time-averaged chordwise $\overline{C}_p$ distributions at $y/l_{\text{ref}} = 0.234$ (inboard), (d) at $y/l_{\text{ref}} = 0.635$ (outboard), and (e) time-averaged, non-dimensional streamwise vorticity $\overline{\omega}_x l_{\text{ref}}/U_\infty$ distributions on cross-sectional planes (inlet side).

forward flight condition.

To assess the influence of the HS on the flow field characteristics in the vicinity of the STR, three cross-sectional planes located at $x/l_{\text{ref}} = -0.6$ (upstream), $x/l_{\text{ref}} = 0$ (fan center), and $x/l_{\text{ref}} = 0.6$ (downstream) are considered. On these planes, the time-averaged, non-dimensional streamwise vorticity $\overline{\omega}_x l_{\text{ref}}/U_\infty$ is presented, as shown in Fig. 5.75(a) and Fig. 5.75(b) for the cases with HS and w/o HS, respectively. Considering the plane located directly upstream of the STR ($x/l_{\text{ref}} = -0.6$), it is observed that the LLFV, divided from the LFV, is located closer to the STR than the LFV of the non-interaction case (w/o HS). The significant deformation of the LLFV occurring by passing the STR inlet region shows that a large part of the LLFV is ingested into the fan, particularly on the lower part of the STR (advancing blade side). Due to the low fan load, specified in this flight condition, the LLFV is not completely ingested into the fan, but the core region is further transported downstream by the main flow, as observed on the plane at $x/l_{\text{ref}} = 0.6$. The HSW also exhibits a strong deformation on the inlet side of the STR. On the contrary, the UFV and the LFV of the case w/o HS do not indicate any significant deformation in the vicinity of the STR inlet as they are convected downstream by the main flow without any significant interactions with the STR at this tail rotor operating point. A further complex $\overline{\omega}_x l_{\text{ref}}/U_\infty$ distribution is found on the STR outlet side at $x/l_{\text{ref}} = 0.6$ in both simulation cases, which is related to the interaction occurring between the low-momentum fan exit flow and the high-momentum incoming cross-flow.

5.5.1.2 Rotor flow field characteristics

The impact of the ingested vortical structures on the inflow condition of the anti-torque rotor is analyzed by comparison of the time-averaged, non-dimensional fan axial velocity $\overline{u}_a/U_\infty$ on the upper domain interface (see Fig. 5.76). The flow region with a positive value of $\overline{u}_a/U_\infty$ indicates a reverse flow region. As discussed in the previous sections, the flow field upstream of the rotor plane bears strongly asymmetric characteristics with respect to the horizontal and vertical center lines. The former asymmetry with respect to the horizontal center line ($\psi_f = 0°$ to $\psi_f = 180°$) is due to the relative motion of the rotating blade to the incoming flow (advancing and retreating blade side), while the latter asymmetry is responsible for the inlet flow distortion in the front part of the STR due to the lip flow separation (reverse flow region along the front part of the collector lip). In addition to that, three significant flow regimes with low levels of negative $\overline{u}_a/U_\infty$ are observed in the fourth quarter of the STR inlet ($270° < \psi_f < 360°$: advancing side) in the case with HS. These are related to the ingested HSV, HSV-HS, HS corner separation, and the LLFV. As expected, in the non-interaction case, only the influence region of the ingested HSV is visible on the upper domain interface. Apart from that, there are no significant differences between the cases with and w/o HS in the first, second, and third quarter of the STR inlet since the interaction mainly occurs on the advancing blade side due to the installation position of the STR with respect to the HS and the tailboom.

To investigate the interaction occurring between the rotating blade and the ingested

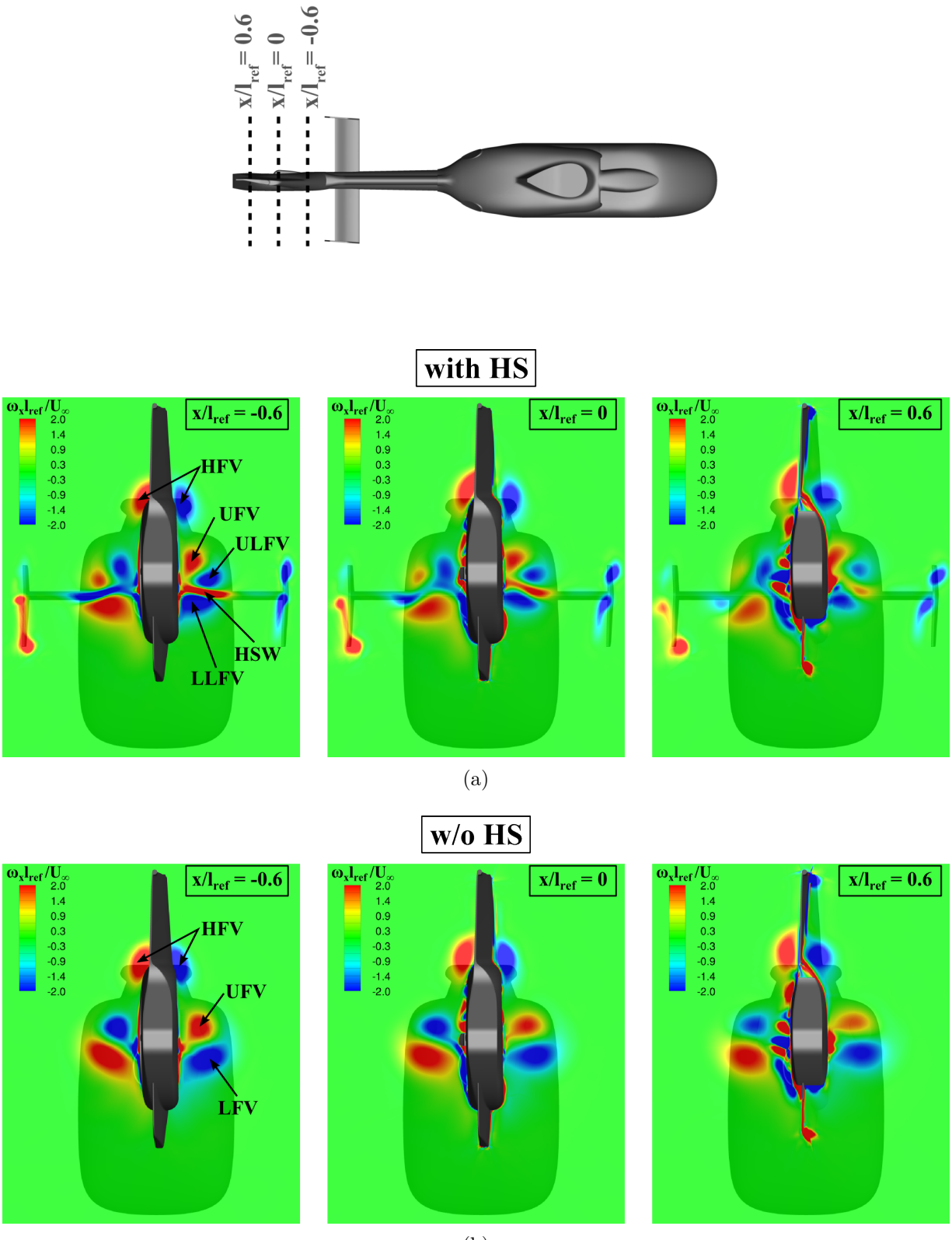

Figure 5.75: Time-averaged non-dimensional streamwise vorticity $\overline{\omega}_x l_{\text{ref}}/U_\infty$ on cross-sectional planes located at $x/l_{\text{ref}} = -0.6$, $x/l_{\text{ref}} = 0$, and $x/l_{\text{ref}} = 0.6$ for the simulation cases (a) with HS and (b) w/o HS.

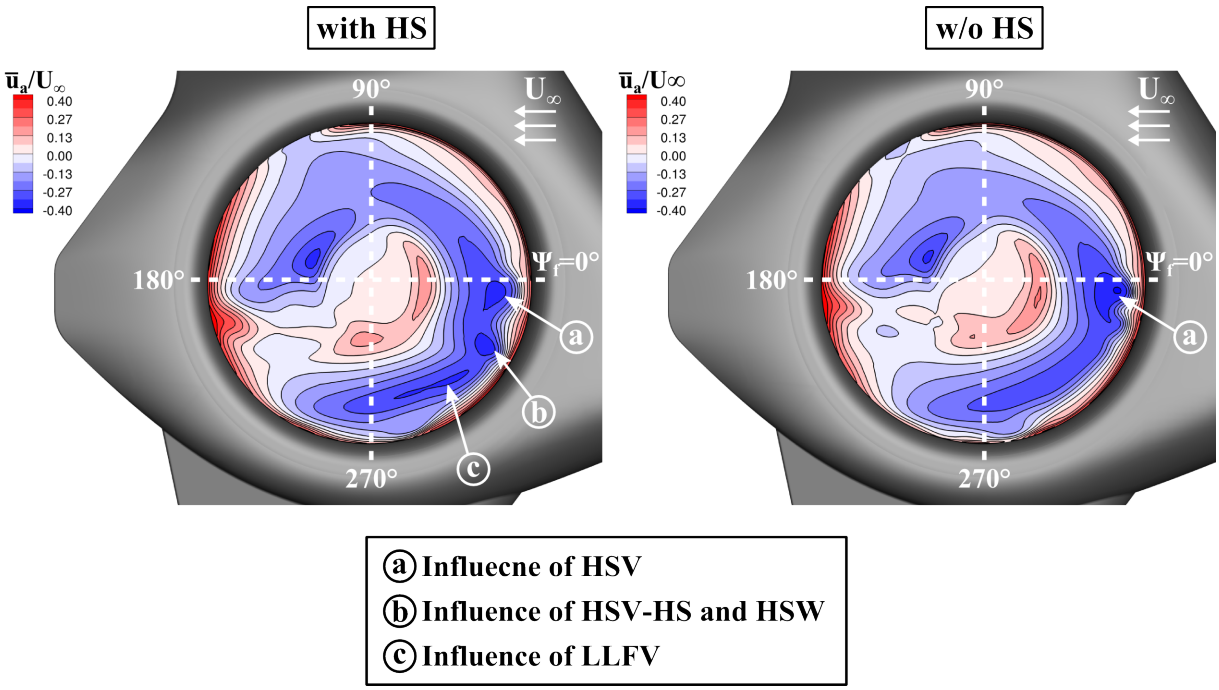

Figure 5.76: Comparison of the time-averaged, non-dimensional fan axial velocity $\overline{u}_a/U_\infty$ distributions on the upper domain interface.

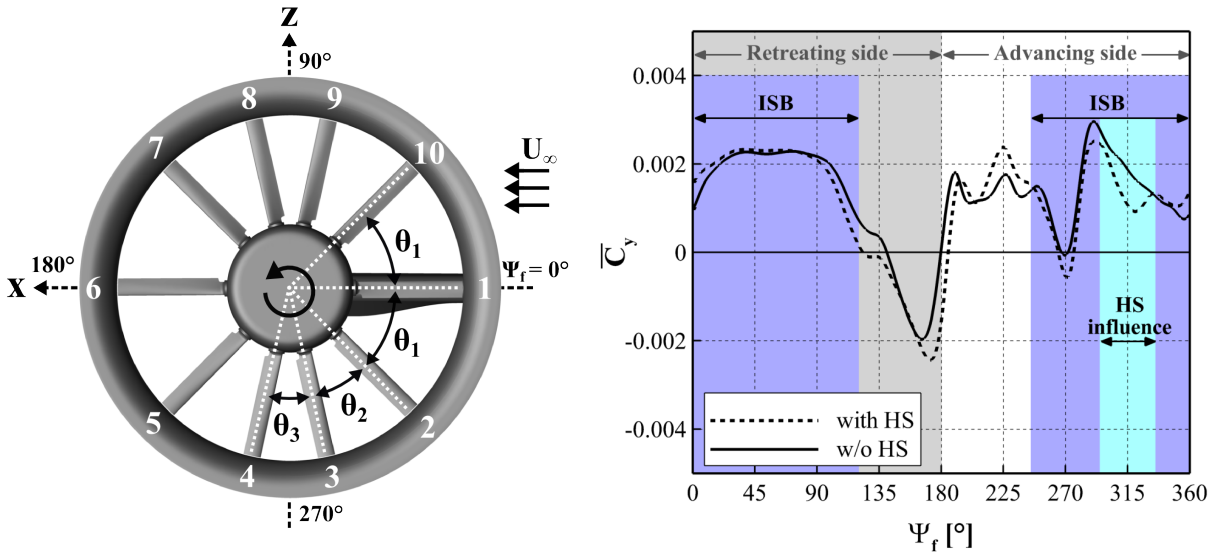

Figure 5.77: Time-averaged blade load history $\overline{C}_y(\psi_f)$ of the blade R2 for the simulation cases with and w/o HS.

vortical structures, the time-averaged blade load history $\overline{C}_y(\psi_f)$ of the reference case (with HS) is compared with that of the non-interaction case (w/o HS) (see Fig. 5.77). The blade load is averaged over three fan revolutions. Similar to the finding in Fig. 5.76, the course of the blade load in both cases is very similar in the fan azimuth range $0° < \psi_f < 270°$, and shows only the impact of the inlet separation bubble and the hub wake (cf. Sec. 5.4.3.4). In the fan azimuth range corresponding to the fourth quarter of the STR inlet

and particularly in $290° < \psi_f < 335°$, the impact of the HS on the blade load is clearly visible. $\overline{C}_y(\psi_f)$ in the case with HS exhibits a more fluctuating behavior than in the case w/o HS.

The spectral characteristics of the interaction between the rotating blade and the ingested vortical structures are investigated by means of the power spectral density analysis of the pressure fluctuations $S_{C_p'}$ (see Figs. 5.78(a) and 5.78(b)). The pressure fluctuations are obtained at the stationary monitor points located directly above the rotor plane ($y/l_{\text{ref}} = 0.04$) and at two different radial positions, namely 70% and 90% of the fan radius. Comparing $S_{C_p'}$ for both simulation cases at the 90% station of the fan radius, a significant difference in the amplitude is observed at the frequency $f/f_{\text{BPF}} = 0.1$, corresponding to the rotational frequency of the anti-torque rotor, and in the fan azimuth range between $290° < \Psi_f < 335°$, which is consistent with the influence region of the ingested vortical structures. Here, the case with HS shows a noticeable increase of $S_{C_p'}$ compared to the case w/o HS, substantiating that the interaction between the rotating blade and the ingested vortical structures leads to a considerable pressure disturbance propagation upstream of the rotor plane. Regarding levels of $S_{C_p'}$ at the frequencies related to the BPF ($f/f_{\text{BPF}} = 1$) and its lower and upper sidebands, there are only small differences between the cases with and w/o HS. This is due to the dominant inlet flow distortion and its interaction with the rotor blades overlay the pressure disturbances caused by the interaction with the ingested vortical structures. A similar analysis can be made for the monitor points at $0.7r$, but the decrease of $S_{C_p'}$ in the case w/o HS in the fan azimuth range between $290° < \Psi_f < 335°$ is less significant than at $0.9r$.

5.5.2 Analysis of Far-Field Radiation

Based on the source information obtained from the URANS simulation, acoustic post-processing is performed for the non-interaction case (w/o HS) and compared with the reference case (with HS). Directivity contours are given in 5.79(a), which are obtained by use of observer points for the xy-plane as well as perpendicular to the rotor plane and distributed with an equivalent distance of $d_{\text{op}}/l_{\text{ref}} = 25$ from the center of the fan. In this analysis, possible reflections and diffraction, which might be caused by the horizontal stabilizer and its end plates, are not taken into account.

Regarding the directivity in the plane perpendicular to the rotor plane (xz-plane), the case w/o HS also indicates a dipole-like radiation pattern, and it is similar to the directivity in the reference case. The overall sound pressure level (OSPL) in the case w/o HS is, however, lower than in the case with HS. The plot in Fig. 5.79(b) indicates the reduction of the OSPL in the non-interaction case ($\Delta\text{OSPL} = \text{OSPL}_{\text{w/oHS}} - \text{OSPL}_{\text{withHS}}$). Removing the horizontal stabilizer and the resulting elimination of unfavorable interactions with the rotating blades result in the reduction of the far-field sound level. The reduction is more significant on the stern side than on the bow side of the STR. A noticeable decrease of the OSPL is found on the stern side of the STR at the helicopter azimuth of $\psi_h = 152.5°$ ((b) in Fig. 5.79(b)) and $\psi_h = 200°$ ((c) in Fig. 5.79(b)), and approximately $\Delta\text{OSPL} = -3\,\text{dB}$

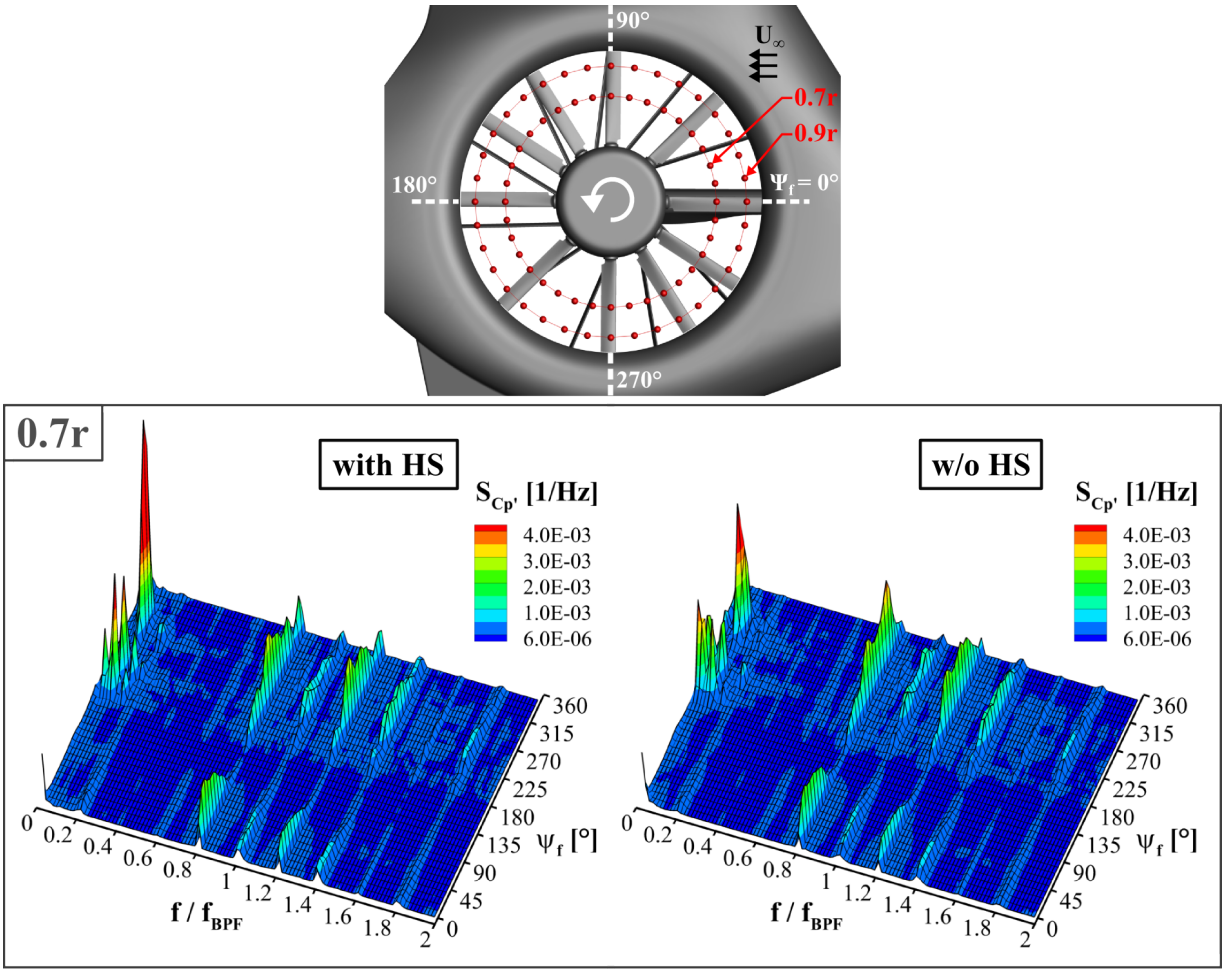

(a)

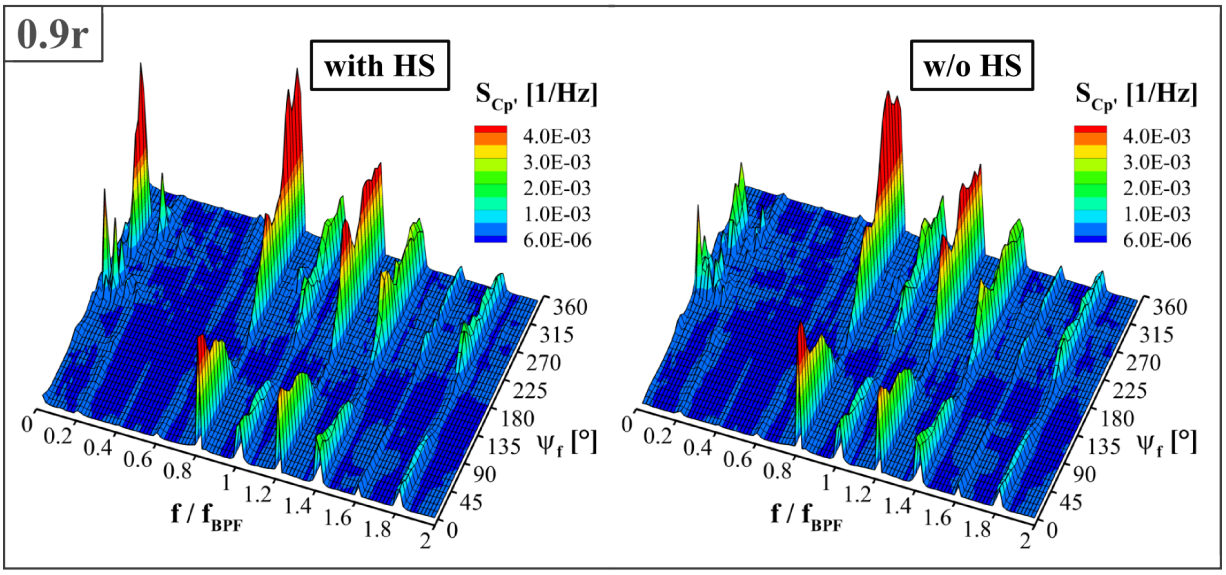

(b)

Figure 5.78: Power spectral densities of pressure fluctuations $S_{C_p'}$ on the cross-sectional plane at $y/l_{\text{ref}} = 0.04$ for 70% and 90% of the fan radius for the simulation cases with and w/o HS.

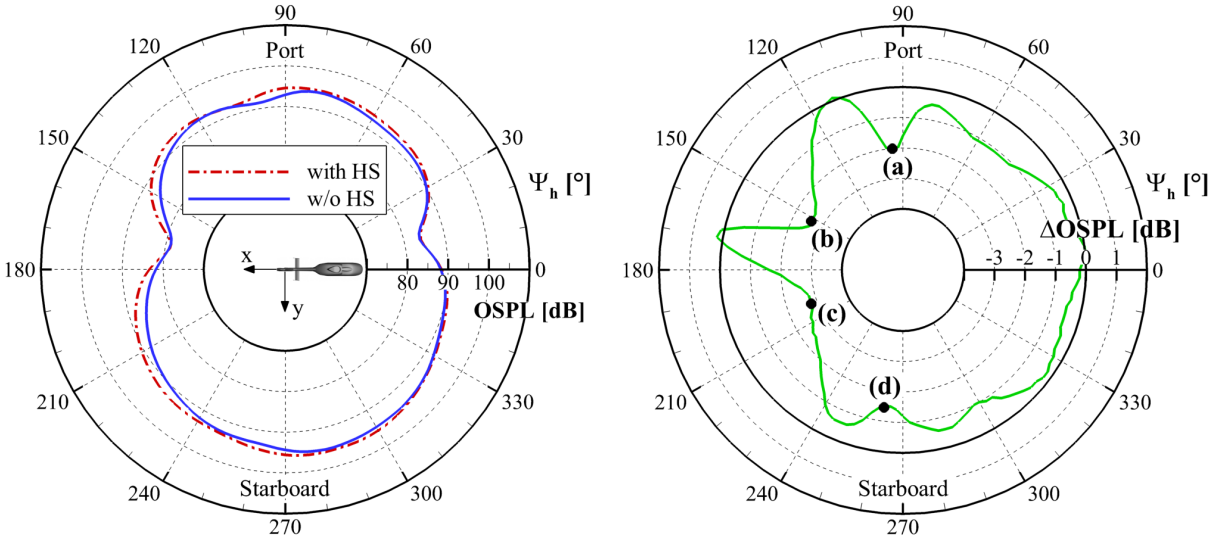

(a) (b)

Figure 5.79: Comparison of sound directivities between the cases w/o and with HS: (a) OSPL, (b) $\Delta\text{OSPL} = \text{OSPL}_{\text{w/oHS}} - \text{OSPL}_{\text{withHS}}$.

at both observer points.

Narrowband spectra of the calculated noise are compared at the selected observer points where the decrease of the OSPL is significant ($\psi_h = 95°$, $\psi_h = 152.5°$, $\psi_h = 200°$, and $\psi_h = 262°$) (see Fig. 5.80). Although the inlet flow distortion as a result of the lip boundary layer separation still exists and is more dominant than the HS influence, the impact of removing the horizontal stabilizer is clearly found in the sound spectra. Since the periodic occurrence of the blade interaction with the ingested wake is eliminated, the case w/o HS yields a noticeable decrease of tonal noise components at the frequencies related to the fan rotation and the uneven blade spacing ($f/f_{\text{BPF}} = 1 \pm 0.2n : \ n = 0, 1, 2$) at all observer points regarded. For the observer point (b) in Fig. 5.79(b) (for the corresponding spectrum, see Fig. 5.80(b)), the reduction in the sound pressure level (SPL) at $f/f_{\text{BPF}} = 1$ and $f/f_{\text{BPF}} = 1.4$ is -10.4 dB and -7.3 dB, respectively. At the observer point (c) in Fig. 5.79(b), the reduction at the same frequencies is -5.9 dB and -9.8 dB, respectively (see also Fig. 5.80(c)). Reduction of the discrete noise component at twice of the fan rotational frequency ($f/f_{\text{BPF}} = 0.2$) is also observed at all observer positions regarded.

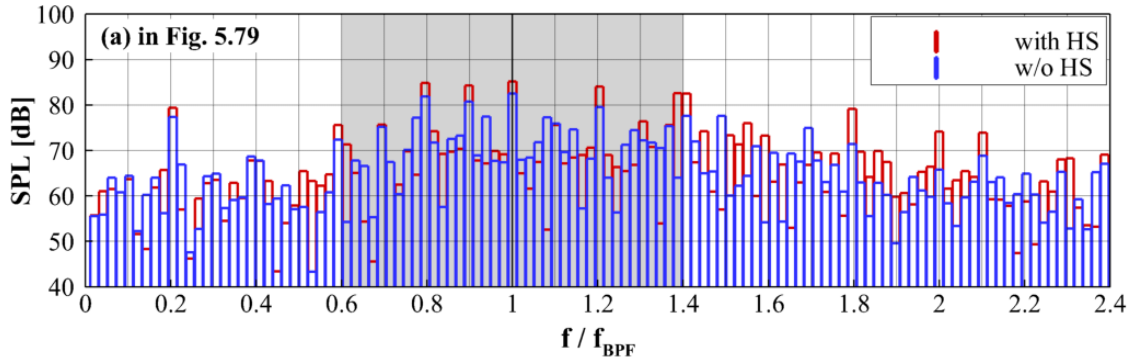

(a)

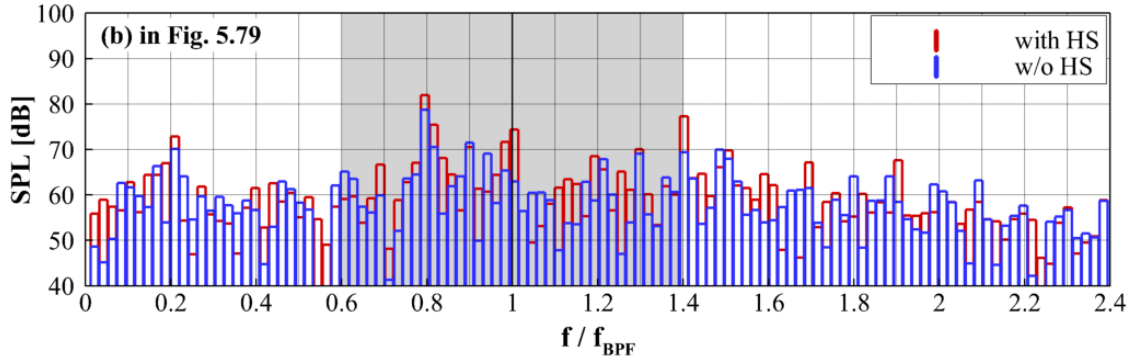

(b)

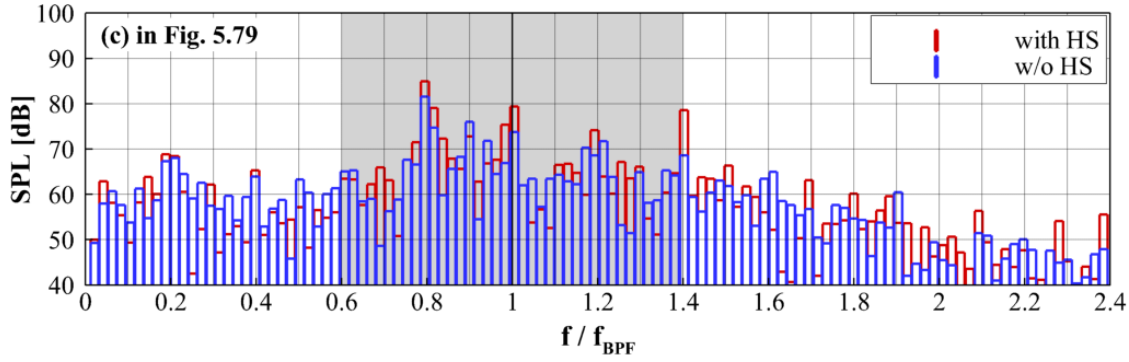

(c)

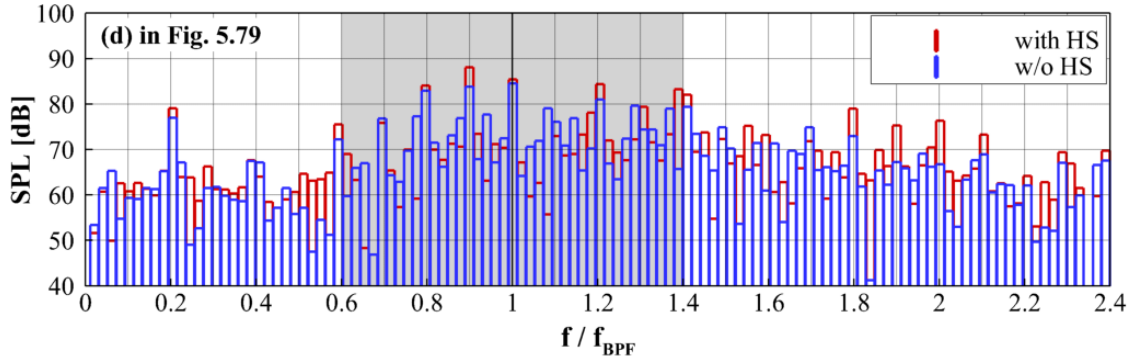

(d)

Figure 5.80: Narrowband spectra at the helicopter azimuth of (a) $\psi_h = 95°$, (b) $\psi_h = 152.5°$, (c) $\psi_h = 200°$, and (d) $\psi_h = 262.5°$ for the simulation cases with and w/o HS.

5.6 Synthesis

This chapter has focused on both the aerodynamic and acoustic characteristics of the shrouded tail rotor in the operating condition under strong impact of incoming cross flow. The numerical investigation has been performed in an analogous way with that for the hovering flight: combined CFD-CAA computations for five fan revolutions and $\Delta\psi_f = 1°$ per time step. Firstly, the aeroacoustic characteristics of the STR in the forward flight condition have been compared with that of the hovering flight. Thereafter, the reference simulation case using the isolated fuselage and STR has been compared with the simulation case where the main rotor downwash effect is modeled by use of an actuator disc to confirmed the assumption that the main rotor downwash is not relevant in this flight. The effect of the modeling order of turbulent flow on the computed far-field pressure has also been assessed by comparing the URANS simulation using the SST turbulence model with that using the SAS method. Afterwards, the noise generation mechanism by the interaction between the inlet flow distortion and rotating blades has been investigated. Finally, the influence of the horizontal stabilizer on the STR far field sound pressure level has been assessed. The predictive capability of the hybrid method in this specific flight condition has been demonstrated by comparing the calculated sound with measured data from DLR. The main observations of this chapter are as follows:

- In the forward flight condition, the STR operates under highly disturbed inflow condition. This is mainly due to the diverse airframe wake (e.g. fuselage, horizontal stabilizer) as well as to the inlet flow distortion provoked by collector lip flow separation. Therefore, the narrowband sound spectrum in the forward flight substantially differ from that in the hovering flight: significant increase in SPL between the rotational noise.
- Comprehensive comparisons of aerodynamic and acoustic characteristics between cases without and with actuator disc of steady-state load distribution conforms the assumption that the main rotor downwash effect is negligible in this flight condition. Hence, further investigations have been performed without actuator disc, which considerably reduces the modeling complexity in the CFD simulation.
- The additional SAS source term in the transport equation of ω significantly reduces the eddy viscosity in the flow regime of high flow unsteadiness. As a result, the SAS method provides a scale-resolved velocity and pressure field, and thus the computed acoustic sources involve more enhanced spectral contents, compared to the SST model.
- Regarding both the directivity and 1/3-octave spectra, a satisfactory agreement is found between the computed and measured sound. Generally, the FWH computation in combination with the SAS method provides a better matching with the flight test compared to the SST model. In particular, the SAS method predicts sound pressure levels high frequency noise with high accuracy due to its capability

to resolve turbulent flow in the source region. The SST model still provides a satisfactory sound pressure level regarding the most relevant frequency range between the lower and upper sidebands of the blade passing frequency with considerably lower computational efforts compared to the SAS method.

- The comparison between the reference simulation case and the case where the collector lip boundary layer separation is suppressed by means of boundary layer suction allows an in-depth understanding of the noise generation mechanism in the forward flight condition. The interaction between the blades and the inlet separation bubble causes significant blade load fluctuations as a consequence of the blade surface pressure distortion and the blade incidence angle change. As a result, the inflow distortion increases the overall sound pressure level by approx. 5 dB. In addition, the interaction results in a significant increase in the sound pressure level at $f/f_{\mathrm{BPF}} = 0.9$. In the case without inflow distortion, the rotor/shaft-fairing interaction becomes relevant and causes a noticeable increase in the sound pressure level of rotational noise. This is more significant for the observer points located on the fan outlet side.
- The horizontal stabilizer (HS)being installed directly upstream of the STR has an significant impact on the inflow condition of the anti-torque rotor. For instance, the HS divides the lower fuselage vortex (LFV) into two parts, thereby the anti-torque rotor ingests a substantial part of them. Together with the HS-wake and horseshoe vortices, the lower LFV is ingested into the fan. As a consequence of the interaction and resulting blade load distortions, the anti-torque rotor emits interaction noise. The maximum increase of the overall sound pressure level due to the HS amounts to 3 dB.

Chapter 6

Conclusion and Outlook

The shrouded tail rotor (STR), well-known as Fenestron, is a single stage axial flow fan embedded in the helicopter vertical tail fin. This type of tail rotor has been confirmed to be less noisy compared to the classical open tail rotor. This is first and foremost due to the duct construction, which surrounds the rotor blades and serves as an acoustic shield, as well as to supplementary measures for low noise emission, such as multi-blade configuration with unequal blade spacing. However, in certain helicopter operating conditions, in which the STR operates under cross flow, the STR becomes a significant source of aerodynamic noise. This is due to the strongly disrupted inflow condition resulting from diverse airframe wakes and collector lip flow separation. Therefore, further optimization in the STR aeroacoustics is of importance in order to satisfy the public demand for low helicopter noise levels and compliance with noise certification rules, which are becoming strict.

An essential prerequisite for the aeroacoustic optimization is an in-depth understanding of the STR aerodynamic behavior associated with the noise generation. In this context, the present work deals with the numerical study of the STR aeroacoustic characteristics for two representative helicopter operating conditions, namely the hovering and high-speed forward flight, with the objective of a detailed understanding of the flow physics associated with the noise generation. The hovering flight represents the ideal STR operating condition with high anti-torque thrust, but without any cross-flow impacts, whereas the high-speed forward flight demonstrates the low load condition under highly distorted inflow condition. The methodology employed in this work is a hybrid approach of the Computational Aeroacoustics (CAA), where aerodynamic noise sources are captured by the use of Computational Fluid Dynamics (CFD) and the noise radiation into the far field is predicted by using the Ffowcs Williams and Hawkings (FWH) acoustic analogy.

Comprehensive flow field analysis has been performed by means of unsteady Reynolds-averaged Navier-Stokes (URANS) simulations with the shear-stress transport (SST) turbulence model. The geometry investigated is a full-scale (1:1) shrouded tail rotor with a high geometric complexity involving ten unevenly spaced rotor blades and eleven evenly spaced stator vanes including a drive shaft fairing. Regarding numerical simulations for the forward flight condition, the helicopter fuselage has been also modeled in order to take into account possible noise generation by the interaction between airframe wake and

rotating blades. In addition to this, the influence of the scale-resolving capturing of aerodynamic noise sources on the prediction accuracy of the far-field sound pressure has been assessed by applying the scale-adaptive simulation (SAS) method. The effect of the main rotor downwash on the STR aeroacoustics in the forward flight condition has been also investigated by using an actuator disc model. The rotation of the anti-torque rotor has been modeled by means of the sliding mesh technique without using the interpolation technique for overlapping grids. An extensive data set, which contains transient flow quantities in the acoustic source region and serves as the input data for subsequent acoustic computations, has been created at every computational time step, corresponding to a blade rotation of $\Delta\psi_f = 1.0106°$ per time step. The accuracy of the CFD simulation has been assessed for the helicopter airframe (fuselage and vertical tail fin) in the wind tunnel model size (1:7.333) and for the forward flight condition. Results of both time-averaged and spectral analysis have shown a satisfactory global agreement with the experimental data provided by previous wind tunnel measurements including aerodynamic forces as well as steady and unsteady surface pressures.

Noise radiation from the STR into the far field has been predicted by applying the acoustic post-processing tool – Sound Prediction by Surface Integration (SPySI). The code is based on the FWH analogy of the porous integration surface extended by Farassat (Formulation I). The far-field noise extraction has been conducted with an acoustic time step size identical to the CFD time step size and performed for five fan revolutions. Due to the capture of the noise sources by the URANS approach and the acoustic solver employed does not evaluate the quadrupole noise term, the present work has focused on the generation and radiation of discrete noise components. Nevertheless, the contribution of quadrupole noise sources to the overall noise level have been implicitly taken into account by choosing two control surfaces that cover the inlet and outlet opening of the STR, respectively. To ensure a certain degree of accuracy of the calculated noise levels, comprehensive parameter and sensitivity studies on the control surface have been conducted. The capability of the acoustic hybrid method employed was evaluated by comparing calculated and measured noise levels. The measured STR noise levels were obtained with flight test campaigns of Airbus Helicopters Deutschland (AHD) and Deutsches Zentrum für Luft- und Raumfahrt (DLR) for the hovering and forward flight condition, respectively. For both flight conditions, a fairly good agreement has been observed between the calculated and measured noise spectra.

A detailed analysis on the STR flow field characteristics has been performed for the ideal hovering condition without any inflow distortions. Significant flow phenomena associated with the noise generation have been identified and documented. The contribution of the rotor/stator interaction on the far-field sound pressure has been investigated by comparing the reference stator configuration with the case where all stator vanes, except the drive shaft fairing, are removed. The main findings of the analysis are as follows:

- The comprehensive CFD simulations have presented noticeable flow phenomena including rotor/stator potential field interaction, blade-wake/stator interaction, tip-

leakage vortex, and corner separation at the vane-to-shroud intersection as well as at the vane-to-hub intersection.

- The interaction between the potential field of blades and stator vanes is one of the most important phenomenon that determines both the aerodynamic and acoustic characteristics of the STR in the hovering flight. The interaction alters the aerodynamic characteristics of the blade as it increases pressure levels on the lower surface of the blade significantly. The interaction is amplified when the blade is located above the drive shaft fairing. The pressure increase on the blade lower surface (at 40 % blade chord) relative to the non-interaction case amounts to 180 % in the interaction case with a stator vane and 670 % by the interaction with the drive shaft fairing.
- The potential field interaction increases the effective incidence angle of the blade and forces significant flow acceleration around the blade leading edge, which in turn results in a strong suction peak on the blade upper side. Consequently, the blade undergoes a sudden increase in the overall blade load. The resulting blade load by the interaction with the shaft fairing is approximately 63 % larger than by the interaction with the stator vane. The rotor/shaft-fairing interaction also induces a strong jet-like flow in the vicinity of the tip leakage. Thus, the formation of the tip-leakage vortex by the interaction becomes more significant compared to the non-interaction case.
- The uneven blade spacing has an effect on the effective blade incidence angle. The incidence angle increases, as the blade spacing to the neighboring blade increases. Consequently, the individual blade load as well as the peak load by the shaft fairing interaction strongly depends on the blade spacing. As a result of the uneven blade spacing and corresponding unequal blade loads, the overall fan thrust exhibits a distributed property. The power spectrum of the fan thrust bears a close similarity to the far-field noise spectrum: additional discrete components at frequencies in the lower ($f/f_{\mathrm{BPF}} = 1 - 0.2m$ with $m = 1, 2$) and upper sideband ($f/f_{\mathrm{BPF}} = 1 + 0.2m$) of the blade passing frequency (BPF, $f/f_{\mathrm{BPF}} = 1$). The discrete component at $f/f_{\mathrm{BPF}} = 0.8$ is even more dominant than at the BPF.
- The comparison of noise directivity between the hybrid method and the flight test of AHD shows a satisfactory agreement. Some overestimation has been observed, especially at observer points located on the bow side of the helicopter. The reason is that the hybrid method does not take into account any effects of the acoustic shielding of the fuselage. The comparison of narrowband spectra has shown that the hybrid approach is not only able to predict the noise level of the predominant discrete noise components at the BPF and in its lower and upper sidebands, but also noise levels between the discrete noise components with acceptable accuracy.

- The rotor/stator interaction (RSI) in the hovering condition causes a pronounced increase in the sound pressure level (SPL) of the discrete noise components, particularly on the port side of the STR. On the starboard side, especially in the azimuth range between $225° < \psi_h < 315°$, the RSI has only a minor impact on the far-field noise characteristics.

Comprehensive investigations on the STR external and internal flow field characteristics under superimposed cross-flow condition have been performed. The contribution of the inlet flow distortion provoked by the collector lip boundary layer separation on the far-field noise characteristics has been assessed by comparing the reference configuration to the non-distortion case with active flow control using boundary layer suction. Impacts of the horizontal stabilizer, installed upstream of the STR, on the aerodynamic and acoustic characteristics of the STR have been also evaluated. The main conclusions of the analysis on the forward flight condition are as follows:

- The internal flow field of the STR in the forward flight condition are strongly affected by (1) the airframe wake emanating from diverse parts of the fuselage and ingested into the anti-torque rotor area, (2) the inlet flow distortion resulting from collector lip boundary layer separation, and (3) the blade position relative to the incoming cross flow (advancing and retreating blade side). Due to the highly disturbed inflow and the interaction with the rotating blades, the acoustic characteristics of the STR in the forward flight condition differs considerably from that in the hovering condition. A significant increase in the SPL has been observed between rotational noise at the BPF and its lower and upper sideband frequencies, leading to a more broadband-like spectrum compared to the hovering condition.
- The influence of the main rotor downwash on the STR acoustics in the forward flight condition has been assessed by comparing the reference configuration (isolated fuselage with the STR) to the case where the main rotor impact is modeled by an actuator disc approach. On the superimposed actuator disc, a steady-state disc load, derived by using the helicopter aeromechanical simulation tool GenSim of AHD, has been distributed by using an in-house Python routine. The influence of the steady-state disc load on the surrounding flow field has been evaluated by solving the momentum equation, in which the disc load is specified as an additional source term. According to the comprehensive unsteady flow simulation and acoustic analysis of both the directivity and narrowband noise spectra, the induced downwash velocity of main rotor has only a small impact on the STR aerodynamic characteristics, thus no significant impact on the far-field noise characteristics. Hence, the isolated approach proves useful and advantageous for the case of high-speed forward flight as it can reduce the modeling complexity of the CFD simulation considerably.
- The effect of the modeling order of turbulent flow on the noise prediction has been evaluated by comparing the SST turbulence model with the scale-resolving SAS method. In the fuselage wake as well as inside the STR duct fairing, the URANS

simulation with the SAS model provides a comparably less dissipative flow field containing smaller turbulent structures than the SST model. This is due to the fact that the additional SAS source term, involving the von Kármán length scale, reduces the eddy viscosity in the flow regime where strong flow unsteadiness is detected.

- The predictive capability of the hybrid method in the forward flight condition has been demonstrated by comparing the computed data with the microphone measurement data obtained from the flight test campaigns of DLR. Comparing noise radiation characteristics on the directivity sphere, the result of the hybrid method shows a good agreement with the flight test data. Both predicted and measured directivities have indicated a dipole-like pattern with two major radiations, namely to the port and starboard side of the helicopter. However, in the case of computed directivities, the main radiation direction has been slightly shifted rearwards. Regarding the noise levels in 1/3-octave spectra, the hybrid method data shows a fairly good agreement with the flight test data, in particular at relevant frequencies, such as at $(f/f_{\mathrm{BPF}})_{1/3} = 0.8$ and $(f/f_{\mathrm{BPF}})_{1/3} = 1$, for different microphone positions. For the relatively high frequency range, the SAS method has provided a better matching with the flight test data than the SST model due to its capability to better resolve aerodynamic noise sources. Concerning the most relevant frequency range in the lower and upper sidebands of the BPF, the SST model still gives satisfactory results with less computational efforts, compared to the SAS method.
- The lip boundary layer separation and thus the resulting recirculating flow zones above the rotor plane is the most important flow phenomenon arising under cross-flow condition. It affects aerodynamic and acoustic characteristics of the STR markedly. The interaction between the separation bubble and the rotating blades results in the blade surface pressure distortion, blade incidence angle change, and consequently blade load distortions. Steady-state analysis using the actuator disc approach and subsequent unsteady CFD simulations using the sliding mesh method demonstrates that active flow control using boundary layer suction is an effective measure against the inflow distortion. The comparison of the far-field noise levels has indicated that the inflow distortion contributes to an increase in the overall sound pressure level by about 5 dB. Moreover, the interaction leads to a significant noise generation at $f/f_{\mathrm{BPF}} = 0.9$.
- The horizontal stabilizer (HS) installed directly upstream of the STR disrupts the fuselage wake significantly. Therefore, the lower fuselage vortex is divided into two parts and partly ingested into the STR anti-torque rotor area. Further vortices generated in the vicinity of the HS-tailboom intersection are also ingested into the fan. As a result, the STR emits interaction noise at the BPF and its sideband frequencies. The interaction noise is, however, less significant than the noise generated by the inflow distortion.

- Based on the computed STR noise signals, a psychoacoustic analysis was also performed in cooperation with the Institute for Human-Machine Communication of Technical University of Munich regarding the sharpness and loudness pattern of the STR noise in the forward flight condition.

Further CFD simulations can be performed with more sophisticated turbulence models, such as Detached Eddy Simulation (DES) and Large Eddy Simulation (LES) in order to obtain the high frequency contents of aerodynamic noise sources. The findings from CFD simulations, particularly related to the inflow distortion, should be validated by wind tunnel experiments by using Particle Image Velocimetry (PIV) and hot-wire as well as steady and unsteady surface pressure measurements, and/or by in-flight measurements. Regarding the application of the acoustic post-processing for the forward flight case, the acoustic solver should be further extended in order to consider the convective amplification, leading to a higher noise level in the flight direction than in the opposite direction.

References

[1] Advisory Council for Aviation Research and Innovation in Europe (ACARE), Flightpath 2050: Europe's Vision for Aviation. European Commission, Luxembourg, 2011.

[2] Chair of Aerodynamics and Fluid mechanics, Technical University of Munich. https://www.aer.mw.tum.de/windkanaele/windkanal-a/, accessed Oct. 31, 2016.

[3] Airbus Helicopters. https://www.airbushelicopters.com/website/en/ref/H135_30.html, accessed Sept. 7, 2016.

[4] A. Akturk and C. Camci. Tip Clearance Investigation of a Ducted Fan Used in VTOL UAVS Part 1: Baseline Experiments and Computational Validation. *Proceedings of the ASME Turbo Expo Turbine Technical Conference IGTI 2011*, Vancouver, Canada, June 2011.

[5] E. Alpman, L. M. Long, and B .D. Kothmann. Understanding Ducted-Rotor Antitorque and Directional Control Characteristics Part I: Steady-State Simulation. *Journal of Aircraft*, Vol. 41, No. 5, 2004, pp. 1042–1053.

[6] E. Alpman, L. M. Long, and B .D. Kothmann. Understanding Ducted-Rotor Antitorque and Directional Control Characteristics Part II: Unsteady Simulations. *Journal of Aircraft*, Vol. 41, No. 6, 2004, pp. 1370–1378.

[7] J. R. Andrews, R. G. Riley Jr., and C. Rahnke. Design and Testing of a Ducted Tail Rotor Concept Demonstrator for Model 222U Helicopter. *Proceedings of the* 22^{nd} *European Rotorcraft Forum*, Brighton, UK, September 1996.

[8] ANSYS. CFX-Solver Modeling Guide. Release 15.0, 2013.

[9] ANSYS. CFX-Solver Theory Guide. Release 15.0, 2013.

[10] ANSYS. ICEM CFD User's Manual. Release 15.0, 2013.

[11] J. E. Bardina, P. G. Huang, and T. J. Coakley. Turbulence Modeling Validation, Testing, and Development. NASA-TM-110446, 1997.

[12] T. J. Barth and D. C. Jespersen. The Design and Application of Upwind Schemes on Unstructured Meshes. *Proceedings of the* 27^{th} *Aerospace Sciences Meeting*, Reno, NV, 1989.

[13] M. Bebesel, A. D'Alascio, S. Schneider, S. Guenther, F. Vogel, C. Wehle, and D. Schimke. Bluecopter Demonstrator – an Approach to ECO-Efficient Helicopter Design. *Proceedings of the* 41^{st} *European Rotorcraft Forum*, Munich, Germany, September 2015.

[14] Willy J. G. Bräunling. Flugzeugtriebwerke - 3. Auflage. Springer Verlag, ISBN 978-3-540-76368-0, 2009.

[15] K. S. Brentner and F. Farassat. An Analytical Comparison of the Acoustic Analogy and Kirchhoff Formulation for Moving Surfaces. *AIAA Journal*, Vol. 36, No. 8, 1998, pp. 1379–1386.

[16] D. Casalino. An advanced time approach for acoustic analogy predictions. *Journal of Sound and Vibration*, Vol. 261, Issue 4, 2003, pp. 583–612.

[17] T. L. Chng, A. Rachman, H. M. Tsai, and Ge-Cheng Zha. Flow Control of an Airfoil via Injection and Suction. *Journal of Aircraft*, Vol. 46, No. 1, 2009, pp. 291–300.

[18] F. Le Chuiton. Acutator Disc Modelling for Helicopter Rotors. *Aerospace Science and Technology*, Vol. 8, Issue 4, 2004, pp. 285–297.

[19] K. H. Chung, K. W. Song, S. B. Kim, C. J. Hwang, and G. Joo. Development of Low Noise Ducted-Fan Tail Rotor for Helicopter Antitorque System. *Proceedings of the* 13^{th} *International Congress on Sound and Vibration*, Vienna, Austria, July 2006.

[20] A. J. Cooper and N. Peake. Rotor-Stator Ineraction Noise in Swirling Flow: Sator Sweep and Lean Effects. *AIAA Journal*, Vol. 44, No. 5, 2006, pp. 981–991.

[21] A. D'Alascio, F. Le Chuiton, E. Mouterde, L. Sudre, Kirstein S, and H.-P. Kau. Aerodynamic Study of the EC135 Fenestron in Hovering Flight Conditions by Means of CFD. *Proceedings of the American Helicopter Society* 64^{th} *Annual Forum*, Montréal, Canada, April 2008.

[22] A. D'Alascio, F. Le Chuiton, and K. Pahlke. Application of a Structured and an Unstructured CFD-Method to the Fuselage Aerodynamics of the EC145 helicopter. Prediction of the Time Averaged Influence of the Main Rotor. *Proceedings of the European Congress on Computational Methods in Applied Sciences and Engineering*, Jyväskylä, Finland, July 2004.

[23] L. Davidson. Evaluation of the SST-SAS Model: Channel Flow, Asymmetric Diffuser and Axi-Symmetric Hill. *Proceedings of the European Conference on Computational Fluid Dynamics*, 2006.

[24] M. Dietz, C. Maucher, and D. Schimke. Addressing Today's Aeromechanic Questions by Industrial Answers. *Proceedings of the American Helicopter Society Aeromechanics Specialists' Conference*, San Francisco, CA, Jan. 2010.

[25] A. Le Duc, P. Spiegel, F. Guntzer, M. Lummer, H. Buchholz, and J. Götz. Simulation of Complete Helicopter Noise in Maneuver Flight using Aeroacoustic Flight Test Database. *Proceedings of the American Helicopter Society* 64^{th} *Annual Forum*, Montréal, Canada, April 2008.

[26] B. Edwards and C. Cox. Revolutionary Concepts for Helicopter Noise Reduction– S.I.L.E.N.T. Program. NASA/CR-2002-211650, May 2002.

[27] Y. Egorov, F. Menter, R. Lechner, and D. Cokljat. The Scale-Adaptive Simulation Method for Unsteady Turbulent Flow Predictions. Part 2: Application to Complex Flows. *Flow, Turbulence and Combustion*, Vol. 85(1), 2010, pp. 139–165.

[28] K. Ehrenfried. Strömungsakustik. *Mensch & Buch Verlag*, ISBN 3-89820-699-8 2004.

[29] D. Ewald, A. Pavlovic, and J. G. Bollinger. Noise Reduction by Applying Modulation Principles. *Acoustical Society of America*, Vol. 49, 1971, pp. 1381–1385.

[30] Federal Aviation Administration (FAA). Stage 3 Helicopter Noise Certification Standards. 14 C.F.R. §36, FAA, 2014.

[31] Federal Aviation Administration (FAA). New York North Shore Helicopter Route. 14 C.F.R. §93, FAA, 2015.

[32] F. Falissard, F. Desmerger, P. Gardarein, L. Binet, and J.-C. Camus. Aeroacoustic Flight Test and Data Analysis for the Validation of Fenestron Noise Computations. *Proceedings of the American Helicopter Society* 67^{th} *Annual Forum*, Virginia Beach, VA, May 2011.

[33] F. Farassat. Derivation of Formulation 1 and 1A of Farassat. NASA/TM-2007-214853, 2007.

[34] H. Fastl, J. Putner, J. H. You, C. Breitsamter, and P. Krämer. Psychoacoustic Aspects of Helicopter Sounds. *Proceedings of the international conference of acoustics AIA-DAGA 2013*, Merano, Italy, March 2013.

[35] J. Fröhlich and D. von Terzi. Hybrid LES/RANS Methods for the Simulation of Turbulent Flows. *Progress in Aerospace Sciences*, Vol. 44, 2008, pp. 349–377.

[36] P. Gardarein, S. Canard, and J. Prieur. Unsteady Aerodynamic and Aeroacoustic Simulations of a Fenestron Tail Rotor. *Proceedings of the American Helicopter Society* 62^{nd} *Annual Forum*, Phoenix, Arizona, May 2006.

[37] P. Gardarein, F. Falissard, L. Binet, and J.-C. Camus. Validation of Aerodynamic and Aeroacoustic Computations of a Fenestron in Real Flight Conditions. *Proceedings of the* 36^{th} *European Rotorcraft Forum*, Paris, France, September 2010.

[38] V. Gareton, M. Gervais, and R. Heger. Acoustic Design and Testing of the Eurocopter EC145T2 and EC175B – a harmonized Franco-German Approach. *Proceedings of the* 39^{th} *European Rotorcraft Forum*, Moscow, Russia, Sepember 2013.

[39] A. R. George and S. T. Chou. A Comparative Study of Tail Rotor Noise Mechanisms. *Journal of the American Helicopter Society*, Vol. 31, No. 4, 1986, pp. 36–42.

[40] P. R. Gliebe. Aeroacoustics in Turbomachines and Propellers–Future Research Needs. edited by H.M. Atassi, Springer-Verlag, 1991, pp. 619–642.

[41] T. Heinemann, C. Scheit, M. Springer, S. Müller, and S. Becker. Stationary and Moving Surface Ffowcs Williams and Hawkings Computations of an Isolated Radial Impeller. *Proceedings of the Fan 2012 Symposium*, Senlis, France, April 2012.

[42] J. C. R. Hunt, A. A. Wray, and P. Moin. Eddies, Streams, and Convergence Zones in Turbulent Flows. *Proceedings of the Summer Program 1988*, Center for Turbulence Research, Report N89–24555, 1988, pp. 193–208.

[43] International Civil Aviation Organization (ICAO). Annex 16 to the Convention on International Civil Aviation: Environmental Protection, Volume I – Aircraft Noise. ICAO, 2011.

[44] International Civil Aviation Organization (ICAO). Helicopter Noise Reduction Technology – Status Report. ICAO, 2015.

[45] E. W. Jacobs, J. Mancini, J. A. Visintainer, and T. A. Jackson. Acousitc Flight Test Results for the Sikorsky S-76 Quiet Tail Rotor at Reduced Tip Speed. *Proceedings of the American Helicopter Society* 53^{rd} *Annual Forum*, Virginia Beach, VA, April 1997.

[46] H. Jasak, H. G. Weller, and A. D. Gosman. High Resolution NVD Differencing Scheme for Arbitrarily Unstructured Meshes. *Int. J. Numer. Meth. Fluids*, Vol. 31, 1999, pp. 431–449.

[47] M. Kainz, F. Danner, H. P. Kau, and F. Le Chuiton. Numerical Investigation into the Unsteady Aerodynamics of a Ducted Helicopter Tail Rotor under Side-Wind Conditions. *Proceedings of the ASME Turbo EXPO 2010*, Glasgow, UK, June 2010.

[48] M. Kainz, H. P. Kau, and F. Le Chuiton. Aeroacoustic Near-Field Study of a Ducted Helicopter Tail Rotor with Different Vane Count by use of Phase-Lagged Boundaries. *Proceedings of the* 14^{th} *International Symposium on Transport Phenomena and Dynamics of Rotating Machinery*, Honolulu, HI, February 2012.

[49] M. Kainz, H. P. Kau, and F. Le Chuiton. Near-Field Noise Reduction of a Ducted Helicopter Tail Rotor due to a Modified Stator Vane Geometry. *Proceedings of the ASME Turbo EXPO 2012*, Copenhagen, Denmark, June 2012.

[50] S. Kaji and T. Okazaki. Generation of Sound by Rotor-Stator Interaction. *Journal of Sound and Vibration*, Vol. 13, Issue 3, 1970, pp. 281–307.

[51] A. Kaltenhauser, S. Kolb, F. Ullrich, and L. Polansky. Neue Modulwaage im Akustikwindkanal von BMW. *Automobiltechnische Zeitschrift (ATZ)*, Jahrgang 108, December 2006.

[52] V. Kolář. Vortex Identification: New Requirements and Limitations. *International Journal of Heat and Fluid Flow*, Vol. 28, Issue 4, 2007, pp. 638–652.

[53] G. Krishnappa. Lifting Fan Noise Studies with Superimposed Cross Flows. *Journal of Aircraft*, Vol. 9, No. 10, 1972, pp. 719–725.

[54] M. Lafargue. The Shrouded Tail Rotor "Fenestron". *Proceedings of the* 2^{nd} *European Rotorcraft Forum*, Bückeburg, Germany, September 1975.

[55] H. D. Lee and O. J. Kwon. Detailed Aerodynamic Analysis of a Shrouded Tail Rotor Using an Unstructured Mesh Flow Solver. *Transactions of the Japan Society for Aeronautical and Space Sciences*, Vol. 47, No. 155, 2004, pp. 23–29.

[56] J. G. Leishman. Principles of Helicopter Aerodynamics – second edition. Cambridge University Press, ISBN 978-0-521-85860-1, 2006.

[57] B.P. Leonard. The ULTIMATE Conservative Difference Scheme Applied to Unsteady One-Dimensional Advection. *Computer Methods in Applied Mechanics and Engineering*, Vol. 88, Issue 1, 1991, pp. 17–74.

[58] J. W. Leverton. Reduction of Helicopter Noise by Use of a Quiet Tail Rotor. *Proceedings of the* 6^{th} *European Rotorcraft Forum*, Bristol, England, September 1980.

[59] J. W. Leverton, J. S. Pollard, and C. R. Wills. Main Rotor Wake/Tail Rotor Interaction. *Proceedings of the* 1^{st} *European Rotorcraft Forum*, Southampton, England, September 1975.

[60] J. M. Lighthill. On Sound Generated Aerodynamically. I. General Theory. *Proceedings of the Royal Society of London. Series A: Mathematical and physical sciences*, Vol. 211(1107), 1952, pp. 564–587.

[61] J. M. Lighthill. On Sound Generated Aerodynamically. II. Turbulence as a Source of Sound. *Proceedings of the Royal Society of London. Series A: Mathematical and physical sciences*, Vol. 222 (1148), 1954, pp. 1–32.

[62] D. P. Lockard and J. H. Casper. Permeable Surface Correction for Ffowcs Williams and Hawkings Integrals. *Proceedings of the* 11^{th} *AIAA/CEAS Aeroacoustic Conferences*, Monterey, CA, May 2005.

[63] Leibniz Supercomputing Centre (LRZ). https://www.lrz.de/services/compute/supermuc/systemdescription/, accessed Oct. 31, 2016.

[64] J. E. Marte and D. W. Kurtz. A Review of Aerodynamic Noise from Propellers, Rotors, and Lift Fans. NASA Technical Report, 32-1462, 1970.

[65] H.-J. R. Marze, V. J.-L. Routhieau, G. L. Arnaud, and R. E. Arnaud. U.S. Patent No. 5,588,618, Dec. 31, 1996.

[66] F. Menter. Two-Equation Eddy-Viscosity Turbulence Models for Engineering Applications. *AIAA Journal*, Vol. 32, No. 8, 1994, pp. 1598–1605.

[67] F. Menter. Best Practice: Scale-Resolving Simulations in ANSYS CFD. Version 2.0, ANSYS, 2015.

[68] F. Menter and Y.Egorov. The Scale-Adaptive Simulation Method for Unsteady Turbulent Flow Predictions. Part 1: Theory and Model Description. *Flow, Turbulence and Combustion*, Vol. 85, Issue 1, 2010, pp. 113–138.

[69] R. Mouille. The "Fenestron", Shrouded Tail Rotor of the SA. 341 Gazelle. *Journal of the American Helicopter Society*, Vol. 15, No. 4, 1970, pp. 31–37.

[70] R. Mouille and F. d'Ambra. The "Fenestron" a Shrouded Tail Rotor Concept for Helicopters. *Proceedings of the American Helicopter Society* 42^{nd} *Annual Forum*, Washington, D.C., June 1986.

[71] E. Mouterde, L. Sudre, A. M. Dequin, A. D'Alascio, and P. Haldenwang. Aerodynamic Computations of Isolated Fenestron in Hover Conditions. *Proceedings of the* 33^{rd} *European Rotorcraft Forum*, Kazan, Russia, September 2007.

[72] W. Neise and U. Michel. Aerodynamic Noise of Turbomachines. DLR Internal Report 22314-94/B5, 1994.

[73] G. Niesl and G. Arnaud. Low Noise Design of the EC 135 Helicopter. *Proceedings of the American Helicopter Society* 52^{nd} *Annual Forum*, Washington, D.C., June 1996.

[74] G. Niesl and G. Arnaud. Reduction of the Noise Signature of the Eurocopter EC135. *Proceedings of the Flight Vehicle Integration Panel Symposium on "Advances in Rotorcraft Technology"*, Ottawa, Canada, May 1996.

[75] T. A. Nygaard and A. C. Dimanlig. Application of a Momentum Source Model to the RAH-66 Comanche FANTAIL. *Proceedings of the American Helicopter Society* 4^{th} *Decennial Specialist's Conference on Aeromechanics*, San Francisco, CA, Jan 2004.

[76] J. Putner and H. Fastl. Klangqualitätsbezogene übertragungspfadanalyse und -synthese. Abschlussbericht: Bayerischer Forschungsverbund zur Lärmminderung von technischen Anlagen (FORLärm) - Methoden und Verfahren zur Reduzierung des Lärms von Maschinen und Anlagen, Bayerische Forschungsstiftung, 2013, pp. 44–51.

[77] R. Ganesh Rajagopalan and C. N. Keys. Detailed Aerodynamic Analysis of the RAH-66 FANTAIL Using CFD. *Journal of the American Helicopter Society*, Vol. 42, No. 4, 1997, pp. 310–320.

[78] O. Recker and G. Neuwerth. Noise Reduction of Fenestrons Using Intergrated Helmholtz Resonators. *Proceedings of the* 24^{th} *European Rotorcraft Forum*, Marseille, France, September 1998.

[79] T. Renaud, D. O'Brien, M. Smith, and M. Potsdam. Evaluation of Isolated Fuselage and Rotor-Fuselage Interaction Using CFD. *Proceedings of the American Helicopter Society* 60^{th} *Annual Forum*, Baltimore, MD, June 2004.

[80] F. Robinson. Component Noise Variables of a Light Observation Helicopter. NASA-CR-114761, 1973.

[81] M. Roger and F. Fournier. An Analysis of In-Fin Tail Rotor Noise. *Proceedings of the* 20^{th} *European Rotorcraft Forum*, Garmisch-Partenkirchen, Germany, September 1986.

[82] M. Roger, S. Moreau, and A. Guédel. Vortex-Shedding Noise and Potential-Interaction Noise Modeling by a Reversed Sears' Problem. *Proceedings of the* 12^{th} *AIAA/CEAS Aeronautics Conference*, Cambridge, MA, May 2006.

[83] J. Rotta. Statistische Theorie nichthomogener Turbulenz. *Zeitschrift für Physik*, Vol. 129, Issue 6, 1951, pp. 547–572.

[84] G. C. Ruzicka, R. C. Strawn, and E. T. Meadowcroft. Discrete-Blade, Navier-Stokes Computational Fluid Dynamics Analysis of Ducted-Fan Flow. *Journal of Aircraft*, Vol. 42, No. 5, 2005, pp. 1109–1117.

[85] C. L. Scheit. Implementation of Ffowcs Williams and Hawkings (FW-H) method for aeroacoustic prediction. Master Thesis, Friedrich-Alexander University Erlangen-Nürnberg, Germany, 2008.

[86] C. L. Scheit, B. Karic, and S. Becker. Effect of blade wrap angle on efficiency and noise of small radial fan impellers – A computational and experimental study. *Journal of Sound and Vibration*, Vol. 331, Issue 5, 2012, pp. 996–1010.

[87] F. H. Schmitz and Y. H. Yu. Transonic Rotor Noise – Theoretical and Experimental Comparisons. NASA-TM-81236, 1980.

[88] I.J. Sharland. Sources of Noise in Axial Flow Fans. *Journal of Sound and Vibration*, Vol. 1, Issue 3, 1964, pp. 302–322.

[89] R. K. Shenoy. U.S. Patent No. 5,137,427, Aug. 11, 1992.

[90] R. K. Shenoy, R. C. Moffitt, C. M. Yoerkie, and O. Childress Jr. Development and Validation of "Quiet Tail Rotor" Technology. *Proceedings of the AHS International Specialists Meeting on Rotorcraft Acoustics and Fluid Dynamics*, Philadelphia, PA, October 1991.

[91] P. Spiegel, F. Guntzer, A. Le Duc, and H. Buchholz. Aeroacousitc Flight Test Data Analysis and Guidelines for Noise-Abatement-Procedure Design and Piloting. *Proceedings of the* 34^{th} *European Rotorcraft Forum*, Liverpool, UK, September 2008.

[92] G. Steidl. Extraction and Analysis of Fenestron Noise from DLR PAVE Flight Test. Final Report for ECO HELI AP 4.1, IB 124-2011/909, Institute of Aerodynamics and Flow Technology, DLR, Braunschweig, Germany, August 2011.

[93] D. L. Stimpert. Effect of Crossflow Velocity on VTOL Lift fan Blade Passing Frequency Noise Generation. NASA-CR-114566, 1973.

[94] B. M. Sullivan, B. D. Edwards, K. S. Brentner, and E. R. Booth Jr. A Subjective Test of Modulated Blade Spacing for Helicopter Main Rotors. *Proceedings of the American Helicopter Society* 58^{th} *Annual Forum*, Montréal, Canada, June 2002.

[95] N. Thouault. Aerodynamic Investigation on Generic Fan-in-Wing Configurations. Ph.D. Dissertation, Technical University of Munich, Verlag Dr. Hut, ISBN 978-3-86853-771-0, 2010.

[96] N. Thouault, C. Breitsamter, and N. A. Adams. Numerical and Experimental Analysis of a Generic Fan-in-Wing Configuration. *Journal of Aircraft*, Vol. 46, No. 2, 2009, pp. 656–666.

[97] N. Thouault, C. Breitsamter, and N. A. Adams. Numerical Investigation of Inlet Distortion on a Wing-Embedded Lift Fan. *Journal of Propulsion and Power*, Vol. 27, No. 1, 2011, pp. 16–28.

[98] J. Tirakala, N. Thouault, C. Breitsamter, and N. A. Adams. Aerodynamic Investigations of a Generic Fan-in-Wing Configuration. *Proceedings of the Internoise 2011*, Osaka, Japan, September 2011.

[99] J. Tirakala, N. Thouault, J. H. You, C. Breitsamter, and N. A. Adams. Aeroacoustic Investigations of a Generic Fan-in-Wing Configuration – Aeroacoustics Research in Europe: The CEAS-ASC Report on 2011 Highlights. *Journal of Sound and Vibration*, Vol. 331, 2012, pp. 4626–4627.

[100] M. Vialle and G. Arnaud. A New Generation of Fenestron Fan–in–Fin Tail Rotor on EC 135. *Proceedings of the* 19^{th} *European Rotorcraft Forum*, Cernobbio, Italy, September 1993.

[101] F. Vogel. Aerodynamische Analysen an Helikopter Zellen-Ausleger Konfigurationen. Ph.D. Dissertation, Technical University of Munich, Verlag Dr. Hut, ISBN 978-3-8439-2696-6, 2016.

[102] A. Vuillet and F. Morelli. New Aerodynamic Design of the Fenestron for Improved Performance. *Proceedings of the* 12^{th} *European Rotorcraft Forum*, Garmisch-Partenkirchen, Germany, September 1986.

[103] M. Weisgerber and G. Neuwerth. Influence of a Helicopter Tail Rotor Shroud on the Interaction Noise due to the Main Rotor Vortices. *Proceedings of the* 29^{th} *European Rotorcraft Forum*, Friedrichshafen, Germany, September 2003.

[104] J. E. Ffowcs Williams and D. L. Hawkings. Sound Generation by Turbulence and Surfaces in Arbitrary Motion. *Philosophical Transactions of the Royal Society A: Mathematical and physical sciences*, Vol. 264(1151), 1969, pp. 321–342.

[105] M. A. Yerry and M. S. Shephard. Automatic Three-Dimensional Mesh Generation by the Modified-Octree Technique. *International Journal for Numerical Methods in Engineering*, Vol. 20, Issue 11, 1984, pp. 1965–1990.

[106] J. H. You and C. Breitsamter. Numerical Investigation of Aeroacoustic Sound Sources in Encapsulated Helicopter Tail Rotor. *Proceedings of the international conference of acoustics AIA-DAGA 2013*, Merano, Italy, March 2013.

[107] J. H. You and C. Breitsamter. Numerische Untersuchung der aeroakustischen Charakteristik des gekapselten Hubschrauber-Heckrotors. Vorkolloquium: Numerische Strömungsakustik, DAGA 2015, Nürnberg, Germany, March 2015.

[108] J. H. You and C. Breitsamter. Aeroacoustic Analysis of Ducted Helicopter Tail Rotor. High Performance Computing in science and engineering – Garching/Munich, Bayrische Akademie der Wissenschaften, 2014, pp. 86–87.

[109] J. H. You, C. Breitsamter, and N. A. Adams. Berechnung aerodynamischer Schallquellen gekapselter Heckrotoren. Abschlussbericht: Bayerischer Forschungsverbund zur Lärmminderung von technischen Anlagen (FORLärm) - Methoden und Verfahren zur Reduzierung des Lärms von Maschinen und Anlagen, Bayerische Forschungsstiftung, 2013, pp. 34–43.

[110] J. H. You, C. Breitsamter, and R. Heger. Numerical Investigations of Fenestron Noise Characteristics Using a Hybrid Method. *Proceedings of the* 62^{th} *Deutscher Luft- und Raumfahrtkongress–DLRK 2013*, Stuttgart, Germany, September 2013.

[111] J. H. You, C. Breitsamter, and R. Heger. Numerical Investigations of Fenestron Noise Characteristics using a Hybrid Method. *CEAS Aeronautical Journal*, Vol. 7, Issue 2, 2016, pp. 185–207.

[112] J. H. You, N. Thouault, and C. Breitsamter. Aeroakustische Untersuchung des gekapselten Hubschrauber-Heckrotors für den Vorwärtsflugzustand. Gemeinsame DGLR- und DEGA-Fachausschusssitzung unter Ausrichtung durch X-Noise-Netzwerk: Simulation und Validierung bei Strömungsschallproblemen in der Luftfahrt, Fahrzeug- und Anlagentechnik, Berlin, Germany, December 2011.

[113] J. H. You, N. Thouault, and C. Breitsamter. Computational Aeroacoustic Analysis of Encapsulated Helicopter Tail Rotor. *Proceedings of the* 16^{th} *Workshop of the Aeroacoustics Specialist Committee of CEAS, simultaneously* 2^{nd} *Scientific Workshop of the European X-Noise EV Network: Aeroacoustic Installation Effects & Novel Aircraft Architectures*, Braunschweig, Germany, October 2012.

[114] J. H. You, N. Thouault, C. Breitsamter, and N. A. Adams. Aeroacoustic Analysis of a Helicopter Confguration with Ducted Tail Rotor. *Proceedings of the* 28^{th} *Congress of the International Council of Aeronautical Sciences, ICAS*, Brisbane, Australia, September 2012.

[115] Y. H. Yu. Rotor Blade–Vortex Interaction Noise. *Progress in Aerospace Sciences*, Vol. 36, Issues 2, 1997, pp. 647–687.

[116] Y. Zurcher. ROSI v1.2 User Manual. *Internal Document*, Airbus Helicopters, August 2014.